Conference Proceedings of the Society for Experimental Mechanics Series

Matt Allen · Randall L. Mayes · Daniel J. Rixen *Editors*

Dynamics of Coupled Structures, Volume 4

Proceedings of the 33rd IMAC, A Conference and Exposition on Structural Dynamics, 2015

SEM

Springer

Conference Proceedings of the Society for Experimental Mechanics Series

Series Editor

Tom Proulx
Society for Experimental Mechanics, Inc.,
Bethel, CT, USA

More information about this series at http://www.springer.com/series/8922

Matt Allen • Randall L. Mayes • Daniel J. Rixen
Editors

Dynamics of Coupled Structures, Volume 4

Proceedings of the 33rd IMAC, A Conference and Exposition on Structural Dynamics, 2015

Springer

Editors
Matt Allen
Engineering Physics Department
University of Wisconsin-Madison
Madison, WI, USA

Randall L. Mayes
Sandia National Laboratories
Albuquerque, NM, USA

Daniel J. Rixen
Lehrstuhl fur Angewandte Mechanik
Technische Universitat Munchen
Garching, Germany

ISSN 2191-5644 ISSN 2191-5652 (electronic)
Conference Proceedings of the Society for Experimental Mechanics Series
ISBN 978-3-319-15208-0 ISBN 978-3-319-15209-7 (eBook)
DOI 10.1007/978-3-319-15209-7

Library of Congress Control Number: 2014932412

Springer Cham Heidelberg New York Dordrecht London

Printed on acid-free paper

Springer International Publishing AG Switzerland is part of Springer Science+Business Media (www.springer.com)

Preface

Dynamics of Coupled Structures represents one of ten volumes of technical papers presented at the 33rd IMAC, A Conference and Exposition on Balancing Simulation and Testing, 2015, organized by the Society for Experimental Mechanics, and held in Orlando, Florida, February 2–5, 2015. The full proceedings also include volumes on Nonlinear Dynamics; Dynamics of Civil Structures; Model Validation and Uncertainty Quantification; Sensors and Instrumentation; Special Topics in Structural Dynamics; Structural Health Monitoring & Damage Detection; Experimental Techniques, Rotating Machinery & Acoustics; Shock & Vibration Aircraft/Aerospace, Energy Harvesting; and Topics in Modal Analysis.

Each collection presents early findings from experimental and computational investigations on an important area within Structural Dynamics. Coupled structures or, substructuring, is one of these areas.

Substructuring is a general paradigm in engineering dynamics where a complicated system is analyzed by considering the dynamic interactions between subcomponents. In numerical simulations, substructuring allows one to reduce the complexity of parts of the system in order to construct a computationally efficient model of the assembled system. A subcomponent model can also be derived experimentally, allowing one to predict the dynamic behavior of an assembly by combining experimentally and/or analytically derived models. This can be advantageous for subcomponents that are expensive or difficult to model analytically. Substructuring can also be used to couple numerical simulation with real-time testing of components. Such approaches are known as hardware-in-the-loop or hybrid testing.

Whether experimental or numerical, all substructuring approaches have a common basis, namely the equilibrium of the substructures under the action of the applied and interface forces and the compatibility of displacements at the interfaces of the subcomponents. Experimental substructuring requires special care in the way the measurements are obtained and processed in order to assure that measurement inaccuracies and noise do not invalidate the results. In numerical approaches, the fundamental quest is the efficient computation of reduced order models describing the substructure's dynamic motion. For hardware-in-the-loop applications, difficulties include the fast computation of the numerical components and the proper sensing and actuation of the hardware component. Recent advances in experimental techniques, sensor/actuator technologies, novel numerical methods, and parallel computing have rekindled interest in substructuring in recent years leading to new insights and improved experimental and analytical techniques.

The organizers would like to thank the authors, presenters, session organizers, and session chairs for their participation in this track.

University of Wisconsin-Madison, Madison, WI, USA	Matt Allen
Sandia National Laboratories, Albuquerque, NM, USA	Randall L. Mayes
Technische Universitat Munchen, Garching, Germany	Daniel J. Rixen

Contents

Chapter 1
Robust Stability and Performance Analysis for Multi-actuator Real-Time Hybrid Substructuring

Rui M. Botelho and Richard E. Christenson

Abstract Real-time hybrid substructuring (RTHS) is a relatively new method of vibration testing for characterizing the system-level performance of physical components or substructures. With RTHS, the coupled system is partitioned into physical and numerical substructures and interfaced together in real-time as cyber-physical system similar to hardware-in-the-loop testing. Control actuation and sensing is used to enforce the compatibility and equilibrium conditions between the physical and numerical substructures. Since RTHS involves a feedback loop, the frequency-dependent magnitude and inherent time delay of the actuator dynamics can introduce inaccuracy and instability. This paper presents a robust stability and performance analysis method for multi-actuator RTHS based on robust stability theory for multiple-input-multiple-output (MIMO) feedback control. This analysis method involves casting the actuator dynamics as a multiplicative uncertainty and applying the small gain theorem to derive the sufficient conditions for robust stability and performance. The attractive feature of this robust stability and performance analysis method is that it accommodates linearized modeled or measured frequency response functions for both the physical substructure and actuator dynamics.

Keywords Experimental structural dynamics • Real-time hybrid testing • Dynamic substructuring • Hardware-in-the-loop testing • Robust stability • Feedback control systems

1.1 Introduction

Real-time hybrid substructuring (RTHS), also called real-time hybrid simulation or real-time dynamic substructuring, is a relatively new method of vibration testing in experimental structural dynamics. RTHS allows a coupled system to be partitioned into separate physical and numerical components or substructures. The substructures that are well understood are simulated in real-time using analytical or numerical models, while those that are highly complex or of particular interest are physically tested using physical specimens. The physical and numerical substructures are interfaced together as cyber-physical system similar to hardware-in-the-loop (HWIL) testing. In a RTHS test, the numerical and experimental substructures communicate together in real-time by transferring displacement and force signals through a feedback loop using controlled actuation and sensing. The physical substructure is usually the experimental component of interest, while the numerical substructure is typically an analytical or numerical model of the remaining system incorporating various complexities that may be difficult to represent physically. RTHS has recently become more feasible due to advances in numerical computing power, digital signal processing, and high-speed servo-hydraulic actuation.

Early developments of RTHS include Horiuchi et al. [1, 2], Nakashima and Masaoka [3], and Darby et al. [4]. RTHS is also a major element of the Network for Earthquake Engineering Simulation (NEES). For example, Christenson and Lin [5] describe a large-scale RTHS test setup at the University of Colorado Boulder NEES facility to examine the system-level performance of multiple 200 kN MR fluid dampers in a three-story building structure. Jiang et al. [6] describe recent RTHS testing at the Lehigh University NEES facility of full-scale MR dampers attached to a bridge structure, and Friedman et al. [7] describe RTHS tests at the Lehigh University NEES facility using the same MR dampers installed in a seismically excited steel moment resisting frame.

Figure 1.1 illustrates the block diagram of a typical RTHS test. At a given time-step, numerical loading is applied to the numerical substructure to simulate the numerical displacements, x_n, to be imposed on the physical substructure in real-time. The numerical displacements are then fed into a controller to apply the command displacement, x_c, to the actuator transfer

R.M. Botelho (✉) • R.E. Christenson
Department of Civil and Environmental Engineering, University of Connecticut, 261 Glenbrook Road
Unit 3037, Storrs, CT 06269-3037, USA
e-mail: rui.botelho@uconn.edu

M. Allen et al. (eds.), *Dynamics of Coupled Structures, Volume 4*, Conference Proceedings of the Society
for Experimental Mechanics Series, DOI 10.1007/978-3-319-15209-7_1

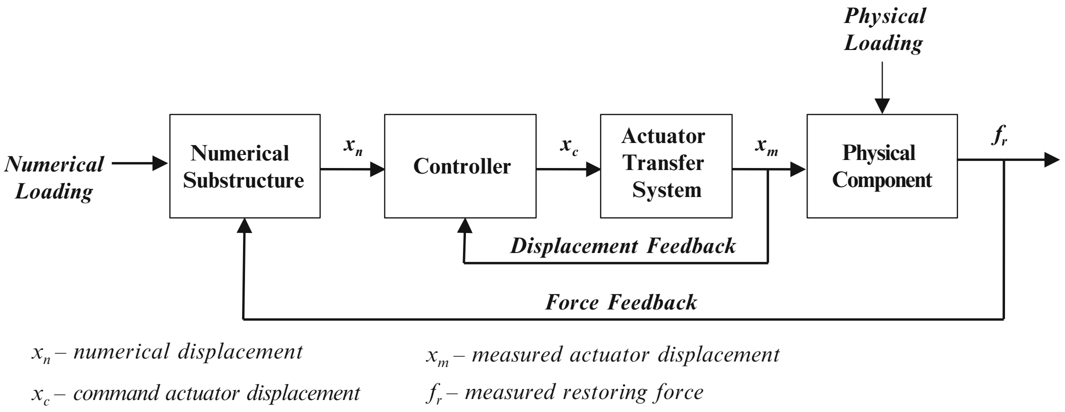

Fig. 1.1 Block diagram of a typical RTHS test

system, which is usually a set of hydraulic actuators controlled by a proportional-integral-derivative (PID) servo-controller using the measured displacement, x_m, as the feedback signal. The measured restoring force, f_r, of the physical substructure is then fed back into the numerical substructure to compute the numerical displacements for the next time step. RTHS also accommodates physical loading of the physical substructure from external shaker forcing of the physical specimen. This closed-loop testing method makes RTHS very similar to HWIL testing, whereby a real-time virtual model is directly interfaced with actual physical hardware forming a cyber-physical system.

Since RTHS involves a feedback loop, the inherent time delay of the actuator transfer system can lead to inaccuracy in the actuator tracking and potential instability during closed-loop testing. The effect of time delay on RTHS testing was initially considered by Horiuchi et al. [1], who showed that actuator delay can cause an increase in the total energy, which is equivalent to introducing negative damping into the system. When the negative damping is larger than the total system damping, the RTHS test will become unstable. Previous RTHS tests without actuator delay compensation had been performed for systems with very low natural frequencies and high damping to ensure stability. There are also other sources of time delay in a RTHS test, including communication delays of the various electrical signals and computational delays for solving the numerical substructure. These time delays are generally much smaller than the inherent time delay of the actuator transfer system.

To improve the closed-loop stability and performance of RTHS, researchers have developed a variety of techniques for compensating the time delay or more generally the frequency dependent dynamics of the actuator transfer system. The techniques range from polynomial extrapolation in Horiuchi et al. [1] and inverse compensation in Chen and Ricles [8] to reduce the actuator delay as well as adaptive techniques in Chen and Ricles [9] and Chae et al. [10]. Carrion and Spencer [11] used a controls approach to develop model-based feedforward-feedback control to compensate the frequency-dependent magnitude and phase of the actuator dynamics. Phillips and Spencer [12] extended this approach with a more accurate feedforward inverse of the actuator dynamics and adding linear-quadratic Gaussian (LQG) feedback control. Christenson and Lin [5] employed virtual coupling to balance closed-loop stability and performance in RTHS testing of large-scale MR dampers. Gao et al. [13] recently developed an H-infinity robust loop-shaping controller to compensate the actuator dynamics for RTHS testing of lightly damped steel frame structures. The ultimate goal of these compensation techniques is to provide effective displacement tracking of the actuator transfer system over the desired frequency range of the RTHS test, called the control band.

Stability and performance analysis is an important tool for understanding the effect of actuator time delay on the stability behavior and accuracy of RTHS. This information is especially useful in guiding the compensation design of the actuator transfer system to reduce its inherent time delay and provide closed-loop stability and performance. Wallace et al. [14] studied the effect of actuator time delay using delay differential equation (DDE) modeling of a single degree of freedom (SDOF) RTHS system comprised of a physical stiffness coupled to an analytically modeled mass-spring oscillator. This approach yields a governing characteristic equation with an exponential delay term whose solution has an infinite number of roots. The purely imaginary roots define the critical frequencies at which switches in the stability behavior of the system occur and can be used to identify the critical time delays of the RTHS system. Kyrychko et al. [15] applied a similar approach to identify the critical time delays for RTHS of a physical pendulum coupled to an analytical mass-spring oscillator, but using neutral DDE's.

Mercan and Ricles [16] applied a pseudodelay technique to solve the DDE for a SDOF RTHS system and identified the critical time delays in terms of the mass, damping, stiffness parameters of the test structure. Mercan and Ricles [17] extended the pseudodelay technique to evaluate multiple sources of time delay including those for multi-actuator RTHS. Fudong et al. [18] employed a Padé rational fraction approach to approximate the exponential delay term and used a root locus technique to investigate the relationship between the closed-loop poles and substructure partitioning parameters on the stability conditions of a SDOF RTHS system. Botelho et al. [19] presented an exact stability analysis technique for single-actuator RTHS of 1-DOF and 2-DOF mass-spring systems to quantify their critical time delays. Although these stability analysis techniques provide insight into the stability behavior of RTHS, they assume pure time delay for the actuator dynamics and are limited to lumped parameter descriptions of the numerical and physical substructures.

While progress has been made in the development of stability analysis techniques for RTHS, performance analysis has received less attention. Maghareh et al. [20] recently proposed a predictive performance indicator for SDOF RTHS to assess the effect of actuator time delay as well as computational and communication delays on the accuracy of RTHS. The predictive performance indicator also provides insight on the effect of mass, stiffness, and damping partitioning of the physical and numerical substructures. This performance indicator can be used in conjunction with a stability switch criterion based on the exact solution for the critical time delays of the RTHS system to derive acceptance criteria for conducting successful RTHS tests.

This paper presents a new robust stability and performance analysis method for multi-actuator RTHS based on the concepts from robust stability theory for multiple-input-multiple-output (MIMO) feedback control systems. This method involves casting the actuator dynamics of the RTHS feedback loop as a multiplicative uncertainty and then applying the small gain theorem to derive sufficient conditions for robust stability and performance for RTHS. Gawthrop et al. [21] was first to consider robust stability in RTHS, in which they used the robust stability criterion in Goodwin et al. [22] to study the stability of single-actuator RTHS, but assumed a pure time delay for the actuator transfer system. Recognizing the versatility of this approach, this paper presents an extension of robust stability analysis to consider robust performance and multi-actuator RTHS. Unlike previous stability analysis techniques which assume pure time delay, this method accommodates the linearized modeled or measured frequency-dependent magnitude and phase of the actuator dynamics as well as linearized modeled or measured frequency response functions of the physical substructure.

1.2 Theory

Multi-actuator RTHS applied to a notional structural dynamic system partitioned into separate numerical and physical substructures is illustrated in Fig. 1.2. The corresponding RTHS feedback loop, which is essentially a multi-input multi-output (MIMO) feedback control system, is shown in Fig. 1.3. For the numerical substructure, the transfer function $N_{XnFn}(s)$ relates input numerical forces, f_n, to output displacement responses, x_n, and the transfer function $N_{XnFr}(s)$ relates input restoring forces, f_r, to output displacement responses, x_n. For the physical substructure, the transfer function $P_{FrFe}(s)$ relates external physical forces, f_e, to measured restoring forces, f_r, and the transfer function $P_{FrXa}(s)$ relates input actuator displacements, x_a, to measured restoring forces, f_r. Although this system illustrates a two interface degrees-of-freedom (DOFs), the subsequent reformulation of dynamic substructuring as a feedback control problem is general and can be applied to cases with many interface DOFs.

To enforce force equilibrium, the measured restoring forces from the physical substructure are fed back to the numerical substructure and applied as equal and opposite input forces. To enforce displacement compatibility, the actuator transfer system with compensation is used to impose the displacement response of the numerical substructure onto the physical substructure. The dynamics of the actuator transfer system with compensation is represented by the actuator transfer function $\hat{A}(s)$. It should be noted that the above block diagram assumes that the sensor dynamics for the measured restoring force of the physical substructure are negligible. With appropriate selection of force sensors with constant magnitude and little phase distortion at low frequencies, this assumption is reasonable for the control band below 100 Hz of a typical RTHS test.

From the above block diagram, the closed-loop response for the numerical displacement is

$$\begin{aligned}\{x_n(s)\} = {} & \left[I + N_{XnFr}(s)P_{FrXa}(s)\widehat{A}(s)\right]^{-1}[N_{XnFn}(s)]\{f_n(s)\} \\ & - \left[I + N_{XnFr}(s)P_{FrXa}(s)\widehat{A}(s)\right]^{-1}[N_{XnFr}(s)]\;[P_{FrFe}(s)]\{f_e(s)\}\end{aligned} \tag{1.1}$$

The closed-loop response for the measured restoring force is

$$\begin{aligned}\{f_r(s)\} = {} & \left[I + P_{FrXa}(s)\widehat{A}(s)N_{XnFr}(s)\right]^{-1}[P_{FrXa}(s)]\;\left[\widehat{A}(s)\right][N_{XnFn}(s)]\{f_n(s)\} \\ & + \left[I + P_{FrXa}(s)\widehat{A}(s)N_{XnFr}(s)\right]^{-1}[P_{FrFe}(s)]\{f_e(s)\}\end{aligned} \tag{1.2}$$

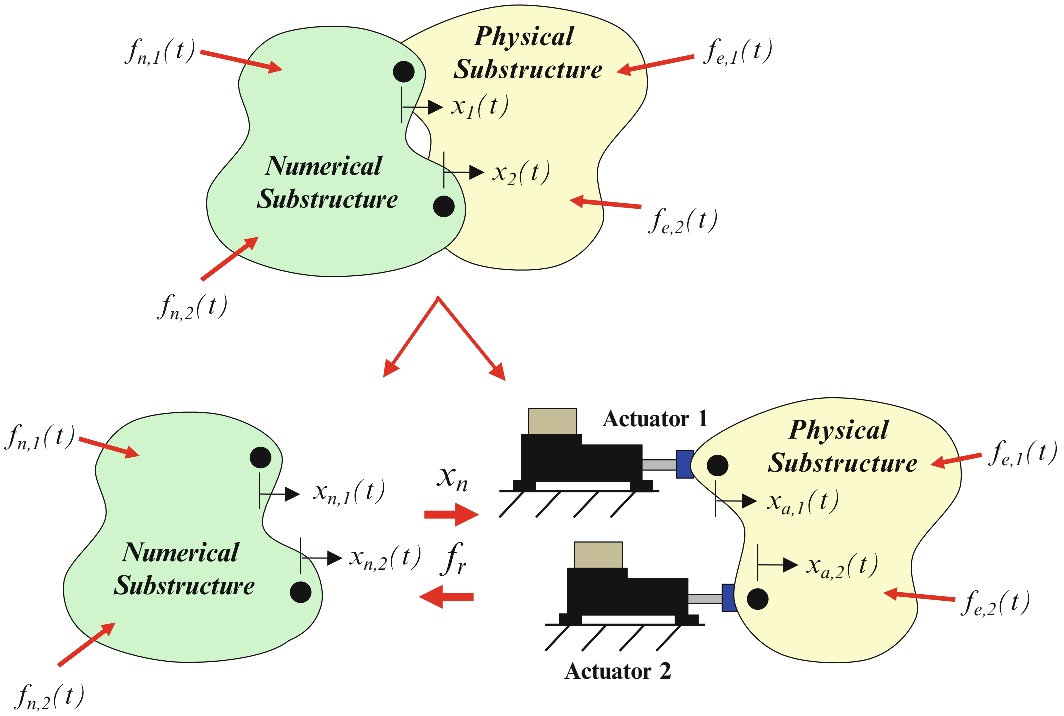

Fig. 1.2 Multi-actuator RTHS applied to a notional structural dynamic system

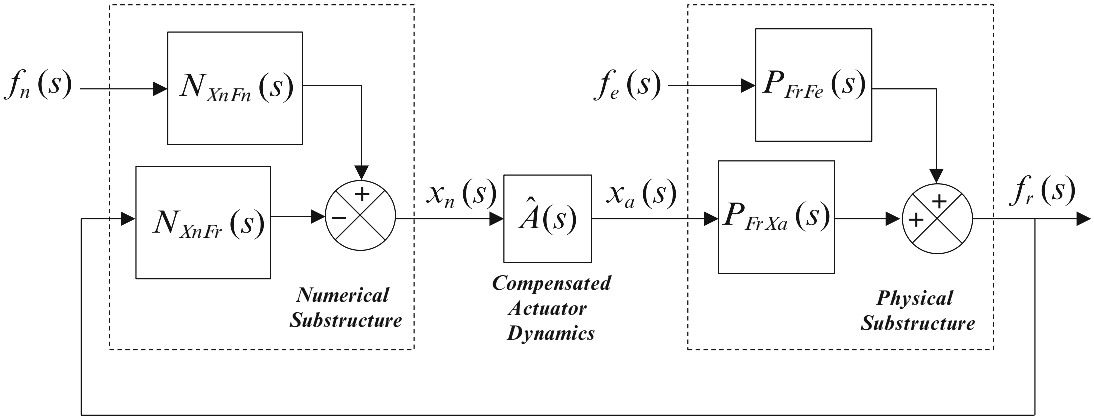

Fig. 1.3 Feedback loop for multi-actuator RTHS

Note that the above expression has a common factor, which is the sensitivity matrix

$$[S(s)] = [I + L(s)]^{-1} \tag{1.3}$$

where, $L(s) = P_{FrXa}(s)\widehat{A}(s)N_{XnFr}(s)$ is the loop gain for RTHS.

The complimentary sensitivity matrix is then defined as

$$[T(s)] = [I + L(s)]^{-1}[L(s)] \tag{1.4}$$

Since the actuator dynamics is in the feedback path, the presence of time delay of the actuator transfer system will have a destabilizing effect on the RTHS closed-loop response. Using concepts from robust stability theory for MIMO feedback control, as in Goodwin et al. [22] and Skogestad and Postlethwaite [23], we cast the compensated actuator dynamics as a multiplicative uncertainty as illustrated in Fig. 1.4.

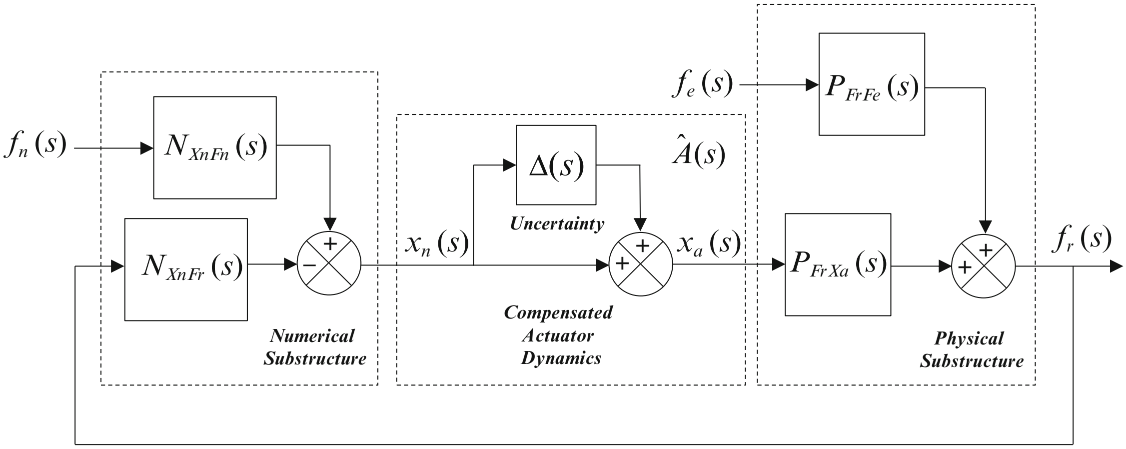

Fig. 1.4 RTHS feedback loop with compensated actuator dynamics cast as multiplicative uncertainty

The compensated actuator dynamics matrix is related to the uncertainty matrix by

$$\left[\widehat{A}(s)\right] = [\Delta(s)] + [I] \tag{1.5}$$

Substituting (1.5) into (1.4), the complimentary sensitivity matrix becomes

$$[T(s)] = [I + P_{FrXa}(s)\,(\Delta(s) + I)\,N_{XnFr}(s)]^{-1}\,[P_{FrXa}(s)]\;[\Delta(s) + I]\;[N_{XnFr}(s)] \tag{1.6}$$

Expanding as

$$[T(s)] = [I + P_{FrXa}(s)N_{XnFr}(s) + P_{FrXa}(s)\Delta(s)N_{XnFr}(s)]^{-1}\,[P_{FrXa}(s)]\;[\Delta(s) + I]\;[N_{XnFr}(s)] \tag{1.7}$$

Factoring $[I + P_{FrXa}(s)N_{XnFr}(s)]^{-1}$ leads to

$$[T(s)] = [I + T_o(s)\Delta(s)]^{-1}\,[T_o(s)]\;[\Delta(s) + I] \tag{1.8}$$

where the nominal complimentary sensitivity matrix is defined as

$$[T_o(s)] = [I + P_{FrXa}(s)N_{XnFr}(s)]^{-1}\,[P_{FrXa}(s)]\;[N_{XnFr}(s)] \tag{1.9}$$

Note that the presence of actuator dynamics introduces the term $T_o(s)\Delta(s)$ in the denominator of (1.8). As this term approaches −1, the RTHS system will go unstable. By employing the small gain theorem, the sufficient condition for robust stability is

$$\|[T_o(s)]\;[\Delta(s)]\|_\infty < 1 \tag{1.10}$$

Where, $\|\,\|_\infty$ denotes the maximum singular value over the RTHS control band.

The above robust stability criterion provides a conservative measure for ensuring that the RTHS system has robust stability in the presence of actuator dynamics. Since multi-actuator RTHS is a MIMO feedback control system, the robust stability criterion involves a singular value decomposition of the nominal complimentary sensitivity matrix multiplied by the uncertainty matrix. The nominal complimentary sensitivity matrix for RTHS is described by (1.9), while the uncertainty matrix is obtained by rearranging (1.5) as

$$[\Delta(s)] = \left[\widehat{A}(s)\right] - [I] \tag{1.11}$$

For single-actuator RTHS, the robust stability criterion simplifies to

$$|T_o(s)\Delta(s)| < 1 \tag{1.12}$$

Where, $|\quad|$ denotes the maximum magnitude over the RTHS control band.

The robust stability criterion alone does not ensure robust performance of the RTHS system in the presence of actuator dynamics. Goodwin et al. [22] suggests one approach for robust performance is to ensure that the actual sensitivities are close to the nominal sensitivities by

$$\|[T_o(s)]\,[\Delta(s)]\|_\infty << 1 \tag{1.13}$$

The above robust performance criterion is similar but more restrictive than the robust stability criterion.

The above sufficient conditions for robust stability and performance analysis assume that the dynamic system without actuator dynamics has nominal stability. A dynamic system is said to have nominal stability if its closed-loop poles are on the right-side of the complex plane. The closed loop response of the dynamic system without actuator dynamics can be found by setting the uncertainty matrix to zero, which yields

$$\begin{aligned}\{x_o(s)\} = {} & [I + N_{XnFr}(s)P_{FrXa}(s)]^{-1}\,[N_{XnFn}(s)]\,\{f_n(s)\} \\ & - [I + N_{XnFr}(s)P_{FrXa}(s)]^{-1}\,[N_{XnFr}(s)]\;[P_{FrFe}(s)]\,\{f_e(s)\}\end{aligned} \tag{1.14}$$

The above response represents the case of perfect actuation with no time delay of the actuator transfer system. The nominal stability of this system can be characterized by determining its closed-loop poles.

The sufficient conditions in (1.10) and (1.13) provide the basis for a new robust stability and performance analysis method for both single and multi-actuator RTHS. The robust stability and performance criterion for RTHS are similar to those for MIMO feedback control with plant uncertainty in Goodwin et al. [22] and Skogestad and Postlethwaite [23]. The differences are in the expressions for the nominal complimentary sensitivity and uncertainty. In most cases, it is more practical to perform the robust stability and performance analysis in the frequency domain instead of the Laplace domain in order to directly utilize measured frequency response functions for the actuator dynamics and physical substructure. The proposed robust stability and performance analysis involves a singular value decomposition of the nominal complimentary sensitivity matrix multiplied by the uncertainty matrix at each frequency. Unlike previous stability analysis techniques which assume pure time delay and lumped parameter descriptions, this method better captures the actual frequency dependence of the magnitude and phase lag of the actuator dynamics as well as accommodates more complex representations of the numerical and physical substructures.

1.3 Conclusions

This paper presents a new analysis method for evaluating the robust stability and performance of multi-actuator RTHS. This MIMO analysis method requires a singular value decomposition of the nominal complimentary sensitivity matrix multiplied by the uncertainty matrix at each frequency. For robust stability, the maximum singular values across frequency should be less than 1 over the RTHS control band. For robust performance, the maximum singular values should be much less than 1 over the control band. These sufficient conditions for robust stability and performance were derived by casting the actuator dynamics in the RTHS feedback loop as a multiplicative uncertainty and applying the small gain theorem. The proposed robust stability and performance analysis method provides a useful tool for pre-test planning and post-test diagnostics of RTHS tests involving multiple actuators. This analysis method can be used to evaluate the robust stability and performance of the actuator transfer system and the compensation approach for RTHS. The attractive feature of this method is that it accommodates linearized modeled or measured frequency response functions for both the physical substructure and actuator dynamics. This presents a major advancement over previous RTHS stability analysis techniques which assume pure time delay for the actuator dynamics and lumped parameter descriptions or the numerical and physical substructures.

Acknowledgments The work is supported by the Office of Naval Research under project DOD/NAVY/ONR, Award No. N00014-11-1-0260, Program Director: Deborah Nalchajian.

References

1. Horiuchi T, Nakagawa M, Sugano M, Konno T (1996) Development of a real-time hybrid experimental system with actuator delay compensation. In: 11th world conference on earthquake engineering, Paper no. 660, ISBN: 0 08 042822 3
2. Horiuchi T, Inoue M, Konno T, Namita Y (1999) Real-time hybrid experimental system with actuator delay compensation and its application to a piping system with energy absorber. Earthq Eng Struct Dyn 28(10):1121–1141
3. Nakashima M, Masaoka N (1999) Real-time on-line test for MDOF systems. Earthq Eng Struct Dyn 28:393–420
4. Darby AP, Blakeborough A, Williams MS (1999) Real-time substructure tests using hydraulic actuator. J Eng Mech 125(10):1133–1139
5. Christenson R, Lin YZ (2008) Real-time hybrid simulation of a seismically excited structure with large-scale magneto-rheological fluid dampers. In: Saouma VE, Sivaselvan MV (eds) Hybrid simulation theory, implementations and applications. Taylor and Francis NL, London. ISBN 978-0-415-46568-7
6. Jiang Z, Kim SJ, Plude S, Christenson R (2013) Real-time hybrid simulation of a complex bridge model with MR dampers using the convolution integral method. J Smart Mater Struct 22(10):105008. doi:10.1088/0964-1726/22/10/105008
7. Friedman A, Dyke SJ, Phillips B, Ahn R, Dong B, Chae Y, Castaneda N, Jiang Z, Zhang J, Cha Y, Ozdagli AI, Spencer BF, Ricles J, Christenson R, Agrawal A, Sause R (2014) Large-scale real-time hybrid simulation for evaluation of advanced damping system performance. J Struct Eng. doi:10.1061/(ASCE)ST.1943-541X.0001093
8. Chen C, Ricles J (2009) Analysis of actuator delay compensation methods for real-time testing. Eng Struct 31:2643–2655
9. Chen C, Ricles J (2010) Tracking error-based servohydraulic actuator adaptive compensation for real-time hybrid simulation. J Struct Eng 136(4):432–440
10. Chae Y, Kazemibidokhti K, Ricles JM (2013) Adaptive time series compensator for delay compensation of servo-hydraulic actuator systems for real-time hybrid simulation. Earthq Eng Struct Dyn 42(11):1697–1715
11. Carrion JE, Spencer B (2007) Model-based strategies for real-time hybrid testing. Newmark Structural Engineering Laboratory report no NSEL-006, University of Illinois at Urbana-Champaign
12. Phillips BM, Spencer B (2012) Model-based framework for real-time dynamic structural performance evaluation. NSEL report no NSEL-031
13. Gao X, Castaneda N, Dyke SJ (2013) Real time hybrid simulation: from dynamic system, motion control to experimental error. Earthq Eng Struct Dyn 42(6):815–832
14. Wallace MI, Sieber J, Neild SA, Wagg DJ, Krauskopf B (2005) Stability analysis of real-time dynamic substructuring using delay differential equation models. Earthq Eng Struct Dyn 34:1817–1832
15. Kyrychko YN, Blyuss KB, Gonzalez-Buelga A, Hogan SJ, Wagg DJ (2006) Real-time dynamic substructuring in a coupled oscillator–pendulum system. Proc R Soc A 462:1271–1294
16. Mercan O, Ricles JM (2007) Stability and accuracy analysis of outer loop dynamics in real-time pseudodynamic testing of SDOF systems. Earthq Eng Struct Dyn 36:1523–1543
17. Mercan O, Ricles JM (2008) Stability analysis for real-time pseudodynamic and hybrid pseudodynamic testing with multiple sources of delay. Earthq Eng Struct Dyn 37:1269–1293
18. Fudong C, Wang J, Feng J (2010) Delay-dependent stability and added damping of SDOF real-time dynamic hybrid testing. Earthq Eng Struct Dyn 9(3):425–438
19. Botelho RB, Christenson R, Franco J (2013) Exact stability analysis for uniaxial real-time hybrid simulation of 1-DOF and 2-DOF structural systems. In: Engineering mechanics institute conference, Northwestern University, Evanston, IL
20. Maghareh A, Dyke SJ, Prakash A, Bunting GB (2014) Establishing a predictive performance indicator for real-time hybrid simulation. Earthq Eng Struct Dyn 43:2299–2318
21. Gawthrop PJ, Wallace MI, Nield SA, Wagg DJ (2007) Robust real-time substructuring techniques for under-damped systems. Struct Control Health Monit 14:591–608
22. Goodwin GC, Graebe SF, Salgado ME (2001) Control system design, 2nd edn. Prentice Hall Inc, Upper Saddle River
23. Skogestad S, Postlethwaite I (2005) Multivariable feedback control analysis and design, 2nd edn. Wiley, Hoboken

Chapter 2
Effect of Actuator Delay on Real-Time Hybrid Simulation Involving Multiple Experimental Substructures

Cheng Chen, Frank Sanchez, and Maryam Khan

Abstract Real-time hybrid simulation provides an economical and effective experimental technique for seismic performance evaluation of civil engineering structures in size limited laboratories. Servo-hydraulic dynamics pose challenges for synchronizing restoring forces between substructures. Actuator tracking therefore contributes most detrimental error to real-time hybrid simulation. Post-experiment reliability assessment through actuator tracking assessment is critical to appropriately interpret real-time hybrid simulation results for the performance of structures under investigation. This study analyzes the effect of actuator delays on the accuracy of real-time hybrid simulations involving multiple experimental substructures. Unlike previous studies focusing on the stability of real-time hybrid simulation, this study acknowledges the fact that delay compensation methods are capable of reducing the tracking errors. The modal analysis technique is evaluated for real-time hybrid simulation involving both time delay and nonlinear structural behavior.

Keywords Real-time hybrid simulation • Actuator delay • Modal analysis • Frequency-domain analysis

2.1 Introduction

Experiments are important for earthquake engineering research. Real-time hybrid simulation (RTHS) splits the structure into experimental substructure(s) and analytical substructure(s), which allows researchers to observe the behavior of critical elements at large or full scale when subjected to dynamic loading [1–3]. The structural response under external excitation is calculated by solving the dynamic equations of motion using an integration algorithm. The desired responses are then imposed onto the experimental substructure(s) using servo-hydraulic actuators and their measured restoring forces are fed back for next step displacement calculation. Real-time hybrid simulation provides an efficient and effective way to evaluate seismic performance of large- or full-scale civil engineering structures in size limited laboratories. Since this experiment is conducted in real-time manner, the RTHS is more approving for rate-dependent seismic devices [4, 5]. After years of development, the RTHS has become a viable alternative to the more well-established shaking table testing method and the pseudo-dynamic testing method [6–9].

However, due to inherent servo-hydraulic dynamics, the actuator has an inevitable time delay in response to the displacement command. Previous researches showed that the time delay would lead to inaccurate test results and even destabilize the entire simulation if not compensated properly [10–12]. Various compensation methods have been proposed to minimize the effect of actuator delay. These compensation methods are either based on constant time delay assumption [13–15] or formulated using adaptive control theory [16, 17]. The advance in delay compensation method has helped reduce the actuator tracking error. Experimental studies however indicated that actuator tracking errors cannot be completely eliminated even when a sophisticated compensation technique is used [18]. This brings concern on how reliably the real-time hybrid simulation results have replicated the actual structural responses under earthquakes. In other words, it poses a great challenge for reliability assessment of real-time hybrid simulation results with the presence of tracking errors since true structural responses are often not available for an immediate comparison.

Various techniques have been used to evaluate the actuator delay induced tracking error, including the maximum tracking error (MTE), root-mean-square (RMS) of the tracking error, tracking indicator (TI) [19] and energy error (EE) [20, 21]. These variables provide qualitative but not quantitative assessment on the effect of actuator tracking. Guo et al. [22] proposed a frequency evaluation index (FEI) method to interpret amplitude error and phrase error existing in actuator tracking, which divides test error into. Chen et al. [23] further verified this method for RTHS tests of a single-story steel moment

---

C. Chen (✉) • F. Sanchez • M. Khan
School of Engineering, San Francisco State University, San Francisco, CA 94132, USA
e-mail: chcsfsu@sfsu.edu; Fsanchez724@yahoo.com; mikhan@mail.sfsu.edu

M. Allen et al. (eds.), *Dynamics of Coupled Structures, Volume 4*, Conference Proceedings of the Society
for Experimental Mechanics Series, DOI 10.1007/978-3-319-15209-7_2

resisting frame with elastomeric damper. The FEI method utilizes the command displacements sent to the servo-hydraulics and the measured displacements measured from experimental substructures. When a real-time hybrid simulation involves multiple experimental substructures associated with multi-degree-of-freedom (MDOF), the FEI method application cannot differentiate between different structural modes, therefore cannot provide quantitative information on the amplitude and phase error for each structural mode. This study evaluates the effect of actuator delay on real-time hybrid simulation involving multiple experimental substructures and explores the application of FEI method on MDOF structure to assess the effect of actuator delay on multiple structural modes.

2.2 Real-Time Hybrid Simulation of Linear Elastic MDOF Structure

For a linear elastic MDOF structure, the equation of motion can be represented as:

$$\underline{M}\cdot\underline{\ddot{x}}+\underline{C}\cdot\underline{\dot{x}}+\underline{K}\cdot\underline{x}=\underline{F} \tag{2.1}$$

where $\underline{M}$, $\underline{C}$ and $\underline{K}$ are the mass, viscous damping and stiffness matrices, respectively; $\underline{\ddot{x}}$, $\underline{\dot{x}}$ and $\underline{x}$ are the acceleration, velocity and displacement response, respectively; and $\underline{F}$ is the external excitation force vector. For the purpose of analysis, a two degree-of-freedom (DOF) structure is analyzed in this paper, where the mass matrix, stiffness matrix, damping matrix and equations of motion can be expressed as $\underline{M}=\begin{bmatrix} m_1 & 0 \\ 0 & m_2 \end{bmatrix}$, $\underline{C}=\begin{bmatrix} c_{11} & c_{12} \\ c_{21} & c_{22} \end{bmatrix}$, $\underline{K}=\begin{bmatrix} k_1+k_2 & -k_2 \\ -k_2 & k_2 \end{bmatrix}$, $\underline{x}=\begin{bmatrix} x_1 \\ x_2 \end{bmatrix}$ and $\underline{F}=\begin{bmatrix} F_1 \\ F_2 \end{bmatrix}$, where m_1 and m_2 are the mass of the first and second story of the 2DOF structure, respectively; k_1 and k_2 represent the story stiffness; c_{11}, c_{12}, c_{21} and c_{22} represent the viscous damping inherent to the structure; F_1 and F_2 represent the external excitation force on the structure; and x_1 and x_2 represent the displacement response of the first and second story, respectively. The equation of motion for each story can also be written as

$$m_1\cdot\ddot{x}_1+c_{11}\cdot\dot{x}_1+c_{12}\cdot\dot{x}_2+k_1\cdot x_1+k_2\cdot(x_1-x_2)=F_1 \tag{2.2a}$$

$$m_2\cdot\ddot{x}_2+c_{21}\cdot\dot{x}_1+c_{22}\cdot\dot{x}_2+k_2\cdot(x_2-x_1)=F_2 \tag{2.2b}$$

Assume that structural components associated with k_1 and k_2 are considered as experimental substructures and actuator delays exist in a real-time hybrid simulation, Eq. (2.1) can be modified as

$$\begin{bmatrix} m_1 & 0 \\ 0 & m_2 \end{bmatrix}\begin{Bmatrix} \ddot{x}_1 \\ \ddot{x}_2 \end{Bmatrix}+\begin{bmatrix} c_{11} & c_{12} \\ c_{21} & c_{22} \end{bmatrix}\begin{Bmatrix} \dot{x}_1 \\ \dot{x}_2 \end{Bmatrix}+\begin{bmatrix} k_1+k_2 & -k_2 \\ -k_2 & k_2 \end{bmatrix}\begin{Bmatrix} x_1(t-\tau_1) \\ x_2(t-\tau_2) \end{Bmatrix}=\begin{Bmatrix} F_1(t) \\ F_2(t) \end{Bmatrix} \tag{2.3}$$

where τ_1 and τ_2 are the delays due to the servo-hydraulic actuators attached to the experimental substructures in the first and second story, respectively. The actuator delays are observed to be coupled for the 2DOF.

Figure 2.1 shows the comparison of the story displacements with and without actuator delay. The ground motion is the 1994 Northridge earthquake recorded by USC in Beverly Hills with a peak ground acceleration of 0.4158 g. The delay incorporated is 3 ms and 3 ms for the actuators attached to the experimental substructures in the first and second story, respectively. The structure has the natural frequencies of 3.88 rad/s and 10.17 rad/s for the first and second mode, respectively. The structure is assumed to have 2 % Rayleigh viscous damping for both the first and second mode. It can be observed that due to the actuator delay, story displacement from real-time hybrid simulation will deviate from the exact solution. Using the definition of MAX error in Eqs. (2.4a) and (2.4b), MAX error in Fig. 2.1 is 20.5 % for the first story and 16.7 % for the second story. This indicates again that small actuator delays can have major effects on the accuracy of RTHS results.

$$MAX_1=100\times\frac{\max(\mathrm{abs}(x_{1c}-x_{1m}))}{\max(\mathrm{abs}(x_{1c}))} \tag{2.4a}$$

$$MAX_2=100\times\frac{\max(\mathrm{abs}(x_{2c}-x_{2m}))}{\max(\mathrm{abs}(x_{2c}))} \tag{2.4b}$$

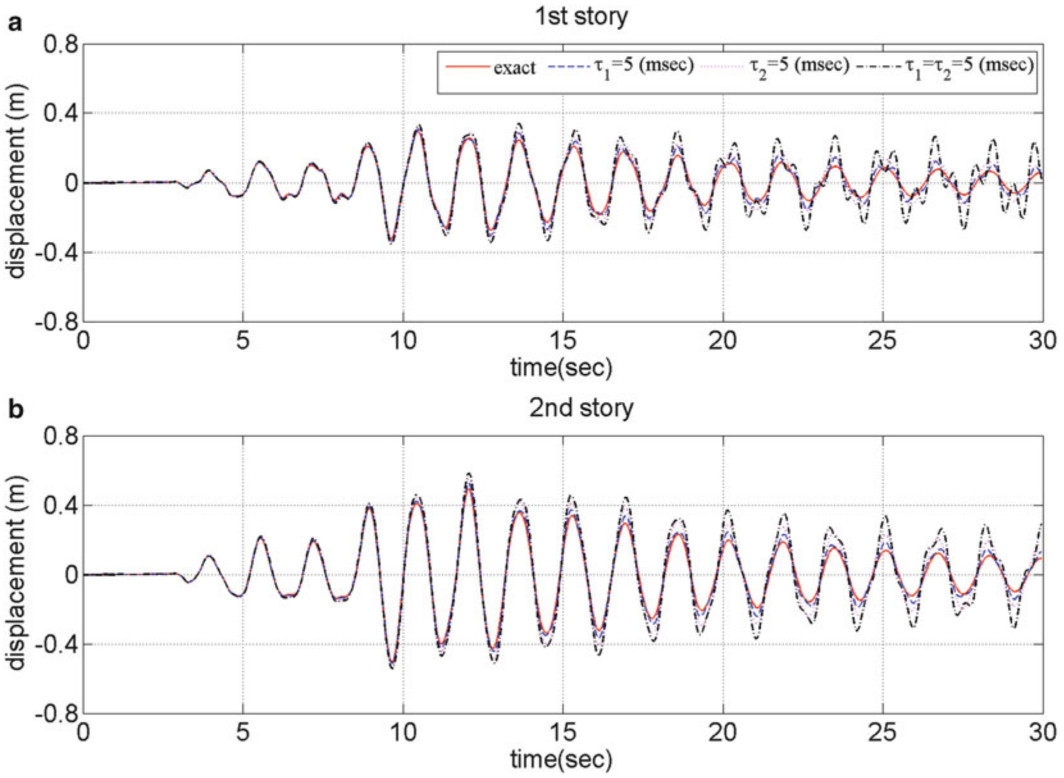

Fig. 2.1 Comparison of story displacements for real-time hybrid simulation of a linear elastic MDOF structure with and without actuator delay

Fig. 2.2 MAX error for real-time hybrid simulation with actuator delay

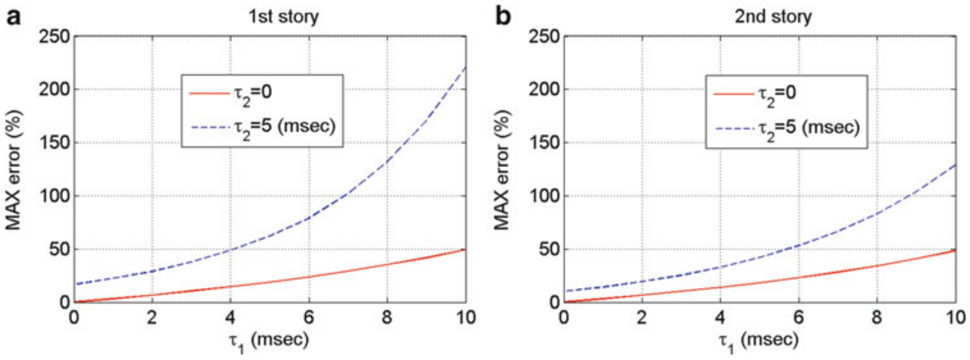

Figure 2.2 presents the increase of MAX errors with respect to the actuator delay associated with the experimental substructures in the first and second story. MAX errors for story displacements are observed even when the associated actuators have no delay. This implies that individual actuator delay affects the all the experimental substructures. For the same actuator delay, the MAX errors are also observed to be different. This indicates that the error in story displacement should not be estimated based on the time delay existing in the associated actuator.

2.3 Modal-Based Frequency-Domain Analysis

The FEI method utilizes the command displacements sent to the servo-hydraulics and the measured displacements measured from experimental substructures. In a more general form, the FEI method can be described as following: (1) Identify the input and output signals and apply Fast Fourier Transform (*FFT*) [24] to the input and output signals. Guo et al. [22] indicated that a Hanning Window technique [19] is necessary to minimize the effect of spectrum leakage. (2) Calculate the frequency evaluation index (*FEI*) between the window transformed input and output signals using Eq. (2.5a). (3) Calculate the amplitude (A) and the phrase angle (ϕ) using from Eqs. (2.5b) and (2.5c). (4) Calculate the equivalent frequency (f^{eq}) for the input signal and the equivalent time delay d due to the servo-hydraulic dynamics using Eqs. (2.5d) and (2.5e).

$$FEI = \sum_{j=1}^{p} \left\{ \frac{\mathcal{F}[O'(t)]_j}{\mathcal{F}[I'(t)]_j} \cdot \frac{\left\| \mathcal{F}[I'(t)]_j \right\|^2}{\sum_{i=1}^{p} \left\| \mathcal{F}[I'(t)]_i \right\|^2} \right\} \tag{2.5a}$$

$$A = \| FEI \| \tag{2.5b}$$

$$\phi = arc\tan\left[\mathrm{Im}(FEI)/\mathrm{Re}(FEI)\right] \tag{2.5c}$$

$$f^{eq} = \frac{\sum_{i=1}^{p} \left(\| \mathcal{F}[I'(t)]_i \|^2 \cdot f_i \right)}{\sum_{i=1}^{p} \| \mathcal{F}[I'(t)]_i \|^2} \tag{2.5d}$$

$$d = -\phi / \left(2\pi \cdot f^{eq}\right) \tag{2.5e}$$

where $I'(t)$ and $O'(t)$ are the input $I(t)$ and output $O(t)$ after the window transform, respectively; F represents the Fast Fourier Transform; i and j are integer indices; and p represents the number of frequencies to be considered; $\| \quad \|$ represents the modulo operation; and $Im(\cdot)$ and $Re(\cdot)$ represent the imaginary and real part, respectively; f^{eq} is the equivalent frequency of the input signal; d is the equivalent time delay corresponding to the equivalent frequency; and f_i is the i^{th} frequency from the FFT analysis. The parameter A in Eq. (2.5b) gives the ratio between the weighted amplitudes of the input and output signals; while the parameter ϕ in Eq. (2.5c) provides the weighted phase difference. Accurate actuator tracking in a real-time hybrid simulation requires that the value of A from Eq. (2.5b) be close to 1.0 and the value of ϕ from Eq. (2.5c) be close to zero. The difference between A and 1 is referred to as amplitude error, where overshooting implies that A is larger than 1 and undershooting for A smaller than 1. The value of ϕ is referred to as phase error, where negative value of ϕ means that the output is lagging behind the input and positive means that the output is leading the input.

To apply the FEI method to assess the effect of actuator delay on different modes of a MDOF structure, modal analysis is explored for the computational simulation results presented in Fig. 2.1. Assuming that ϕ_1 and ϕ_2 are the first and second mode for the 2DOF structure, Eq. (2.1) can be rewritten as

$$\mathrm{M}_1 \cdot \ddot{\mathrm{q}}_1 + \mathrm{C}_1 \cdot \dot{\mathrm{q}}_1 + \mathrm{K}_1 \cdot \mathrm{q}_1\,(\mathrm{t}) = \mathrm{F}_1\,(\mathrm{t}) \tag{2.6a}$$

$$\mathrm{M}_2 \cdot \ddot{\mathrm{q}}_2 + \mathrm{C}_2 \cdot \dot{\mathrm{q}}_2 + \mathrm{K}_2 \cdot \mathrm{q}_2\,(\mathrm{t}) = \mathrm{F}_2\,(\mathrm{t}) \tag{2.6b}$$

where the modal masses are defined as $\mathrm{M}_1 = \phi_1{}^{\mathrm{T}} \cdot \underline{\mathrm{M}} \cdot \phi_1$ and $\mathrm{M}_2 = \phi_2{}^{\mathrm{T}} \cdot \underline{\mathrm{M}} \cdot \phi_2$; the modal damping is defined as $\mathrm{C}_1 = \phi_1{}^{\mathrm{T}} \cdot \underline{\mathrm{C}} \cdot \phi_1$ and $\mathrm{C}_2 = \phi_2{}^{\mathrm{T}} \cdot \underline{\mathrm{C}} \cdot \phi_2$; the modal stiffness is defined as $\mathrm{K}_1 = \phi_1{}^{\mathrm{T}} \cdot \underline{\mathrm{K}} \cdot \phi_1$ and $\mathrm{K}_2 = \phi_2{}^{\mathrm{T}} \cdot \underline{\mathrm{M}} \cdot \phi_2$; the excitation forces are defined as $\mathrm{F}_1 = \phi_1{}^{\mathrm{T}} \cdot \underline{\mathrm{F}}$ and $\mathrm{F}_2 = \phi_2{}^{\mathrm{T}} \cdot \underline{\mathrm{F}}$; $\mathrm{q}_1(\mathrm{t})$ and $\mathrm{q}_2(\mathrm{t})$ are modal displacement for the first and second story, respectively; and $\phi_1{}^{\mathrm{T}}$ and $\phi_2{}^{\mathrm{T}}$ represent the transpose of ϕ_1 and ϕ_2, respectively. Assume that modal orthogonality is valid for real-time hybrid simulation of the 2DOF structure with actuator delay in Eq. (2.3),

$$\mathrm{M}_1 \cdot \ddot{\mathrm{q}}_1 + \mathrm{C}_1 \cdot \dot{\mathrm{q}}_1 + \mathrm{K}_1 \cdot \mathrm{q}_{1\mathrm{m}}\left(\mathrm{t} - \tau_{\mathrm{q}1}\right) = \mathrm{F}_1\,(\mathrm{t}) \tag{2.7a}$$

$$\mathrm{M}_2 \cdot \ddot{\mathrm{q}}_2 + \mathrm{C}_2 \cdot \dot{\mathrm{q}}_2 + \mathrm{K}_2 \cdot \mathrm{q}_{2\mathrm{m}}\left(\mathrm{t} - \tau_{\mathrm{q}1}\right) = \mathrm{F}_2\,(\mathrm{t}) \tag{2.7b}$$

where $\mathrm{q}_{1\mathrm{m}}(\mathrm{t})$ and $\mathrm{q}_{2\mathrm{m}}(\mathrm{t})$ are modal displacement for the first and second story, respectively, when actuator delays exist in a real-time hybrid simulation; $\tau_{\mathrm{q}1\mathrm{m}}$ and $\tau_{\mathrm{q}2}$ are the delay corresponding to the first and second mode, respectively. The value

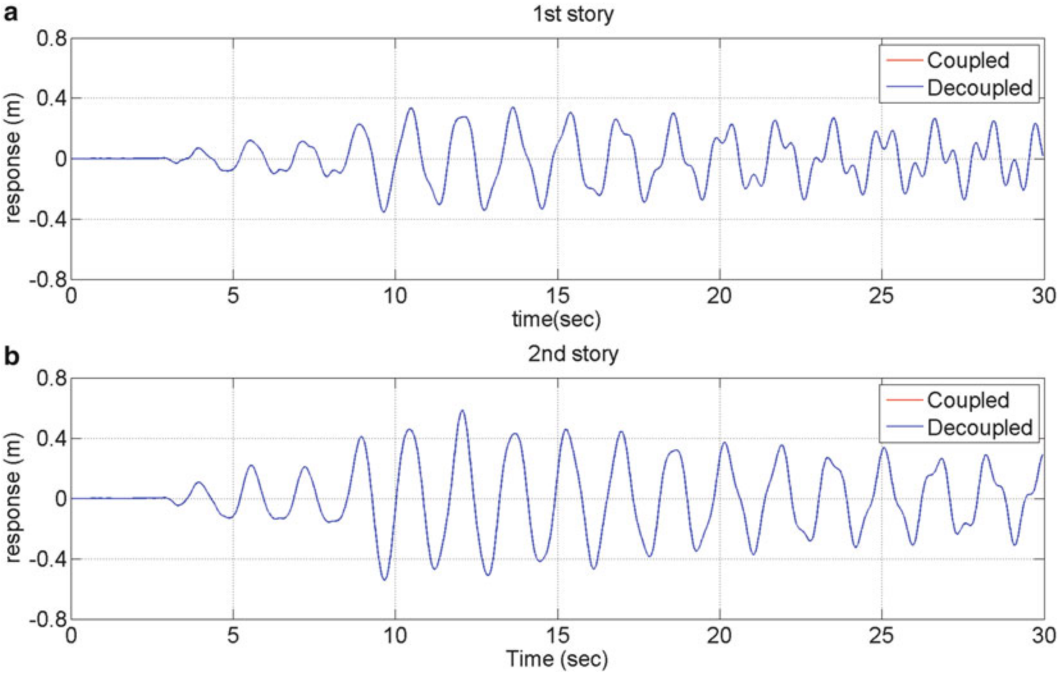

Fig. 2.3 Comparison of story displacements from approximate analysis

of τ_{q1m} and τ_{q2} can be calculated by applying the FEI method to the modal displacements $q_1(t)$ and $q_{1m}(t)$, $q_2(t)$ and $q_{2m}(t)$, respectively. The story displacements can be derived using the modal displacements as

$$\begin{Bmatrix} x_1(t) \\ x_2(t) \end{Bmatrix} = \phi_1 \cdot q_{1m}(t) + \phi_2 \cdot q_{2m}(t) \tag{2.7c}$$

To evaluate the accuracy of the approximation in Eqs. (2.7a) and (2.7b), the story displacements from Eq. (2.7c) are compared with the story displacements derived from Eq. (2.3). The comparison is presented in Fig. 2.3, where *coupled* represents the accurate solution from MDOF delay different equation, and *decoupled* represents the approximate solution from Eq. (2.7c). It can be observed that the story displacements match each other very well, indicating that the assumption of modal orthogonality for MDOF equation of motion in Eq. (2.3) enables the FEI method to qualitatively identify the delay for each structural mode. Figure 2.4 presents the FEI analysis results of delay for the first and second mode. Same delays for the actuators associated with experimental substructures are observed to result in same values of delay for both first and second modes. The same first story delay is observed to lead to different delay in different modes. For instance, when $\tau 1$ is 8 ms and $\tau 2$ is zero, the resulting delay is about 2.0 ms for first mode and 6.0 ms for second mode. While when $\tau 2$ is 8 ms and $\tau 1$ is zero, the resulting delay is about 3.5 ms for first mode and 7.2 ms for second mode.

2.4 Evaluation for Real-Time Hybrid Simulation of Nonlinear MDOF Structure

To further evaluate the effect of actuator delay on real-time hybrid simulation involving multiple experimental substructures, computational simulation of nonlinear MDOF structure is conducted. The non-linear structural behavior is simulated using the Bouc-Wen model [25]. The equations of motion for a 2DOF non-linear structure can be expressed in Eq. (2.8), where r_1 and r_2 are the restoring forces for the first and second story, respectively.

$$\begin{bmatrix} m_1 & 0 \\ 0 & m_2 \end{bmatrix} \begin{Bmatrix} \ddot{x}_1 \\ \ddot{x}_2 \end{Bmatrix} + \begin{bmatrix} c_{11} & c_{12} \\ c_{21} & c_{22} \end{bmatrix} \begin{Bmatrix} \dot{x}_1 \\ \dot{x}_2 \end{Bmatrix} + \begin{Bmatrix} r_1 \\ r_2 \end{Bmatrix} = \begin{Bmatrix} F_1(t) \\ F_2(t) \end{Bmatrix} \tag{2.8}$$

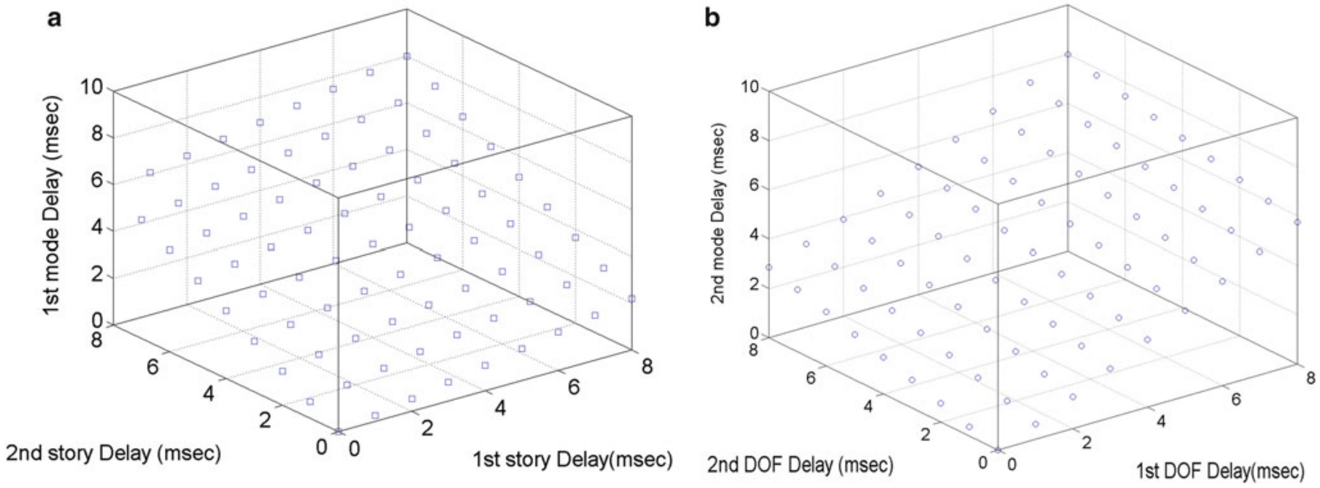

Fig. 2.4 FEI analysis results of delay for (**a**) first structural mode, (**b**) second structural mode

Table 2.1 Parameter of the Bouc-Wen model

Parameter	η	β	γ	q
Value	0.01	0.55	0.45	2

The nonlinear restoring force is simulated using the Bouc-Wen model [25], which is defined as

$$r(t) = \eta \cdot k \cdot x(t) + (1 - \eta) \cdot k \cdot x_y \cdot z(t) \tag{2.9a}$$

In Eq. (2.9a), x_y is the yield displacement; η is the ratio of the post- to pre-yield stiffness; and $z(t)$ is the evolutionary parameter of the Bouc-Wen model governed by the following equation:

$$x_y \cdot \dot{z}(t) + \gamma \left|\dot{x}(t)\right| \cdot z(t) \cdot \left|z(t)\right|^{q-1} + \beta \cdot \dot{x}(t) \cdot \left|z(t)\right|^{q} - \dot{x}(t) = 0 \tag{2.9b}$$

The dimensionless parameters (γ, β and q) control the shape of the hysteretic loop. Table 2.1 lists the values of the Bouc-Wen model parameters used in this study, with same linear elastic properties as the 2DOF structure presented previously.

Figure 2.5 presents the comparison of story displacement for real-time hybrid simulation of the nonlinear 2DOF structure with and without actuator delay. Smaller difference can be observed when compared those in Fig. 2.1. MAX errors for the story displacements are presented in Fig. 2.6. When τ_2 is equal to 10 ms and 20 ms, respectively, the MAX error in first story displacement has an almost constant value of 10 % and 22 %, respectively, while the MAX error in second story displacement monotonically increases with respect to the value of τ_1.

Figure 2.7 presents the FEI analysis results of delay for the first and second mode using the nonlinear simulation results. Unlike Fig. 2.4, same delays for the actuators are observed to result in different values of delay for both first and second modes. For instance, when τ_1 and τ_2 both equal to 10 ms, the resulting delay is about 1.4 ms for first mode and 10.0 ms for second mode, respectively. For the particular structure presented in Fig. 2.7, it can be observed that the actuator delay has more significant impact on the second mode than on the first mode, where the delay from FEI analysis for the second mode is much larger than that for the first mode.

2.5 Summary and Conclusions

The effect of actuator delay is investigated for real-time hybrid simulation involving multiple experimental substructures in this study. Both linear elastic and nonlinear structural behavior are studied for two degrees of freedom structures. Actuator delays associated with different experimental substructures in different degrees of freedom are observed to be coupled. Modal analysis is then explored in this paper to decouple the actuator delays associated with different degree-of-freedom

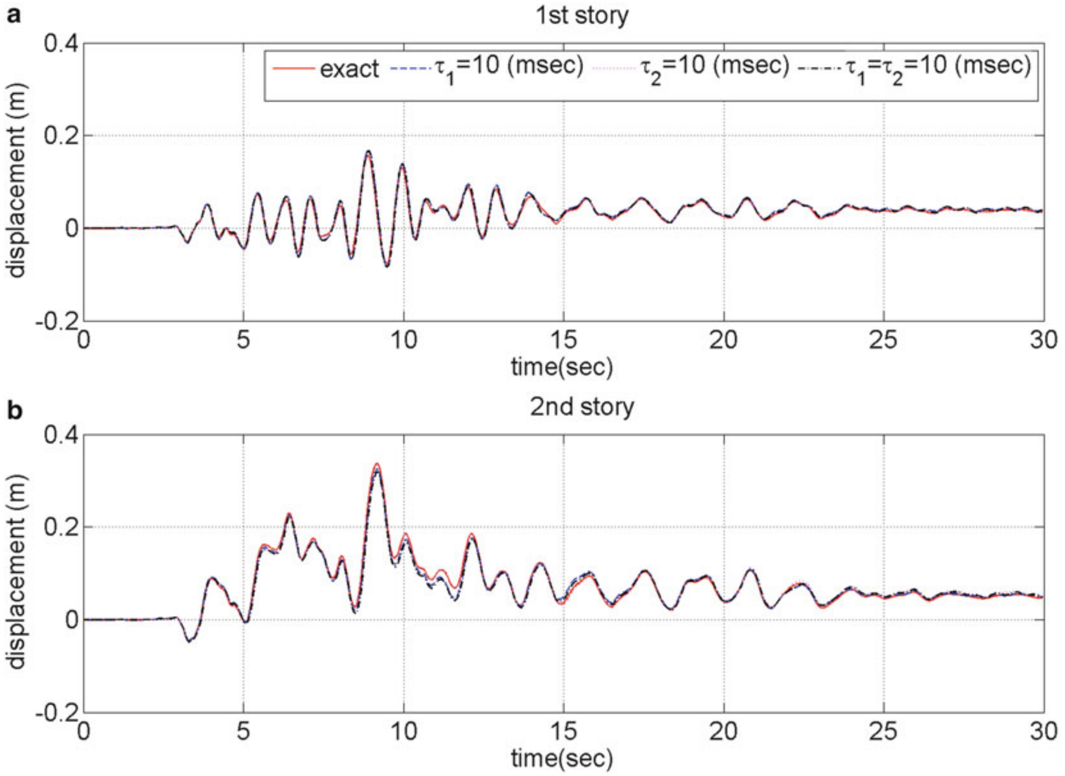

Fig. 2.5 Comparison of story displacement for real-time hybrid simulation of a nonlinear MDOF structure with and without actuator delay

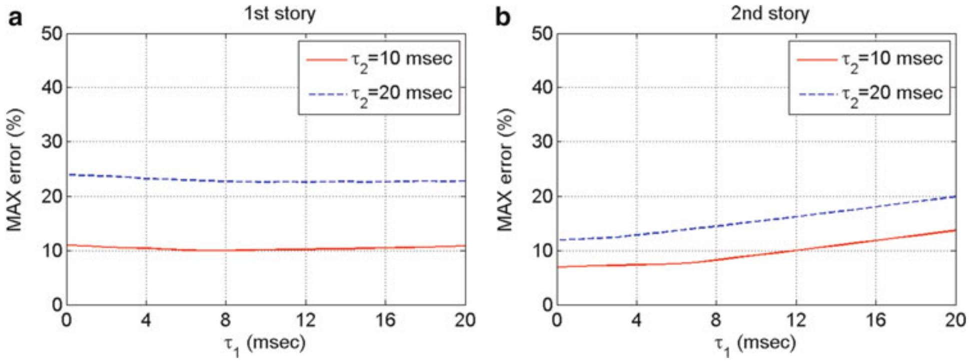

Fig. 2.6 MAX error for real-time hybrid simulation of a nonlinear MDOF structure with actuator delay

into time delay for different modes using the FEI method. The comparison of story displacements shows good accuracy of the approach for the cases presented in this study. It is then extended to real-time hybrid simulation involving multiple nonlinear experimental substructures. Analysis results show that the actuator delays have different effect on different structural modes. For the selected case, the second mode is observed to be influenced by the actuator delays. The presented study focuses on limited number of cases. Future study will evaluate the proposed approach to more general simulations including different ground motion and different structural properties as well as different number of degrees of freedom.

Acknowledgements The authors would like to acknowledge the support from National Science Foundation under the award number CMMI-1227962, and the support from Office of Research and Sponsored Program at San Francisco State University. The real-time hybrid simulation results presented in this study were conducted during the first author's post-doctoral study at the NEES Real-Time Multi-Directional Facility at Lehigh University. Any opinions, findings, and recommendations expressed in this paper are those of the authors and do not necessarily reflect those of the sponsors.

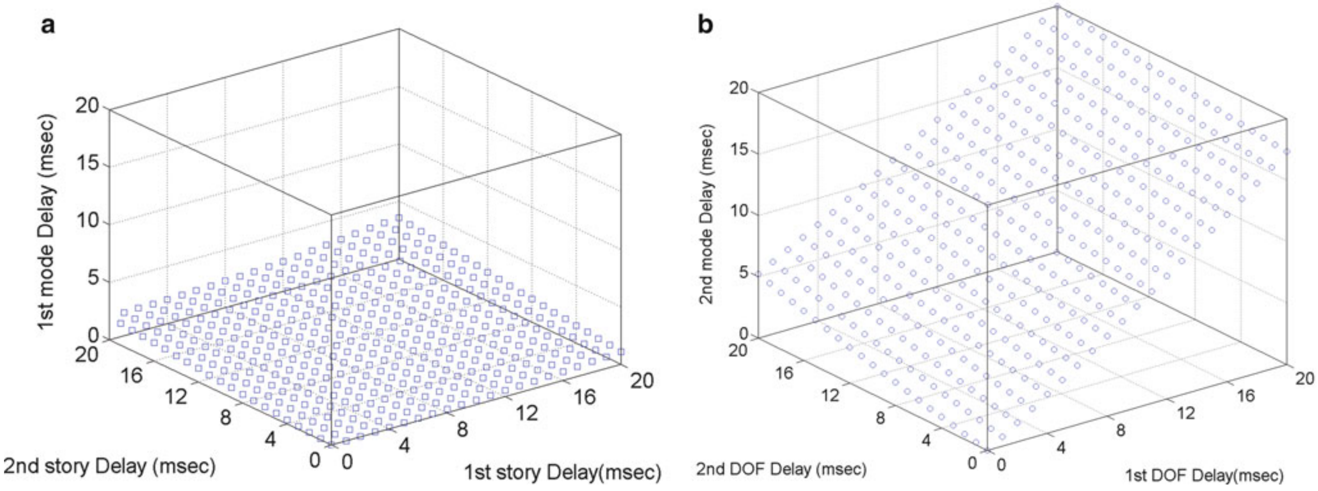

Fig. 2.7 FEI analysis results of delay for (**a**) first structural mode, (**b**) second structural mode

References

1. Nakashima M, Kato H, Takaoka E (1992) Development of real-time pseudodynamic testing. Earthq Eng Struct Dyn 21(1):79–92
2. Darby AP, Blakeborough A, Williams MS (1999) Real-time substructure tests using hydraulic actuators. J Eng Mech 125:1133–1139
3. Blakeborough A, Williams MS, Darby AP, Williams DM (2001) The development of real-time substructure testing. Philos Trans R Soc Lond A 359:1869–1891
4. Christenson R, Lin YZ, Emmons A, Bass B (2008) Large-scale experimental verification of semi-active control through real-time hybrid simulation. J Struct Eng 134(4):522–534
5. Chen C, Ricles JM, Karavasilis T, Chae Y, Sause R (2012) Real-time hybrid simulation system for performance evaluation of structures with rate dependent devices subjected to seismic loading. Eng Struct 35:71–82
6. Mosalam KM, Günay S (2014) Seismic performance evaluation of high voltage disconnect switches using real-time hybrid simulation: I. System development and validation. Earthq Eng Struct Dyn 43(8):1205–1222
7. Xu H, Zhang C, Li H (2014) Real-time hybrid simulation approach for performance validation of structural active control systems: a linear motor actuator based active mass driver case study. Struct Control Health Monit 21(4):574–589
8. Friedman A, Dyke SJ, Phillips B (2014) Large-scale real-time hybrid simulation for evaluation of advanced damping system performance. J Struct Eng, 04014150
9. Asai T, Chang CM, Spencer Jr BF (2014) Real-time hybrid simulation of a smart base-isolated building. J Eng Mech, 141(3):04014128
10. Wallace MI, Sieber J, Neild SA, Wagg DJ, Krauskopf B (2005) Stability analysis of real-time dynamic substructuring using delay differential equation models. Earthq Eng Struct Dyn 34(15):1817–1832
11. Chen C, Ricles JM (2008) Stability analysis of SDOF real-time hybrid testing systems with explicit integration algorithms and actuator delay. Earthq Eng Struct Dyn 37(4):597–613
12. Darby AP, Blakeborough A, Williams MS (2002) Stability and delay compensating for real-time substructure testing. J Eng Mech 128: 1276–1284
13. Horiuchi T, Inoue M, Konno T, Namita Y (1999) Real-time hybrid experimental system with actuator delay compensation and its application to a piping system with energy absorber. Earthq Eng Struct Dyn 28(10):1121–1141
14. Horiuchi T, Konno T (2001) A new method for compensating actuator delay in real-time hybrid experiment. Philos Trans R Soc Lond A 359:1893–1909
15. Chen C, Ricles JM (2008) Improving the inverse compensation method for real-time hybrid simulation through a dual compensation scheme. Earthq Eng Struct Dyn 38(10):1237–1255
16. Chen C, Ricles JM (2010) Tracking error-based servo-hydraulic actuator adaptive compensation for real-time hybrid simulation. J Struct Eng 136(4):432–440
17. Phillips BM, Spencer BF Jr (2012) Model-based multiactuator control for real-time hybrid simulation. J Eng Mech 139(2):219–228
18. Chen C, Sharma R (2012) A reliability assessment approach for real-time hybrid simulation results. In: Canadian Society for Civil Engineering annual conference and 3rd international structural specialty conference, Edmonton, Alberta, 6–9 June 2012
19. Mercan O (2007) Analytical and experimental studies on large scale real-time pseudodynamic testing. Ph.D. dissertation, Department of Civil and Environmental Engineering, Lehigh University, Bethlehem
20. Mosqueda G, Stojadinovic B, Mahin SA (2007) Real-time error monitoring for hybrid simulation. Part I: methodology and experimental verification. J Struct Eng 133(8):1100–1108

21. Mosqueda G, Stojadinovic B, Mahin SA (2007) Real-time error monitoring for hybrid simulation. Part II: structural response modification due to errors. J Struct Eng 133(8):1109–1117
22. Guo T, Chen C, Xu W, Sanchez F (2014) A frequency response analysis approach for quantitative assessment of actuator tracking for real-time hybrid simulation. Smart Mater Struct, 045042
23. Chen C, Xu W, Guo T (2014) Frequency response evaluation of servo-hydraulic dynamics effects in real-time hybrid simulation. J Struct Eng (under review)
24. Bracewell RN (2000) The fourier transform and its applications, 3rd edn. McGraw-Hill, Boston
25. Wen YK (1980) Equivalent linearization for hysteretic systems under random excitation. J Appl Mech 47:150–154

Chapter 3
Effective Control of a Six Degree of Freedom Shake Table

Joseph A. Franco III, Rui M. Botelho, and Richard E. Christenson

Abstract Real-Time Hybrid Substructuring (RTHS) is a new method of vibration testing that can be used to effectively characterize the system level performance of mechanical equipment. RTHS allows mechanical equipment to be physically tested while coupled through what is called a transfer system to a real-time numerical simulation of the support structure. The challenge in applying RTHS to test mechanical equipment is twofold: the equipment itself can have little inherent damping which, coupled with the inherent dynamics in the transfer system, can result in unstable RTHS tests; and the interface at the attachment points can be complex with multi-directional and rotational motion and reactions which adds significant complexity to the RTHS transfer system. To insure stability and accurately represent the complex interface between the physical and numerical substructures, a high fidelity multiple-input-multiple-output (MIMO) servo-hydraulic actuator system is needed for the RTHS transfer system. This paper presents a methodology to achieve effective control of a six degree-of-freedom (6DOF) shake table and describes the corresponding MIMO system identification and model-based feedforward feedback compensation to facilitate both stable and accurate RTHS testing of lightly damped mechanical systems. Results show that the proposed compensation method can improve the magnitude and phase tracking of a 6DOF shake table located at the University of Connecticut.

Keywords Real time hybrid simulation • Actuator dynamics • Feedforward compensation • Multiple input multiple output • Coordinate transformation

3.1 Introduction

Real-time hybrid substructuring (RTHS) provides the capability to isolate and physically test the critical components of a mechanical system early on in the design phase of a system. This capability is accomplished by including the dynamic interaction at the time of the component testing by using a numerical representation of the remainder structural system not being physically tested. RTHS is a relatively new method of vibration testing, made more practical due to advances in computer power, digital signal processing hardware/software, and hydraulic control. RTHS has the potential to accurately capture the dynamics of the coupled system at the lower frequencies as well as provide system level insight into the design of mechanical systems during the component level testing. In doing so, RTHS can potentially remove unnecessary conservatism from the design of the mechanical system. Figure 3.1 shows a general diagram of a RTHS closed loop test which illustrates the closed loop nature of this type of testing.

Early research in RTHS focused on earthquake engineering and structural engineering [1–4]. RTHS was a significant element of the Network for Earthquake Engineering Simulation (NEES) with a comprehensive list of projects and publications posted at https://nees.org/wiki/RTHSwiki. A major focus of past RTHS research is the development of actuator control methods for effective displacement tracking of the servo-hydraulic transfer system. Horiuchi et al. [4] used a frequency independent time-delay model to approximate the servo-hydraulic actuator dynamics, and then a polynomial prediction to compensate for the servo-hydraulic actuator dynamics. Jung and Shing [14] and Chen and Ricles [15] used similar compensation methods based on a control signal error-compensation methods. These methods rely on a simplified

---

J.A. Franco III (✉) • R.M. Botelho • R.E. Christenson
Department of Civil and Environmental Engineering, University of Connecticut, 261 Glenbrook Road,
Unit 3037 Storrs, Mansfield, CT 06269-3037, USA
e-mail: joseph.franco@uconn.edu

M. Allen et al. (eds.), *Dynamics of Coupled Structures, Volume 4*, Conference Proceedings of the Society
for Experimental Mechanics Series, DOI 10.1007/978-3-319-15209-7_3

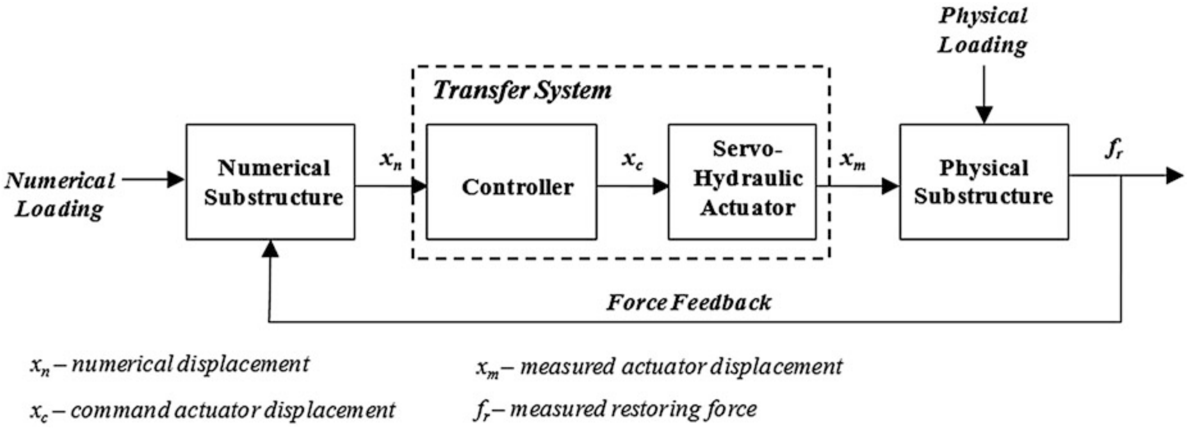

Fig. 3.1 General block diagram for RTHS closed-loop testing

time domain representation of stationary servo-hydraulic actuator dynamics with relatively small time delays. Carrion and Spencer [16] and Phillips and Spencer [17] proposed compensation techniques that involve higher order model-based strategies including a feedforward compensator, that creates an approximate inverse of the actuator model to compensate for the servo-hydraulic actuator dynamics in the transfer system. Phillips and Spencer [18] and Gao et al. [19] applied this approximate inverse method to multi degree of freedom (MDOF) servo-hydraulic actuator systems for actuators providing collinear displacements on a steel building frame. These tests involved testing frames or dampers (not mechanical equipment) with higher levels of inherent damping and with transfer systems mostly limited to uniaxle motion.

A similar test method to RTHS is hardware-in-the-loop (HWIL). HWIL testing is typically used in mechanical applications to test control systems. In HWIL testing, the physical substructure is often an electrical component and the interface between the numerical and physical substructures is achieved through the direct transfer of electrical signals. As such, the transfer system, as the system connecting the physical and numerical components is called in RTHS, does not require any servo-hydraulic control system for HWIL. HWIL testing has been conducted on mechanical equipment including HWIL research done in the design of electro-mechanical systems [7, 8] and Bouscayrol [9] and Carmeli et al. [10] who use HWIL to predict the electrical performance of electric motors and distributed electric generators, respectively. Similar research topics used a mechanical automotive engine as the physical substructure, referred to as engine-in-the-loop [11–13].

RTHS allows for the combined testing of physical and numerical substructures as shown in Fig. 3.1. This figure illustrates the closed loop nature of RTHS. The interface forces at the physical substructure connection points are measured by sensors, converted to digital signals and transmitted to the numerical substructure. The numerical substructure uses the measured interface forces along with any numerical loading to calculate the displacements at the same substructure connection points. These numerical displacements are then imposed upon the physical substructure through a transfer system, typically a servo-hydraulic actuator transfer system. While the transfer systems of typical RTHS tests in civil earthquake engineering are usually single hydraulic actuators and uniaxial, the transfer system for the support of a piece of mechanical equipment can be more complex, involving not only multiple translations, but rotations as well.

Since RTHS involves a feedback loop, it is critical for test stability and accuracy that all the forces and displacements are transmitted between the two substructures accurately and timely, to insure compatibility of the substructures and stability of the system. Accuracy and delay in a RTHS test can be a result of the sensors, the analog to digital and digital to analog converters, and the computation time. However, it is typically dominated by the inherent dynamics (i.e. apparent time delay and magnitude distortion) of the transfer system. This effect can be compounded when considering multiple actuators tuned to work synchronously with one another.

This paper presents a methodology to achieve effective control of a six degree-of-freedom (6DOF) shake table for use in RTHS of mechanical equipment. A MIMO system identification is conducted for the 6DOF shake table and model-based feedforward feedback compensation is implemented to facilitate both stable and accurate RTHS testing of lightly damped mechanical systems. This approach compensates the actuator dynamics of the six individual actuators of the shake table to provide effective displacement tracking of the six Cartesian degrees-of-freedom (i.e., translations and rotations) of the shake table. This nonlinear transformation was determined by Nakata et al. [20] for pseudo-dynamic hybrid testing. However, direct application of this nonlinear transformation with linearized feedforward inverse compensation techniques can be problematic.

This paper simplifies the nonlinear transformation by linearizing it for use with feedforward inverse compensation. Results show that the proposed compensation method can improve the magnitude and phase tracking of the Cartesian degrees-of-freedom of the 6DOF shake table located at the University of Connecticut to levels needed to conduct RTHS of mechanical equipment.

3.2 Six Degree of Freedom Shake Table

Real Time Hybrid Simulation (RTHS) is the combination of a physical substructure with a numerical substructure. This combination is performed by the use of sensors that transmit reactant forces from the physical substructure to the numerical substructure and servo-hydraulic actuators that transmit displacements, calculated by the numerical substructure, to the physical substructure. Figure 3.2 shows the general layout of a MIMO RTHS test of mechanical equipment at the University of Connecticut using a 6-DOF servo-hydraulic shake table. The real time digital signal processor (DSP) is a dSPACE DS1103 PPC controller board. The numerical substructure, along with any compensation scheme is built in MATLAB Simulink and then downloaded to the DS1103 through dSPACE's real time interface (RTI). The DS1103 has eight BNC D/A channels and twenty BNC A/D channels. The DSP controller sends commanded actuator displacements to the ShoreWestern SC6000 servo valve controller which has an internal analog PID reference tracking controller to keep the system stable but is not sufficient for the level of reference tracking required for RTHS. Each actuator has an LVDT which measures the displacement of that actuator. This measured displacement is fed back into the internal PID control loop and the outer RTHS compensation control loop as well as the DataPhysics data acquisition system. A picture of the 6DOF shake table is shown in Fig. 3.3.

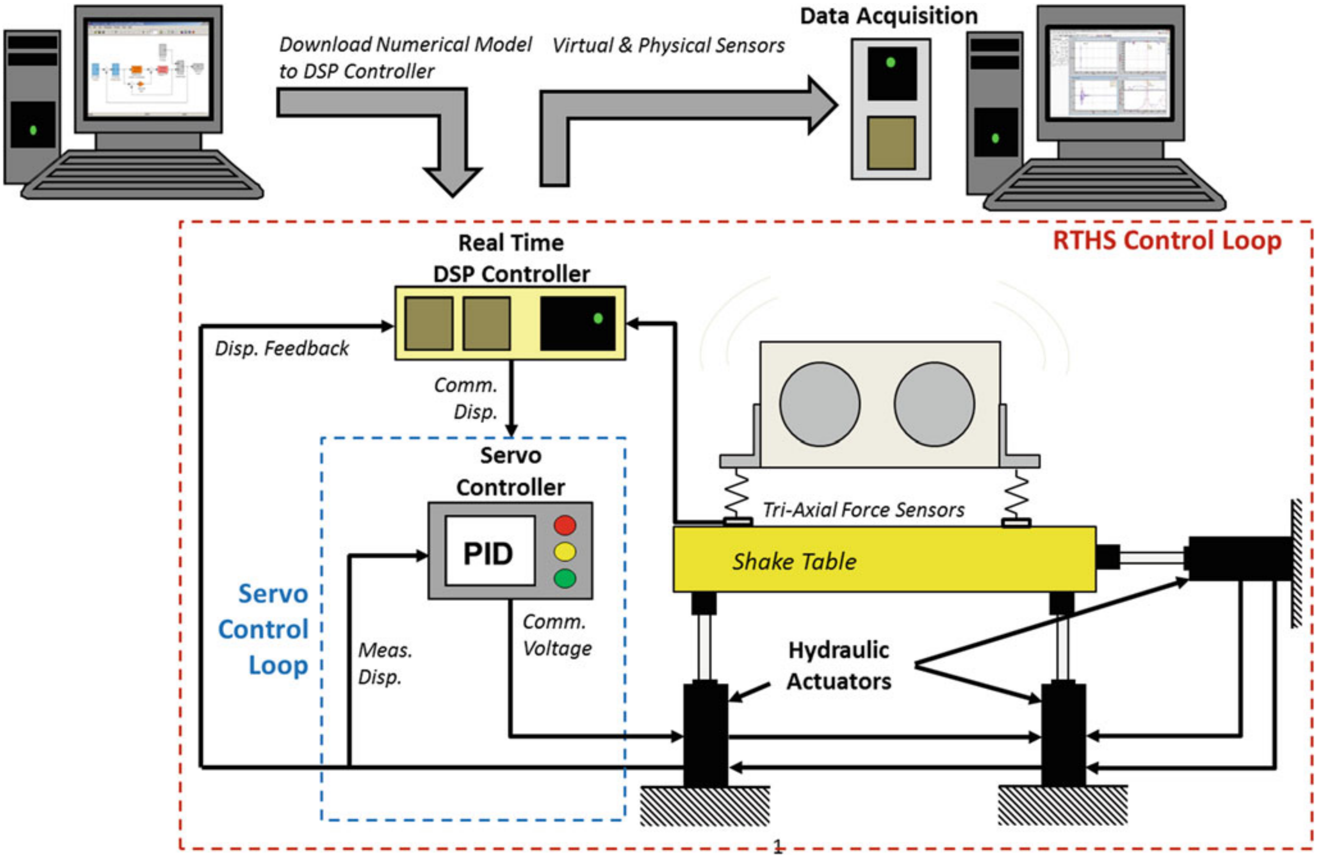

Fig. 3.2 System diagram of RTHS substructuring of mechanical equipment

Fig. 3.3 Six degree of freedom shake table

3.3 Actuator Dynamics System Identification

The first step to derive a feedforward compensator is to experimentally obtain the frequency response of the transfer system. For a single actuator transfer system, single input single output (SISO) system identification is required. For a multi-actuator transfer system, multiple input, multiple output (MIMO) system identification can be conducted since the operation of each actuator can affect the dynamics of other actuators in the system due to cross-coupling from physical connections and hydraulic fluid.

A MIMO system identification test for a six actuator shake table requires six reference channels which are also the command channels and six measured channels. A compensated MIMO system identification test for a six actuator shake table requires six reference channels, six command different command channels and six measured channels. Between the six reference channels and the six command channels, twelve output signals are needed. The dSPACE DS1103 PPC controller board, described above, has less D/A BNC outputs than are required for a compensated MIMO system identification test. Because of this, six single input multiple output (SIMO) test are required .In this paper, it is verified that this multiple SIMO system identification technique is equivalent to a single MIMO system identification technique which is used to measure the frequency response of the multi-actuator system are described. The derivations of both SIMO and MIMO transfer functions are described in full detail in Bendat and Piersol [21].

Using the theory of linear superposition, all of the actuators can be driven simultaneously with uncorrelated signals and the complete transfer function matrix can be calculated in one system identification test [21]. As long as each actuator is driven with a signal that is uncorrelated with the other input signals, the correlation between each of the outputs and the inputs can also be calculated forming a coherence matrix of the MIMO system.

Let **X** be a column vector of the Fourier transforms of the m inputs to the system, the commanded actuator displacement, and **Y** a column vector of the Fourier transforms of the n outputs of the system, the measured actuator displacement.

$$\mathbf{X} = \begin{bmatrix} X_1 \\ X_2 \\ \vdots \\ X_m \end{bmatrix} \quad \mathbf{Y} = \begin{bmatrix} Y_1 \\ Y_2 \\ \vdots \\ Y_n \end{bmatrix} \tag{3.1}$$

Let **X***, **Y*** be the complex conjugate vectors of **X**, **Y,** respectively, $\mathbf{G}_{\mathrm{xx}}$, $\mathbf{G}_{\mathrm{yy}}$ the input and output auto spectral density matrices, respectively, $\mathbf{G}_{\mathrm{yx}}$ the cross spectral density matrix between the input and outputs can be determined as

$$\mathbf{G}_{\mathrm{xx}} = E\left\{\begin{bmatrix} X_1^* \\ X_2^* \\ \vdots \\ X_n^* \end{bmatrix} \begin{bmatrix} X_1 \; X_2 \; \cdots \; X_m \end{bmatrix}\right\} = \begin{bmatrix} G_{x_1x_1} & G_{x_1x_2} & \cdots & G_{x_1x_n} \\ G_{x_2x_1} & G_{x_2x_2} & \cdots & G_{x_2x_n} \\ \vdots & \vdots & \ddots & \vdots \\ G_{x_mx_1} & G_{x_mx_2} & \cdots & G_{x_mx_n} \end{bmatrix} \tag{3.2}$$

$$\mathbf{G}_{\mathrm{yy}} = E\left\{\begin{bmatrix} Y_1^* \\ Y_2^* \\ \vdots \\ Y_n^* \end{bmatrix} \begin{bmatrix} Y_1 \; Y_2 \; \cdots \; Y_n \end{bmatrix}\right\} = \begin{bmatrix} G_{y_1y_1} & G_{y_1y_2} & \cdots & G_{y_1y_n} \\ G_{y_2y_1} & G_{y_2y_2} & \cdots & G_{y_2y_n} \\ \vdots & \vdots & \ddots & \vdots \\ G_{y_ny_1} & G_{y_ny_2} & \cdots & G_{y_ny_n} \end{bmatrix} \tag{3.3}$$

$$\mathbf{G}_{\mathrm{yx}} = E\left\{\begin{bmatrix} X_1^* \\ X_2^* \\ \vdots \\ X_m^* \end{bmatrix} \begin{bmatrix} Y_1 \; Y_2 \; \cdots \; Y_n \end{bmatrix}\right\} = \begin{bmatrix} G_{y_1x_1} & G_{y_1x_2} & \cdots & G_{y_1x_m} \\ G_{y_2x_1} & G_{y_2x_2} & \cdots & G_{y_2x_m} \\ \vdots & \vdots & \ddots & \vdots \\ G_{y_nx_1} & G_{y_nx_2} & \cdots & G_{y_nx_m} \end{bmatrix} \tag{3.4}$$

The frequency response function matrix, H_{yx} the and the coherence matrix, γ_{yx}, can then be determined as

$$\mathbf{H}_{\mathrm{yx}} = \mathbf{G}_{\mathrm{xx}}^{-1}\mathbf{G}_{\mathrm{yx}} = \begin{bmatrix} H_{y_1x_1} & H_{y_1x_2} & \cdots & H_{y_1x_m} \\ H_{y_2x_1} & H_{y_2x_2} & \cdots & H_{y_2x_m} \\ \vdots & \vdots & \ddots & \vdots \\ H_{y_nx_1} & H_{y_nx_2} & \cdots & H_{y_nx_m} \end{bmatrix} \tag{3.5}$$

$$\boldsymbol{\gamma}_{\mathrm{yx}}^2 = \left[\mathbf{G}_{\mathrm{yy}}\mathbf{G}_{\mathrm{xx}}\right]^{-1}\left|\mathbf{G}_{\mathrm{yx}}\right|^2 = \begin{bmatrix} \gamma_{y_1x_1}^{\mathbf{2}} & \gamma_{y_1x_2}^{\mathbf{2}} & \cdots & \gamma_{y_1x_m}^{\mathbf{2}} \\ \gamma_{y_2x_1}^{\mathbf{2}} & \gamma_{y_2x_2}^{\mathbf{2}} & \cdots & \gamma_{y_2x_m}^{\mathbf{2}} \\ \vdots & \vdots & \ddots & \vdots \\ \gamma_{y_nx_1}^{\mathbf{2}} & \gamma_{y_nx_2}^{\mathbf{2}} & \cdots & \gamma_{y_nx_m}^{\mathbf{2}} \end{bmatrix} \tag{3.6}$$

Figure 3.4, shows the coherence of the six actuators. These results indicate that each actuator acts independently. The coherence matrix shows unity coherence along the diagonal, which is the coherence of the actuator with itself. The off diagonal terms of the coherence matrix are very low indicating negligible cross-coupling between the six actuators. Therefore when one actuator is excited, the response of the other five actuators is negligible.

Figure 3.5 shows the measured diagonal terms of the frequency response matrix of measured to commanded actuator displacement obtained from testing. Each of the actuators has its own dynamics but they are somewhat similar. All the actuators show frequency-dependent magnitude attenuation that is approximately 20–25 dB over the 30 Hz bandwidth. The actuators also have a frequency dependent effective time delay that is approximately 25–30 ms.

3.4 Feedforward Inverse Compensation

The servo-hydraulic control system used to interface the physical and numerical substructures has frequency dependent dynamics that need to be compensated to provide accurate and timely tracking of desired displacements for stability and accuracy of a RTHS. Figure 3.6 illustrates the model-based feedforward-feedback control architecture from Carrion and

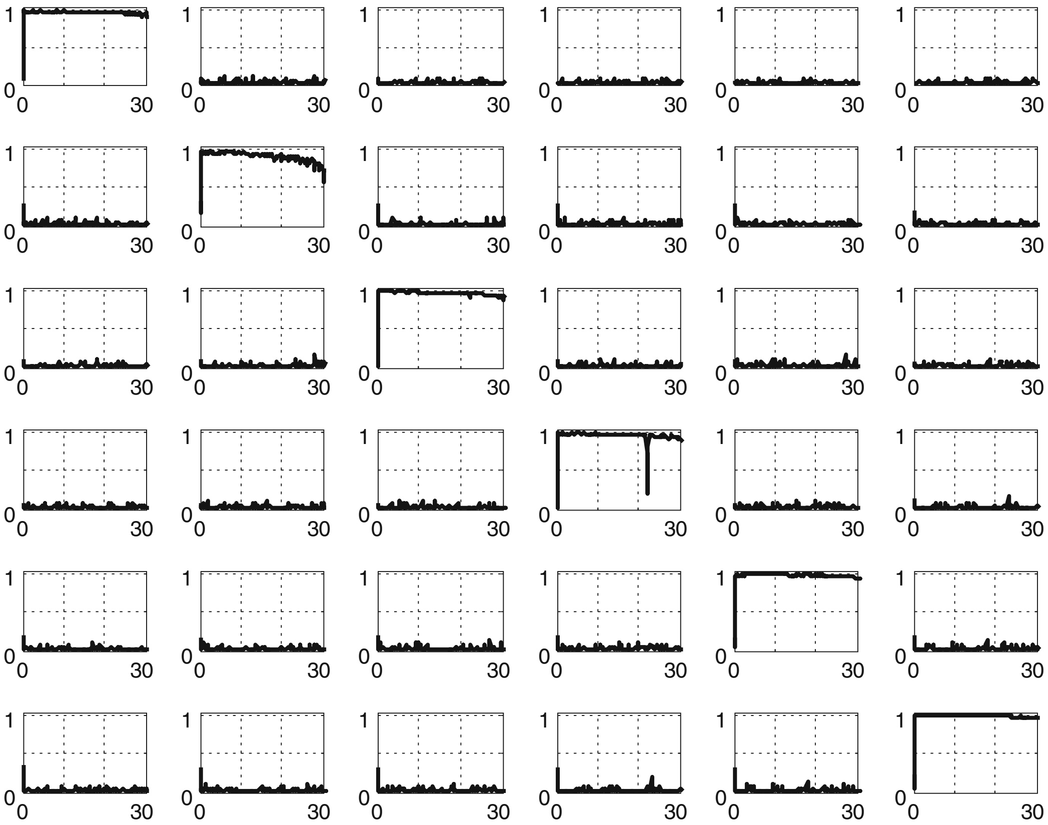

Fig. 3.4 Coherence matrix, γ_{yx}

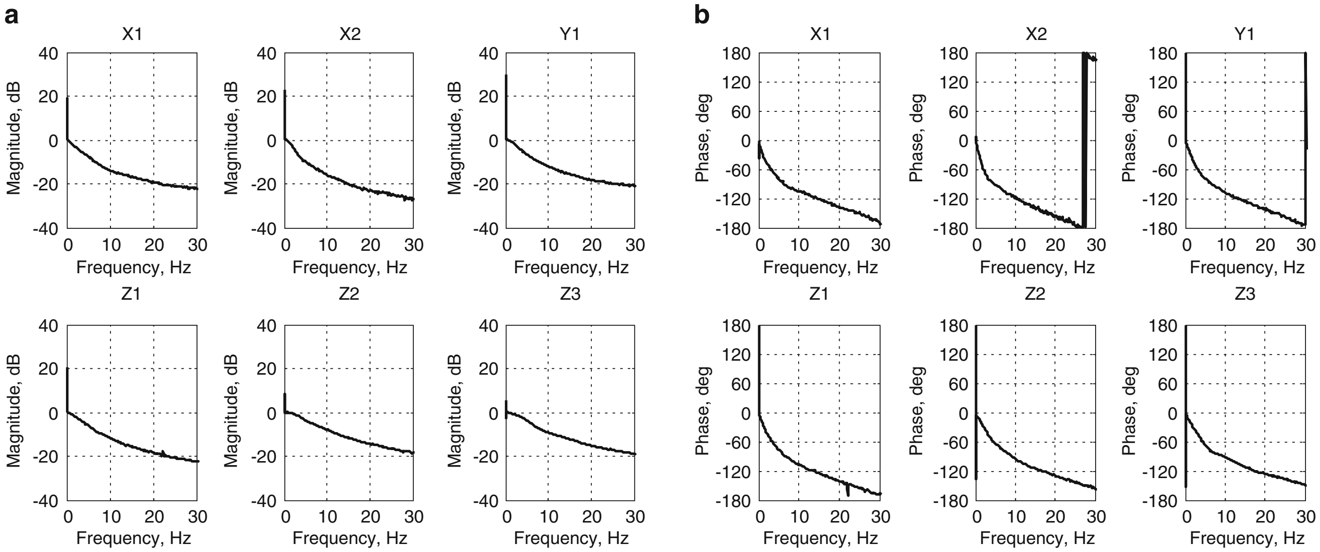

Fig. 3.5 MIMO system identification frequency response function magnitude (**a**) and phase (**b**)

Spencer [16] used for compensating the actuator dynamics. The feedforward compensator is used to cancel the modeled actuator dynamics, while the feedback gain is tuned experimentally to provide robustness due to modeling errors and changes in physical substructure during the experiment.

The feedforward inverse compensator is designed to cancel the modeled actuator dynamics of the servo-hydraulic system. Ideally, an exact inverse of the model fit of the servo hydraulic transfer function would be the perfect compensator.

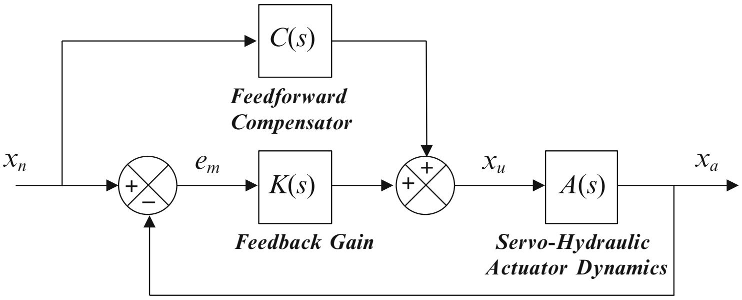

Fig. 3.6 Feedforward-feedback control for actuator dynamics compensation

The development of feedforward inverse compensator starts with deriving a Laplace domain transfer function model of the servo hydraulic dynamics from the *m*th commanded to the *n*th measured actuator displacement, which can be expressed as

$$A_{y_n x_m}(s) = \frac{\prod_{i=1}^{l} (s - z_{i,m,n})}{\prod_{i=1}^{k} (s - p_{i,m,n})} \tag{3.7}$$

where k is the number of poles and l is the number of zeros. The feedforward inverse compensator is determined by

$$C_{y_n x_m}(s) = A_{y_n x_m}(s)^{-1} \tag{3.8}$$

where

$$\mathbf{C} = \begin{bmatrix} C_{y_1 x_1} & C_{y_1 x_2} & \cdots & C_{y_1 x_m} \\ C_{y_2 x_1} & C_{y_2 x_2} & \cdots & C_{y_2 x_m} \\ \vdots & \vdots & \ddots & \vdots \\ C_{y_n x_1} & C_{y_n x_2} & \cdots & C_{y_n x_m} \end{bmatrix} \tag{3.9}$$

If the transfer function model fit has equal number of poles and zeroes then an exact inverse can be used. However, in most cases, the model has less zeroes than poles making its inverse an improper transfer function, i.e. having more zeroes than poles. Low pass compensation, as discussed subsequently, can be used to address this issue.

The feedback gain matrix can be selected term by term through experimental trial and error to provide stable and robust performance of the servo-hydraulic system.

3.4.1 Cascaded Feedforward Inverse Compensation

The dynamics of the actuators are displacement and load dependent and therefore non-linear. To deal with the inherent non-linearity of the actuator system and the very large frequency dependent dynamics, an approach referred to here as cascaded feedforward inverse compensation was implemented. In this approach, the system identification of the uncompensated system is used to develop an initial compensator. When this compensator is implemented, the commanded displacement can become a lot larger in at some frequencies to compensate for the frequency dependent attenuation in magnitude. Because the actuators are commanded a significantly larger displacement than the initial system identification, the dynamics of the system change. The initial compensator may no longer be sufficient to achieve the desired actuator dynamics and additional system identification is necessary. The dynamics of the actuator including the initial compensator is used to develop a second compensator using the same methodology of the initial compensator in order to compensate for the remaining time delay. These two compensators are then used in series as the feedforward compensator. Figure 3.7 illustrates the block diagram of the feedforward-feedback compensation with cascaded feedforward compensators.

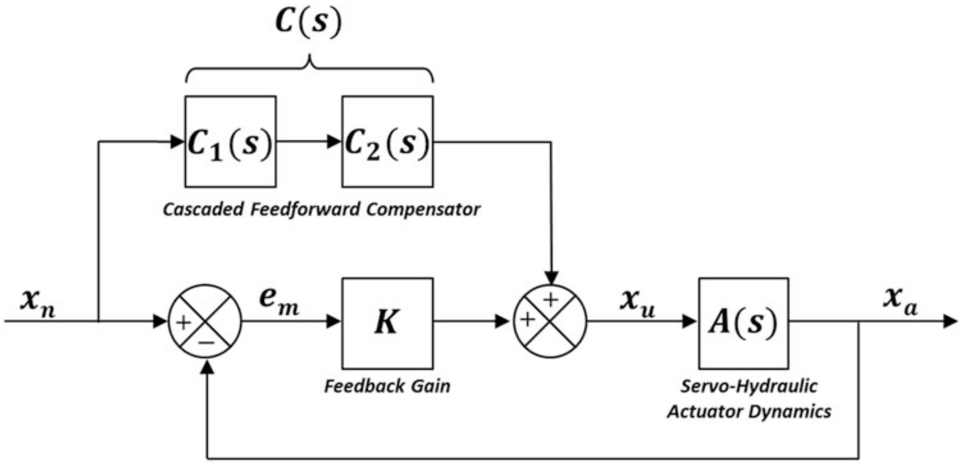

Fig. 3.7 Block diagram of cascaded feedforward inverse compensation

3.4.2 Low Pass Inverse Compensation

One approach is to multiply the improper actuator inverse by a low pass transfer function to make a proper transfer function. As described in Carrion and Spencer [16], this low pass inverse compensation (LPIC) technique involves an alpha scalar value to duplicate the poles of the actuator transfer function as additional poles at higher frequencies. These additional poles are used to create the low pass filter given by

$$L_{y_n x_m}(s) = \frac{\prod_{i=1}^{k} \alpha_i p_{i,m,n}}{\prod_{i=1}^{k} (s - \alpha_i p_{i,m,n})} \tag{3.10}$$

where k is the number of required additional poles. Multiplying the improper inverse of the actuator model by the low pass transfer functions yields the LPIC transfer function

$$C_{y_n x_m}(s) = A_{y_n x_m}(s)^{-1} L_{y_n x_m}(s) \tag{3.11}$$

Instead of using an alpha scalar to multiply the existing poles, the additional poles here are forced to be a specific frequency. This frequency should be high enough to minimize the effect on the low frequency dynamics over the control band but not too close to the sampling frequency so that accurate numerical integration is possible. The low pass transfer function is represented by

$$L_{y_n x_m}(s) = \frac{\prod_{i=1}^{k} \omega_i}{\prod_{i=1}^{k} (s - \omega_i)} \tag{3.12}$$

An independent inverse compensator was derived for each of the input output pairs of the MIMO transfer function matrix. Each of the elements of the MIMO transfer function matrix diagonal was treated as s SISO transfer function and was curve fit using the *invfreqs* MATLAB function. A constant (zero order) numerator and a fourth order denominator was found to the best fit of the frequency response data. The form of the curve fit is shown as

$$A_j(s) = \frac{n_{0j}}{d_{4j}s^4 + d_{3j}s^3 + d_{2j}s^2 + d_{1j}s + d_{0j}} \tag{3.13}$$

where j is the number of actuators. These SISO transfer function were place in a MIMO transfer function matrix along the diagonal as

$$\boldsymbol{A}(s) = \begin{bmatrix} A_1(s) & \cdots & 0 \\ \vdots & \ddots & \vdots \\ 0 & \cdots & A_j(s) \end{bmatrix} \tag{3.14}$$

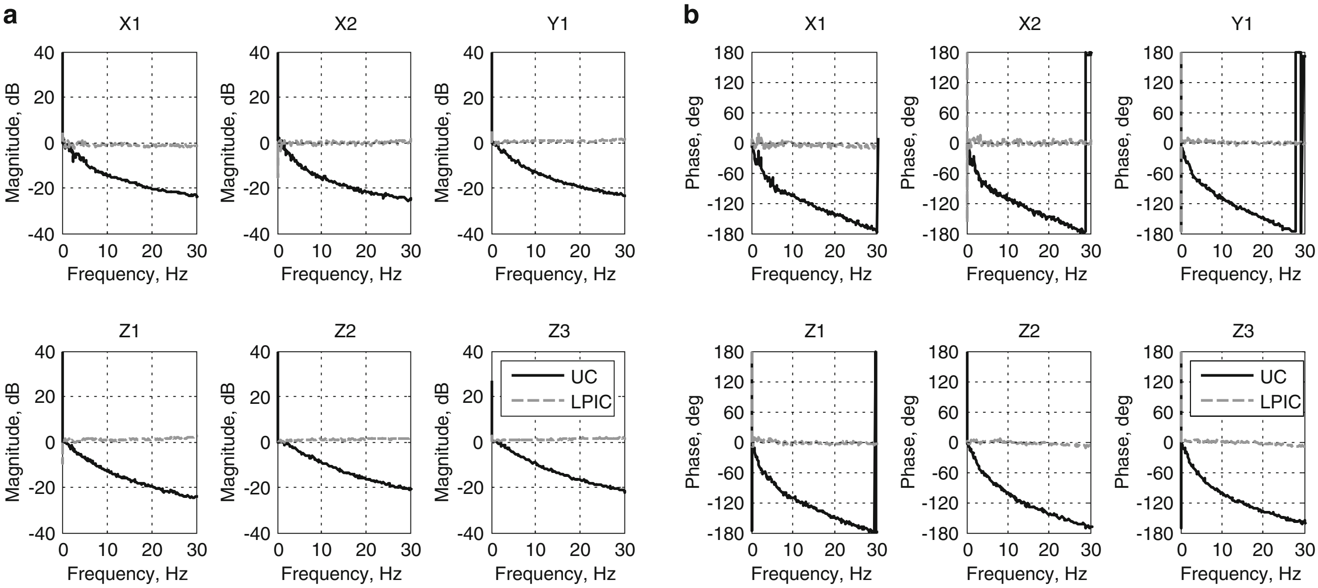

Fig. 3.8 Frequency response function magnitude (**a**) and phase (**b**) of the six actuators uncompensated and with cascaded LPIC compensator

Since this MIMO transfer function matrix is diagonal, each SISO transfer function along the diagonal can be independently inverted, which is the same as inverting the MIMO transfer function matrix. The LPIC transfer function matrix is then determined by

$$\boldsymbol{C}(s) = \boldsymbol{A}(s)^{-1} = \begin{bmatrix} C_1(s) & \cdots & 0 \\ \vdots & \ddots & \vdots \\ 0 & \cdots & C_j(s) \end{bmatrix} = \begin{bmatrix} A_1(s)^{-1}L_1(s) & \cdots & 0 \\ \vdots & \ddots & \vdots \\ 0 & \cdots & A_j(s)^{-1}L_j(s) \end{bmatrix} \tag{3.15}$$

System identification of the actuators was performed incorporating the initial low pass inverse feedforward compensator.

All the actuators show a significant decrease in the frequency dependent magnitude attenuation that was approximately 20–25 dB and was improved to approximately 0–2 dB and the time delay that was approximately 25–30 ms and was improved to approximately 2–3 ms. The addition of the second LPIC compensator left the magnitude mostly unchanged since that was not the goal of the additional compensation. The time delay that was approximately 2–3 ms was improved to approximately 1 ms. After two iterations of system identification, sufficient performance was seen from the actuators. Figure 3.8 shows uncompensated actuator frequency response functions versus the compensated actuator frequency response functions using the cascaded LPIC compensator.

3.5 Cartesian to Actuator Transformation

The 6-DOF shake table uses external command inputs to drive each of the six individual actuators. The output of the numerical substructure during the RTHS test will be in six Cartesian directions (three translation and three rotations). The original nonlinear transformation matrix developed by Nakata [20] takes an initial pin location p_i in 3D space and, by using translation and yaw-pitch-roll matrixes, locates a new pin location. The Euclidean normal from the base point coordinates q_i to the new pin location is calculated and then the length of the initial actuator is subtracted which determines the necessary displacement of the actuator δl_i. The displacement calculation is done for each actuator in the control system given a set of input translations and rotations, $t_{x,y,z}$ and $\theta_{x,y,z}$ respectively.

The linear actuator displacements necessary to achieve Cartesian displacements of the shake table causes various issues when combined with linearized feedforward inverse compensation techniques. To achieve certain Cartesian displacements, certain actuators are sent signals with sharp discontinuities. These discontinuities cause high frequency content which causes unstable behavior in the simulation.

The nonlinear transformation can be linearized by assuming linear small angle theorem. This simplifies the terms of the transformation matrix by eliminating non-linear trigonometric functions, which also eliminates the normal direction movement because of rotations. Using the small angle theorem,

$$sin\theta \approx \theta \quad cos\theta \approx 1$$

The linear transformation matrix becomes

$$\Psi\left(t_x, t_y, t_z, \theta_x, \theta_y, \theta_z\right) = \begin{bmatrix} 1 & -\theta_z & \theta_y & t_x \\ \theta_z + \theta_x\theta_y & 1 - \theta_x\theta_y\theta_z & -\theta_x & t_y \\ \theta_x\theta_z - \theta_y & \theta_x + \theta_y\theta_z & 1 & t_z \\ 0 & 0 & 0 & 1 \end{bmatrix} \tag{3.16}$$

The next step to simplify the transformation is to ignore any displacement that is not in the normal direction of the actuator. This is done by inspection of the transformation terms of each of the actuators. This simplification of the transformation matrix converts it from a 3D transformation into a 1D normal only transformation. The last step is to simplify the transformation by assuming that the horizontal actuators are vertically aligned with the CG of the table. This eliminates negligible vertical moment arms that require small actuator extensions. The final linear transformation matrix is then

$$\begin{Bmatrix} \delta l_1 \\ \delta l_2 \\ \delta l_3 \\ \delta l_4 \\ \delta l_5 \\ \delta l_6 \end{Bmatrix} = \begin{bmatrix} 1 & 0 & 0 & 0 & 0 & -p_{1y} \\ 1 & 0 & 0 & 0 & 0 & -p_{2y} \\ 0 & 1 & 0 & 0 & 0 & p_{3x} \\ 0 & 0 & 1 & p_{4y} & -p_{4x} & 0 \\ 0 & 0 & 1 & p_{5y} & -p_{5x} & 0 \\ 0 & 0 & 1 & p_{6y} & -p_{6x} & 0 \end{bmatrix} \begin{Bmatrix} t_x \\ t_y \\ t_z \\ \theta_x \\ \theta_y \\ \theta_z \end{Bmatrix} \tag{3.17}$$

Where p_{ij} is the pin location of the ith in the jth direction. The above linearized transformation for the six degree of freedom shake table can be easily used to determine the required actuator displacements to create the Cartesian displacements and rotations of the shake table. In addition, a simple inverse of this transformation matrix can be used to calculate the shake table displacements and rotations from the measured actuator displacements.

The linearized transformation was used to transform six table Cartesian command signal inputs into six actuator command signals. These six actuator signals were then passed through the cascaded LPIC feedforward compensators described above. The output of the feedforward compensators were commanded to the shake table actuators and the response of the table were then recorded. This response is the displacement of each of the six actuators. To calculate Cartesian frequency response functions, the responses of the actuators needed to be transformed back into the table Cartesian responses. This was done using the inverse of the linearized transformation. The results of this calculation are shown in Fig. 3.9.

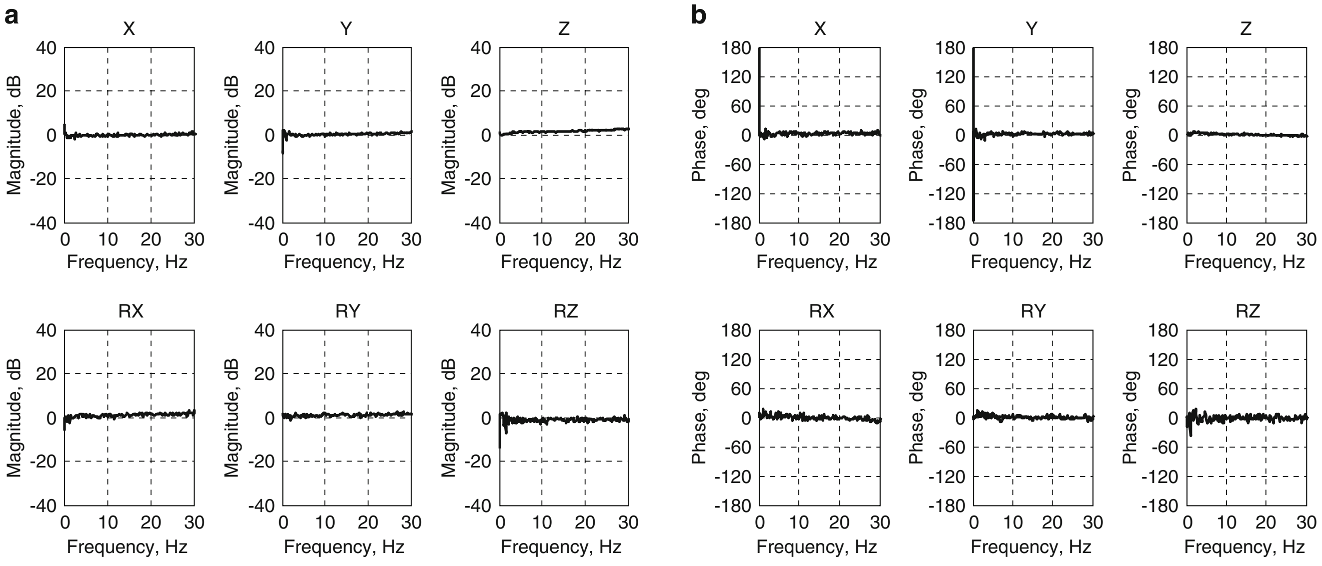

Fig. 3.9 Frequency response function magnitude (**a**) and phase (**b**) of six cartesian directions using the linearized transformation

Using the same cascaded LPIC compensator as shown in Fig. 3.8 demonstrates consistent performance for the Cartesian frequency response functions than the actuator frequency response functions shown in Fig. 3.8.

3.6 Conclusion

This paper described MIMO system identification and model-based feedforward feedback compensation of a six degree of freedom shake table for conducting stable RTHS testing of lightly damped mechanical systems. This approach involved compensating the actuator dynamics of the six individual actuators of the shake table to provide effective displacement tracking of the six Cartesian degrees of freedom (i.e., x, y, z translations and rotations) of the shake table. This was accomplished by calculating a MIMO transfer function matrix quantifying the frequency dependent magnitude and time delay. Once the actuator dynamics was quantified, a cascaded feedforward inverse compensation was developed to linearize the actuator dynamics and reduce the inherent time delay. The nonlinear transformation matrix relating the Cartesian degrees of freedom of the shake table to the six individual actuators was linearized to enable the use of feedforward inverse compensators designed for the shake table control. The cascaded feedforward inverse compensation and linearized transformation can be used to perform multiple degree of freedom RTHS testing of lightly damped mechanical systems using the six degree of freedom shake table as part of future research.

Acknowledgement The work is supported by the Office of Naval Research under project DOD/NAVY/ONR, Award No. N00014-11-1-0260, Program Director Deborah Nalchajian, Code 331.

References

1. Nakashima M, Masaoka N (1999) Real time on-line test for MDOF systems. Earthq Eng Struct Dyn 28:393–420
2. Darby AP, Blakeborough A, Williams MS (1999) Real time substructure test using hydraulic actuator. J Eng Mech 125(10):1133–1139
3. Dimig J, Shield C, French C, Bailey F, Clark A (1999) Effective force testing: a method of seismic simulation for structural testing. J Struct Eng 125(9):1028–1037
4. Horiuchi T, Inoue M, Konno T, Namita Y (1999) Real time hybrid experimental system with actuator delay compensation and it's applications to a piping system with energy absorber. Earthq Eng Struct Dyn 28(10):1121–1141
5. Christenson R, Lin YZ (2008) Real time hybrid simulation of a seismically excited structure with large scale magneto rheological fluid dampers. In: Hybrid simulation theory, implementation and applications. Taylor & Francis, London
6. Jiang Z, Kim SJ, Plude S, Christenson R (2013) Real time hybrid simulation of a complex bridge model with MR dampers using the convolution integral method. J Smart Mater Struct 22(10):105008
7. Hanselmann H (1993) Hardware-in-the loop simulation as a standard approach for development, customization, and production test of ECU's. SAE technical paper, 1993
8. Isermann R, Schaffnit J, Sinsel S (1999) Hardware-in-the-loop simulation for the design and testing of engine-control systems. Control Eng Pract 7(5):643–655
9. Bouscayrol A (2008) Different types of hardware-in-the-loop simulation for electric drives. Industrial Electronics, pp 2146–2151
10. Carmeli MS, Castelli-Dezzaa F, Mauri M, Marchegiani G (2013) Novel mechanical hardware in the loop platform for distributed generation systems. Distrib Gener Altern Energy J 28(3):7–27
11. Fathy HK, Ahlawat R, Stein JL (2005) Proper powertrain modeling for engine-in-the-loop simulation. ASME 2005 international mechanical engineering congress and exposition, pp 1195–1201
12. Filipi Z, Fathy H, Hagena J, Knafl A, Ahlawat R, Liu J, Jung D, Assanis D, Peng H, Stein J (2006) Engine-in-the-loop testing for evaluating hybrid propulsion concepts and transient emissions-HMMWV case study. AE technical paper
13. Filipi Z, Kim YJ (2010) Hydraulic hybrid propulsion for heavy vehicles: combining the simulation and engine-in-the-loop techniques to maximize the fuel economy and emission benefits. Oil Gas Sci Technol (Revue de l'Institut Francais du Petrole) 65(1):155–178
14. Jung RY, Shing PB (2006) Performance evaluation of a real time pseudodynamic test system. Earthq Eng Struct Dyn 35(7):789–810
15. Chen C, Ricles JM (2010) Tracking error based servohydraulic actuator adaptive compensation for real time hybrid simulation. J Struct Eng 10:432–440
16. Carrion JE, Spencer B (2007) Model based strategies for real time hybrid testing. NSEL report no NSEL-006
17. Phillips BM, Spencer BF (2011) Model based servo hydraulic control for real time hybrid simulation. Newmark Structural Engineering Laboratory report number NSE-028. University of Illinois, Urbana-Champaign
18. Phillips BM, Spencer BF (2012) Model-based multiactuator control for real-time hybrid simulation. J Eng Mech 139(2):219–228
19. Gao X, Castaneda N, Dyke SJ (2013) Experimental validation of a generalized procedure for MDOF real-time hybrid simulation. J Eng Mech 140(4):04013006
20. Nakata N, Spencer B, Elnashai A (2007) Multi-dimensional mixed-mode hybrid simulation control and applications. Newmark Structural Engineering Laboratory/University of Illinois at Urbana-Champaign, Urbana, Illionis
21. Bendat JS, Piersol AG (2011) Random data: analysis and measurement procedures. John Wiley & Sons, Hoboken, NJ

Chapter 4
Mathematical Equivalence Between Dynamic Substructuring and Feedback Control Theory

Rui M. Botelho and Richard E. Christenson

Abstract This paper presents a reformulation of dynamic substructuring for vibrating structural systems as a feedback control problem. Frequency based substructuring (FBS) using admittance coupling of two substructures is shown to be mathematically equivalent to a feedback control system with the primary substructure acting as the controller and the secondary substructure acting as the plant. This formulation can be used to perform time-domain simulations of dynamic substructuring problems using MATLAB's Simulink environment, whereby the primary substructure can be modeled by three possible approaches: (1) Laplace domain transfer functions, (2) state-space models, or (3) finite impulse response functions. The secondary substructure can be represented by a variety of Simulink blocks including nonlinear elements. By inserting an actuator transfer system between the two substructures, this formulation also provides the basis for real-time hybrid substructuring (RTHS) for coupling numerical and physical substructures as a cyber-physical system similar to hardware-in-the-loop testing. In typical RTHS the numerical substructure acts as the controller and the actuator with physical substructure acts as the plant. This feedback control formulation will lead to further advancements for both dynamic substructuring and RTHS by adapting methods from classical and modern feedback control theory.

Keywords Frequency based substructuring • Experimental structural dynamics • Real-time hybrid testing • Dynamic substructuring • Feedback control systems

4.1 Introduction

Dynamic substructuring has played a significant role in the field of structural dynamics since the advent of computational methods, particularly the finite element method (FEM). Dynamic substructuring involves dividing a structural dynamic system into parts or components, analyzing them separately, and then coupling them together by an assembly procedure. This methodology was introduced over four decades ago to reduce the complexity and computational size of structural finite element models, de Klerk et al. [1]. Although substructuring was initially conceived for computational modeling, it has also been successfully applied to experimental structural dynamics and is shown to provide a foundation for real-time hybrid substructuring (RTHS), which is a relatively new method of vibration testing that enables numerical and physical components to be coupled together in real-time as a cyber-physical system similar to hardware-in-the-loop (HWIL) testing.

One of the first approaches for dynamic substructuring of structural finite element models is the reduction method from Guyan [2]. Guyan reduction involves reducing the mass and stiffness matrices of a structural component using a transformation matrix relating the static displacements between the retained and condensed degrees of freedom. The reduced stiffness matrix is equivalent to static condensation and therefore an exact reduction, but the reduced mass matrix is approximate. Due to its simplicity, Guyan reduction has become very popular and is still in wide use today for computational dynamic substructuring of large finite element models. Since this method creates reduced mass and stiffness matrices in physical coordinates, Guyan reduction is most convenient for creating numerical substructures from finite element models.

Component mode synthesis (CMS) is another popular method for dynamic substructuring, which was also originally developed for computational modeling and then adapted for experimental structural dynamics. There are many flavors of CMS, including the method from Craig and Brampton [3] using fixed-interface vibration modes and constraint modes and the method from MacNeal [4] and Rubin [5] using free-interface vibration modes and residual flexibility modes. CMS was later extended by Duarte and Ewins [6] for experimental dynamic substructuring using modal analysis techniques. CMS provides

---

R.M. Botelho (✉) • R.E. Christenson
Department of Civil and Environmental Engineering, University of Connecticut, 261 Glenbrook Road
Unit 3037, Storrs, CT 06269-3037, USA
e-mail: rui.botelho@uconn.edu

M. Allen et al. (eds.), *Dynamics of Coupled Structures, Volume 4*, Conference Proceedings of the Society for Experimental Mechanics Series, DOI 10.1007/978-3-319-15209-7_4

a dynamic substructuring framework for deriving a hybrid model of a structural system comprised of numerical and experimental components or substructures described by their individual component modes. The component modes for the numerical substructure can be obtained from an eigenvalue analysis of the finite element model, while those for the experimental substructure can be obtained from experimental modal analysis as well as system identification techniques. Equilibrium and compatibility at the connection points are then used to couple the numerical and experimental substructures together into a reduced-order model of the original system. CMS is most appropriate for structural dynamic systems with negligible frequency-dependent effects that can be described by a relatively few number of lightly damped modes.

Frequency based substructuring (FBS) from Jetmundsen et al. [7] and its subsequent extensions by Gordis [8] and de Klerk et al. [9] provides a dynamic substructuring framework to couple numerical and experimental substructures together as a frequency-domain hybrid model. FBS uses frequency response function (FRF) matrices, which can be obtained for the experimental substructure using frequency response measurements and for the numerical substructure using finite element analysis. The substructure matrices are then assembled together using equilibrium and compatibility relations using either impedance coupling or its inverse called admittance coupling methods. An alternative method using Lagrange multipliers to couple the FRF matrices of numerical and experimental substructures, called Lagrange Multiplier Frequency Based Substructuring (LM-FBS), was introduced by de Klerk et al. [9]. These FBS methods can accommodate structural dynamic systems with many modes, high damping, and frequency-dependent behavior. But as with most frequency domain approaches, FBS methods assumes linearity and care must be taken to ensure reciprocity and passivity in the FRF matrices.

de Klerk et al. [1] and Maia and Silva [10] provide excellent reviews of the mathematical formulations for CMS and FBS methods for both model reduction and experimental dynamic substructuring. Allen and Mayes [11] compared CMS and FBS applied to a two-beam structures comprised of analytical and experimental beam substructures. While these approaches can be effective, they are limited to linear time-invariant systems, which may be inadequate for capturing highly complex, rate-dependent, and nonlinear behavior.

An approach to couple substructure state-space models was developed by Su and Juang [12]. This state-space coupling approach was developed to take advantage of system identification techniques commonly used in the aerospace engineering and controls systems analysis to identify state-space models. With this approach, the substructure state-space models are first identified either in the frequency-domain using frequency response data or in the time-domain using impulse response data or Markov parameters. Substructure state-space models are then assembled using transformations that enforce compatibility and equilibrium at the substructure interfaces. Sjövall and Abrahamsson [13] applied a similar state-space coupling approach but transforms the substructure state-space models into a coupling form to apply kinematic constraints and equilibrium conditions at the interfaces. They identified that the order of the state-space models used during the system identification process is critical to accurately synthesizing the coupled response.

Recently, Rixen and van der Valk [14] developed a time-domain counterpart to LM-FBS called Impulse Based Substructuring (IBS) using impulse response functions (IRF's) for the numerical and experimental substructures. The numerical IRF's can be obtained by transient finite element analysis of the numerical substructure subjected to impulse force loading, while the experimental IRF's can be obtained by hammer testing of the experimental substructure. The IBS method assembles the coupled system and computes the time history of the system response by evaluating the convolution product between the IRF's and the applied external forces as well as the interface forces between the substructures. IBS enforces compatibility at the interface of the substructures using Lagrange multipliers in a similar way as LM-FBS. IBS is most useful for analyzing linear time-invariant systems subjected to impact or other transient loading. IBS can also be used to perform computational hybrid simulation whereby linear numerical and experimental substructures described by IRF's are coupled to a numerical model of a nonlinear component solved by direct time integration.

Real-time hybrid substructuring (RTHS), also called real-time hybrid simulation or real-time dynamic substructuring, is a relatively new method of structural dynamic testing made feasible by recent advances in numerical computing power, digital signal processing, and high-speed servo-hydraulic actuation. RTHS allows a coupled system to be partitioned into separate physical and numerical substructures. The substructures that are well understood are simulated in real-time using analytical or numerical models, while those that are highly complex or nonlinear are physical tested using actual hardware specimens. The numerical and physical substructures communicate together in real-time by transferring displacement and force signals through a feedback loop using controlled actuation and sensing. The physical substructure is usually the experimental component of interest, while the numerical substructure is typically an analytical or numerical model of the remaining system incorporating various complexities that may be difficult to represent physically.

RTHS evolved from Pseudo Dynamic (PsD) testing to enable system-level characterization of physical structural components with strong rate-dependent effects, such as base isolators and nonlinear damping devices, particularly magneto-rheological (MR) fluid dampers, for seismic applications. Early developments of RTHS include Horiuchi et al. [15], Nakashima and Masaoka [16], and Darby et al. [17]. RTHS is also a major element of the Network for Earthquake Engineering Simulation (NEES). For example, Christenson and Lin [18] describe a large-scale RTHS test setup at the University of Colorado Boulder NEES facility to examine the system-level performance of multiple 200 kN MR fluid dampers in a three-story building structure. RTHS offers a more general approach than CMS, FBS and IBS methods to couple numerical and physical substructures together. CMS, FBS and IBS methods are essentially post-test experimental dynamic substructuring techniques that use linearized mathematical models of the physical substructures derived from measured data. RTHS is an online experimental dynamic substructuring technique, whereby the numerical and physical substructures communicate together in real-time by transferring displacement and force signals through a feedback loop using controlled actuation and sensing. Since RTHS involves a feedback loop, actuator dynamic compensation is needed to reduce the inherent time delay of the actuator transfer system and provide effective actuator tracking and closed-loop stability during RTHS testing.

Kim et al. [19] introduced the convolution integral method for RTHS (CIM-RTHS) as an alternative approach for solving the numerical substructure in real-time by exploiting linear superposition. In CIM-RTHS, the displacements imposed on the physical substructure are computed by convolving the measured restoring forces with pre-calculated impulse response functions of the numerical substructure combined with pre-calculated displacements due to the applied numerical loading. With this approach, the computational burden is moved from the RTHS testing into pre- and post-processing where real-time calculations are not required, allowing larger numerical models with increased complexity to be used. Jiang et al. [20] applied CIM-RTHS to evaluate large-scale MR dampers coupled to a complex bridge numerical substructure derived from a detailed finite element model. Recently, Botelho et al. [21] extended CIM-RTHS using discrete convolution with finite impulse response (FIR) filters for the numerical substructure and experimentally verified this method using RTHS testing of a cantilevered beam as the numerical substructure coupled to a viscous damper as the physical component.

It should be noted that the IBS method from Rixen [14] has similarities to CIM-RTHS form Kim et al. [19]. IBS was developed as the time-domain counterpart to LM-FBS to more efficiently perform computational and experimental dynamic substructuring for transient loading. CIM-RTHS was specifically developed for RTHS to reduce the computational burden of solving the numerical substructure by employing discrete convolution using pre-calculated impulse response functions. The common ingredient in both methods is the innovative use of impulse response functions to represent the numerical substructure. IBS can also be used to derive a hybrid time-domain model of the system by coupling numerical impulse response functions with experimental impulse response functions, but this method assumes that the physical substructure is linear. On the other hand, CIM-RTHS interfaces the impulse response functions of the numerical substructure to an actual physical specimen in real-time through an actuator transfer system, allowing nonlinear behavior of the physical substructure to be captured.

This paper presents a reformulation of dynamic substructuring as a feedback control problem. FBS using admittance coupling of two substructures is shown to be mathematically equivalent to a feedback control system with the primary substructure acting as the controller and the secondary substructure acting as the plant. This formulation can be used to perform time-domain simulations of dynamic substructuring problems using MATLAB's Simulink environment. By inserting an actuator transfer system between the two substructures, this formulation also provides the basis for RTHS for coupling numerical and physical substructures together in real-time. In typical RTHS, the numerical substructure acts as the controller and the actuator with physical substructure acts as the plant. This feedback control formulation will lead to further advancements for both dynamic substructuring and RTHS by adapting methods from classical and modern feedback control theory.

4.2 Feedback Control Theory

To illustrate the mathematical equivalence between dynamic substructuring and feedback control, the closed loop response for a typical multiple-input-multiple-output (MIMO) feedback control system for reference tracking and disturbance rejection is first reviewed. Figure 4.1 shows the Laplace domain block diagram of a typical feedback control system.

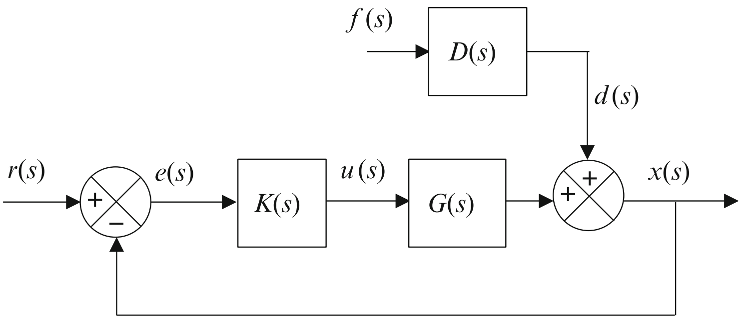

Fig. 4.1 Block diagram of a typical feedback control system

In the diagram, *D(s)* is the disturbance transfer function relating the force inputs, *f(s)*, to the disturbance outputs, *d(s)*, *G(s)* is the plant transfer function relating the control inputs, *u(s)*, to the response outputs, *x(s)*, and *K(s)* is the controller transfer function relating the error signals, *e(s)*, to the control inputs.

The error signals are related to reference inputs, *r(s)*, and response outputs by

$$\{e(s)\} = \{r(s)\} - \{x(s)\} \tag{4.1}$$

The response outputs are related to the force input and error by

$$\{x(s)\} = [D(s)]\{f(s)\} + [G(s)][K(s)]\{e(s)\} \tag{4.2}$$

Substituting (4.2) into (4.1) and rearranging yields the closed loop response

$$\{x(s)\} = [I + G(s)K(s)]^{-1}[G(s)][K(s)]\{r(s)\} + [I + G(s)K(s)]^{-1}[D(s)]\{f(s)\} \tag{4.3}$$

Note that the above expression has a common factor, which is the sensitivity matrix

$$[S_{FB}(s)] = [I + L_{FB}(s)]^{-1} \tag{4.4}$$

where, $L_{FB}(s) = G(s)K(s)$ is the loop gain.

Using the above expression, (4.3) becomes

$$\{x(s)\} = [S_{FB}(s)][G(s)][K(s)]\{r(s)\} + [S_{FB}(s)][D(s)]\{f(s)\} \tag{4.5}$$

The above equation represents the closed-loop response of a typical feedback control system subjected to a reference and a disturbance input. The first term corresponds to the closed-loop response for reference tracking, while the second term corresponds to the closed-loop response for disturbance rejection. This equation will be used later to contrast against the coupled response for a dynamic substructuring problem. Note that the sensitivity matrix above has the subscript FB to denote feedback control and differentiate it from the ones that will be derived for dynamic substructuring (DS) and real-time hybrid substructuring (RTHS) in the following sections.

4.3 Dynamic Substructuring

Now consider the dynamic substructuring problem shown in Fig. 4.2, in which a notional structural dynamic system is partitioned into two components, a primary substructure and a secondary substructure. The primary substructure is subjected to a driving force, $f_d^{(p)}$, while the secondary substructure is subjected to a driving force, $f_d^{(s)}$. Although this system illustrates a two interface degrees-of-freedom (DOFs), the subsequent reformulation of dynamic substructuring as a feedback control problem is general and can be applied to cases with many interface DOFs.

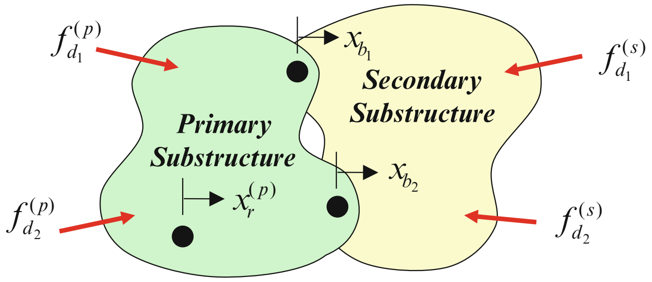

Fig. 4.2 Dynamic substructuring applied to a notional structural dynamic system

The traditional approach to couple two dynamic substructures is to employ FBS using either impedance or admittance coupling methods. To illustrate the relationship to feedback control, FBS using admittance coupling and cast in the Laplace domain provides a convenient starting point. Using $s = i\omega$, the response of the primary substructure can be written as

$$\begin{Bmatrix} x_r^{(p)}(s) \\ x_b^{(p)}(s) \end{Bmatrix} = \begin{bmatrix} H^{(p)}_{x_r f_d}(s) \\ H^{(p)}_{x_b f_d}(s) \end{bmatrix} \left\{ f_d^{(p)}(s) \right\} + \begin{bmatrix} H^{(p)}_{x_r f_b}(s) \\ H^{(p)}_{x_b f_b}(s) \end{bmatrix} \left\{ f_b^{(p)}(s) \right\} \tag{4.6}$$

In the above equation, $x_r^{(p)}$ are the displacements of the primary substructure at particular DOF's of interest, $x_b^{(p)}$ are the displacements of the primary substructure at the interface boundary DOF's, $f_b^{(p)}$ are the boundary forces of the primary substructure at the interface boundary DOF's, and $H^{(p)}_{x_i f_j}$ are the frequency dependent admittance matrix of the primary substructure relating a force input at the jth DOF to a displacement output at the ith DOF.

From force equilibrium, the boundary forces of the primary substructure are related to the boundary forces of the secondary substructure by

$$\left\{ f_b^{(p)}(s) \right\} = -\left\{ f_b^{(s)}(s) \right\} \tag{4.7}$$

From displacement compatibility, the boundary displacements of the primary substructure are related to the boundary displacements of the secondary substructure by

$$\left\{ x_b^{(p)}(s) \right\} = \left\{ x_b^{(s)}(s) \right\} \tag{4.8}$$

For the secondary substructure, the dynamic equilibrium equation can be written in the frequency domain as

$$\begin{bmatrix} D^{(s)}_{f_d x_d}(s) & D^{(s)}_{f_d x_b}(s) \\ D^{(s)}_{f_b x_d}(s) & D^{(s)}_{f_b x_b}(s) \end{bmatrix} \begin{Bmatrix} x_d^{(s)}(s) \\ x_b^{(s)}(s) \end{Bmatrix} = \begin{Bmatrix} f_d^{(s)}(s) \\ f_b^{(s)}(s) \end{Bmatrix} \tag{4.9}$$

In the above equation, $x_d^{(s)}$ are the displacements of the secondary substructure at the drive force DOF's, $x_b^{(s)}$ are the displacements of the secondary substructure at the interface boundary DOF's, $f_b^{(s)}$ are the boundary forces of the secondary substructure at the interface boundary DOF's, and $D^{(s)}_{f_i x_j}$ are the frequency dependent dynamic stiffness matrix relating a displacement input at the *jth* DOF to the reaction force output at the *ith* DOF. The upper equation of (4.9) leads to

$$\left\{ x_d^{(s)}(s) \right\} = \left[D^{(s)}_{f_d x_d}(s) \right]^{-1} \left\{ f_d^{(s)}(s) \right\} - \left[D^{(s)}_{f_d x_d}(s) \right]^{-1} \left[D^{(s)}_{f_d x_b}(s) \right] \left\{ x_b^{(s)}(s) \right\} \tag{4.10}$$

Substituting (4.10) into the lower equation of (4.9) and rearranging yields

$$\left\{ f_b^{(s)}(s) \right\} = \left[\tilde{D}^{(s)}_{f_b x_b}(s) \right] \left\{ x_b^{(s)}(s) \right\} + \left[\tilde{D}^{(s)}_{f_b f_d}(s) \right] \left\{ f_d^{(s)}(s) \right\} \tag{4.11}$$

Where, $\left[\tilde{D}^{(s)}_{f_b x_b}(s) \right] = \left[D^{(s)}_{f_b x_b}(s) \right] - \left[D^{(s)}_{f_b x_d}(s) \right] \left[D^{(s)}_{f_d x_d}(s) \right]^{-1} \left[D^{(s)}_{f_d x_b}(s) \right]$ and $\left[\tilde{D}^{(s)}_{f_b f_d}(s) \right] = \left[D^{(s)}_{f_b x_d}(s) \right] \left[D^{(s)}_{f_d x_d}(s) \right]^{-1}$

The boundary forces at interface DOF's are found by substituting (4.7) and (4.8) into the lower equation of (4.6) and then substituting into (4.11), which yields

$$\left\{ f_b^{(s)}(s) \right\} = \left[\tilde{D}^{(s)}_{f_b x_b}(s) \right] \left[H^{(p)}_{x_b f_d}(s) \right] \left\{ f_d^{(p)}(s) \right\} - \left[\tilde{D}^{(s)}_{f_b x_b}(s) \right] \left[H^{(p)}_{x_b f_b}(s) \right] \left\{ f_b^{(s)}(s) \right\} + \left[\tilde{D}^{(s)}_{f_b f_d}(s) \right] \left\{ f_d^{(s)}(s) \right\} \tag{4.12}$$

Rearranging as

$$\begin{aligned} \left\{ f_b^{(s)}(s) \right\} = {} & \left[I + \tilde{D}^{(s)}_{f_b x_b}(s) H^{(p)}_{x_b f_b}(s) \right]^{-1} \left[\tilde{D}^{(s)}_{f_b x_b}(s) \right] \left[H^{(p)}_{x_b f_d}(s) \right] \left\{ f_d^{(p)}(s) \right\} \\ & + \left[I + \tilde{D}^{(s)}_{f_b x_b}(s) H^{(p)}_{x_b f_b}(s) \right]^{-1} \left[\tilde{D}^{(s)}_{f_b f_d}(s) \right] \left\{ f_d^{(s)}(s) \right\} \end{aligned} \tag{4.13}$$

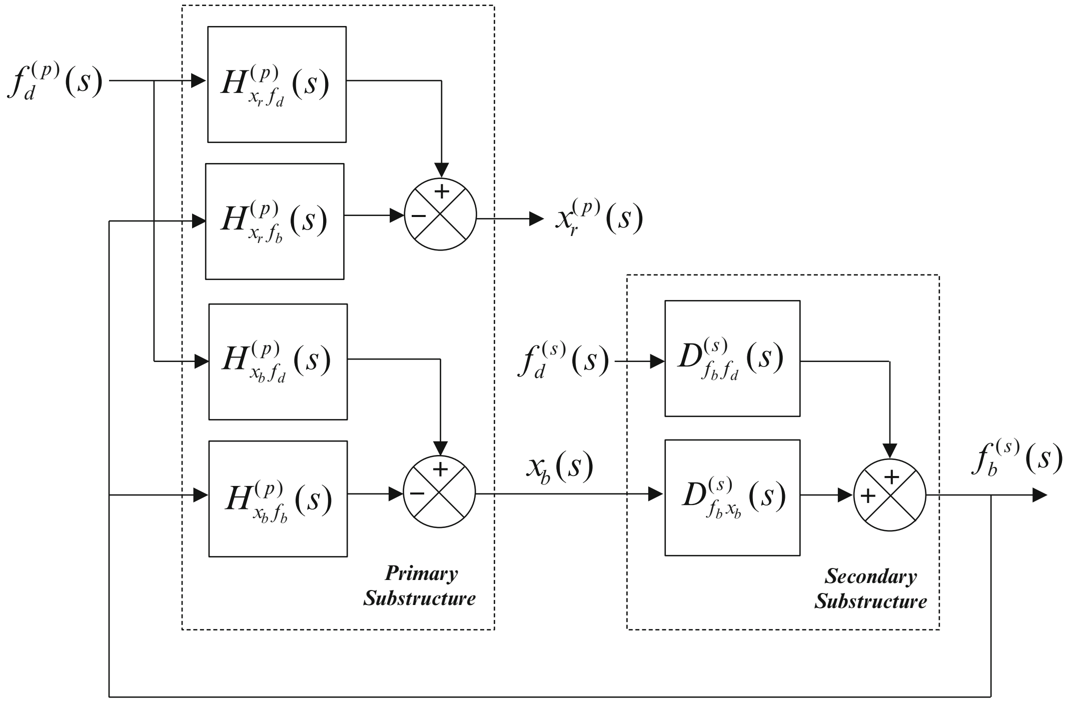

Fig. 4.3 Block diagram of dynamic substructuring formulated as feedback control system

Comparing (4.13) to (4.3), we see that the above expression is essentially the same as that for the closed-loop response of a MIMO feedback control system. The primary substructure admittance matrix, $H^{(p)}_{x_b f_b}(s)$, acts as the controller and the secondary substructure dynamic stiffness, $\tilde{D}^{(s)}_{f_b x_b}(s)$, acts as the plant. Using this analogy, we see that the sensitivity matrix for dynamic substructuring is

$$[S_{DS}(s)] = [I + L_{DS}(s)]^{-1} \tag{4.14}$$

where, $L_{DS}(s) = \tilde{D}^{(s)}_{f_b x_b}(s) H^{(p)}_{x_b f_b}(s)$ is the loop gain for dynamic substructuring.

Using the above expression, (4.13) becomes

$$\left\{f_b^{(s)}(s)\right\} = [S_{DS}(s)]\left[\tilde{D}^{(s)}_{f_b x_b}(s)\right]\left[H^{(p)}_{x_b f_d}(s)\right]\left\{f_d^{(p)}(s)\right\} + [S_{DS}(s)]\left[\tilde{D}^{(s)}_{f_b f_d}(s)\right]\left\{f_d^{(s)}(s)\right\} \tag{4.15}$$

The above equation for dynamic substructuring resembles (4.5) for feedback control. The first term resembles the closed-loop response for reference tracking, while the second term resembles the closed-loop response for disturbance rejection. The corresponding block diagram for dynamic substructuring formulated as a feedback control problem is illustrated in Fig. 4.3.

Using the multiplication and summation operations, the above block diagram can also be used to derive the interface boundary forces in (4.15). Using the block diagram or the upper equation of (4.6), the displacement responses are

$$\{x_r^{(p)}(s)\} = \left[H^{(p)}_{x_r f_d}(s)\right]\left\{f_d^{(p)}(s)\right\} - \left[H^{(p)}_{x_b f_b}(s)\right]\left\{f_b^{(s)}(s)\right\} \tag{4.16}$$

and the interface boundary displacements are

$$\left\{x_b^{(p)}(s)\right\} = \left[H^{(p)}_{x_b f_d}(s)\right]\left\{f_d^{(p)}(s)\right\} - \left[H^{(p)}_{x_b f_b}(s)\right]\left\{f_b^{(s)}(s)\right\} \tag{4.17}$$

Substituting (4.13) into (4.16), the displacement responses are then

$$\begin{aligned}\{x_r^{(p)}(s)\} = {} & \left(\left[H^{(p)}_{x_r f_d}(s)\right] - \left[H^{(p)}_{x_r f_b}(s)\right]\left[I + \tilde{D}^{(s)}_{f_b x_b}(s) H^{(p)}_{x_b f_b}(s)\right]^{-1}\left[\tilde{D}^{(s)}_{f_b x_b}(s)\right]\left[H^{(p)}_{x_b f_d}(s)\right]\right)\left\{f_d^{(p)}(s)\right\} \\ & - \left[H^{(p)}_{x_r f_b}(s)\right]\left[I + \tilde{D}^{(s)}_{f_b x_b}(s) H^{(p)}_{x_b f_b}(s)\right]^{-1}\left[\tilde{D}^{(s)}_{f_b f_d}(s)\right]\left\{f_d^{(s)}(s)\right\}\end{aligned} \tag{4.18}$$

Substituting (4.13) into (4.17), the interface boundary responses are then

$$\left\{x_b^{(p)}(s)\right\} = \left(\left[H_{x_b f_d}^{(p)}(s)\right] - \left[H_{x_b f_b}^{(p)}(s)\right]\left[I + \tilde{D}_{f_b x_b}^{(s)}(s) H_{x_b f_b}^{(p)}(s)\right]^{-1}\left[\tilde{D}_{f_b x_b}^{(s)}(s)\right]\left[H_{x_b f_d}^{(p)}(s)\right]\right)\left\{f_d^{(p)}(s)\right\}$$
$$- \left[H_{x_b f_b}^{(p)}(s)\right]\left[I + \tilde{D}_{f_b x_b}^{(s)}(s) H_{x_b f_b}^{(p)}(s)\right]^{-1}\left[\tilde{D}_{f_b f_d}^{(s)}(s)\right]\left\{f_d^{(s)}(s)\right\} \tag{4.19}$$

Substituting (4.14) into (4.19) and expressing in matrix form, the displacement responses are

$$\begin{Bmatrix} x_r^{(p)}(s) \\ x_b^{(p)}(s) \end{Bmatrix} = \begin{bmatrix} H_{x_r f_d}^{(p)}(s) - H_{x_r f_b}^{(p)}(s) \\ H_{x_b f_d}^{(p)}(s) - H_{x_{br} f_b}^{(p)}(s) \end{bmatrix} S_{DS}(s) \tilde{D}_{f_b x_b}^{(s)}(s) H_{x_b f_d}^{(p)}(s) \left\{f_d^{(p)}(s)\right\}$$
$$- \begin{bmatrix} H_{x_r f_b}^{(p)}(s) \\ H_{x_b f_b}^{(p)}(s) \end{bmatrix} S_{DS}(s) \tilde{D}_{f_b f_d}^{(s)}(s) \left\{f_d^{(s)}(s)\right\} \tag{4.20}$$

The above feedback control formulation for dynamic substructuring can be used to solve coupled response of two substructures. The primary substructure is represented by frequency-dependent admittance matrices, while the secondary substructure is represented by frequency dependent dynamic stiffness matrices. By substituting $s = i\omega$, similar equations can be derived in the frequency domain. The Laplace domain description however allows the use of MATLAB's Control System Toolbox for solving the frequency and time domain response of dynamic substructuring problems. This toolbox has several methods from classical and modern feedback control theory, which can be directly applied to dynamic substructuring.

Using the block diagram, the above feedback control formulation for dynamic substructuring can also be used to perform time-domain simulations using MATLAB's Simulink environment. In Simulink, the primary substructure can be modeled by three possible approaches: (1) Laplace domain transfer functions, (2) state-space models, or (3) finite impulse response (FIR) filters. The secondary substructure, which is in the form of a dynamic stiffness matrix relating input displacements to output forces, can be represented by combinations of gain and time derivative blocks as well as nonlinear element blocks available Simulink. This approach facilitates the development of more complex and realistic simulations of dynamic substructuring, including nonlinear substructures.

4.4 Real Time Hybrid Substructuring

By inserting an actuator transfer system between the two substructures, the above feedback control formulation for dynamic substructuring provides the basis for real-time hybrid substructuring (RTHS). With RTHS, a structural dynamic system is partitioned into separate numerical and physical substructures and interfaced together in real-time using controlled actuation and sensing as a cyber-physical system similar to HWIL testing. Figure 4.4 illustrates RTHS applied to the same notional structural dynamic system, but now partitioned into separate numerical and physical substructures.

The corresponding block diagram for RTHS, which is essentially a MIMO feedback control system, is shown in Fig. 4.5. The numerical substructure is subjected to a numerical driving force, $f_d^{(n)}$, while the physical substructure is subjected to an experimental driving force, $f_d^{(e)}$. The numerical response, $x_r^{(n)}$, are the displacements of the numerical substructure at particular DOF's of interest, $x_b^{(n)}$ are the displacements of the numerical substructure at the interface boundary DOF's, $x_b^{(e)}$ are the experimental displacements of the physical substructure at the interface boundary DOF's imposed by the actuator transfer system, $f_b^{(e)}$ are the experimental restoring forces of the physical substructure measured at the interface boundary DOF's. For the numerical substructure, $H_{x_i f_j}^{(n)}$ corresponds to the frequency dependent admittance relating a force input at the *jth* DOF to a displacement output at the *ith* DOF. The force inputs include the numerical drive forces and the experimental restoring forces at the interface boundary DOF's. For the physical substructure, $D_{f_b x_b}^{(s)}$ corresponds to the frequency dependent dynamic stiffness relating an actuator displacement input to the experimental restoring force at the interface boundary DOF, and $D_{f_b f_d}^{(s)}$ corresponds to the frequency dependent force transmissibility relating an experimental driving force input to the experimental restoring forces at the interface boundary DOF's.

To enforce force equilibrium, the experimental restoring forces from the physical substructure are fed back to the numerical substructure and applied as equal and opposite input forces. To enforce displacement compatibility, the actuator transfer system with compensation is used to impose the numerical displacement response onto the physical substructure. The dynamics of the actuator transfer system with appropriate compensation is represented by the actuator transfer function $\hat{A}(s)$. It should be noted that sensor dynamics for the measured restoring force of the physical substructure are neglected.

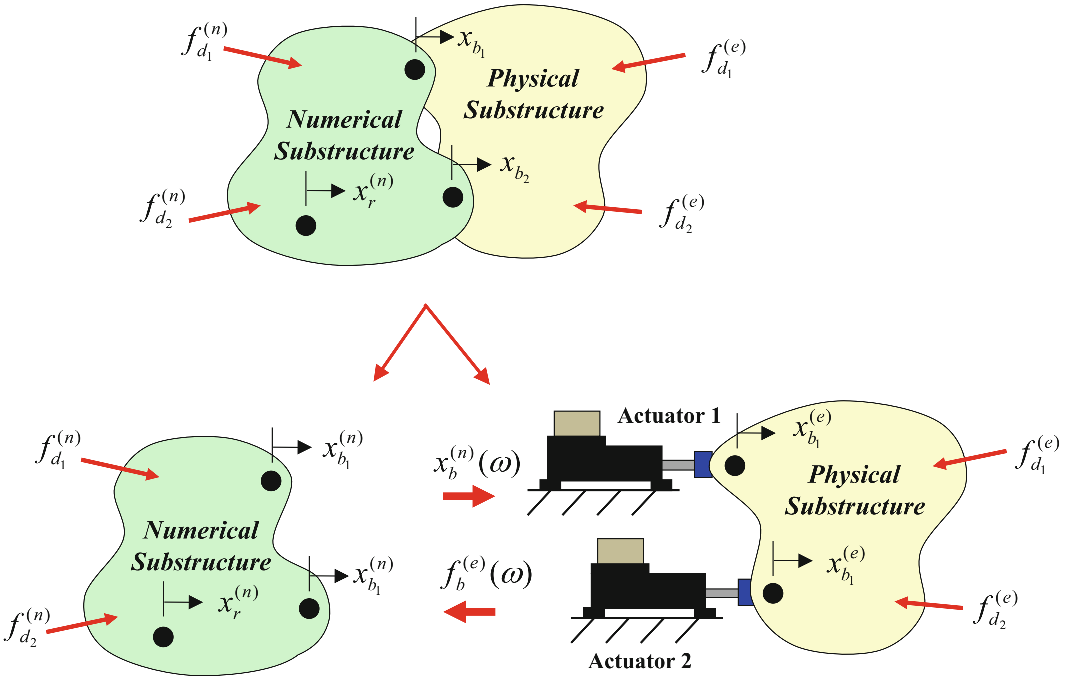

Fig. 4.4 RTHS applied to a notional structural dynamic system

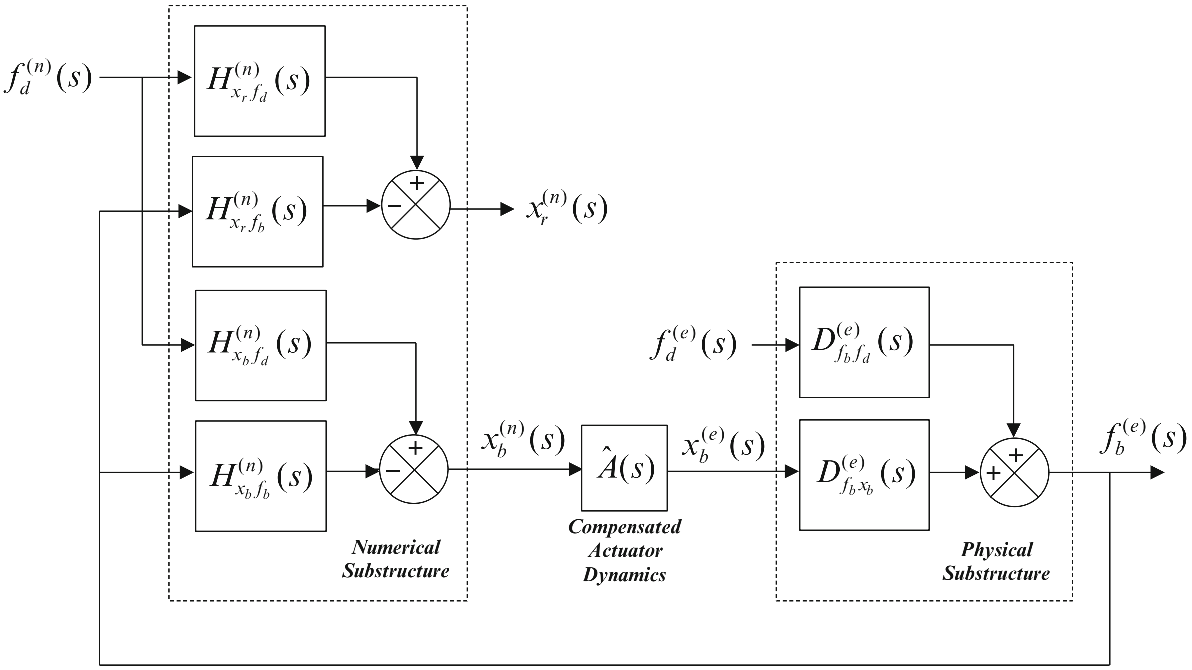

Fig. 4.5 Block diagram for RTHS of notional structural dynamic system

With appropriate selection of force sensors with constant magnitude and little phase distortion at low frequencies, this is a reasonable assumption for the control band of a typical RTHS test below 100 Hz.

From the above block diagram, the closed-loop response for the experimental restoring force is

$$\left\{f_b^{(e)}(s)\right\} = \left[I + D_{f_b x_b}^{(e)}(s)\widehat{A}(s)H_{x_b f_b}^{(n)}(s)\right]^{-1}\left[D_{f_b x_b}^{(e)}(s)\right]\left[\widehat{A}(s)\right]\left[H_{x_b f_d}^{(n)}(s)\right]\left\{f_d^{(n)}(s)\right\}$$
$$+\left[I + D_{f_b x_b}^{(e)}(s)\widehat{A}(s)H_{x_b f_b}^{(n)}(s)\right]^{-1}\left[D_{f_b f_d}^{(e)}(s)\right]\left\{f_d^{(e)}(s)\right\} \quad (4.21)$$

Comparing (4.21) to (4.3), we see again that the above expression is similar to the closed-loop response of a MIMO feedback control system. For RTHS, the numerical substructure admittance, $H^{(n)}_{x_b f_b}(s)$, acts as the controller and the actuator dynamics with physical substructure dynamic stiffness, $D^{(e)}_{f_b x_b}(s)\widehat{A}(s)$, acts as the plant. Using this analogy, we see that the sensitivity matrix for RTHS is

$$[S_{RTHS}(s)] = [I + L_{RTHS}(s)]^{-1} \tag{4.22}$$

where $L_{RTHS}(s) = D^{(e)}_{f_b x_b}(s)\widehat{A}(s)H^{(n)}_{x_b f_b}(s)$ is the loop gain for RTHS.

Using the above expression, (4.21) becomes

$$\left\{f_b^{(e)}(s)\right\} = [S_{RTHS}(s)]\left[D^{(e)}_{f_b x_b}(s)\right]\left[\widehat{A}(s)\right]\left[H^{(n)}_{x_b f_d}(s)\right]\left\{f_d^{(n)}(s)\right\} + [S_{RTHS}(s)]\left[D^{(e)}_{f_b f_d}(s)\right]\left\{f_d^{(e)}(s)\right\} \tag{4.23}$$

The above equation for dynamic substructuring in terms of sensitivities resembles (4.5) for feedback control and (4.15) for dynamic substructuring. The first term resembles the closed-loop response for reference tracking, while the second term resembles the closed-loop response for disturbance rejection.

Using the block diagram, the closed-loop response for the displacement responses are

$$\begin{aligned}\begin{Bmatrix} x_r^{(n)}(s) \\ x_b^{(n)}(s) \end{Bmatrix} &= \begin{bmatrix} H^{(n)}_{x_r f_d}(s) - H^{(n)}_{x_r f_b}(s) \\ H^{(n)}_{x_b f_d}(s) - H^{(n)}_{x_{br} f_b}(s) \end{bmatrix} S_{RTHS}(s) D^{(e)}_{f_b x_b}(s)\widehat{A}(s)H^{(n)}_{x_b f_d}(s)\left\{f_d^{(n)}(s)\right\} \\ &\quad - \begin{bmatrix} H^{(n)}_{x_r f_b}(s) \\ H^{(n)}_{x_b f_b}(s) \end{bmatrix} S_{RTHS}(s) D^{(e)}_{f_b f_d}(s)\left\{f_d^{(e)}(s)\right\}\end{aligned} \tag{4.24}$$

The above feedback control formulation for RTHS can be used to couple a numerical substructure to a physical specimen and solve the coupled system response in real-time. Figure 4.6 illustrates the general block diagram of the feedback loop for a typical RTHS test. At a given time-step, numerical loading is applied to the numerical substructure to simulate the numerical displacements, x_n, to be imposed on the physical substructure in real-time. The numerical displacements are then fed into a controller to apply the command displacements, x_c, to the actuator transfer system, which is usually a set of hydraulic actuators controlled by a proportional-integral-derivative (PID) servo-controller using the measured displacement, x_m, as the feedback signal. The measured restoring force, f_r, of the physical substructure is then fed back into the numerical substructure to compute the numerical displacements for the next time step. RTHS also accommodates physical loading of the physical substructure from external shaker forcing of the physical specimen.

In a typical RTHS test, a real-time processing board is used to solve the numerical substructure and apply the actuator dynamics compensation, which is needed to reduce the inherent time delay of the actuator transfer system. These components can be programmed on a host computer and transferred to real-time processing board using MATLAB's Real-Time Workshop. To drive the physical substructure, the displacement commands from real-time processing board can be sent to the motion controller of the servo-hydraulic actuator. The measured restoring force signals are then sent back into real-time processing board to complete the RTHS feedback loop. The measured data from the physical accelerometer and force sensors

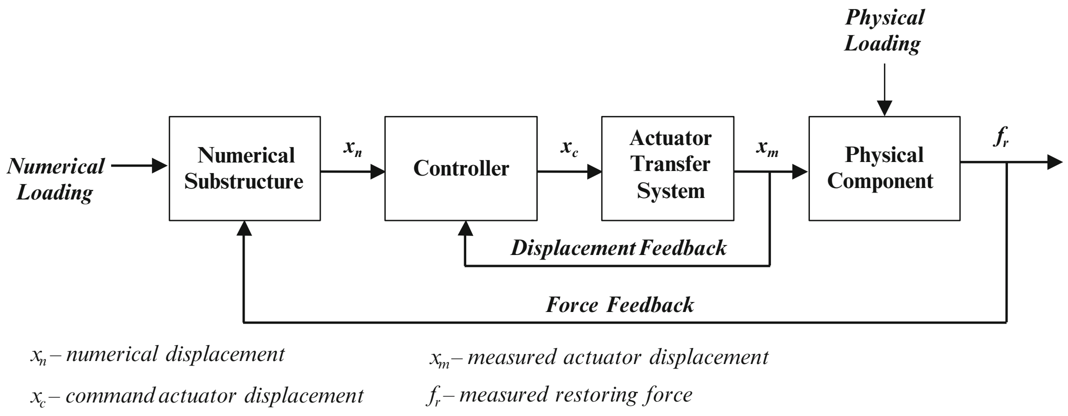

Fig. 4.6 Block diagram of a typical RTHS test

on the physical substructure and the virtual displacement sensors of the numerical substructure from real-time processing board can be acquired using a standard data acquisition system. When using Simulink to program to setup an RTHS test, the numerical substructure can be modeled by Laplace domain transfer functions or state-space models. Recently, Botelho et al. [21] modeled the numerical substructure in a RTHS test using FIR filters.

4.5 Conclusions

This paper presented a reformulation of dynamic substructuring as a feedback control problem to illustrate their mathematical equivalence. It was shown that FBS using admittance coupling of two substructures is mathematically equivalent to a feedback control system with the primary substructure acting as the controller and the secondary substructure acting as the plant. In addition, the formulation shows that the coupled response from a force input on the primary substructures resembles the closed-loop response for reference tracking, while the coupled response from a force input on the secondary substructures resembles the closed-loop response for disturbance rejection. By inserting an actuator transfer system between the two substructures, this formulation also provides the basis for RTHS for coupling numerical and physical substructures together in real-time. For RTHS, the numerical substructure acts as the controller and the actuator with physical substructure acts as the plant. This feedback control formulation will lead to further advancements for both dynamic substructuring and RTHS by adapting methods from classical and modern feedback control theory.

Acknowledgments The work is supported by the Office of Naval Research under project DOD/NAVY/ONR, Award No. N00014-11-1-0260, Program Director: Deborah Nalchajian.

References

1. de Klerk D, Rixen DJ, Voormeeren SN (2008) General framework for dynamic substructuring: history, review and classification of techniques. AIAA J 46(5):1169–1181
2. Guyan R (1965) Reduction of stiffness and mass matrices. AIAA J 3:380
3. Craig R, Bampton M (1968) Coupling of substructures for dynamic analysis. AIAA J 6(7):1313–1319
4. MacNeal R (1971) Hybrid method of component mode synthesis. Comput Struct 1(4):581–601
5. Rubin S (1975) Improved component-mode representation for structural dynamic analysis. AIAA J 13(8):995–1006
6. Duarte M, Ewins D (1996) Improved experimental component mode synthesis with residual compensation based on purely experimental results. In: Proceedings of the 14th international modal analysis conference, Society for Experimental Mechanics
7. Jetmundsen B, Bielawa R, Flannelly W (1988) Generalized frequency domain substructure synthesis. J Am Helicopter Soc 33(1):55–65
8. Gordis JH (1994) Structural synthesis in the frequency domain, a general formulation. Shock Vib 1(5):461–471
9. de Klerk D, Rixen DJ, de Jong J (2006) The frequency based substructuring (FBS) method reformulated according to the dual domain decomposition method. In: Proceedings of the 24th international modal analysis conference, Society for Experimental Mechanics
10. Maia NMM, Silva JMM (1998) Theoretical and experimental modal analysis. Research Studies Press, Baldock, Hertfordshire
11. Allen MS, Mayes RL (2007) Comparison of FRF and modal methods for combining experimental and analytical substructures. In: Proceedings of the 25th international modal analysis conference, Society for Experimental Mechanics
12. Su T-J, Juang J-N (1994) Substructure system identification and synthesis. J Guid Control Dyn 17(5):1087–1095
13. Sjövall P, Abrahamsson TJS (2007) State-space model identification for component synthesis. In: Proceedings of the 25th international modal analysis conference, Society for Experimental Mechanics
14. Rixen DJ, van der Valk PLC (2013) An impulse based substructuring approach for impact analysis and load case simulations. J Sound Vib 332:7174–7190
15. Horiuchi T, Inoue M, Konno T, Namita Y (1999) Real-time hybrid experimental system with actuator delay compensation and its application to a piping system with energy absorber. Earthq Eng Struct Dyn 28(10):1121–1141
16. Nakashima M, Masaoka N (1999) Real-time on-line test for MDOF systems. Earthq Eng Struct Dyn 28:393–420
17. Darby AP, Blakeborough A, Williams MS (1999) Real-time substructure tests using hydraulic actuator. J Eng Mech 125(10):1133–1139
18. Christenson R, Lin YZ (2008) Real-time hybrid simulation of a seismically excited structure with large-scale magneto-rheological fluid dampers. In: Saouma VE, Sivaselvan MV (eds) Hybrid simulation theory, implementations and applications. Taylor and Francis NL, London. ISBN 978-0-415-46568-7
19. Kim SJ, Christenson R, Wojtkiewicz S, Johnson E (2011) Real-time hybrid simulation using the convolution integral method. Smart Mater Struct 20(2)
20. Jiang Z, Kim SJ, Plude S, Christenson R (2013) Real-time hybrid simulation of a complex bridge model with MR dampers using the convolution integral method. J Smart Mater Struct 22(10):105008. doi:10.1088/0964-1726/22/10/105008
21. Botelho RM, Christenson RE, Johnson EA, Wojtkiewicz SF (2014) Enhancements to the convolution integral method for real-time hybrid simulation. In: Proceedings of the 6th world conference on structural control and monitoring, Barcelona, Spain

Chapter 5
Feasibility of a Transmission Simulator Technique for Dynamic Real Time Substructuring

Andreas Bartl and Daniel J. Rixen

Abstract Real time substructuring is an approach which couples numerical models and physical structures in a real time experimental test. This can be a beneficial technique for several types of applications where neither full experimental tests nor full simulations are applicable. This contribution tries to make use of decoupling techniques inspired by dynamic substructuring (e.g. FIBS) in real time testing. In this study an experimental test rig (denoted as AB) is considered which consists of substructure A and substructure B. Substructure B is the specimen, which needs to be tested in the real time test as it is hard to model. Substructure A is an so called transmission simulator and is replaced in the real time test by the numerical substructure C, such that the system CB is emulated. The approach can help to reduce the control effort and to include more realistic interface dynamics in the test.

Keywords Hybrid modeling • Hardware in the loop • Real-time substructuring • Interface control • Transmission simulator

5.1 Introduction

5.1.1 Background & Problem Statement

Realtime Substructuring—also denoted as Hardware-In-The-Loop—is a tool for conducting vibration tests with virtual prototypes. The idea is to split a system in one substructure which is analysed experimentally and one substructure which is simulated numerically. Both are coupled by a control system. The experimental substructure is hard to model or/and subject to a safety or certification test. The numerical substructure may have large dimensions or is subject to frequent changes during a design process. The first methods for realtime substructuring have been presented by Nakashima et al. [7], Horiuchi et al. [5] and Blakeborough et al. [3]. Application include certification tests, long term tests, error analysis and rapid prototyping. So far realtime substructuring has mainly been used in applications for civil engineering. However there are numerous potential application fields in mechanical engineering. Ideas for new application fields include microsystems, satellite testing, high-precision machinery and wind turbines. In this study we propose a transmission-simulator based approach to improve performance of realtime substructuring tests. The idea is that the test rig mimics the dynamic behavior of the emulated system with the help of a so-called transmission simulator. The controller only has to compensate the difference between testrig and the emulated system. The testrig also includes the real interface dynamics. The process is illustrated in Fig. 5.1. This idea is inspired by decoupling within the FRF-based substructuring framework discussed by Voormeeren and Rixen [11] and [10]. An transmission simulator based approach has also been presented for component mode synthesis based techniques in [6]. In order to demonstrate the problem setting consider the testrig (denoted as TR in the following) consisting of the test specimen (denoted as EXP) and a transmission simulator (denoted as TS). It is assumed that a numerical model of TS exists (denoted as NTS). The objective of the experimental test is to emulate a system consisting of a numerical substructure (denoted as N) and the experimental specimen. This is achieved by decoupling the dynamics of TS and adding the dynamics of the numerical substructure N with the help a controller in real time.The emulated system is denoted as EMU.

A. Bartl (✉) • D.J. Rixen
Technische Universität München, Boltzmannstraße 15, 85748 Garching, Germany
e-mail: andreas.bartl@tum.de; rixen@tum.de

M. Allen et al. (eds.), *Dynamics of Coupled Structures, Volume 4*, Conference Proceedings of the Society for Experimental Mechanics Series, DOI 10.1007/978-3-319-15209-7_5

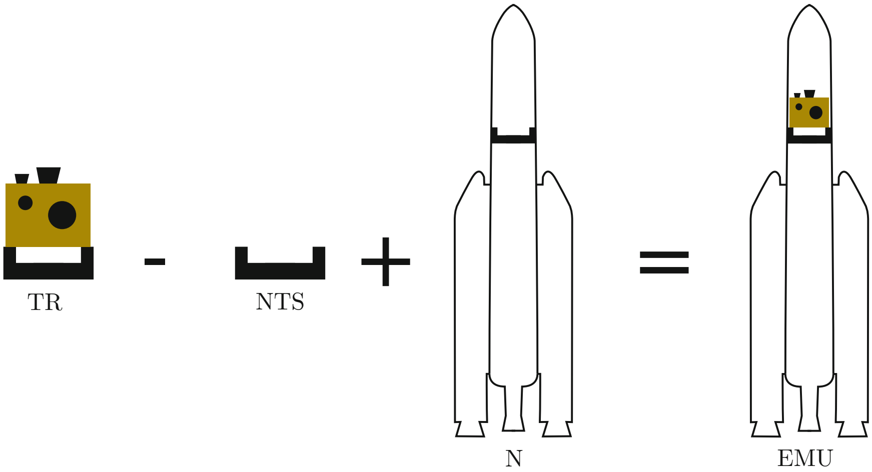

Fig. 5.1 The emulated system (EMU) is mimiced by removing the dynamics of the transmission simulator with the help of its numerical model (NTS) and adding the dynamics of a different numerical model (N)

5.2 The Transmission Simulator Problem

5.2.1 *Compatibility and Equilibrium on the Interface*

Two conditions need to be satisfied as accurately as possible in order to perform a real time substructuring test: the equilibrium condition and the compatibility condition. This also holds for replacing a transmission simulator by a numerical model in realtime. The compatibility condition states that the interface displacements of the three substructures $\boldsymbol{u}_{N,c}$,$\boldsymbol{u}_{TR,c}$ and $\boldsymbol{u}_{TS,c}$ must be equal. The compatibility is represented by the Eq. (5.1). The subscript c of the displacements denotes the coupling DoFs.

$$\begin{aligned} \boldsymbol{u}_{N,c} &= \boldsymbol{u}_{TR,c} \\ \boldsymbol{u}_{N,c} &= \boldsymbol{u}_{NTS,c} \end{aligned} \tag{5.1}$$

The compatibility displacements can be assigned by Boolean matrices $\bar{\boldsymbol{B}}_{TR}$, $\bar{\boldsymbol{B}}_{N}$ and $\bar{\boldsymbol{B}}_{NTS}$.

$$\begin{aligned} \boldsymbol{u}_{TR,c} &= \bar{\boldsymbol{B}}_{TR}\boldsymbol{u}_{TR} \\ \boldsymbol{u}_{NTS,c} &= \bar{\boldsymbol{B}}_{NTS}\boldsymbol{u}_{NTS} \\ \boldsymbol{u}_{N,c} &= \bar{\boldsymbol{B}}_{N}\boldsymbol{u}_{N} \end{aligned} \tag{5.2}$$

They are chosen in this case as following. The subscripts m,n and l represent the number of transmission simulator's internal DoFs (m), interface DoFs (n) and the test specimen's DoFs (l).

$$\begin{aligned} \bar{\boldsymbol{B}}_{TR} &= [\mathbf{0}_{nm}\ \boldsymbol{I}_{nn}\ \mathbf{0}_{nl}] \\ \bar{\boldsymbol{B}}_{N} &= [\mathbf{0}_{nm}\ \boldsymbol{I}_{nn}] \\ \bar{\boldsymbol{B}}_{NTS} &= [\mathbf{0}_{nm}\ \boldsymbol{I}_{nn}] \end{aligned} \tag{5.3}$$

The equilibrium condition for replacing a transmission simulator by a numerical model can be obtained by the following consideration (the approach is illustrated in Fig. 5.2): suppose a force excitation on the test rig TR. It is obvious that, as the test rig is excited, the transmission simulator TS is subject to a force from the experimental specimen EXP. Now a force which is opposing the connection forces $\boldsymbol{g}_{TS}$ between TS and EXP can be applied to the test rig TR in order to let the specimen EXP behave as if it was not coupled to the transmission simulator. Subsequently the connection forces $\boldsymbol{g}_{N}$ between test rig TR and the new numerical substructure N are applied to the test rig TR. The equilibrium can then be represented

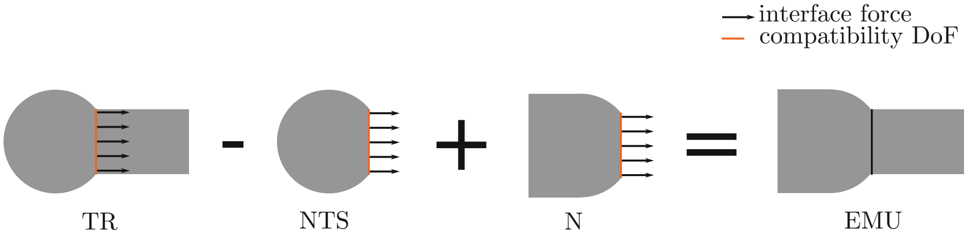

Fig. 5.2 The transmission simulator approach with equilibrium and compatibility on the interface DoFs

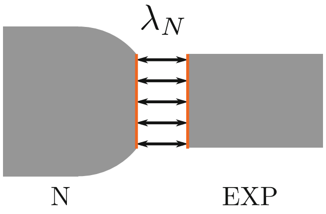

Fig. 5.3 The emulated system consists of the new numerical substructure and the test specimen. They are coupled with the force amplitudes λ_N

by Eq. (5.4). The vectors λ_{TR}, λ_{TS} and λ_N are the force amplitudes on the corresponding boundary. The resulting emulated system is illustrated in Fig. 5.3.

$$0 = \lambda_{TR} - \lambda_{NTS} + \lambda_N \tag{5.4}$$

The forces on the substructure are than assigned by the Boolean matrices $\bar{\boldsymbol{B}}_{TR}$, $\bar{\boldsymbol{B}}_N$ and $\bar{\boldsymbol{B}}_{NTS}$.

$$\begin{aligned} \boldsymbol{g}_{TR} &= \bar{\boldsymbol{B}}_{TR}^T \lambda_{TR} \\ \boldsymbol{g}_{NTS} &= \bar{\boldsymbol{B}}_{NTS}^T \lambda_{NTS} \\ \boldsymbol{g}_N &= \bar{\boldsymbol{B}}_N^T \lambda_N \end{aligned} \tag{5.5}$$

Note that both N and EXP can be subject to the external forces $\boldsymbol{f}_{N,ext}$ and $\boldsymbol{f}_{EXP,ext}$. The force amplitude vector λ_{TS} can be obtained by the use of a numerical model of transmission simulator TS in a control loop. It is than denoted as λ_{NTS} in this study. Regardless of the control structure equilibrium equation (5.4) always has to be solved for one unknown force amplitude vector. However, it depends on the selection of the control structure which force amplitude vector will be obtained by the equilibrium equation.

5.2.2 *Compatibility and Equilibrium on an Extended Interface*

As it will be shown in the numerical case study, differences between the transmission simulator (TS) and its numerical model (NTS) can cause the synchronization between the substructures to fail. These differences can be generated by measurement inaccuracies and modelling errors. For FRF-based experimental subtructuring techniques a similar effect has been shown in [10]. It was shown for FRF-based experimental substructuring techniques in [2] and [1] that coupling on additional DoF can help alleviating this problem. In this study we investigate if that approach also can be applied to realtime subtructuring. In the following we will refer to the original interface as direct interface and to the additional coupling DoF as extended interface. The idea is that the responses of the extended interface are influenced by the forces on direct interface. The additional information on the state of the internal Dof of the transmission simulator could be used to reduce the influence of the measurement and model errors on the control. The coupling of additional DoF on an extended interface also implies that this extended interface has to be identical in all substructures, namely the test rig TR, the transmission simulator TS and the replacing numerical substructure N. The approach is illustrated in Fig. 5.4. The Boolean matrices are in this case defined

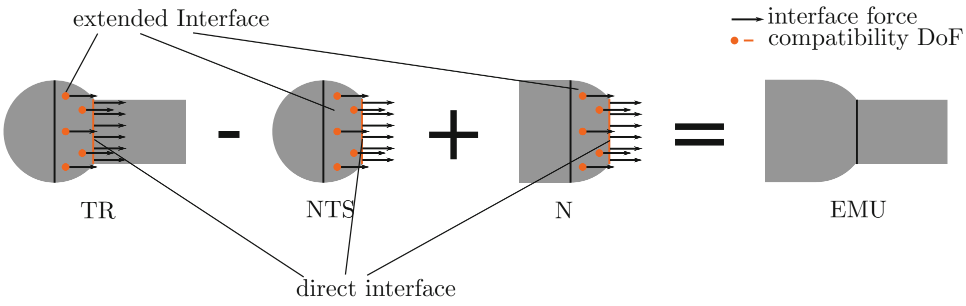

Fig. 5.4 Transmission simulator approach with compatibility and equilibrium on an extended interface

by (5.7). The subscripts m,n,q and l represent the number of the transmission simulator's internal DoFs (m), the extended interface DoFs (q), the interface DoFs (n) and the test specimen's DoFs (l).

$$\begin{aligned}\bar{\boldsymbol{B}}_{TR} &= \begin{bmatrix}\mathbf{0}_{qn} & \boldsymbol{I}_{qq} & \mathbf{0}_{qm} & \mathbf{0}_{nl}\\ \mathbf{0}_{mn} & \mathbf{0}_{mq} & \boldsymbol{I}_{mm} & \mathbf{0}_{ml}\end{bmatrix}\\ \bar{\boldsymbol{B}}_{N} &= \begin{bmatrix}\mathbf{0}_{qn} & \boldsymbol{I}_{qq} & \mathbf{0}_{qm}\\ \mathbf{0}_{mn} & \mathbf{0}_{mq} & \boldsymbol{I}_{mm}\end{bmatrix}\\ \bar{\boldsymbol{B}}_{NTS} &= \begin{bmatrix}\mathbf{0}_{qn} & \boldsymbol{I}_{qq} & \mathbf{0}_{qm}\\ \mathbf{0}_{mn} & \mathbf{0}_{mq} & \boldsymbol{I}_{mm}\end{bmatrix}\end{aligned} \tag{5.6}$$

One can also think about enforcing compatibility and equilibrium only on the extended interface. Without the need to place sensors and actuators on the direct interface, this approach would make it possible to include more realistic interface dynamics in the measurement, which is one objective of a transmission simulator technique. Additionally it may be infeasible for some practical applications to place sensors and actuators directly on the interface. With this approach the Boolean matrices are:

$$\begin{aligned}\bar{\boldsymbol{B}}_{TR} &= \begin{bmatrix}\mathbf{0}_{qn} \, \boldsymbol{I}_{qq} \, \mathbf{0}_{nm} \, \mathbf{0}_{nl}\end{bmatrix}\\ \bar{\boldsymbol{B}}_{N} &= \begin{bmatrix}\mathbf{0}_{qn} \, \boldsymbol{I}_{qq} \, \mathbf{0}_{qm}\end{bmatrix}\\ \bar{\boldsymbol{B}}_{NTS} &= \begin{bmatrix}\mathbf{0}_{qn} \, \boldsymbol{I}_{qq} \, \mathbf{0}_{qm}\end{bmatrix}\end{aligned} \tag{5.7}$$

5.2.3 Extended Interface with Non-collocated Equilibrium and Compatibility Condition

In many practical applications it may be useful to enforce compatibility and equilibrium on non-collocated DoF. The approach is illustrated in Fig. 5.5. The Boolean matrices for compatibility and equilibrium now are not identical anymore. We now refer to them as $\bar{\boldsymbol{C}}$ for the compatibility matrix and $\bar{\boldsymbol{E}}$ for the equilibrium matrix. That means that the displacements used for the compatibility are now defined by (5.8) and the interface forces are defined by (5.9).

$$\begin{aligned}\boldsymbol{u}_{TR,c} &= \bar{\boldsymbol{C}}_{TR}\boldsymbol{u}_{TR}\\ \boldsymbol{u}_{NTS,c} &= \bar{\boldsymbol{C}}_{NTS}\boldsymbol{u}_{NTS}\\ \boldsymbol{u}_{N,c} &= \bar{\boldsymbol{C}}_{N}\boldsymbol{u}_{N}\end{aligned} \tag{5.8}$$

$$\begin{aligned}\boldsymbol{g}_{TR} &= \bar{\boldsymbol{E}}_{TR}^{T}\lambda_{TR}\\ \boldsymbol{g}_{NTS} &= \bar{\boldsymbol{E}}_{NTS}^{T}\lambda_{NTS}\\ \boldsymbol{g}_{N} &= \bar{\boldsymbol{E}}_{N}^{T}\lambda_{N}\end{aligned} \tag{5.9}$$

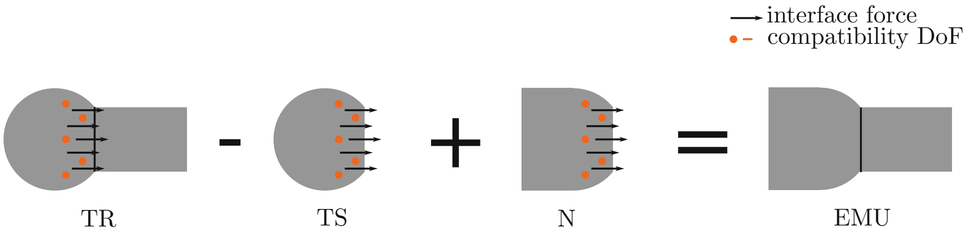

Fig. 5.5 Transmission simulator approach with non-collocated compatibility and equilibrium conditions on the extended interface

One possible choice for the Boolean matrices is shown in (5.10). In this case compatibility is enforced on the direct interface and equilibrium is enforced on the extended interface.

$$\begin{aligned} \bar{\boldsymbol{C}}_{TR} &= \left[\mathbf{0}_{mn}\ \mathbf{0}_{mq}\ \boldsymbol{I}_{mm}\ \mathbf{0}_{ml}\right] & \bar{\boldsymbol{E}}_{TR} &= \left[\mathbf{0}_{qn}\ \boldsymbol{I}_{qq}\ \mathbf{0}_{nm}\ \mathbf{0}_{nl}\right] \\ \bar{\boldsymbol{C}}_{N} &= \left[\mathbf{0}_{mn}\ \mathbf{0}_{mq}\ \boldsymbol{I}_{mm}\right] & \bar{\boldsymbol{E}}_{N} &= \left[\mathbf{0}_{qn}\ \boldsymbol{I}_{qq}\ \mathbf{0}_{ql}\right] \\ \bar{\boldsymbol{C}}_{NTS} &= \left[\mathbf{0}_{mn}\ \mathbf{0}_{mq}\ \boldsymbol{I}_{mm}\right] & \bar{\boldsymbol{E}}_{NTS} &= \left[\mathbf{0}_{qn}\ \boldsymbol{I}_{qq}\ \mathbf{0}_{ql}\right] \end{aligned} \tag{5.10}$$

One can also imagine methods where the number of compatibility and equilibrium condition is not identical. However, in this study we will not address this possibility.

5.3 An Emulated-System Based Control Concept

Basically, the control in realtime substructuring has two objectives—synchronization of the substructures' forces and displacements as well as stability of the overall system. As stated in the previous section, the control structure of the realtime substructuring system depends on the choice from the following three possibilities:

- control the displacement on the interface of N and NTS and apply the resulting forces $\boldsymbol{g}_{TR}$ to TR.
- control the displacement on the interface of TR and N and apply the resulting forces $\boldsymbol{g}_{TS}$ to TS.
- control the displacement on the interface of TR and NTS and apply the resulting forces $\boldsymbol{g}_{N}$ to N.

In this study, we limit ourselves to the latter case. However, this choice was based on the control structure used for a test rig in the authors' institute and it has to be investigated in further studies which concept is preferable in application scenarios.

Using the above-mentioned structure the equilibrium equation (5.4) can be expressed by (5.11). Here, $\bar{\boldsymbol{E}}_{N}^{T}$ refers to the Boolean matrix which assigns the force amplitudes to the corresponding DoFs of N and $\boldsymbol{g}_{N}$ denotes the force vector on N.

$$\begin{aligned} \lambda_{N} &= -\lambda_{TR} + \lambda_{TS} \\ \boldsymbol{g}_{N} &= \bar{\boldsymbol{E}}_{N}^{T}\lambda_{N} \end{aligned} \tag{5.11}$$

This strategy can be explained in other words as follows: at a certain time step the numerical model N predicts a displacement on the interface (extended or direct). This displacement is then imposed to the NTS model and to the TR (using displacement controlled actuators). The forces computed on the displacement driven DoFs on NTS and measured on the driven DoFs of TR are then used to compute the force on N (Eq. (5.4) recasted in (5.11)). That force is then used to compute the response of N in the next time step. The control system now consists of two so-called inner loop controls and an outer loop control. It is illustrated in Fig. 5.6. The inner loop control enforces the compatibility between the substructures. The outer loop enforces the equilibrium condition and improves the displacement error dynamics. It is important to note in that context that in this study we choose a so-called emulator-based substructuring as described in [4]. It implies that the dynamics of all substructures and the transmission system are known in advance and are used to design the controllers. However, it will be part of future research to adapt the transmission simulator approach to more sophisticated control concepts. This is necessary for instance when the test object has unknown dynamics. In the following the controllers will be designed in state space as proposed in [8] and [9].

Fig. 5.6 Overview of the outer loop control

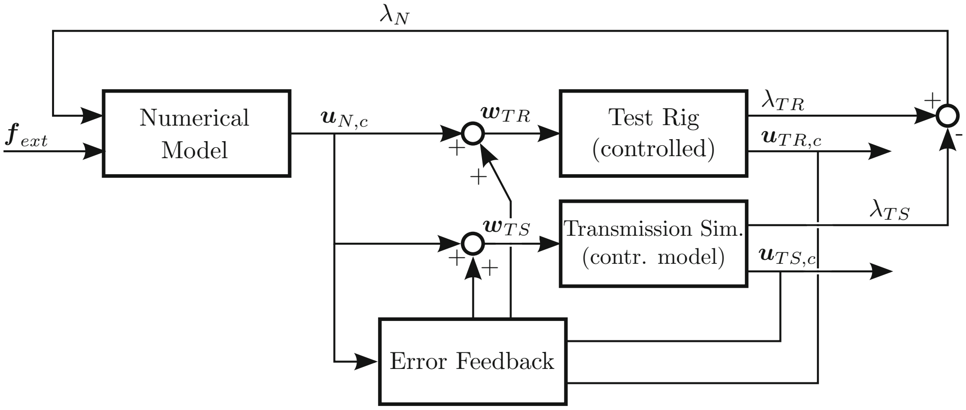

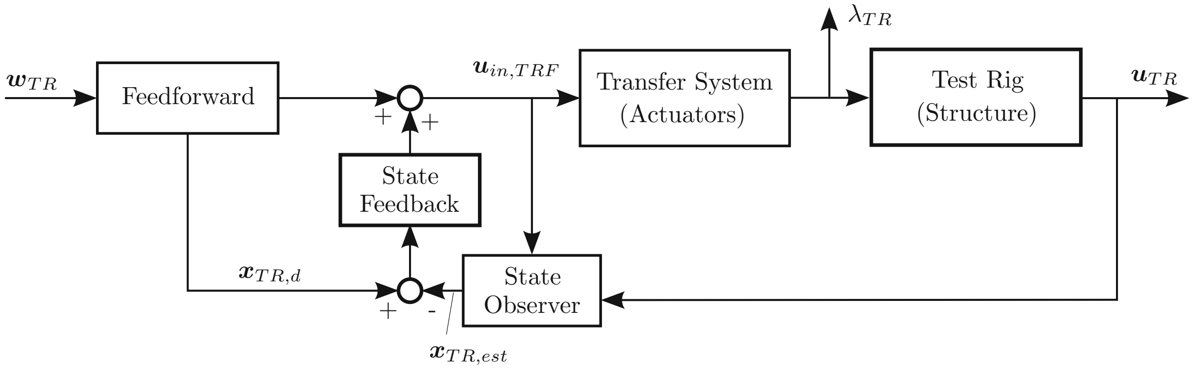

Fig. 5.7 The innerloop control for the test rig model enforces compatibility between $\boldsymbol{u}_{N,c}$ and $\boldsymbol{u}_{TR,c}$

5.3.1 *Inner Loop*

The dynamics of the actuated system without inner loop control are described by the state space model (5.12).

$$\begin{aligned}\dot{\hat{\boldsymbol{x}}}_{TR} &= \hat{\boldsymbol{A}}_{TR}\hat{\boldsymbol{x}}_{TR} + \hat{\boldsymbol{B}}_{TR}\boldsymbol{u}_{in,TR}\\ \boldsymbol{u}_{TR,c} &= \hat{\boldsymbol{C}}_{TR}\hat{\boldsymbol{x}}_{TR}\\ \lambda_{TR} &= \hat{\boldsymbol{C}}_{TR,f}\hat{\boldsymbol{x}}_{TR} + \hat{\boldsymbol{D}}_{TR,f}\boldsymbol{u}_{in,TR}\end{aligned} \tag{5.12}$$

The numerical model of the transmission simulator is described by the state space model (5.13).

$$\begin{aligned}\dot{\hat{\boldsymbol{x}}}_{NTS} &= \hat{\boldsymbol{A}}_{NTS}\hat{\boldsymbol{x}}_{NTS} + \hat{\boldsymbol{B}}_{NTS}\lambda_{NTS}\\ \boldsymbol{u}_{NTS,c} &= \hat{\boldsymbol{C}}_{NTS}\hat{\boldsymbol{x}}_{NTS}\end{aligned} \tag{5.13}$$

The inner loop consists of a feed forward control and a state feedback, which is fed by a Kalman filter. The structures of the inner loop control for test rig and transmission simulator are illustrated in Figs. 5.7 and 5.8. The feedforward compensator includes a model based dynamical compensation of the actuation system. The systems with closed inner loop control are represented by the following state space models. The vectors $\boldsymbol{u}_{TR}$ and $\boldsymbol{u}_{NTS}$ are the internal and interface displacements of the test rig and the numerical transmission simulator. The vectors $\boldsymbol{w}_{TR}$ and $\boldsymbol{w}_{NTS}$ represent the inputs for the displacement demand.

$$\begin{aligned}\dot{\boldsymbol{x}}_{TR} &= \boldsymbol{A}_{TR}\boldsymbol{x}_{TR} + \boldsymbol{B}_{TR}\boldsymbol{w}_{TR}\\ \boldsymbol{u}_{TR} &= \boldsymbol{C}_{TR}\boldsymbol{x}_{TR}\end{aligned} \tag{5.14}$$

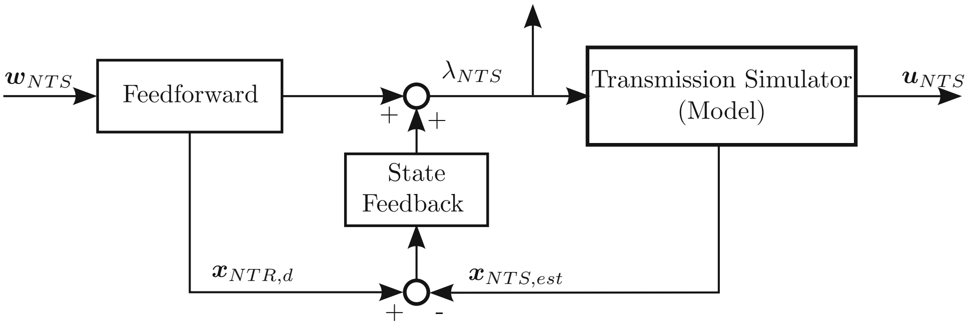

Fig. 5.8 The innerloop control for the numerical transmission simulator model enforces compatibility between $\boldsymbol{u}_{N,c}$ and $\boldsymbol{u}_{NTS,c}$

$$\begin{aligned}\lambda_{TR} &= \boldsymbol{C}_{TR,f}\boldsymbol{x}_{TR} + \boldsymbol{D}_{TR,f}\boldsymbol{w}_{TR}\\ \dot{\boldsymbol{x}}_{NTS} &= \boldsymbol{A}_{NTS}\boldsymbol{x}_{NTS} + \boldsymbol{B}_{NTS}\boldsymbol{w}_{NTS}\\ \boldsymbol{u}_{NTS} &= \boldsymbol{C}_{NTS}\boldsymbol{x}_{NTS}\\ \lambda_{NTS} &= \boldsymbol{C}_{NTS,f}\boldsymbol{x}_{NTS} + \boldsymbol{D}_{NTS,f}\boldsymbol{w}_{NTS}\end{aligned} \tag{5.15}$$

The numerical model, which is replacing the transmission simulator is described by the state space representation (5.16). The force input vector is $\boldsymbol{f}_N$ and the output displacement vector is $\boldsymbol{u}_N$.

$$\begin{aligned}\dot{\boldsymbol{x}}_N &= \boldsymbol{A}_N\boldsymbol{x}_N + \boldsymbol{B}_N\boldsymbol{f}_N\\ \boldsymbol{u}_N &= \boldsymbol{C}_N\boldsymbol{x}_N\end{aligned} \tag{5.16}$$

5.3.2 *Outer Loop*

5.3.2.1 Displacement Demand & Force Feedback

The displacement demand is applied to the test rig and the numerical transmission simulator by setting $\boldsymbol{w}_{TR}$ and $\boldsymbol{w}_{NTS}$. The new input vectors $\boldsymbol{w}^*_{TR}$ and $\boldsymbol{w}^*_{NTS}$ can be used for stabilization and improvement of the error dynamics.

$$\boldsymbol{w}_{TR} = \boldsymbol{u}_{N,c} + \boldsymbol{w}^*_{TR} = \boldsymbol{C}_N\boldsymbol{x}_N + \boldsymbol{w}^*_{TR} \tag{5.17}$$

$$\boldsymbol{w}_{NTS} = \boldsymbol{u}_{N,c} + \boldsymbol{w}^*_{NTS} = \boldsymbol{C}_N\boldsymbol{x}_N + \boldsymbol{w}^*_{NTS} \tag{5.18}$$

Equilibrium is enforced by setting the force input of the numerical substructure N as

$$\boldsymbol{f}_N = \boldsymbol{f}_{ext,N} + \boldsymbol{g}_N = \boldsymbol{f}_{ext,N} + \bar{\boldsymbol{E}}^T_N\lambda_N \tag{5.19}$$

$$\lambda_N = -\lambda_{TR} + \lambda_{NTS} \tag{5.20}$$

The dynamics of the overall system then are represented as state space model:

$$\begin{aligned}
\begin{bmatrix}\dot{\boldsymbol{x}}_{TR}\\ \dot{\boldsymbol{x}}_{NTS}\\ \dot{\boldsymbol{x}}_{N}\end{bmatrix} &= \underbrace{\begin{bmatrix} \boldsymbol{A}_{TR} & \boldsymbol{0} & \boldsymbol{B}_{TR}\bar{\boldsymbol{C}}_{N}\boldsymbol{C}_{N} \\ \boldsymbol{0} & \boldsymbol{A}_{NTS} & \boldsymbol{B}_{NTS}\bar{\boldsymbol{C}}_{N}\boldsymbol{C}_{N} \\ -\boldsymbol{B}_{N}\bar{\boldsymbol{E}}_{N}^{T}\boldsymbol{C}_{TR,f} & \boldsymbol{B}_{N}\bar{\boldsymbol{E}}_{N}^{T}\boldsymbol{C}_{NTS,f} & \boldsymbol{A}_{N}\end{bmatrix}}_{\boldsymbol{A}^{*}} \underbrace{\begin{bmatrix}\boldsymbol{x}_{TR}\\ \boldsymbol{x}_{NTS}\\ \boldsymbol{x}_{N}\end{bmatrix}}_{x^{*}} \\
&+ \underbrace{\begin{bmatrix} \boldsymbol{B}_{TR} & \boldsymbol{0} \\ \boldsymbol{0} & \boldsymbol{B}_{NTS} \\ -\boldsymbol{B}_{N}\bar{\boldsymbol{E}}_{N}^{T}\boldsymbol{D}_{TR,f} & \boldsymbol{B}_{N}\bar{\boldsymbol{E}}_{N}^{T}\boldsymbol{D}_{NTS,f}\end{bmatrix}}_{\boldsymbol{B}^{*}} \underbrace{\begin{bmatrix}\boldsymbol{w}^{*}_{TR}\\ \boldsymbol{w}^{*}_{NTS}\end{bmatrix}}_{\boldsymbol{w}^{*}} + \underbrace{\begin{bmatrix}\boldsymbol{0}\\ \boldsymbol{B}_{N}\end{bmatrix}}_{\boldsymbol{F}^{*}} \boldsymbol{f}_{ext,N} \\
\boldsymbol{x}_{e} = \begin{bmatrix}\boldsymbol{x}_{e,TR}\\ \boldsymbol{x}_{e,NTS}\end{bmatrix} &= \underbrace{\begin{bmatrix} -\bar{\boldsymbol{C}}_{TR}\boldsymbol{C}_{TR} & \boldsymbol{0} & \bar{\boldsymbol{C}}_{N}\boldsymbol{C}_{N} \\ \boldsymbol{0} & -\bar{\boldsymbol{C}}_{NTS}\boldsymbol{C}_{NTS} & \bar{\boldsymbol{C}}_{N}\boldsymbol{C}_{N}\end{bmatrix}}_{\boldsymbol{C}^{e}} \begin{bmatrix}\boldsymbol{x}_{TR}\\ \boldsymbol{x}_{NTS}\\ \boldsymbol{x}_{N}\end{bmatrix} \\
\boldsymbol{y}^{*} &= \begin{bmatrix} \bar{\boldsymbol{C}}_{TR}\boldsymbol{C}_{TR} & \boldsymbol{0} & \boldsymbol{0} \\ \boldsymbol{0} & \bar{\boldsymbol{C}}_{NTS}\boldsymbol{C}_{NTS} & \boldsymbol{0} \\ \boldsymbol{0} & \boldsymbol{0} & \bar{\boldsymbol{C}}_{N}\boldsymbol{C}_{N}\end{bmatrix} \begin{bmatrix}\boldsymbol{x}_{TR}\\ \boldsymbol{x}_{NTS}\\ \boldsymbol{x}_{N}\end{bmatrix}
\end{aligned} \tag{5.21}$$

5.3.2.2 Error Feedback

The knowledge about the overall system can be used to improve the error dynamics and the robustness of the system. In this study, a feedback in the form of the control law (5.22) is used. The regulator should minimize the synchronization error. The state feedback matrix $\boldsymbol{R}$ is obtained as a linear-quadratic regulator minimizing the cost function $J = \int_0^\infty \boldsymbol{x}_e^T \boldsymbol{Q} \boldsymbol{x}_e + \boldsymbol{w}^{*T} \boldsymbol{P} \boldsymbol{w}^*$. The matrix $\boldsymbol{Q}$ is weighting the square of the synchronization error $\boldsymbol{x}_e$. The matrix $\boldsymbol{P}$ is weighting the square of the displacement demand $\boldsymbol{w}^*$. The estimated state vector of the overall system $\boldsymbol{x}^*_{est}$ is obtained by the use of a Kalman filter.

$$\boldsymbol{w}^* = -\boldsymbol{R}\boldsymbol{x}^*_{est} \tag{5.22}$$

With this control law the overall systems dynamics is changed to Eq. (5.23). The systems dynamics is now manipulated such that the above-mentioned cost function is minimized and the stability of the overall test dynamics is assured.

$$\dot{\boldsymbol{x}}^* = (\boldsymbol{A}^* - \boldsymbol{B}^*\boldsymbol{R})\boldsymbol{x}^* + \boldsymbol{F}^*\boldsymbol{f}_{ext,N} \tag{5.23}$$

5.3.3 Consistency, Stability and Accuracy: Properties of a Test Method

For the evaluation of a test method it is crucial to consider consistency, stability and accuracy. Consistency in the context of this study means that the overall dynamics of the test system should converge exactly to the dynamics of the emulated system as the time step size is reduced. A general mathematical proof for the consistency of the described methods is not part of this study. However, we will investigate consistency of the methods for a simple numerical system in the following section. With stability here we refer to asymptotical stability. This means that, if $\boldsymbol{f}_{ext,N} = \boldsymbol{0}$, $\boldsymbol{x}^*(t \to \infty) = \boldsymbol{0}$ holds for arbitrary initial conditions $\boldsymbol{x}(t_0)$. In this study the stability is ensured by the linear quadratic regulator. However, without knowledge of the overall system—as it may be the case in a practical realtime substructuring test—we can not use this technique to guarantee stability and have to rely on more sophisticated control strategies. Accuracy is indicated by the norm of the displacement error between the desired emulated system and the test system. It can be visualized by synchronization plots as they can be seen in the following section.

5.4 Numerical Case Study

In order to investigate the approach described in the previous section, it is applied to a simple numerical example. We want to address the following questions with the numerical case study:

- Are the described transmission simulator methods potentially consistent?
- Is it feasible to enforce compatibility and equilibrium only on the extended interface without enforcing it on the direct interface?
- Is it feasible to enforce compatibility and equilibrium on non-collocated DoF?
- Do additional coupling DoF on the extended interface improve performance of the test?

The system used for the case study is illustrated in Fig. 5.9. The parameters for the system are given in Table 5.1. The system is lightly damped. The system was discretized with the trapezoidal rule. As input forces sweeps are used (1–50 Hz in 50 s on mass $m_{N,1}$, 50–200 Hz in 10 s on mass $m_{N,2}$ and 50–100 Hz in 20 s on mass $m_{N,4}$). Figure 5.10 is an example of the time response of the corresponding displacements of all substructures on the interface. The results of the investigation are shown in synchronization plots. They show the displacement of mass $m_{EXP,3}$ of the test rig during the realtime substructuring ($u_{EXP,3,t}$) test over the corresponding displacement of the desired system ($u_{EXP,3,d}$). The synchronization show an elliptic shape if a phase lag between desired response and test response is existent. If an amplitude error is existent the slope of the curve differs from 1. Perfect synchronization is indicated by a line crossing the coordinate origin with the slope 1.

5.4.1 Consistency of Transmission Simulator Test Methods

How can one verify consistency for a given numerical system? For the simulation, a perfect system is used. Namely, no measurement errors were and an actuator with perfect transfer behavior was used. For this we choose the actuation system's transfer function to $\boldsymbol{G}_A = \boldsymbol{I}$. The time step size of the simulation is then gradually decreased. If the results are converging to perfect synchronization, we assume consistency of the method for the given system. In this study, the simulation is performed with three different time step sizes (the smallest period related to a mode of the emulated system is 0.15 s and the biggest period is 2.28 s):

- $\Delta t = 10^{-2}$ s
- $\Delta t = 10^{-3}$ s
- $\Delta t = 10^{-4}$ s

The different sets for the coupling DoF are listed in Table 5.2. Figures 5.11 and 5.12 show the results for different test methods:

- Test 1: The coupling is performed on the direct interface. It seems that the synchronization error is converging to zero as the time step size is decreasing. This was to be expected since the theory predicts that with exact decoupling of the transmission simulator TS and coupling of N one should find the exact emulated systems response. This test thus shows that the control strategy, can impose the necessary compatibility conditions.
- Test 2: The coupling is performed on the direct interface and one additional DoF on an extended interface. It seems that the synchronization error is converging to zero as the time step size is decreasing.
- Test 3: The coupling is performed on the direct interface and two additional DoF on an extended interface. It seems that the synchronization error is converging to zero as the time step size is decreasing.
- Test 4: The coupling is performed on only one DoF on the direct interface. No synchronization is present.
- Test 5: The coupling is performed on two DoF on an extended interface. It seems that synchronization error is converging to zero as the time step size is decreasing. However, the convergence is slower than observed in the test 1–3.
- Test 6: A non-collocated coupling is performed: equilibrium is enforced on the direct interface and compatibility is enforced on the extended interface. The synchronization is converging to a state where phase lag is present.
- Test 7: A non-collocated coupling is performed: equilibrium is enforced on the extended interface and compatibility is enforced on the direct interface. The synchronization is converging to a state where phase lag is present. The phase lag here is smaller than the phase lag observed in test 6.

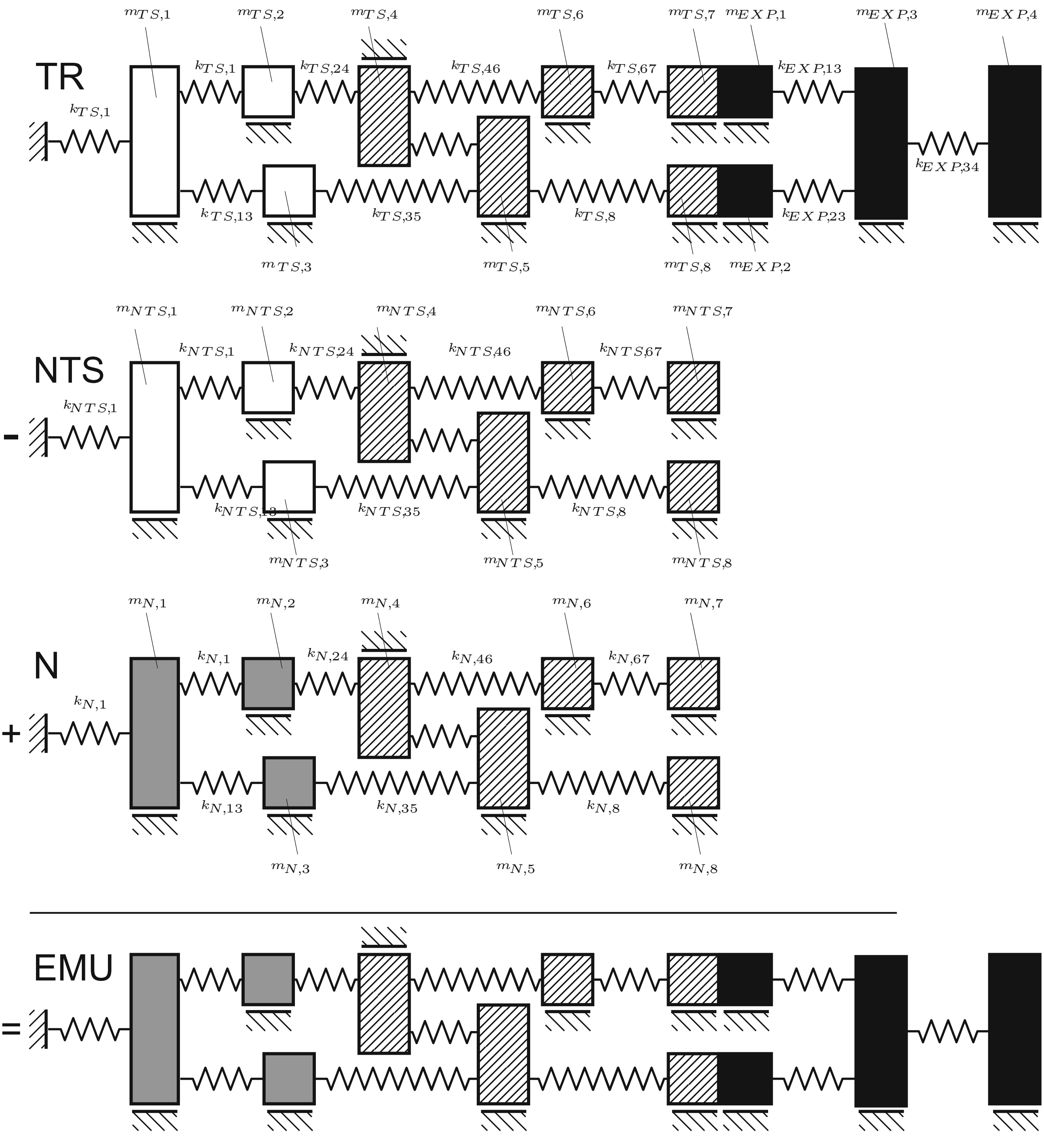

Fig. 5.9 Mass-spring test system used for the numerical case study

All techniques including the coupling of the direct interface are consistent as far as it can be seen in the presented numerical study. It is remarkable that also the technique coupling only DoF on the extended interface seems to be consistent. For comparison a simulation on a technique which is obviously not consistent is performed: coupling only one DoF on the direct interface yields no satisfying synchronisation. For both non-collocated techniques simulated in this numerical study a phase lag exists. The non-collocated method therefore is not consistent. However, the phase lag has to be seen in relation to the

Table 5.1 Parameters of the system used for the numerical case study

Transmission simulator (TS)				Replacing numerical substructure (N)			
Stiffness (N/m)		Mass (kg)		Stiffness (N/m)		Mass (kg)	
$k_{TS,1}$	2,000	$m_{TS,1}$	10	$k_{N,1}$	2,500	$m_{N,1}$	6
$k_{TS,12}$	2,000	$m_{TS,2}$	3	$k_{N,12}$	500	$m_{N,2}$	6
$k_{TS,13}$	200	$m_{TS,3}$	3	$k_{N,13}$	500	$m_{N,3}$	1
$k_{TS,24}$	1,000	$m_{TS,4}$	3	$k_{N,24}$	1,000	$m_{N,4}$	3
$k_{TS,35}$	1,000	$m_{TS,5}$	3	$k_{N,35}$	1,000	$m_{N,5}$	3
$k_{TS,45}$	500	$m_{TS,6}$	2	$k_{N,45}$	500	$m_{N,6}$	2
$k_{TS,58}$	1,000	$m_{TS,7}$	2	$k_{N,58}$	1,000	$m_{N,7}$	2
$k_{TS,46}$	200	$m_{TS,8}$	4	$k_{N,46}$	200	$m_{N,8}$	4
$k_{TS,67}$	200			$k_{N,67}$	200		
Test Specimen (EXP)							
Stiffness (N/m)		Mass (kg)					
$k_{EXP,13}$	2,000	$m_{EXP,1}$	2				
$k_{EXP,23}$	200	$m_{EXP,2}$	4				
$k_{EXP,34}$	1,000	$m_{EXP,3}$	8				
		$m_{EXP,4}$	5				

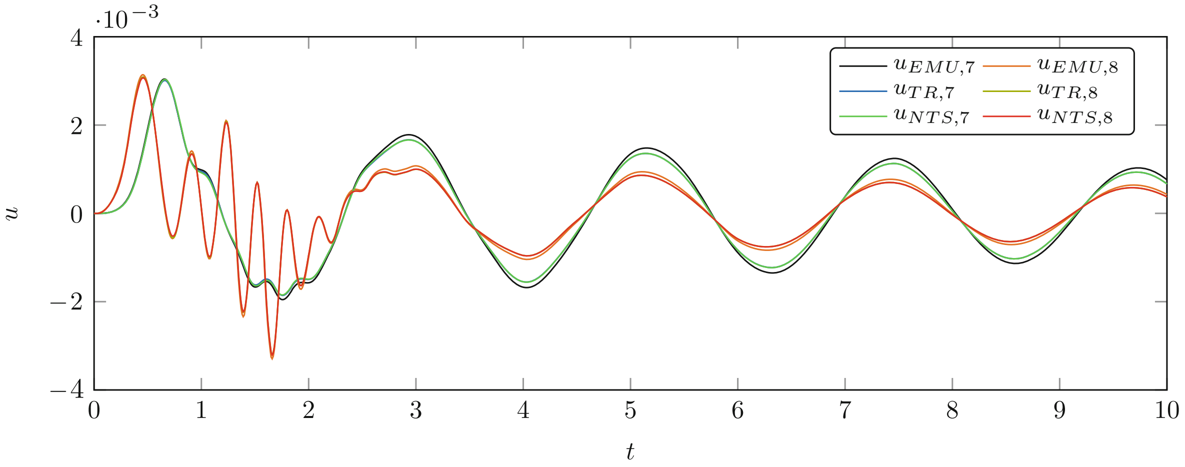

Fig. 5.10 Time response of the interface displacements (coupling on the two interface DoF, time step size $\Delta t = 10^{-3}$ s)

Table 5.2 Coupling sets used for the consistency test

Test no.	Compatibility DoF no.	Equilibrium DoF no.
1	7 and 8	7 and 8
2	6, 7 and 8	6, 7 and 8
3	5, 6, 7 and 8	5, 6, 7 and 8
4	7	7
5	5 and 6	5 and 6
6	5 and 6	7 and 8
7	7 and 8	5 and 6

error caused by the actuation system. This error will be present in a real test. If one can find an error bound, the method may still be usefull for some applications were the collocation of actuation and displacement measurement is not possible.

5.4.2 *Influence of Model Inaccuracy of the Numerical Transmission Simulator*

In practice, model inaccuracies (transmission simulator) or measurement errors may be inevitable. The effects of these inaccuracies can cause the test to fail. For this reason, in this paragraph we investigate the influence of model inaccuracies

Fig. 5.11 Synchronization plots: verifying the consistency of test methods

Coupling on direct interface (Test 1)

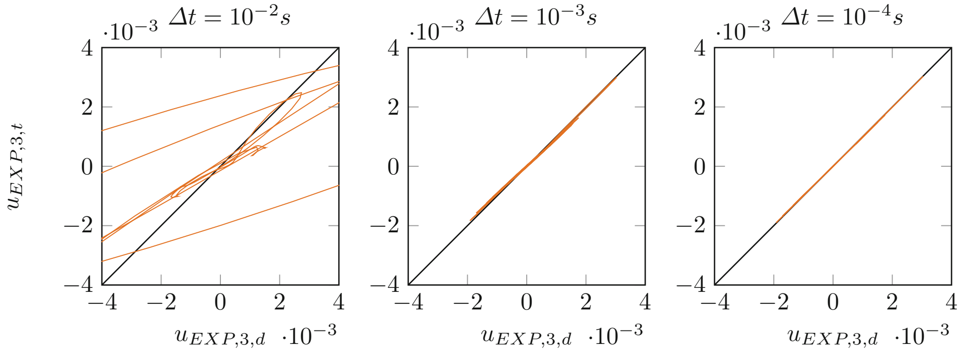

Coupling on direct interface and 1 DoF on the extended interface (Test 2)

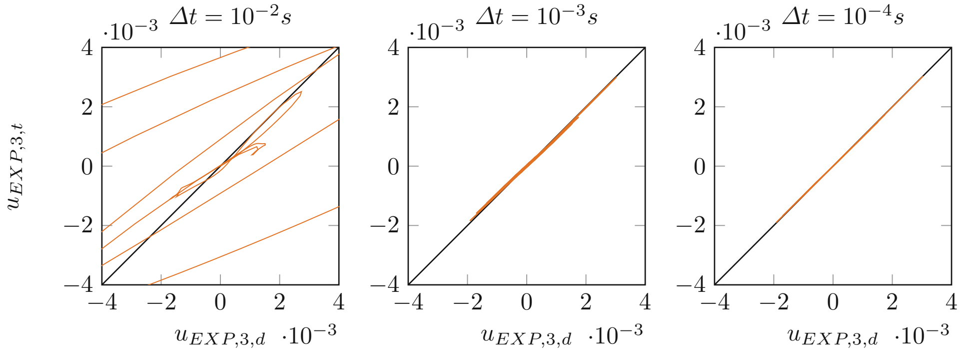

Coupling on direct interface and 2 DoF on the extended interface (Test 3)

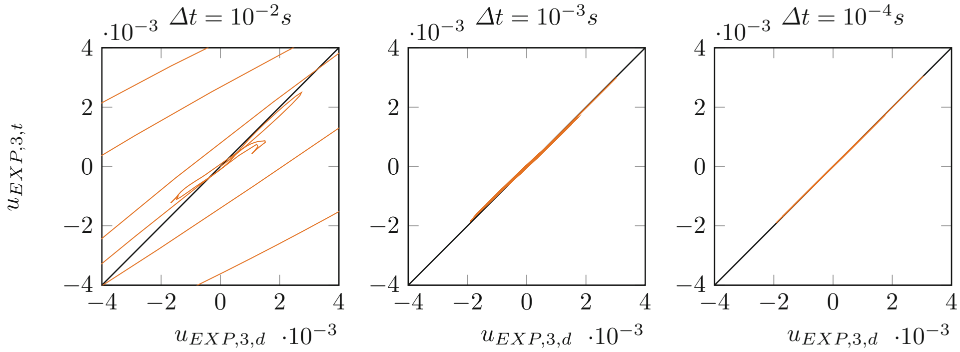

Coupling on the direct interface with 1 DoF (Test 4)

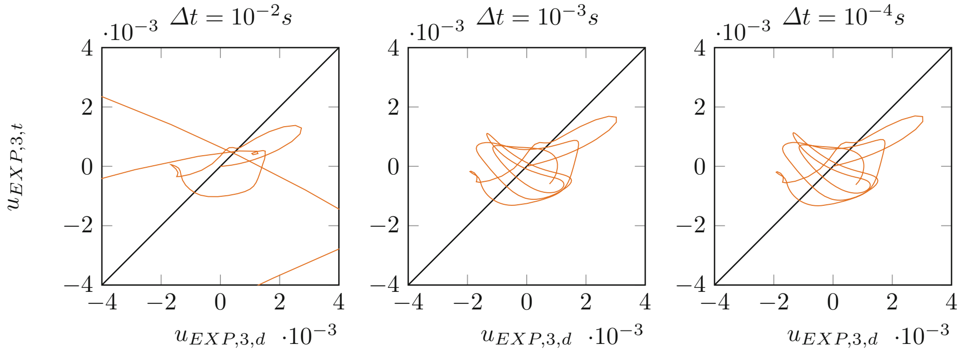

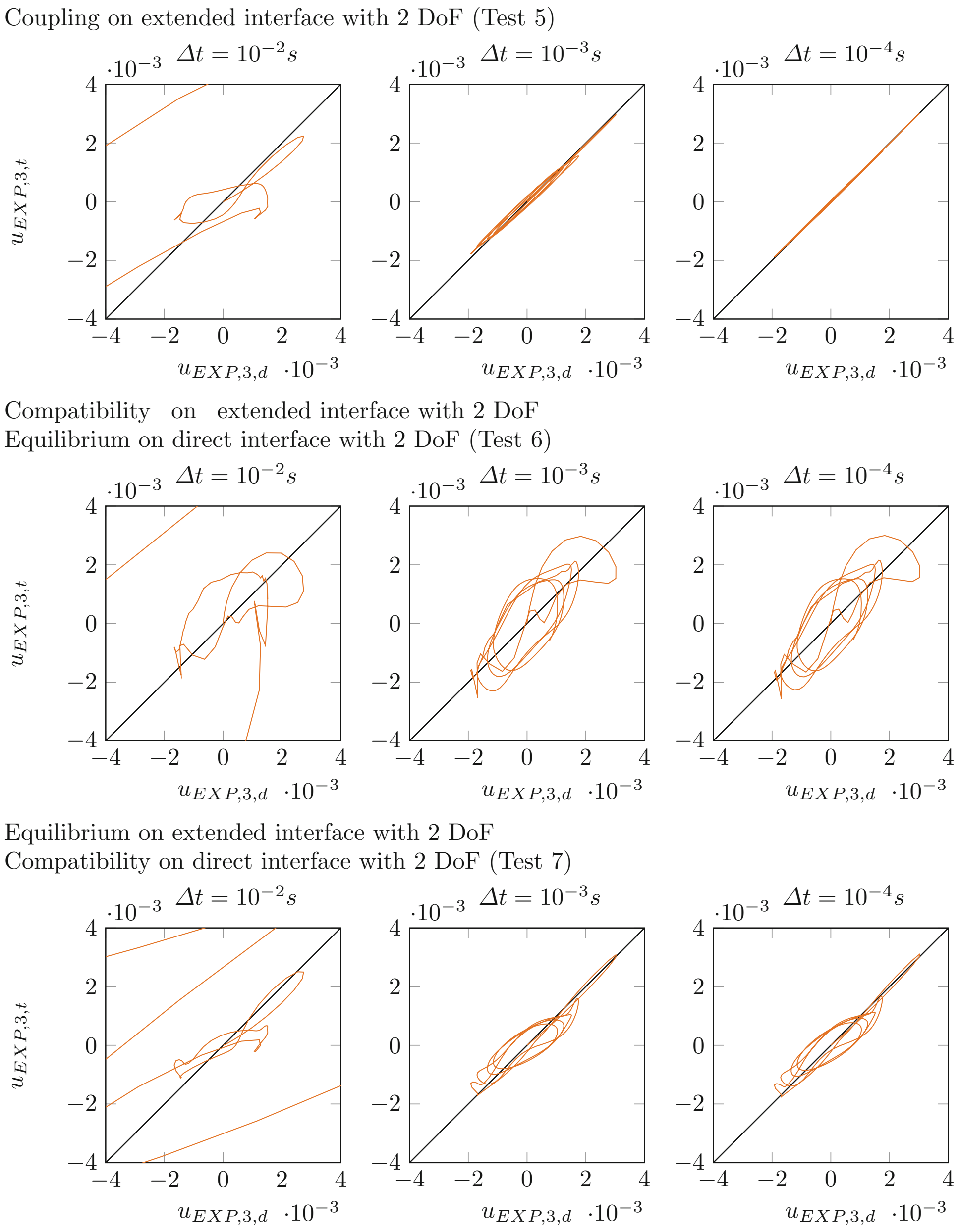
Coupling on extended interface with 2 DoF (Test 5)

Compatibility on extended interface with 2 DoF
Equilibrium on direct interface with 2 DoF (Test 6)

Equilibrium on extended interface with 2 DoF
Compatibility on direct interface with 2 DoF (Test 7)

Fig. 5.12 Synchronization plot: verifying the consistency of test methods

on the synchronization. We multiply all masses and spring constants with the factor 0.9. Again, the simulation is performed with three different time step sizes:

- $\Delta t = 10^{-2}$ s
- $\Delta t = 10^{-3}$ s
- $\Delta t = 10^{-4}$ s

The different sets for the coupling DoF are listed in Table 5.3.

Table 5.3 Coupling sets used for simulating the effects of model inaccuracies on the test

Test no.	Compatibility DoF no.	Equilibrium DoF no.
8	7 and 8	7 and 8
9	6, 7 and 8	6, 7 and 8
10	5, 6, 7 and 8	5, 6, 7 and 8
11	5 and 6	5 and 6

Figure 5.13 shows the results for different test methods:

- Test 8: The coupling is performed on the direct interface. There is no satisfying synchronization for all time step sizes. The results do not seem to improve for decreasing time step size.
- Test 9: The test is now performed with one additional DoF on the extended interface. The synchronization shows improved results compared to the coupling on the direct interface. However, there is still a phase lag present. The results do not seem to improve with further reduction of the time step size.
- Test 10: The test is now performed with two additional DoF on the extended interface. The synchronization shows improved results compared to the coupling on the direct interface. However, there is still a phase lag present. It is comparable with the one observed in test 9. The results do not seem to improve with further reduction of the time step size.
- Test 11: The test is now performed coupling only two DoF on the extended interface. The synchronization shows improved results compared to the coupling on the direct interface. However, there is still a phase lag present. It is remarkable that the results are still comparable to those with coupling of 3 or 4 DoF.

Coupling additional DoF on the extended interface seem to improve the quality of the synchronization. However the effect does not increase with further addition of more coupling DoF. Also the use of only two DoF on the extended interface shows an improvement. A fact that is not consistent with the assumption that only additional coupling is improving the performance. For that reason, further investigations are necessary here.

5.5 Conclusion

In this paper a family of transmission simulator based methods for real time substructuring techniques has been proposed. The idea is to reduce the control effort and to include the interface dynamics more naturally in the test. The method has been integrated in a simple emulated-system based real time substructuring system. Consistency of the method has been shown for a numerical example, but not in general. It has been shown that coupling additional DoFs besides the direct interface can help reducing the effects of model inaccuracies.

Further theoretical work is needed in order to proof the consistency of the proposed techniques mathematically. Criteria for the selection of the coupling DoF (maybe based on their observability and controllability) need to be developed. Further investigation is also needed on the effect of measurement errors. It is also may be helpful to extend the approach by techniques which can make use o a higher number of compatibility conditions than equilibrium conditions. In that context it may be also necessary to use techniques for sensor localization. In order to show the practical relevance of the techniques the methods have to be implemented on a real test rig. It may be necessary to combine them with more sophisticated control approaches in order to overcome the constraints by an emulator based control concept.

Compatibility on direct Interface with 2 DoF (Test 8)

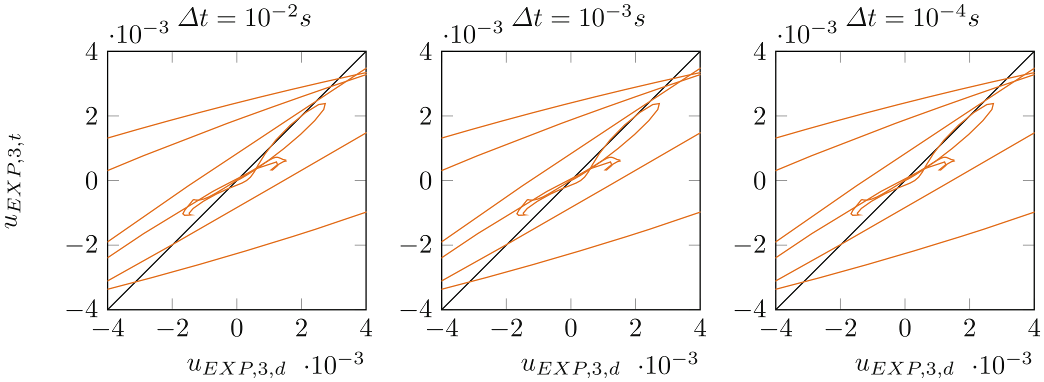

Compatibility on extended interface with 2 DoF, equilibrium on direct interface with 2 DoF (Test 9)

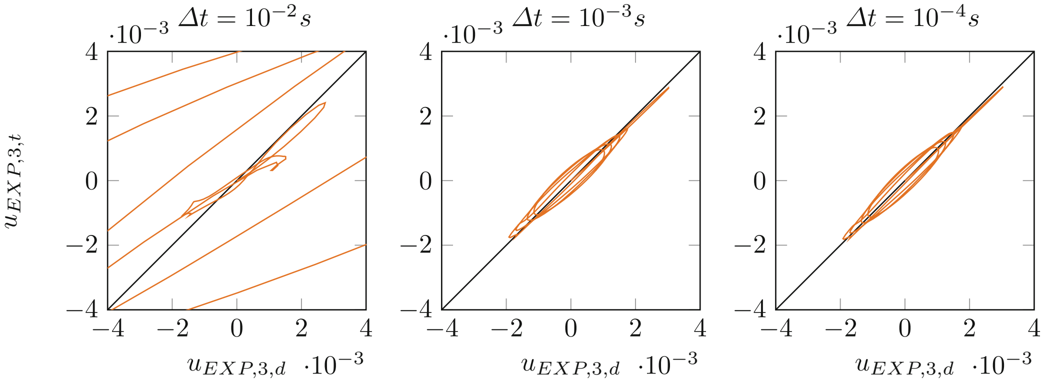

Equilibrium on extended interface with 2 DoF, compatibility on direct interface with 2 DoF (Test 10)

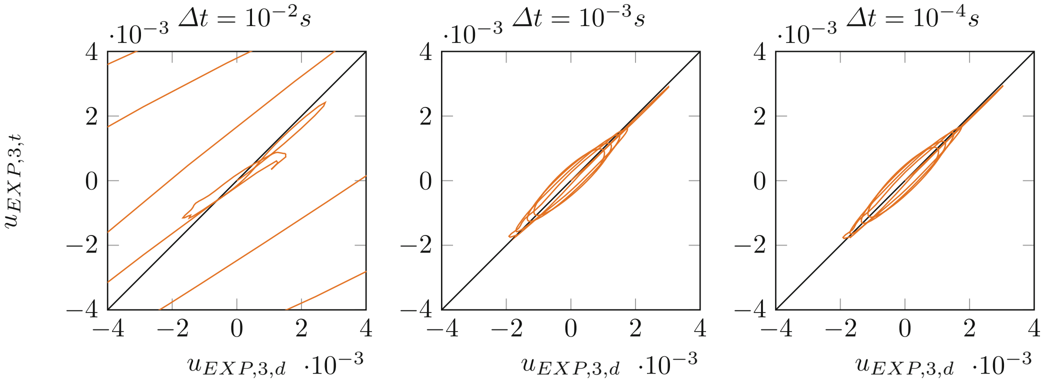

Coupling on extended interface with 2 DoF (Test 11)

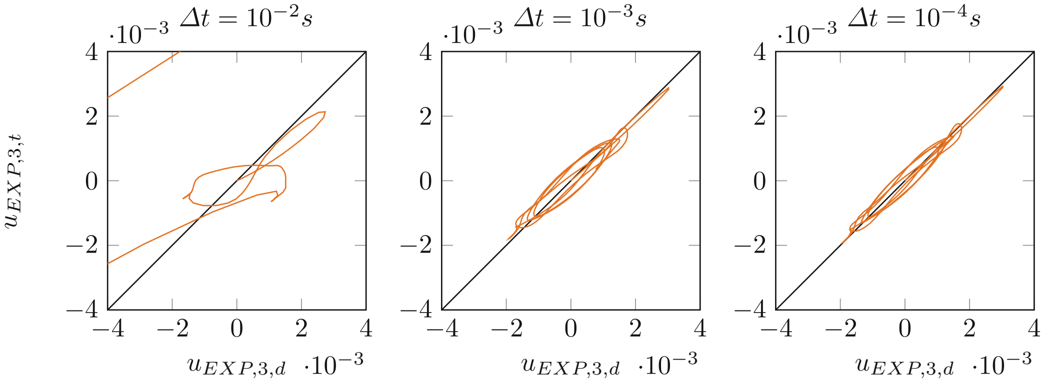

Fig. 5.13 Synchronization plots: effects of extended interface methods on the test accuracy. The simulations were performed using an inaccurate model of the transmission simulator

References

1. Ambrogio W, Fregolent A (2010) Decoupling procedures in the general framework of Frequency Based Substructuring. In: Proceedings of 27th international modal analysis conference, society for experimental mechanics, Bethel
2. Ambrogio W, Fregolent A (2010) The role of interface DoFs in decoupling of substructures based on the dual domain decomposition. Mech Syst Signal Process 24(7):2035–2048
3. Blakeborough A et al. (2001) The development substructure of real-time testing. Philos Trans 359(1786):1869–1891
4. Gawhrop P et al (2008) Emulator-basedcontrolforactuator-basedhardware-in-the-looptesting. Control Eng Pract 16:897–907
5. Horiuchi T et al (1999) Real-time hybrid experimental system with actuator delay compensation and its application to a piping system with energy absorber. Earthq Eng Struct Dyn 28(10):1121–1141
6. Kammer D et al (2013) Formulation of a Craig-Bampton experimental substructure using a transmission simulator. In: Proceedings of the 31st IMAC, a conference on structural dynamics
7. Nakashima M et al (1992) Development of real-time pseudo dynamic testing. Earthq Eng Struct Dyn 21(1):79–92
8. Tu J (2013) Development of numerical-substructure-based and output-based substructuring controllers. Struct Control Health Monit 20: 918–936
9. Tu J et al (2011) A state-space approach for the control of multivariable dynamically substructured systems. J Syst Control Eng 225(7):935–953
10. Voormeeren S, Rixen DJ (2009) Substructure decoupling techniques—a review and uncertainty propagation analysis. In: 2009 IMAC-XXVII: conference & exposition on structural dynamics
11. Voormeeren S, Rixen DJ (2012) A family of substructure decoupling techniques based on a dual assembly approach. Mech Syst Signal Process 27:379–396. ISSN:08883270

Chapter 6

Ignoring Rotational DoFs in Decoupling Structures Connected Through Flexotorsional Joints

Walter D'Ambrogio and Annalisa Fregolent

Abstract Substructure decoupling consists in the identification of the dynamic behaviour of a structural subsystem, starting from the dynamic behaviour of both the assembled system and the residual subsystem (the known portion of the assembled system). The degrees of freedom (DoFs) of the coupled system can be partitioned into internal DoFs (not belonging to the couplings) and coupling DoFs. In direct decoupling, a fictitious subsystem that is the negative of the residual subsystem is added to the coupled system, and appropriate compatibility and equilibrium conditions are enforced at interface DoFs. Compatibility and equilibrium can be required either at coupling DoFs only (standard interface), or at additional internal DoFs of the residual subsystem (extended interface), or at some coupling DoFs and some internal DoFs of the residual subsystem (mixed interface). In this paper, a test bench is considered made by a cantilever column with two staggered short arms coupled to a horizontal beam. This involves both flexural and torsional DoFs, on which rotational FRFs are quite difficult to measure. Using a mixed interface, rotational DoFs are neglected and substituted by internal translational DoFs. Experimental results are presented and discussed.

Keywords Substructure decoupling • Rotational DoFs • Flexotorsional joints • Mixed interface • Experimental dynamic substructuring

6.1 Introduction

Substructure decoupling consists in the identification of the dynamic behaviour of a structural subsystem, starting from the dynamic behaviour of both the assembled system and the residual subsystem (the known portion of the assembled system). Decoupling is a need for subsystems that cannot be measured separately, but only when coupled to their neighboring substructure(s) (e.g. fixtures needed for testing or subsystems in operational conditions).

Substructure decoupling represents a special case of experimental dynamic substructuring, where experimental means that the model of at least one subsystem derives from tests. In Frequency Based Substructuring, Frequency Response Functions (FRFs) are used instead of modal parameters to avoid modal truncation problems. A general framework for dynamic substructuring is provided in [1], where primal and dual assembly are introduced.

A well known issue in experimental dynamic substructuring is related to rotational DoFs. In substructure coupling, whenever coupling DoFs include rotational DoFs, the related rotational FRFs must be obtained experimentally. This becomes a quite complicated task when measuring only translational FRFs, as shown in [2]. Several techniques for measuring rotational responses have been devised since then, see e.g. [3, 4]. However, when such rotational FRFs are used for substructure coupling, results are still unsatisfactory.

Substructure decoupling techniques can be classified as reverse coupling techniques or direct decoupling techniques. In reverse coupling, the equations written for the coupling problem are rearranged to isolate (as unknown) one of the substructures instead of the assembled structure. Examples of reverse coupling are impedance and mobility approaches [5, 6].

In direct decoupling, a fictitious subsystem that is the negative of the residual subsystem is added to the coupled system, and appropriate compatibility and equilibrium conditions are enforced at interface DoFs. To solve the decoupling problem,

---

W. D'Ambrogio
Dipartimento di Ingegneria Industriale e dell'Informazione e di Economia, Università dell'Aquila, Via G. Gronchi 18, 67100 L'Aquila (AQ), Italy
e-mail: walter.dambrogio@univaq.it

A. Fregolent (✉)
Dipartimento di Ingegneria Meccanica e Aerospaziale, Università di Roma La Sapienza, Via Eudossiana 18, 00184 Rome, Italy
e-mail: annalisa.fregolent@uniroma1.it

M. Allen et al. (eds.), *Dynamics of Coupled Structures, Volume 4*, Conference Proceedings of the Society for Experimental Mechanics Series, DOI 10.1007/978-3-319-15209-7_6

a dual assembly [7], a primal assembly [8] or an hybrid assembly [9, 10] can be used. Compatibility and equilibrium can be required either at coupling DoFs only (standard interface), or at additional internal DoFs of the residual subsystem (extended interface), or at subsets of coupling DoFs and internal DoFs of the residual subsystem (mixed interface). The choice of interface DoFs determines a set of frequencies at which the decoupling problem is ill conditioned, as shown in [7].

For some time, it was believed that issues related to rotational DoFs also applied to substructure decoupling. However, in this case the actions exchanged through the connecting DoFs, and specifically through rotational DoFs, are already embedded in each FRF of the assembled system. In practice, a mixed interface [11] can in fact be considered that allows to substitute undesired coupling DoFs with internal DoFs of the residual subsystem. This approach is introduced in [12] using simulated test data.

In this paper, a test bed is considered made by a cantilever column with two staggered short arms coupled to a horizontal beam. This involves both flexural and torsional DoFs, on which rotational FRFs are quite difficult to measure. Using a mixed interface, rotational DoFs are neglected and substituted by internal translational DoFs. Experimental results are presented and discussed.

6.2 Direct Decoupling Using Dual Assembly

The unknown substructure U (N_U DoFs) is a portion of a larger structure RU (N_{RU} DoFs). The known portion of the assembled structure RU, defined as residual substructure R (N_R DoFs), is joined to the unknown substructure through a number of couplings (see Fig. 6.1). The degrees of freedom (DoFs) can be partitioned into internal DoFs (not belonging to the couplings) of substructure U (u), internal DoFs of substructure R (r), and coupling DoFs (c).

The goal is to find the FRF of the unknown substructure U starting from the FRFs of the assembled structure RU and of the residual substructure R. The dynamic behaviour of the unknown substructure U can be extracted from that of the assembled structure RU by taking out the dynamic effect of the residual subsystem R. This can be accomplished by considering a negative structure, i.e. by adding to the assembled structure RU a fictitious substructure with a dynamic stiffness opposite to that of the residual substructure R and satisfying compatibility and equilibrium conditions. The dynamic equilibrium of the assembled structure RU and of the negative substructure is expressed in block diagonal format as:

$$\begin{bmatrix} \mathbf{Z^{RU}} & \mathbf{0} \\ \mathbf{0} & -\mathbf{Z^{R}} \end{bmatrix} \begin{Bmatrix} \mathbf{u^{RU}} \\ \mathbf{u^{R}} \end{Bmatrix} = \begin{Bmatrix} \mathbf{f^{RU}} \\ \mathbf{f^{R}} \end{Bmatrix} + \begin{Bmatrix} \mathbf{g^{RU}} \\ \mathbf{g^{R}} \end{Bmatrix} \tag{6.1}$$

where:

- $\mathbf{Z^{RU}}$, $-\mathbf{Z^{R}}$ are the dynamic stiffness matrices of the assembled structure RU and of the negative structure, respectively;
- $\mathbf{u^{RU}}$, $\mathbf{u^{R}}$ are the vectors of degrees of freedom of the assembled structure RU and of the negative structure, respectively;
- $\mathbf{f^{RU}}$, $\mathbf{f^{R}}$ are the external force vectors on the assembled structure RU and on the negative structure, respectively;
- $\mathbf{g^{RU}}$, $\mathbf{g^{R}}$ are the vectors of disconnection forces exchanged between the assembled structure and the negative structure (constraint forces associated with compatibility conditions).

Compatibility and equilibrium conditions must be considered at the interface between the assembled structure RU and the negative structure: such interface includes not only all the coupling DoFs between substructures U and R, but includes as well all the internal DoFs of substructure R (the bottom part of the structure in Fig. 6.1). However, it is not required to

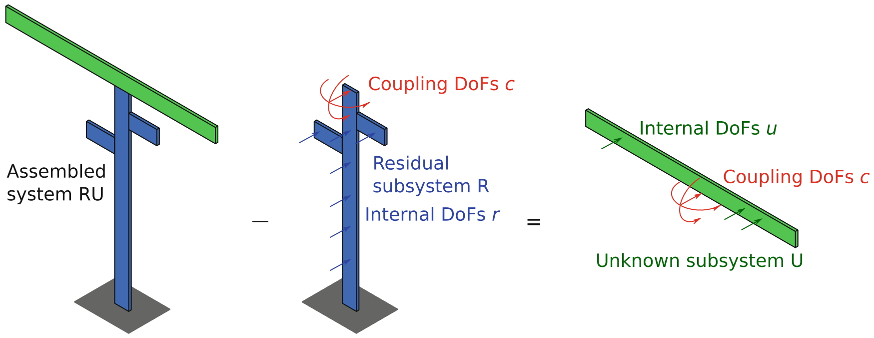

Fig. 6.1 Scheme of the direct decoupling problem

consider all these interface DoFs, because it is sufficient that the number of interface DoFs be not less than the number of coupling DoFs n_c. Therefore, several options for interface DoFs can be considered:

- standard interface, including only the coupling DoFs (c) between substructures U and R;
- extended interface, including also a subset of internal DoFs ($i \subseteq r$) of the residual substructure R;
- mixed interface, including subsets of coupling DoFs ($d \subseteq c$) and/or internal DoFs ($i \subseteq r$) of substructure R.

The use of a mixed interface may allow to ignore rotational coupling DoFs by substituting them with translational internal DoFs.

The compatibility condition at the (standard, extended, mixed) interface DoFs implies that any pair of matching DoFs u_l^{RU} and u_m^R, i.e. DoF l on the coupled system RU and DoF m on subsystem R must have the same displacement, that is $u_l^{RU} - u_m^R = 0$. Let the number of interface DoFs on which compatibility is enforced be denoted as N_C.

The compatibility condition can be generally expressed as:

$$\begin{bmatrix} \mathbf{B_C^{RU}} \; \mathbf{B_C^{R}} \end{bmatrix} \begin{Bmatrix} \mathbf{u^{RU}} \\ \mathbf{u^{R}} \end{Bmatrix} = \mathbf{0} \tag{6.2}$$

where each row of $\mathbf{B_C} = \begin{bmatrix} \mathbf{B_C^{RU}} \; \mathbf{B_C^{R}} \end{bmatrix}$ corresponds to a pair of matching DoFs. Note that $\mathbf{B_C}$ has size $N_C \times (N_{RU} + N_R)$ and is, in most cases, a signed Boolean matrix.

It should be noted that the interface DoFs involved in the equilibrium condition need not to be the same used to enforce the compatibility condition, as long as compatibility can be ensured by disconnection forces applied at a different set of DoFs. If the compatibility and the equilibrium DoFs are not the same, the approach is called non-collocated [11]. Obviously, the traditional approach, in which compatibility and equilibrium DoFs are the same, is called collocated.

Let N_E denote the number of interface DoFs on which equilibrium is enforced. The equilibrium of disconnection forces implies that their sum must be zero for any pair of matching DoFs belonging to the equilibrium interface, i.e. $g_r^{RU} + g_s^R = 0$. Furthermore, for any DoF k on the coupled system RU (or on the residual subsystem R) not belonging to the equilibrium interface, it must be $g_k^{RU} = 0$ ($g_k^R = 0$).

Overall, the above conditions can be expressed as:

$$\begin{bmatrix} \mathbf{L_E^{RU}} \\ \mathbf{L_E^{R}} \end{bmatrix}^T \begin{Bmatrix} \mathbf{g^{RU}} \\ \mathbf{g^{R}} \end{Bmatrix} = \mathbf{0} \tag{6.3}$$

where the matrix $\mathbf{L_E} = \begin{bmatrix} \mathbf{L_E^{RU}} \, \mathbf{L_E^{R}} \end{bmatrix}$ is a Boolean localisation matrix. Note that the number of columns of $\mathbf{L_E}$ is equal to the number N_E of equilibrium interface DoFs plus the number N_{NE} of DoFs not belonging to the equilibrium interface. Note that $N_{NE} = N_{RU} + N_R - 2N_E$: in fact, the number of DoFs belonging to the equilibrium interface must be subtracted once from N_{RU} and once from N_R. Therefore, the size of $\mathbf{L_E}$ is $(N_{RU} + N_R) \times (N_{RU} + N_R - N_E)$.

Equations (6.1)–(6.3) can be gathered to obtain the so-called 3-field formulation. Starting from the 3-field formulation, several assembly techniques can be devised:

- dual assembly [1, 7] where equilibrium is satisfied exactly by defining a unique set of disconnection force intensities;
- primal assembly [1, 8] where compatibility is satisfied exactly by defining a unique set of interface DoFs;
- hybrid assembly [9, 10] where both compatibility and equilibrium are satisfied exactly.

In the sequel, only the dual assembly is recalled. It can be shown [9] that whenever $N_C = N_E$, i.e. the number of compatibility DoFs is the same as the number of equilibrium DoFs, all assembly techniques provide the same result.

6.2.1 Dual Assembly

In the dual assembly, the equilibrium condition $g_r^{RU} + g_s^R = 0$ at a pair of equilibrium interface DoFs is ensured by choosing $g_r^{RU} = -\lambda$ and $g_s^R = \lambda$. If a Boolean matrix $\mathbf{B_E}$ related to interface equilibrium DoFs is defined similarly to $\mathbf{B_C}$, the overall interface equilibrium can be ensured by writing the disconnection forces in the form:

$$\begin{Bmatrix} \mathbf{g^{RU}} \\ \mathbf{g^{R}} \end{Bmatrix} = - \begin{bmatrix} \mathbf{B_E^{RU}}^T \\ \mathbf{B_E^{R}}^T \end{bmatrix} \boldsymbol{\lambda} \tag{6.4}$$

where $\boldsymbol{\lambda}$ are Lagrange multipliers corresponding to disconnection force intensities and $\mathbf{B_E}$ is a $N_E \times (N_{RU} + N_R)$ matrix. Since there is a unique set of disconnection force intensities $\boldsymbol{\lambda}$, the interface equilibrium condition is satisfied automatically for any $\boldsymbol{\lambda}$, i.e.

$$\begin{bmatrix} \mathbf{L_E^{RU}} \\ \mathbf{L_E^{R}} \end{bmatrix}^T \begin{Bmatrix} \mathbf{g^{RU}} \\ \mathbf{g^{R}} \end{Bmatrix} = -\begin{bmatrix} \mathbf{L_E^{RU}} \\ \mathbf{L_E^{R}} \end{bmatrix}^T \begin{bmatrix} \mathbf{B_E^{RU}}^T \\ \mathbf{B_E^{R}}^T \end{bmatrix} \boldsymbol{\lambda} = \mathbf{0} \tag{6.5}$$

In the dual assembly, the total set of DoFs is retained, i.e. each interface DoF appears twice. Since Eq. (6.5) is always satisfied, the 3-field formulation reduces to:

$$\begin{cases} \begin{bmatrix} \mathbf{Z^{RU}} & \mathbf{0} \\ \mathbf{0} & -\mathbf{Z^{R}} \end{bmatrix} \begin{Bmatrix} \mathbf{u^{RU}} \\ \mathbf{u^{R}} \end{Bmatrix} + \begin{bmatrix} \mathbf{B_E^{RU}}^T \\ \mathbf{B_E^{R}}^T \end{bmatrix} \boldsymbol{\lambda} = \begin{Bmatrix} \mathbf{f^{RU}} \\ \mathbf{f^{R}} \end{Bmatrix} & (6.1^*) \\ \begin{bmatrix} \mathbf{B_C^{RU}} & \mathbf{B_C^{R}} \end{bmatrix} \begin{Bmatrix} \mathbf{u^{RU}} \\ \mathbf{u^{R}} \end{Bmatrix} = \mathbf{0} & (6.2) \end{cases}$$

or in more compact form:

$$\begin{cases} \mathbf{Zu} + \mathbf{B_E}^T \boldsymbol{\lambda} = \mathbf{f} & (6.1^*) \\ \mathbf{B_C u} = \mathbf{0} & (6.2) \end{cases}$$

To eliminate $\boldsymbol{\lambda}$, Eq. (6.1*) can be written:

$$\mathbf{u} = -\mathbf{Z}^{-1}\mathbf{B_E}^T\boldsymbol{\lambda} + \mathbf{Z}^{-1}\mathbf{f}$$

which substituted in Eq. (6.2) gives:

$$\mathbf{B_C Z}^{-1}\mathbf{B_E}^T\boldsymbol{\lambda} = \mathbf{B_C Z}^{-1}\mathbf{f} \tag{6.6}$$

from which $\boldsymbol{\lambda}$, to be back-substituted in Eq. (6.1*), is found as:

$$\boldsymbol{\lambda} = \left(\mathbf{B_C Z}^{-1}\mathbf{B_E}^T\right)^+ \mathbf{B_C Z}^{-1}\mathbf{f} \tag{6.7}$$

To obtain a determined or overdetermined matrix for the generalized inversion operation, the number of rows of $\mathbf{B_C}$ must be greater or equal than the number of rows of $\mathbf{B_E}$, i.e.

$$N_C \geq N_E \geq n_c \tag{6.8}$$

Note that, if $N_C > N_E$, Eq. (6.6) is not satisfied exactly by vector $\boldsymbol{\lambda}$ given by Eq. (6.7), but only in the minimum square sense. This implies that also Eq. (6.2) is not satisfied exactly, i.e. compatibility conditions at interface are approximately satisfied. On the contrary, equilibrium is satisfied exactly due to the introduction of the disconnection force intensities $\boldsymbol{\lambda}$ as in Eq. (6.4).

By substituting $\boldsymbol{\lambda}$ in Eq. (6.1*), it is obtained:

$$\mathbf{Zu} + \mathbf{B_E}^T \left(\mathbf{B_C Z}^{-1}\mathbf{B_E}^T\right)^+ \mathbf{B_C Z}^{-1}\mathbf{f} = \mathbf{f} \tag{6.9}$$

Finally, $\mathbf{u}$ can be written as $\mathbf{u} = \mathbf{Hf}$, which provides the FRF of the unknown subsystem U:

$$\mathbf{u} = \left(\mathbf{Z}^{-1} - \mathbf{Z}^{-1}\mathbf{B_E}^T \left(\mathbf{B_C Z}^{-1}\mathbf{B_E}^T\right)^+ \mathbf{B_C Z}^{-1}\right)\mathbf{f} \tag{6.10}$$

i.e., by noting that the inverse of the block diagonal dynamic stiffness matrix can be expressed as:

$$\begin{bmatrix} \mathbf{Z^{RU}} & \mathbf{0} \\ \mathbf{0} & -\mathbf{Z^{R}} \end{bmatrix} = \mathbf{Z}^{-1} = \mathbf{H} = \begin{bmatrix} \mathbf{H^{RU}} & \mathbf{0} \\ \mathbf{0} & -\mathbf{H^{R}} \end{bmatrix} \tag{6.11}$$

where $\mathbf{H^{RU}}$ and $\mathbf{H^{R}}$ are the FRFs of the assembled structure and of the residual substructure, it is:

$$\mathbf{H^{U}} = \mathbf{H} - \mathbf{H}\mathbf{B_E}^T \left(\mathbf{B_C}\mathbf{H}\mathbf{B_E}^T\right)^+ \mathbf{B_C}\mathbf{H} \tag{6.12}$$

With the dual assembly, the rows and the columns of $\mathbf{H^{U}}$ corresponding to compatibility and equilibrium DoFs appear twice. Furthermore, when using an extended or mixed interface, $\mathbf{H^{U}}$ contains some meaningless rows and columns: those corresponding to the internal DoFs of the residual substructure R. Obviously, only meaningful and independent entries are retained.

6.2.2 *Interface Flexibility Matrix*

In Eq. (6.12), the product of the three matrices to be inverted can be defined as *interface flexibility matrix*. The interface flexibility matrix can be rewritten in expanded form as:

$$\begin{bmatrix} \mathbf{B_C^{RU}} & \mathbf{B_C^{R}} \end{bmatrix} \begin{bmatrix} \mathbf{H^{RU}} & \mathbf{0} \\ \mathbf{0} & -\mathbf{H^{R}} \end{bmatrix} \begin{bmatrix} \mathbf{B_E^{RU}}^T \\ \mathbf{B_E^{R}}^T \end{bmatrix} = \mathbf{B_C^{RU}}\mathbf{H^{RU}}\mathbf{B_E^{RU}}^T - \mathbf{B_C^{R}}\mathbf{H^{R}}\mathbf{B_E^{R}}^T \tag{6.13}$$

It can be noticed that

$$\mathbf{B_C^{RU}}\mathbf{H^{RU}}\mathbf{B_E^{RU}}^T = \hat{\mathbf{H}}^{\mathbf{RU}}$$

where $\hat{\mathbf{H}}^{\mathbf{RU}}$ is a subset of the FRF matrix of the coupled structure: pre-multiplication by $\mathbf{B_C^{RU}}$ extracts rows at compatibility DoFs, and post-multiplication by $\mathbf{B_E^{RU}}$ extracts columns at the equilibrium DoFs. Similarly,

$$\mathbf{B_C^{R}}\mathbf{H^{R}}\mathbf{B_E^{R}}^T = \hat{\mathbf{H}}^{\mathbf{R}}$$

where $\hat{\mathbf{H}}^{\mathbf{R}}$ is the FRF of the residual structure at the same DoFs as above.

Therefore, the interface flexibility matrix becomes:

$$\mathbf{B_C^{RU}}\mathbf{H^{RU}}\mathbf{B_E^{RU}}^T - \mathbf{B_C^{R}}\mathbf{H^{R}}\mathbf{B_E^{R}}^T = \hat{\mathbf{H}}^{\mathbf{RU}} - \hat{\mathbf{H}}^{\mathbf{R}} \tag{6.14}$$

The interface flexibility matrix (6.14) is strictly related to singularity. In [7, 8], it is shown that the interface flexibility matrix is singular at the resonant frequencies of the residual substructure with coupling DoFs grounded, both for standard interface and for non collocated extended interface when equilibrium condition is enforced on coupling DoFs only. In other cases, it is not so easy to find the frequencies at which the interface flexibility matrix is singular.

6.3 Test Structure

The proposed decoupling technique is tested on an aluminium structure (Fig. 6.2). The residual substructure R consists of a cantilever column with two staggered short arms. The unknown substructure U is a horizontal beam. The horizontal beam is bolted to the top of the column, involving both translational and rotational DoFs.

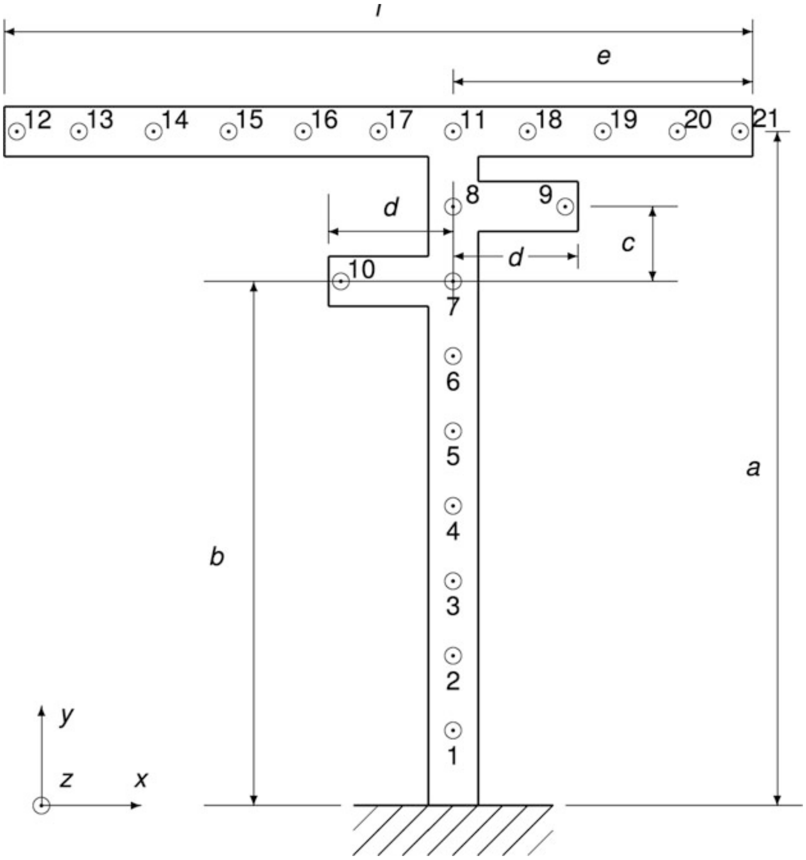

Fig. 6.2 Sketch of the test structure

Table 6.1 Geometrical dimensions (mm)

a	*b*	*c*	*d*	*e*	*l*
540	420	60	100	240	600

The geometrical dimensions are reported in Table 6.1. The cross section is 40 × 8 mm for all beams, with the short side along the *z*-direction.

The experimental FRFs of the assembled system RU up to 2,000 Hz are obtained by applying impact excitation and measuring the resulting accelerations along *z*-direction at seven locations (3, 6, 9, 10, 11, 13, 20), as shown in Fig. 6.3. For the residual subsystem R (column) the experimental FRFs are similarly measured at five locations (3, 6, 9, 10, 11), as shown in Fig. 6.4. A detail of the bolted junction between the beam and the column is shown in Fig. 6.5. Finally, to check decoupling results, FRFs are measured also at three locations (11, 13, 20) of the unknown subsystem U (beam), supported by an inflated rubber tube, shown in Fig. 6.6, giving rigid body eigenfrequencies well separated from the first flexible mode of the beam.

Measurements are performed by placing the accelerometers at the underside of each (sub)structure. In order to obtain a complete FRF matrix, as required by the decoupling technique, impact excitation is sequentially provided on all DoFs at the topside of each (sub)structure.

A reciprocity check is performed on the experimental FRFs showing that reciprocity is acceptable for all FRF pairs involving coupling DoFs and internal DoFs of the residual subsystem, i.e. the DoFs that can be used to enforce compatibility and equilibrium conditions. Figures 6.7 and 6.8 show the reciprocity check on experimental FRFs of the assembled structure RU and of the residual subsystem R. No indication about possible FRFs that should be discarded because of lack of reciprocity is provided by this check.

Fig. 6.3 Assembled system

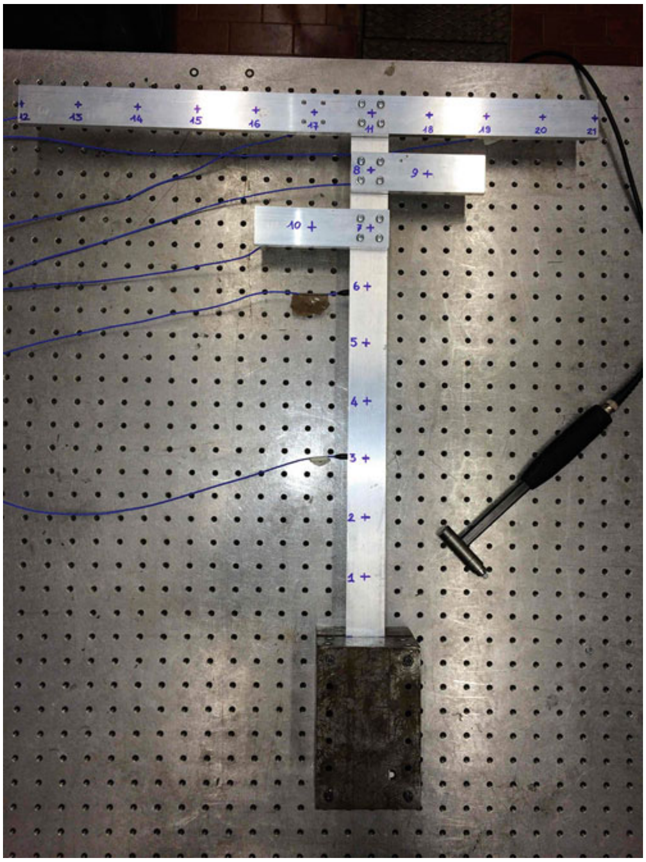

Fig. 6.4 Residual subsystem

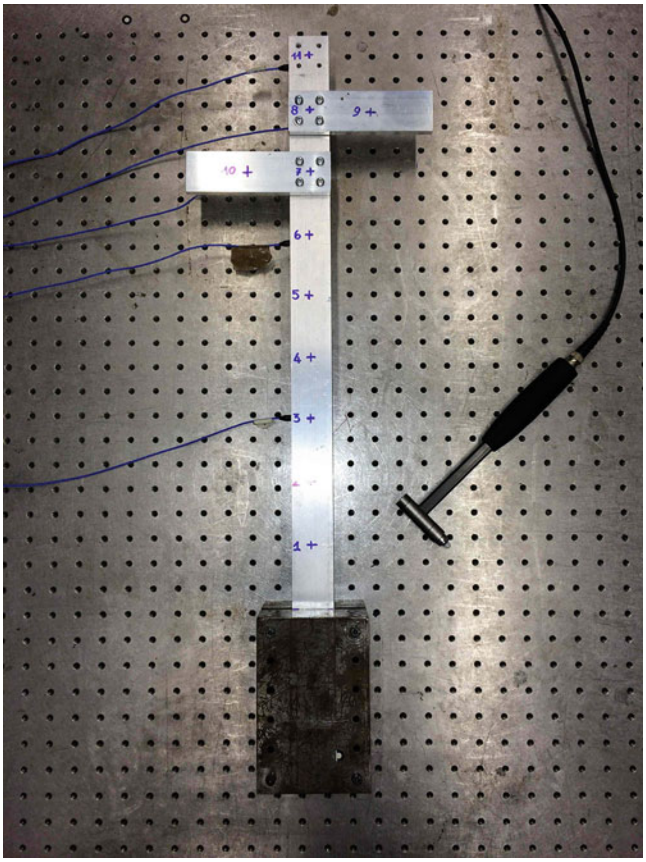

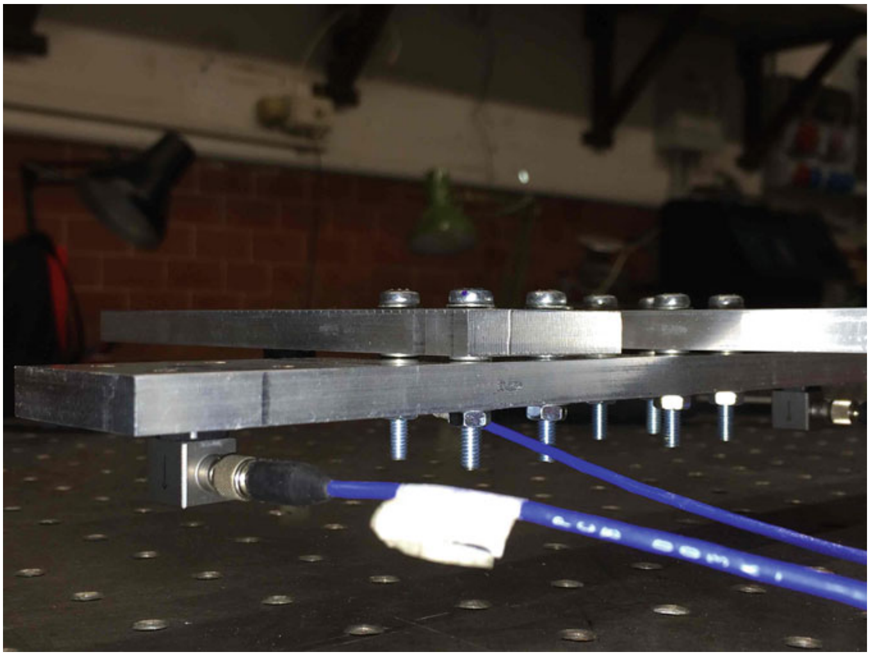

Fig. 6.5 Detail of the bolted junction

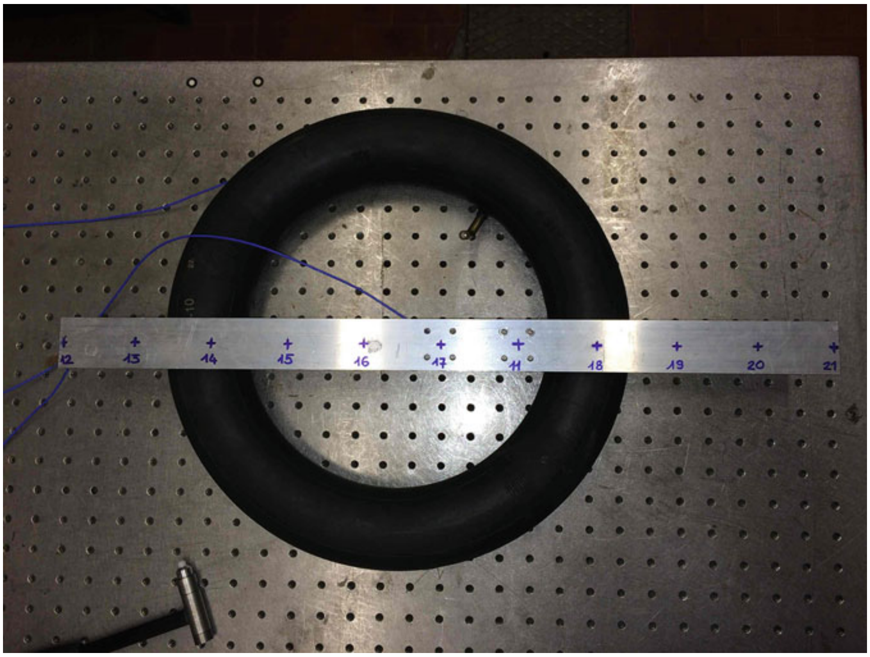

Fig. 6.6 Unknown subsystem

6.4 Decoupling

The FRFs of subsystem U can be determined through the procedure described previously and summarized in Eq. (6.12), where compatibility and equilibrium DoFs are defined case by case. A collocated approach is adopted in which compatibility and equilibrium DoFs are the same.

FRFs to be used in decoupling can be either the raw FRFs or can be obtained by a curve fitting procedure. In the latter case, results are very bad and are not shown in the paper. This occurs although curve fitting is performed using a global procedure that gives rise to a unique modal model plus low and high frequency residuals obtained for all FRFs. Therefore, raw FRFs are used in the sequel.

Fig. 6.7 Reciprocity check on experimental FRFs of the assembled structure RU among DoFs 3, 6, 9, 10, 11 (Color figure online)

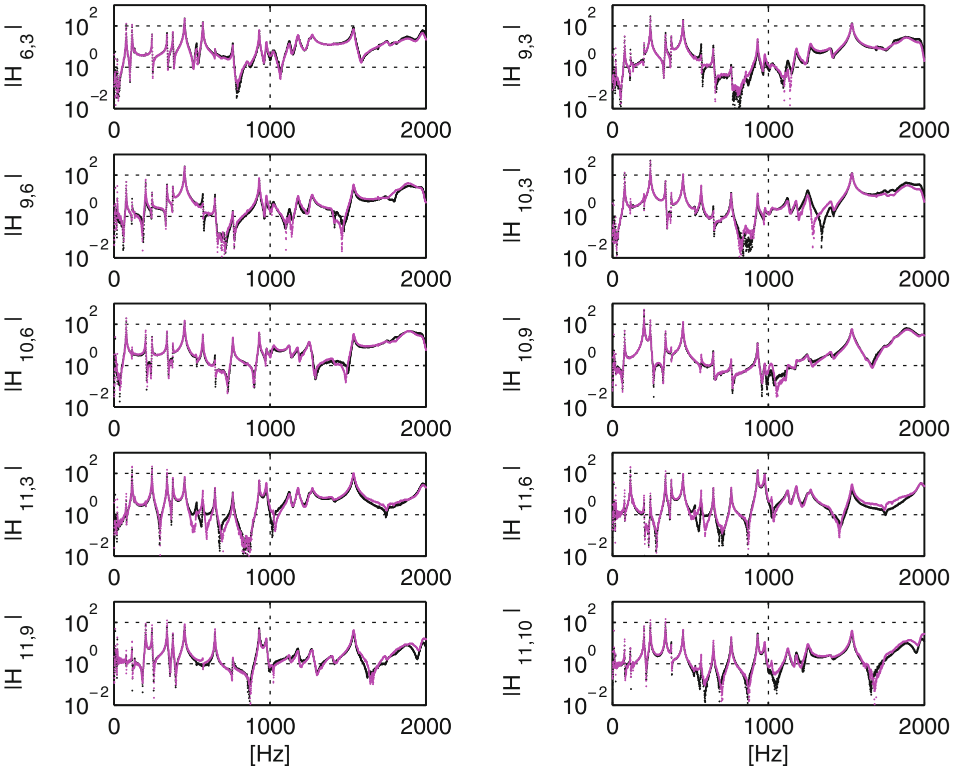

Fig. 6.8 Reciprocity check on experimental FRFs of the residual structure RU among DoFs 3, 6, 9, 10, 11 (Color figure online)

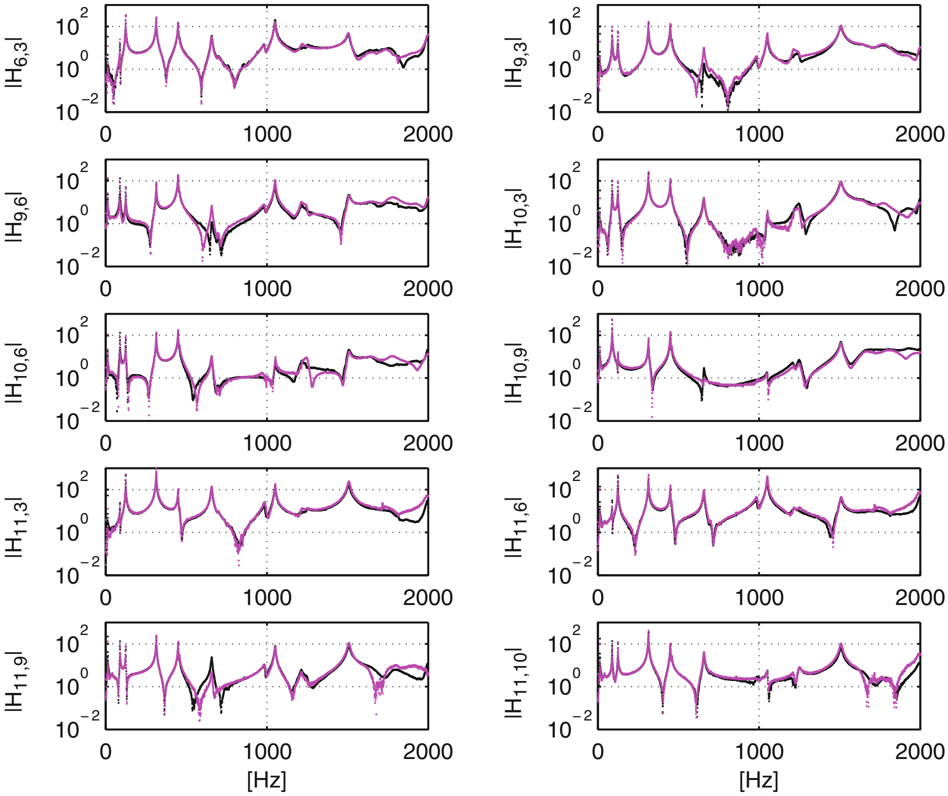

6.4.1 Results Using Raw FRFs

Since rotational DoFs at the junction between the residual subsystem and the unknown subsystem can not be measured, neither the standard interface nor the extended interface can be used. Therefore, only mixed interfaces can be considered. The number n_c of coupling DoFs is 3 so that it must be $N_E \geq n_c = 3$. To deal with overdetermined problems, a set of attempts using mixed interfaces with $N_C = N_E = 4$ is performed.

First, an interface including DoFs $3z$, $6z$, $9z$ and $11z$ is used. Therefore

$$\mathbf{B_C} = \mathbf{B_E} = \begin{array}{c} \begin{array}{cccccccc} u^{RU}_{3z} & u^{RU}_{6z} & u^{RU}_{9y} & u^{RU}_{11z} & u^{R}_{3z} & u^{R}_{6z} & u^{R}_{9z} & u^{R}_{11z} \end{array} \\ \left[\begin{array}{cccc|cccc} 1 & 0 & 0 & 0 & -1 & 0 & 0 & 0 \\ 0 & 1 & 0 & 0 & 0 & -1 & 0 & 0 \\ 0 & 0 & 1 & 0 & 0 & 0 & -1 & 0 \\ 0 & 0 & 0 & 1 & 0 & 0 & 0 & -1 \end{array}\right] \\ \begin{array}{cc} \mathbf{B^{RU}_C} & \qquad\qquad \mathbf{B^{R}_C} \end{array} \end{array} \tag{6.15}$$

The FRF of the unknown substructure U is shown in Fig. 6.9. It can be noticed that, although the FRF is not very scattered, the peak around 1,000 Hz is not well described and some other peaks are shifted towards higher frequencies.

Another mixed interface including DoFs $3z$, $6z$, $10z$ and $11z$ is used. The signed Boolean matrices $\mathbf{B_C}$ and $\mathbf{B_E}$ are built as in the previous case. The FRF of the unknown substructure U is shown in Fig. 6.10. It can be noticed that around 500 Hz a spurious peak appear and another peak is considerably forward shifted. However, the peak around 1,000 Hz is better described.

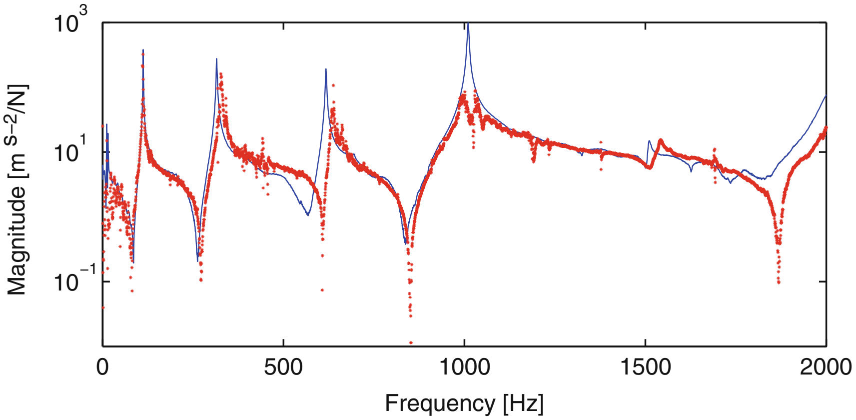

Fig. 6.9 $H^U_{11z,11z}$: measured (*blue line*), computed using mixed interface with coupling DoF $11z$, and internal DoFs $3z$, $6z$, $9z$ (*red asterisks*) (Color figure online)

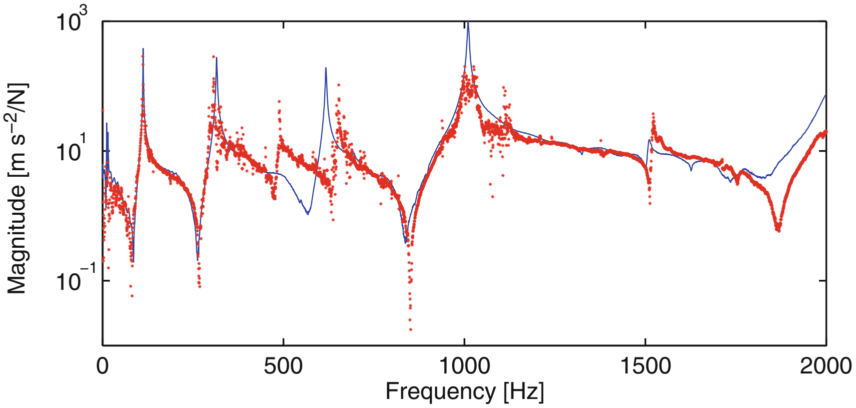

Fig. 6.10 $H^U_{11z,11z}$: measured (*blue line*), computed using mixed interface with coupling DoF $11z$, and internal DoFs $3z$, $6z$, $10z$ (*red asterisks*) (Color figure online)

Fig. 6.11 $H^{U}_{11z,11z}$: measured (*blue line*), computed using mixed interface with coupling DoF 11*z*, and internal DoFs 3*z*, 9*z*, 10*z* (*red asterisks*) (Color figure online)

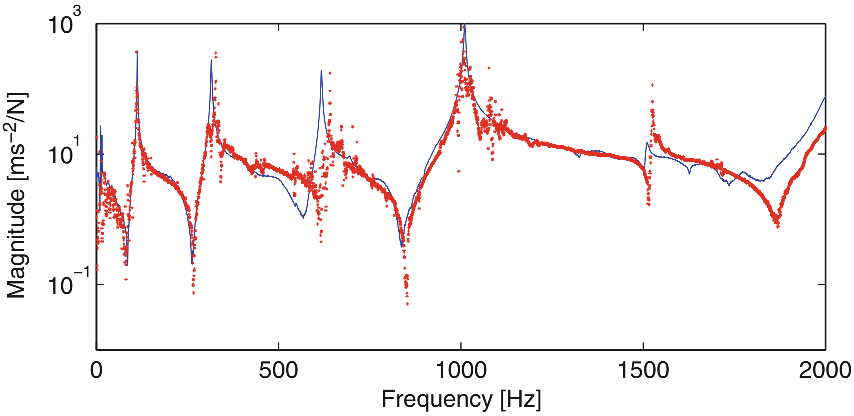

Fig. 6.12 $H^{U}_{11z,11z}$: measured (*blue line*), computed using mixed interface with coupling DoF 11*z*, and internal DoFs 6*z*, 9*z*, 10*z* (*red asterisks*) (Color figure online)

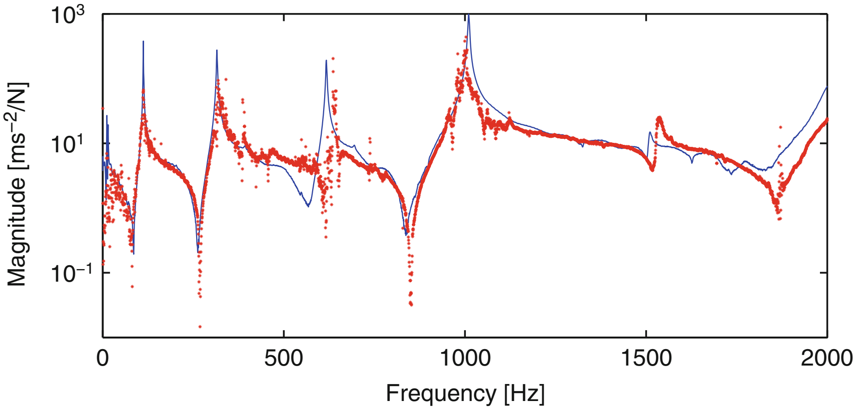

Fig. 6.13 $H^{U}_{11z,11z}$: measured (*blue line*), computed using mixed interface with coupling DoF 11*z*, and internal DoFs 3*z*, 9*z* (*red asterisks*) (Color figure online)

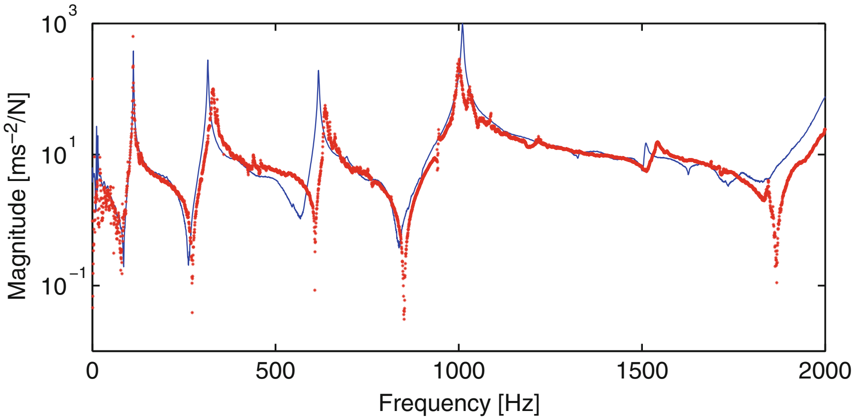

Subsequently, a mixed interface including DoFs 3*z*, 9*z*, 10*z* and 11*z* is used. The signed Boolean matrices $\mathbf{B_C}$ and $\mathbf{B_E}$ are built as in the first case. The FRF of the unknown substructure *U* is shown in Fig. 6.11. It can be noticed that around 600 Hz the peak is shifted forward and around this peak the FRF is a bit scattered. However, the peak around 1,000 Hz is very well described.

Finally, a mixed interface including DoFs 6*z*, 9*z*, 10*z* and 11*z* is used. The signed Boolean matrices $\mathbf{B_C}$ and $\mathbf{B_E}$ are built as in the first case. The FRF of the unknown substructure *U* is shown in Fig. 6.12. At a first glance, the result looks very similar to the previous one (interface DoFs 3*z*, 9*z*, 10*z* and 11*z*), but it is definitely worse because of several spikes and because the FRF around 1,000 Hz is described less accurately than in the previous case.

A new set of attempts is performed using mixed interfaces including only 3 DoFs that give rise to determined problems. Based on the previous results, a mixed interface that includes DoFs 3*z*, 9*z* and 11*z* is used. Such DoFs represent the set intersection between DoFs 3*z*, 6*z*, 9*z*, 11*z* and 3*z*, 9*z*, 10*z*, 11*z* that provide the best results using 4 interface DoFs. The signed Boolean matrices $\mathbf{B_C}$ and $\mathbf{B_E}$ are built similarly to the first case. The FRF of the unknown substructure *U* is shown in Fig. 6.13. It can be noticed that the result is quite clean with no significant drawbacks.

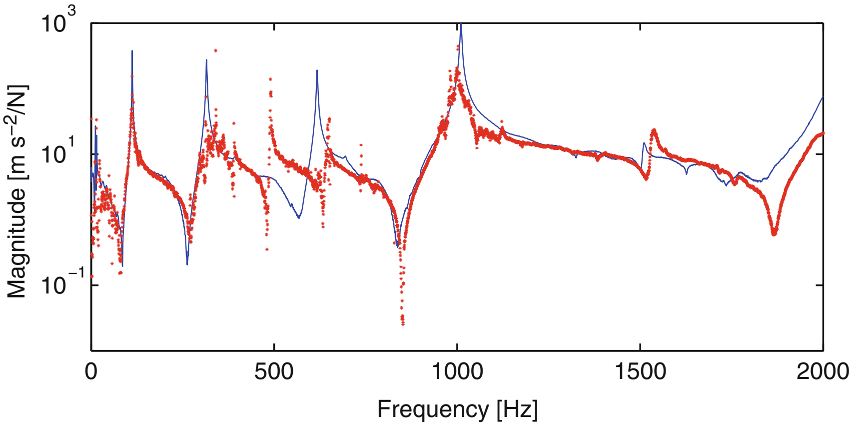

Fig. 6.14 $H^U_{11z,11z}$: measured (*blue line*), computed using mixed interface with coupling DoF 11z, and internal DoFs 6z, 10z (*red asterisks*) (Color figure online)

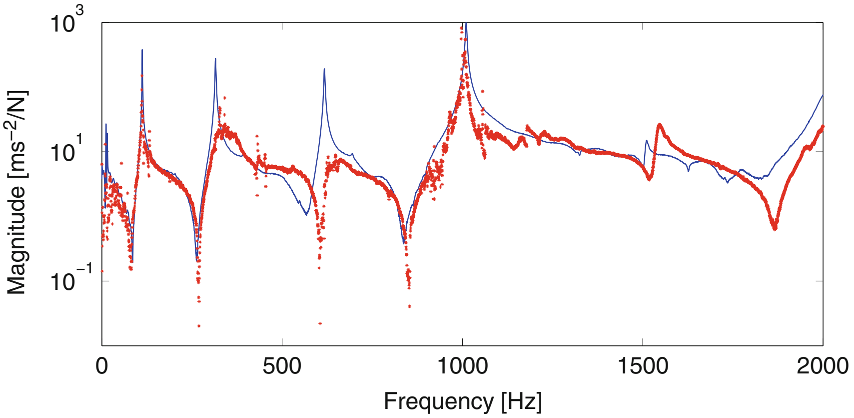

Fig. 6.15 $H^U_{11z,11z}$: measured (*blue line*), computed using mixed interface with coupling DoF 11z, and internal DoFs 9z, 10z (*red asterisks*) (Color figure online)

To cross-check this result, a mixed interface that includes DoFs 6z, 10z and 11z is used. Such DoFs represent the set intersection between DoFs 3z, 6z, 10z, 11z and 6z, 9z, 10z, 11z that provide the worst results using 4 interface DoFs. The FRF of the unknown substructure U is shown in Fig. 6.14. It can be noticed that the result is quite bad with significant scatter around the natural frequencies and several spurious peaks.

A further check is performed using a mixed interface that includes DoFs 9z, 10z and 11z. DoFs 9z, 10z are both able to provide information about the rotational DoF θ_y (torsion of the column) but may miss the information about the rotational DoF θ_x (bending of the column). The FRF of the unknown substructure U is shown in Fig. 6.15. It can be noticed that the result is very bad because the two modes around 315 and 615 Hz are not clearly visible.

6.5 Concluding Remarks

In this paper, a procedure that ignores rotational DoFs in decoupling of substructures, connected to each other through translational and rotational DoFs, is verified on an experimental test bed. The test bed is made by a cantilever column with two staggered short arms coupled to a horizontal beam. This involves both flexural and torsional DoFs, on which rotational FRFs are quite difficult to measure. Using a mixed interface, such FRFs are neglected and substituted by FRFs involving internal translational DoFs.

Measured FRFs can be curve fitted to try to smooth out noise before using them in the decoupling procedure. However, in this case, very bad results are obtained. Therefore, raw FRFs are used. Using a mixed interface including the single translational coupling DoF and several combinations of 3 internal DoFs, the obtained results are not satisfactory in different frequency bands: in two cases results are slightly better than in other cases. Further attempts are performed using a mixed interface including the single translational coupling DoF and different combinations of 2 internal DoFs. In one case, the result is almost satisfactory, whilst in the other cases results are worse than those obtained with 3 internal DoFs. (It can be noticed that the minimum number of interface equilibrium DoFs is 3.) Therefore, increasing the number of interface DoFs to deal with an overdetermined problem does not necessarily improve the results. Conversely, decreasing the number of interface DoFs increases the variability of the results: this can lead to better results but care must be taken to avoid worse results.

Acknowledgements This research is supported by grants from University of Rome La Sapienza and University of L'Aquila.

References

1. de Klerk D, Rixen DJ, Voormeeren S (2008) General framework for dynamic substructuring: history, review, and classification of techniques. AIAA J 46(5):1169–1181
2. Sestieri A, Salvini P, D'Ambrogio W (1991) Reducing scatter from derived rotational data to determine the frequency response function of connected structures. Mech Syst Signal Process 5(1):25–44
3. Stanbridge A, Ewins D (1996) Measurement of translational and angular vibration using a scanning laser Doppler vibrometer. Shock Vib 3:141–152
4. Bello M, Sestieri A, D'Ambrogio W, La Gala F (2003) Development of PZT's as rotational transducers. Mech Syst Signal Process 17(5): 1069–1081
5. D'Ambrogio W, Fregolent A (2008) Promises and pitfalls of decoupling procedures. In: Proceedings of 26th IMAC, Orlando
6. Sjövall P, Abrahamsson T (2008) Substructure system identification from coupled system test data. Mech Syst Signal Process 22(1):15–33
7. D'Ambrogio W, Fregolent A (2010) The role of interface DoFs in decoupling of substructures based on the dual domain decomposition. Mech Syst Signal Process 24(7):2035–2048. doi:10.1016/j.ymssp.2010.05.007, also in Proceedings of ISMA 2010, 1863–1880, Leuven (Belgium)
8. D'Ambrogio W, Fregolent A (2011) Direct decoupling of substructures using primal and dual formulation. In: Conference proceedings of the society of experimental mechanics series, vol 4. Linking models and experiments, vol 2, 31 January–3 February 2011. Springer, Jacksonville, pp 47–76
9. D'Ambrogio W, Fregolent A (2012) Direct hybrid formulation for substructure decoupling. In: Conference proceedings of the society for experimental mechanics series, vol 27. Topics in experimental dynamics substructuring and wind turbine dynamics, vol 2, 30 January–2 February 2012. Springer, Jacksonville, pp 89–107
10. D'Ambrogio W, Fregolent A (2014) Inverse dynamic substructuring using direct hybrid assembly in the frequency domain. Mech Syst Signal Process 45(2):360–377
11. Voormeeren SN, Rixen DJ (2012) A family of substructure decoupling techniques based on a dual assembly approach. Mech Syst Signal Process 27:379–396. doi:10.1016/j.ymssp.2011.07.028
12. D'Ambrogio W, Fregolent A (2014) Are rotational DoFs essential in substructure decoupling? In: Allen M, Mayes R, Rixen D (eds) Dynamics of coupled structures, vol 1. Conference proceedings of the society for experimental mechanics series. Springer International Publishing, Heidelberg, pp 27–36

Chapter 7
A Comparison of Two Component TPA Approaches for Steering Gear Noise Prediction

M.V. van der Seijs, E.A. Pasma, D. de Klerk, and Daniel J. Rixen

Abstract This paper presents a comparison of two component Transfer Path Analysis methods to predict the transmission of steering gear vibrations into the vehicle. The blocked-force TPA concept is used, allowing to measure the electric steering system on a test bench, separately from the car. Following up on an earlier study, a new test bench has been designed that is more compliant and therefore better suited for matrix-inverse force determination. Equivalent blocked forces are determined on this test bench using the in-situ method. A comparison is made with the blocked forces that were measured directly on the former stiff test bench. It is shown that the two methods lead to very similar equivalent force spectra for the operational steering system and therefore make a similar prediction for the noise in the vehicle.

Keywords Transfer path analysis • Dynamic substructuring • Experimental substructuring • Blocked force • In-situ

7.1 Introduction

Component Transfer Path Analysis (TPA) methods are aimed at characterising vibration sources in an assembled product by quantities that are properties of the active components only. As with any TPA method, the goal is to investigate dominant transmission paths from active excitation sources to certain locations of interest, such that design efforts can be directed to optimising/reducing their contributions if NVH[1] targets so require. Whereas *classical* and *operational* TPA methods [4, 12, 17] are used to expose transfer paths in existing designs, *component* TPA methods [2, 10] are valuable in design stages when the end-product or prototype is not yet there and an early prediction of vibration transfer is to be made. For instance a supplier of high-precision machinery could be interested in the excitations and dynamic properties of the factory floor on which the machinery is to be installed. Knowing the admittance and free velocity vibration levels of the floor at the interfaces with the machine beforehand, the supplier can design a support structure such that critical requirements on vibration levels are met [9, 21]. A vehicle manufacturer on the other hand would use excitation profiles from active components or other vibration sources to predict the contribution to the noise level in the vehicle's interior [1, 6, 16]. In the latter case it is preferred to characterise the operational component excitations by (blocked) forces at its interfaces.

This paper reports on the application of component TPA to predict the noise from the electric power steering system (EPS) inside the vehicle. In particular, two different procedures are followed to determine the so-called equivalent or blocked forces, that have led to the construction of two distinct test benches. The first test bench is designed for maximum rigidness such that boundary conditions are appropriate for direct measurement of *blocked interface forces*. Early results from EPS measurements on this test bench have previously been reported in [16, 20]. Based on these findings, a second test bench was designed that is more compliant in the directions of interest. The increased flexibility allows for matrix-inverse force reconstruction schemes using acceleration measurements. Rather than applying conventional matrix-inverse in a classical TPA sense (which would yield the interface forces), the *in-situ* force determination method is used as proposed by Moorhouse en Elliott [5, 10]. This method allows to reconstruct equivalent blocked forces using only the admittance of the assembly of the EPS system and the test bench.

---

[1] NVH is short for Noise Vibration and Harshness.

M.V. van der Seijs (✉) • E.A. Pasma • D. de Klerk
Department of Precision and Microsystems Engineering, Delft University of Technology, Mekelweg 2, 2628CD Delft, The Netherlands
e-mail: m.v.vanderseijs@tudelft.nl

D.J. Rixen
Technische Universität München, Institute of Applied Mechanics, Boltzmannstr. 15, 85748 Garching, Germany

M. Allen et al. (eds.), *Dynamics of Coupled Structures, Volume 4*, Conference Proceedings of the Society for Experimental Mechanics Series, DOI 10.1007/978-3-319-15209-7_7

The theoretic background of component TPA as derived from dynamic substructuring is briefly discussed in Sect. 7.2. The application to steering gear vibrations is presented in Sect. 7.3 for two different test bench measurement campaigns. Details on the test benches are included. The paper is concluded with a summary in Sect. 7.4.

7.2 Theory of Equivalent-Force TPA

This section summarises the substructuring theory needed to derive the equivalent force determination schemes for the steering gear application in Sect. 7.3. An extensive derivation is found in [20]. The notation of Lagrange Multiplier Frequency Based Substructuring (LM-FBS) as defined in [3] is adopted. In order to provide an appropriate framework for experimentally modelled substructures, all systems are described by admittance matrices in a dual assembly. The interface dynamics are described by 6-DoF FRF matrices per connection point; details on how the subsystems have been modelled from experiments can be found in [18, 19].

7.2.1 Response to an Excitation for the Assembled Problem

The vibration transfer problem is illustrated by the dynamic system AB, schematically depicted as subsystems A and B in Fig. 7.1. The active subsystem A contains the source excitation at node 1 (i.e. the vibrations of the steering gear); subsystem B represents the passive receiver structure comprising the responses of interest at node 3 (i.e. the acoustic response inside the vehicle). The subsystems are rigidly interconnected at their interfaces; for ease of notation they are represented by the single node 2.

Approaching the vibration transmission problem top-down, the transfer problem to be approximated, relating the response spectra at the receiving locations ($\mathbf{u}_3$) for an excitation spectrum only at the source ($\mathbf{f}_1$), reads:

$$\mathbf{u}_3(\omega) = \mathbf{Y}_{31}^{\mathrm{AB}}(\omega)\,\mathbf{f}_1(\omega) \tag{7.1}$$

Matrix $\mathbf{Y}^{\mathrm{AB}}(\omega)$ contains admittance Frequency Response Functions[2] (FRFs) measured on the total assembly, i.e. total vehicle including the steering gear. Although trivial in this case, Eq. (7.1) governs the main transfer path problem that will be approximated in the following sections by means of test bench measurements.

7.2.2 Equivalent Source Problem for a Substructured System

The total transfer function is first derived using the admittance FRF matrices of the individual subsystems $\mathbf{Y}^{\mathrm{A}}$ and $\mathbf{Y}^{\mathrm{B}}$ as shown in Fig. 7.1. The system of equations is put in a block-diagonal format and augmented with unknown interface forces $\mathbf{g}_2$ at both sides of node 2. Regarding that the system is only excited at node 1 of the active subsystem, the dual system reads:

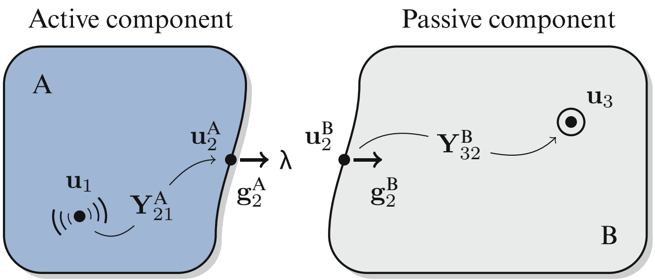

Fig. 7.1 The transfer path problem based on the admittances of substructures A and B

---

[2] The explicit frequency dependency (ω) is assumed for all further variables and will be omitted for clarity of notation.

$$\begin{bmatrix} \mathbf{u}_1 \\ \mathbf{u}_2^{\mathrm{A}} \\ \mathbf{u}_2^{\mathrm{B}} \\ \mathbf{u}_3 \end{bmatrix} = \begin{bmatrix} \mathbf{Y}_{11}^{\mathrm{A}} & \mathbf{Y}_{12}^{\mathrm{A}} & \mathbf{0} & \mathbf{0} \\ \mathbf{Y}_{21}^{\mathrm{A}} & \mathbf{Y}_{22}^{\mathrm{A}} & \mathbf{0} & \mathbf{0} \\ \mathbf{0} & \mathbf{0} & \mathbf{Y}_{22}^{\mathrm{B}} & \mathbf{Y}_{23}^{\mathrm{B}} \\ \mathbf{0} & \mathbf{0} & \mathbf{Y}_{32}^{\mathrm{B}} & \mathbf{Y}_{33}^{\mathrm{B}} \end{bmatrix} \begin{bmatrix} \mathbf{f}_1 \\ \mathbf{g}_2^{\mathrm{A}} \\ \mathbf{g}_2^{\mathrm{B}} \\ \mathbf{0} \end{bmatrix} \tag{7.2}$$

From the unassembled system of Eq. (7.2), a coupled system is obtained by imposing coordinate compatibility and force equilibrium at the interface.[3] We write $\mathbf{u}_2^{\mathrm{A}} = \mathbf{u}_2^{\mathrm{B}}$ to enforce the compatibility condition; interface force equilibrium is satisfied by defining a unique set of interface forces $\boldsymbol{\lambda} = \mathbf{g}_2^{\mathrm{A}} = -\mathbf{g}_2^{\mathrm{B}}$. Hence the required set of interface forces $\boldsymbol{\lambda}$ to couple the two subsystems can be determined by equating the second and third line of Eq. (7.2):

$$\begin{aligned} \mathbf{Y}_{21}^{\mathrm{A}}\mathbf{f}_1 + \mathbf{Y}_{22}^{\mathrm{A}}\mathbf{g}_2^{\mathrm{A}} &= \mathbf{Y}_{22}^{\mathrm{B}}\mathbf{g}_2^{\mathrm{B}} \\ \left(\mathbf{Y}_{22}^{\mathrm{A}} + \mathbf{Y}_{22}^{\mathrm{B}}\right)\boldsymbol{\lambda} &= -\mathbf{Y}_{21}^{\mathrm{A}}\mathbf{f}_1 \\ \boldsymbol{\lambda} &= -\left(\mathbf{Y}_{22}^{\mathrm{A}} + \mathbf{Y}_{22}^{\mathrm{B}}\right)^{-1}\mathbf{Y}_{21}^{\mathrm{A}}\mathbf{f}_1 \end{aligned} \tag{7.3}$$

Equation (7.3) provides the interface forces caused by the operational excitation $\mathbf{f}_1$ inside the active component A at the coinciding interface DoFs $\mathbf{u}_2^{\mathrm{A}}$ and $\mathbf{u}_2^{\mathrm{B}}$. Finally the response at the receiving side $\mathbf{u}_3^{\mathrm{B}}$ is found by substituting Eq. (7.3) back into the last line of Eq. (7.2):

$$\mathbf{u}_3 = -\mathbf{Y}_{32}^{\mathrm{B}}\boldsymbol{\lambda} = \left[\mathbf{Y}_{32}^{\mathrm{B}}\left(\mathbf{Y}_{22}^{\mathrm{A}} + \mathbf{Y}_{22}^{\mathrm{B}}\right)^{-1}\mathbf{Y}_{21}^{\mathrm{A}}\right]\mathbf{f}_1 \tag{7.4}$$

The terms between the brackets represent the assembled admittance from Eq. (7.1) expressed in terms of its subsystem admittances, which is a standard result of applying Dynamic Substructuring.

Rather than expressing the response $\mathbf{u}_3$ as a function of the excitation $\mathbf{f}_1$, one is interested in finding an equivalent set of forces $\mathbf{f}_2^{\mathrm{eq}}$ that, applied at the interface of the assembly, yield the same response at the receiving side. This is illustrated by the applied force in Fig. 7.2. Analogue to Eq. (7.4), the response for an excitation at the interface $\mathbf{f}_2^{\mathrm{eq}}$ is governed by:

$$\mathbf{u}_3 = \mathbf{Y}_{32}^{\mathrm{AB}}\mathbf{f}_2^{\mathrm{eq}} = \left[\mathbf{Y}_{32}^{\mathrm{B}}\left(\mathbf{Y}_{22}^{\mathrm{A}} + \mathbf{Y}_{22}^{\mathrm{B}}\right)^{-1}\mathbf{Y}_{22}^{\mathrm{A}}\right]\mathbf{f}_2^{\mathrm{eq}} \tag{7.5}$$

Again the terms between the brackets represent the admittance assembled from its subsystems. Comparing Eqs. (7.4) and (7.5), it follows naturally that the equivalent force $\mathbf{f}_2^{\mathrm{eq}}$ should have the form:

$$\boxed{\mathbf{f}_2^{\mathrm{eq}} = \left(\mathbf{Y}_{22}^{\mathrm{A}}\right)^{-1}\mathbf{Y}_{21}^{\mathrm{A}}\,\mathbf{f}_1} \tag{7.6}$$

Indeed the equivalent forces in Eq. (7.6) are dependent on the active component A only and lead to the same response $\mathbf{u}_3$ once applied to the interface of the assembled structure. In the next section various approaches will be discussed to obtain such an equivalent force from practical test bench measurements.

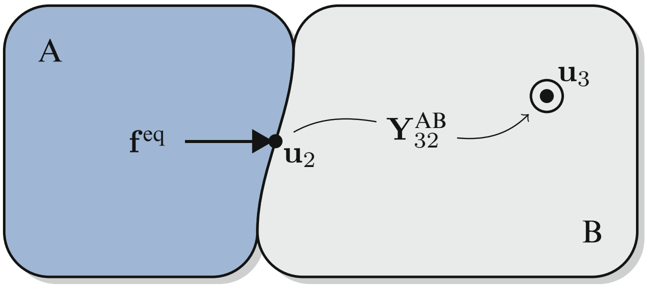

Fig. 7.2 Application of equivalent forces to the interface of the assembly

---

[3] More information on the expression of the compatibility and equilibrium condition is found in [3].

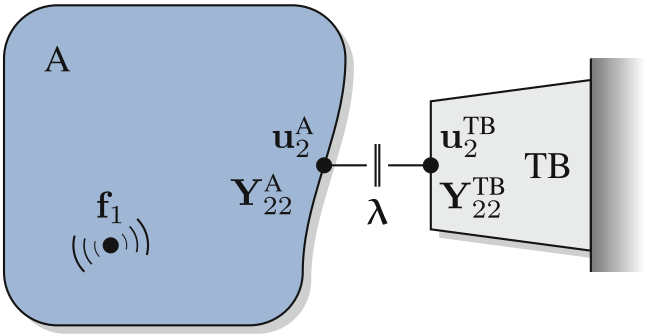

Fig. 7.3 Measurement of interface forces and displacements on a test bench

7.2.3 *Equivalent Force Strategies for Test Bench Measurement*

The goal of a component TPA is to characterise the active component by means of operational forces/motion that are an inherent property of the active component only. Let us therefore consider a test bench TB upon which the active component A is mounted, visualised in Fig. 7.3. The interfaces A–TB are supposed to resemble those of the assembly A–B as closely as possible, both in number and connection type.

It is important to note that the test bench is fully passive: no additional excitation is acting upon or coming from the test bench. Therefore its dynamics are governed solely by the admittance at the interface $\mathbf{Y}_{22}^{\mathrm{TB}}$, which can be anything between a fully rigid (zero admittance) and a fully free (infinite admittance) boundary. The following system of equations can thus be established for the general case:

$$\begin{bmatrix} \mathbf{u}_1^{\mathrm{A}} \\ \mathbf{u}_2^{\mathrm{A}} \\ \mathbf{u}_2^{\mathrm{TB}} \end{bmatrix} = \begin{bmatrix} \mathbf{Y}_{11}^{\mathrm{A}} & \mathbf{Y}_{12}^{\mathrm{A}} & \mathbf{0} \\ \mathbf{Y}_{21}^{\mathrm{A}} & \mathbf{Y}_{22}^{\mathrm{A}} & \mathbf{0} \\ \mathbf{0} & \mathbf{0} & \mathbf{Y}_{22}^{\mathrm{TB}} \end{bmatrix} \begin{bmatrix} \mathbf{f}_1 \\ \mathbf{g}_2^{\mathrm{A}} \\ \mathbf{g}_2^{\mathrm{TB}} \end{bmatrix} \tag{7.7}$$

Furthermore, as the active component is rigidly connected to the test bench, coordinate compatibility and force equilibrium at the interface are again assumed, i.e. $\mathbf{u}_2^{\mathrm{A}} = \mathbf{u}_2^{\mathrm{TB}}$ and $\mathbf{g}_2^{\mathrm{A}} = -\mathbf{g}_2^{\mathrm{TB}}$. Analogue to the derivation of Eq. (7.3), the interface force and interface displacement can be expressed as a function of the source excitation $\mathbf{f}_1$:

$$\textit{Operational interface forces}: \quad \mathbf{g}_2^{\star} = -\boldsymbol{\lambda} \;=\left(\mathbf{Y}_{22}^{\mathrm{A}} + \mathbf{Y}_{22}^{\mathrm{TB}}\right)^{-1} \mathbf{Y}_{21}^{\mathrm{A}}\, \mathbf{f}_1 \tag{7.8a}$$

$$\textit{Operational interface displacements}: \quad \mathbf{u}_2^{\star} = \;\mathbf{u}_2^{\mathrm{A}} \;=\left[\mathbf{I} - \mathbf{Y}_{22}^{\mathrm{A}} \left(\mathbf{Y}_{22}^{\mathrm{A}} + \mathbf{Y}_{22}^{\mathrm{TB}}\right)^{-1}\right] \mathbf{Y}_{21}^{\mathrm{A}}\, \mathbf{f}_1 \tag{7.8b}$$

The superscripts are replaced by $(\cdot)^{\star}$ to emphasize that it now concerns measured states during operational tests (active source excitation $\mathbf{f}_1$) obtained by means of force sensors[4] and accelerometers. The goal is then to construct an equivalent set of forces $\mathbf{f}_2^{\mathrm{eq}}$ according to the definition of Eq. (7.6). It is readily observed that, regardless of the properties of the test bench or active component, the equivalent force is formed as follows:

$$\boxed{\mathbf{f}_2^{\mathrm{eq}} = \mathbf{g}_2^{\star} \;+\; \left(\mathbf{Y}_{22}^{\mathrm{A}}\right)^{-1} \mathbf{u}_2^{\star}} \tag{7.9}$$

This expression for equivalent forces can be generally applied for any test bench setup and was originally proposed in [2]. Special cases of Eq. (7.9) and alternative equivalent force strategies are discussed next.

---

[4] Note that the sign of $\mathbf{g}_2^{\star}$ corresponds with the interface force acting on the test bench. This is a different convention than in [16, 20] where it was defined as seen from the side of the active component.

7.2.3.1 Blocked Interface Force/Free Interface Motion

Consider an infinitely stiff test bench, i.e. $\mathbf{Y}^{\mathrm{TB}} = \mathbf{0}$. Under these conditions, interface forces are measured against a rigid boundary and are therefore the true blocked forces, while displacement of the interface is null, as can be found from substitution into Eq. (7.8). As a consequence the equivalent force is simply constituted by:

$$\left.\begin{aligned} \mathbf{g}_2^\star &= \left(\mathbf{Y}_{22}^{\mathrm{A}}\right)^{-1} \mathbf{Y}_{21}^{\mathrm{A}} \mathbf{f}_1 \\ \mathbf{u}_2^\star &= \mathbf{0} \end{aligned}\right\} \implies \boxed{\mathbf{f}_2^{\mathrm{eq}} = \mathbf{g}_2^\star} \tag{7.10}$$

As discussed earlier in [2, 20] this method is particularly suited for lower frequencies for which the rigidness assumption is valid. An additional difficulty is the measurement of interface moments, as not many sensors that are currently available are capable of measuring rotational forces.

At the other utmost, an infinitely compliant test bench, i.e. $\mathbf{Y}^{\mathrm{TB}} = \infty$, leaves the interface entirely free. This yields a set of equivalent forces that are completely composed from the interface displacements in a matrix-inverse procedure with the admittance of the active component:

$$\left.\begin{aligned} \mathbf{g}_2^\star &= \mathbf{0} \\ \mathbf{u}_2^\star &= \mathbf{Y}_{21}^{\mathrm{A}} \mathbf{f}_1 \end{aligned}\right\} \implies \boxed{\mathbf{f}_2^{\mathrm{eq}} = \left(\mathbf{Y}_{22}^{\mathrm{A}}\right)^{-1} \mathbf{u}_2^\star} \tag{7.11}$$

In practice one would need to suspend the active component somehow to be able to measure the interface motion at the active component under operation, for instance with soft springs. Apart from any practical issues and the fact that the true rigid body modes are in practice suppressed by a suspending system, the free interface motion method is expected to perform best for higher frequencies.

Both variants are well-known special cases that were historically deduced from respectively the Thévenin and Norton equivalent source problem (see for instance [7, 8, 11, 13]). They are indeed complementary and combine to the generic case of Eq. (7.9).

7.2.3.2 In-situ Force Determination

Let us recall Eq. (7.9) and substitute for the interface forces $\mathbf{g}_2^\star$ the interface displacement $\mathbf{u}_2^\star$ with the matrix-inverse of the admittance of the test bench $\mathbf{Y}_{22}^{\mathrm{TB}}$, according to the last line of the system of Eq. (7.7):

$$\mathbf{f}_2^{\mathrm{eq}} = \left(\mathbf{Y}_{22}^{\mathrm{TB}}\right)^{-1} \mathbf{u}_2^\star + \left(\mathbf{Y}_{22}^{\mathrm{A}}\right)^{-1} \mathbf{u}_2^\star$$

The two inverted admittance terms can be collected as they together represent the interface impedance of the assembled subsystems A and TB. It follows naturally that one can determine equivalent forces directly from the admittance measured on the assembly:

$$\boxed{\mathbf{f}_2^{\mathrm{eq}} = \left(\mathbf{Y}_{22}^{\mathrm{ATB}}\right)^{-1} \mathbf{u}_2^\star} \tag{7.12}$$

This method has been introduced as the *in-situ* force determination method in [6, 10]. In fact it can be seen as the reverse of Eq. (7.5) but in this case it is written for a larger set of responses $\mathbf{u}_2$ instead of $\mathbf{u}_3$ and an assembly of the active component with the test bench is considered, rather than with the vehicle.

Other variants can be derived from Eq. (7.9) which is not covered here; see for more details [20]. The application in the following section will focus on two methods in particular: the blocked interface force and in-situ method.

7.3 Application to Steering Gear Vibrations

This section discusses the noise prediction of the steering gear (active component) into the interior of the vehicle (passive component). The steering gear is bolted at four connection point to the chassis, hence the interface problem is described by 24 DoFs. These are regarded as the dominant structure-borne transmission paths to the interior [18]. The response point of interest is a microphone positioned at the left driver's ear. All operational excitations result from a constant-speed steering manoeuvre from maximum left to right at a vehicle speed of 0 km/h.

The equivalent forces are determined on two test benches with different stiffness properties. Furthermore, the two methods require different measurement equipment. In the next section the two test benches and the corresponding measurement equipment are shortly described.

7.3.1 Design of Test Benches

Equation (7.8) suggests that the dynamic properties of the test bench influence the measured states $\mathbf{g}_2^\star$ and $\mathbf{u}_2^\star$. Nevertheless, by proper application of the described methodology, similar equivalent forces $\mathbf{f}_2^{\mathrm{eq}}$ should be obtained. Regardless of the chosen method, it is of great importance that the measured states have a significant signal-to-noise ratio (SNR).

Both test benches have four supports for the connection of the steering gear, bolted onto a rigid test table. The supports of the first test bench (TB1) are designed for maximum stiffness to ensure proper conditions for the *blocked interface force* method. Additionally the *in-situ* method is applied on TB1, although lower levels of accelerations (i.e. lower SNR) are expected due to the high stiffness. The second test bench (TB2) is designed to apply the *in-situ* force determination method. The supports of TB2 are more compliant than TB1, as can be observed from the receptance plots in Fig. 7.4. A more compliant test bench improves the SNR on $\mathbf{u}_2$ for both the admittance FRF measurements and the operational measurements.

Figure 7.5 shows a support of both test benches. Note that TB1 has a tri-axial force sensor clamped between the support and the steering gear, whereas TB2 has the steering gear mounted directly onto the support. In both cases all quantities (i.e. $\mathbf{g}_2^\star$ and $\mathbf{u}_2^\star$) are measured on the test bench side. Properties of both test benches are summarised in Table 7.1.

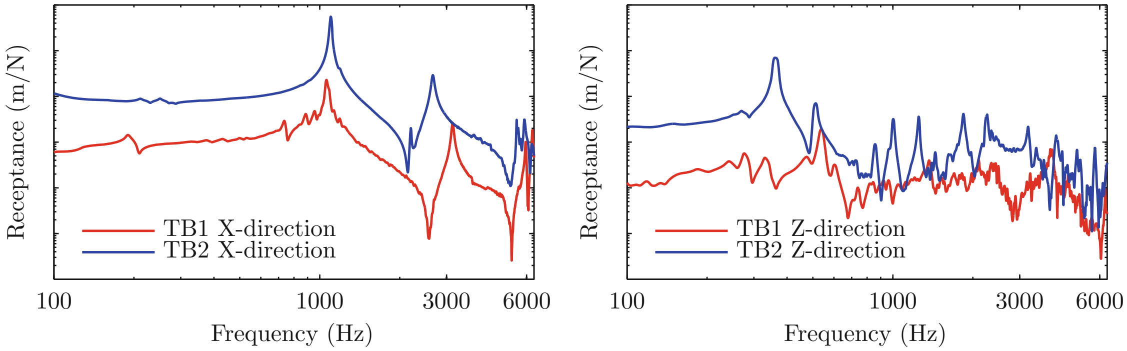

Fig. 7.4 The (displacement) receptance of the test benches in X-direction (*left*) and in Z-direction (*right*)

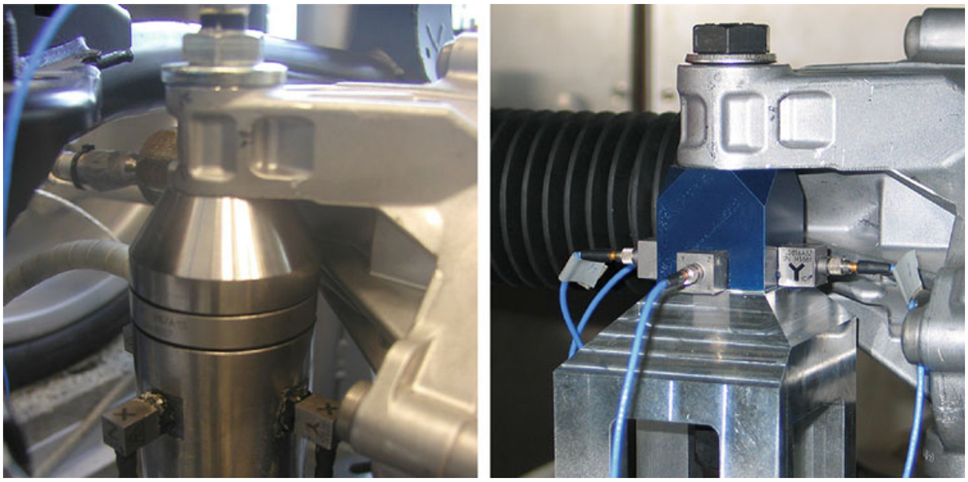

Fig. 7.5 A stiff support of the test bench TB1 (*left*) and a more compliant support of test bench TB2 (*right*)

Table 7.1 Properties of the two test benches

	Test bench 1	Test bench 2
Construction	Steel cylindrical supports	Aluminium asymmetrical supports
Measurement equipment	One tri-axial force sensor Four tri-axial accelerometers	Four tri-axial accelerometers
Eq. force method	Direct interface force (in-situ)	In-situ

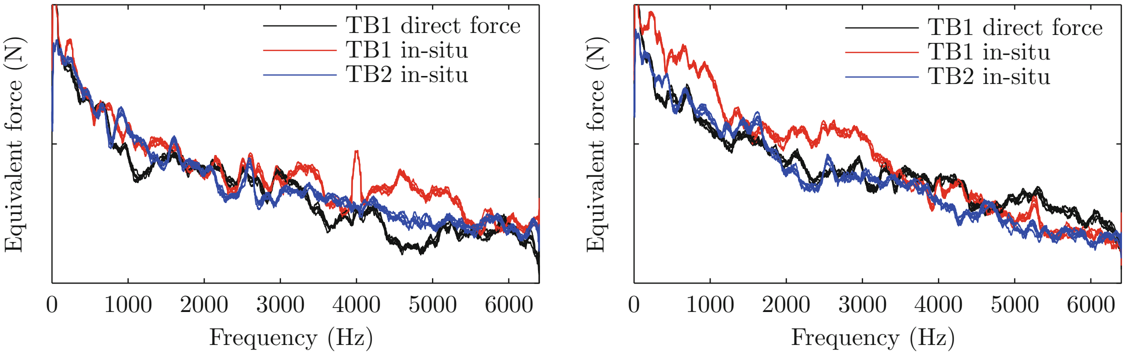

Fig. 7.6 The equivalent forces in X-direction (*left*) and in Z-direction (*right*) determined on the two test benches via the directly measured interface forces and the in-situ force determination method

7.3.2 Determination of Equivalent Forces

The equivalent forces are determined on both test-benches by application of the direct interface force method and the in-situ method. The measured interface forces are used directly as equivalent forces without further processing, as indicated by Eq. (7.10). The in-situ method however relies on a two-stage measurement to obtain the equivalent forces according to Eq. (7.12):

1. Determination of admittance FRFs $\mathbf{Y}_{22}^{\text{ATB}}$ on the passive assembly;
2. Measurement of interface accelerations $\mathbf{u}_2^\star$ with the EPS in operation.

All measurement equipment is equally located for both measurement phases. That means that accelerations measured during operational testing are at the same place as where the admittance FRFs correspond to, hence no transformation or mapping is needed. Concerning the equivalent forces however, it is needed to determine forces and moments that are compatible with the model of the vehicle. The virtual point transformation [19] was therefore used to transform the force side of the admittance $\mathbf{Y}_{22}^{\text{ATB}}$ to six virtual forces and moments in the centre of the connection. Therefore the in-situ set of $\mathbf{f}^{\text{eq}}$ in Eq. (7.12) is calculated in an over-determined manner, as for each support 12 acceleration channels are used to determine a total of six forces and moments.

Figure 7.6 shows the equivalent forces for the two test benches. Three series of five curves each are shown, obtained from repeated measurements. The series represent respectively $\mathbf{f}_2^{\text{eq}}$ as determined from:

Black line Blocked interface force from directly measured interface force $\mathbf{g}_2^\star$ on stiff TB1;
Red line In-situ force determination from measured accelerations $\mathbf{u}_2^\star$ on stiff TB1;
Blue line In-situ force determination from measured accelerations $\mathbf{u}_2^\star$ on compliant TB2.

Two methods are evaluated on the setup with the stiff test bench TB1. It was mentioned in Sect. 7.2.3 that the blocked interface force method constitutes a limit case, i.e. for an infinitely stiff boundary with zero interface displacement. However the in-situ method exists merely by the grace of flexibility, which is in contradiction with the former assumption. Note that therefore, strictly speaking, both methods cannot be true at the same time.

Apart from the fact that all methods follow roughly the same trend, several observations can be made. The direct forces on TB1 (black) in X-direction dive on three points clearly below the two in-situ determined force (red). This is due to the dynamics of TB1, which indeed exhibits flexibilities around e.g. 1,100 Hz. Compensation for test bench flexibility is possible in theory, but often results in an over-estimation of the equivalent forces [16]. The peak of the TB1 in-situ curve at 4,000 Hz can be assigned to the switching frequency of the external servo actuator needed to operate the steering gear; this caused a distortion on the accelerometer measurement channels.

Fig. 7.7 The prediction of the steering gear noise in at the left driver's ear in dB(A)

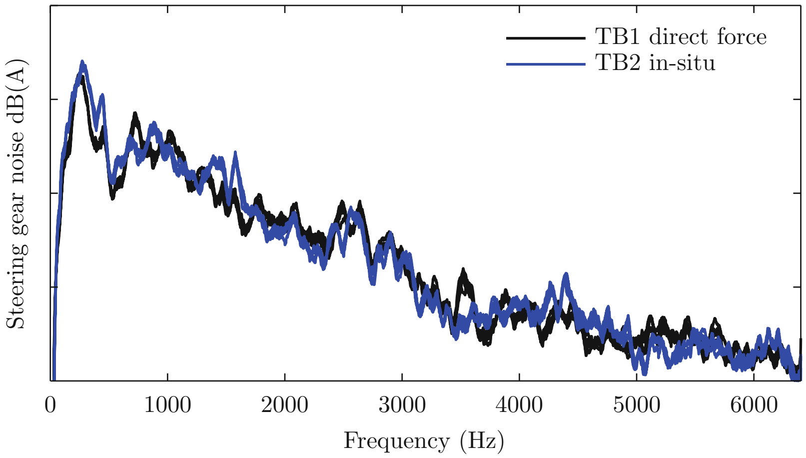

The in-situ forces in Z-direction of TB1 show a significant higher amplitude up to 3,500 Hz compared with the direct force measurement on TB1 and the in-situ method on TB2. This overestimation of the forces is due to the high stiffness of the total system in Z-direction, as was observed form Fig. 7.4. Acceleration levels are consequently in the noise range and, due to the inverse procedure of the in-situ method, measurement errors are amplified.

7.3.3 Prediction of Steering Gear Noise

The steering gear noise in the at the driver's left ear is synthesised in this section from the blocked interface forces on TB1 and the *in-situ* method on TB2. The prediction comprises a multiplication of the equivalent force spectra with the mechanical-acoustic total vehicle FRFs from the 24 interface DoFs to the response microphone according to Eq. (7.5). In Fig. 7.7 the A-weighted acoustic pressures are shown at the reference point of interest for the two methods. Some noteworthy observations:

- The synthesised acoustic pressures following from the two different equivalent force determination schemes *and* two different test benches are remarkably similar, even for high frequencies. This result shows that the equivalent forces determined on both test benches are independent from the test bench dynamics.
- The response up to 500 Hz determined with *in-situ* method is slightly higher than the directly measured forces. Over-estimation of the response in the low frequency band has been observed in earlier studies with matrix-inverse equivalent force determination schemes [20]. However various regularisation methods can be employed to improve matrix conditioning; see for instance [14, 15].
- The prediction from direct forces of TB1 is computed using translational forces only, as moments were not measurable with the available measurement equipment. Still, it is for the present case believed that a total of 12 translational forces are sufficient to synthesise a response. On the other hand, the predictions from in-situ methods are built from $4 \times 6 = 24$ DoFs, i.e. 12 translational forces *plus* 12 rotational moments. As those are determined from a matrix-inverse method, it is interesting to investigate if the operational excitation could also be represented by fewer degrees of freedom. Again, more insight could be gained from singular value decomposition of the equivalent force spectra or matrix regularisation.

7.4 Summary

Component TPA has been conducted for steering gear vibrations using two different test benches. Theoretically, test bench independent forces can be derived that represent the internal excitations of the steering gear. A comparison has been made between equivalent forces obtained from directly measured interface forces and from a matrix-inverse determination following the in-situ method. Both methods show similar results over the full bandwidth of 6 kHz. This confirms the theoretical assumption and demonstrates that the equivalent forces, if determined from a methodology that is appropriate for the test bench at hand, are indeed a property of the steering gear only.

Acknowledgements This research is supported and funded by the BMW Group.

References

1. de Klerk D (2009) Dynamic response characterization of complex systems through operational identification and dynamic substructuring. Ph.D. thesis, Delft University of Technology
2. de Klerk D, Rixen DJ (2010) Component transfer path analysis method with compensation for test bench dynamics. Mech Syst Signal Process 24(6):1693–1710
3. de Klerk D, Rixen DJ, Voormeeren SN (2008) A general framework for dynamic substructuring. History, review and classification of techniques. AIAA J 46(8):1169–1181
4. de Klerk D, Lohrmann M, Quickert M, Foken W (2009) Application of operational transfer path analysis on a classic car. In: DAGA, Rotterdam, 2009
5. Elliott AS, Moorhouse AT, Pavíc G (2007) Characterisation of a structure borne sound source using independent and in situ measurement. In: International congress on acoustics (ICA), Madrid, 2–7 Sept 2007
6. Elliott AS, Moorhouse AT, Huntley T, Tate S (2013) In-situ source path contribution analysis of structure borne road noise. J Sound Vib 332(24):6276–6295
7. Gardonio P, Brennan MJ (2002) On the origins and development of mobility and impedance methods in structural dynamics. J Sound Vib 249(3):557–573
8. Hixson EL (1961) Mechanical impedance and mobility. In: Harris CM, Crede CE (eds) Shock and vibration handbook, chapter 10, 1st edn. McGraw-Hill, New York, pp 1–59
9. Moorhouse AT, Gibbs BM (1993) Prediction of the structure-borne noise emission of a machines: development of a methodology. J Sound Vib 167(2):223–237
10. Moorhouse AT, Elliott AS, Evans TA (2009) In situ measurement of the blocked force of structure-borne sound sources. J Sound Vib 325(4–5): 679–685
11. Norton EL (1926) Design of finite networks for uniform frequency characteristic. Technical report, TM26-0-1860, Bell Laboratories
12. Plunt J (2005) Finding and fixing vehicle NVH problems with transfer path analysis. Sound Vib 39(11):12–17
13. Thévenin L (1883) Sur un nouveau théoreme d'électricité dynamique [On a new theorem of dynamic electricity]. CR des Séances de l'Académie des Sciences 97:159–161
14. Thite AN, Thompson DJ (2003) The quantification of structure-borne transmission paths by inverse methods. Part 1: improved singular value rejection methods. J Sound Vib 264(2):411–431
15. Thite AN, Thompson DJ (2003) The quantification of structure-borne transmission paths by inverse methods. Part 2: use of regularization techniques. J Sound Vib 264(2):433–451
16. van den Bosch DD, van der Seijs MV, de Klerk D (2014) Validation of blocked-force transfer path analysis with compensation for test bench dynamics. In: Proceedings of the 32th international modal analysis conference, Orlando. Society for Experimental Mechanics, Bethel
17. van der Auweraer H, Mas P, Dom S, Vecchio A, Janssens K, Van de Ponseele P (2007) Transfer path analysis in the critical path of vehicle refinement: the role of fast, hybrid and operational path analysis. Technical report, SAE International, 05 2007
18. van der Seijs MV, de Klerk D, Rixen DJ, Rahimi S (2013) Validation of current state frequency based substructuring technology for the characterisation of steering gear – vehicle interaction. In: Proceedings of the 31st international modal analysis conference, Los Angeles. Society for Experimental Mechanics, Bethel
19. van der Seijs MV, van den Bosch DD, Rixen DJ, de Klerk D (2013) An improved methodology for the virtual point transformation of measured frequency response functions in dynamic substructuring. In: Papadrakakis M, Papadopoulos V, Plevris V (eds) COMPDYN 2013 4th, ECCOMAS thematic conference on computational methods in structural dynamics and earthquake engineering, Kos Island, 12–14 June 2013
20. van der Seijs MV, Pasma EA, de Klerk D, Rixen DJ (2014) A robust transfer path analysis method for steering gear vibrations on a test bench. In: Proceedings of the international conference on noise and vibration engineering (ISMA 2014), Leuven, 17–19 Sept 2014
21. van Schothorst G, Boogaard MA, van der Poel GW, Rixen DJ (2012) Analysis of ground vibration transmission in high precision equipment by frequency based substructuring. In: Proceedings of the international conference on noise and vibration engineering (ISMA 2012), Leuven, Belgium, 15–17 Sept 2012

Chapter 8
Experimental Dynamic Substructuring of a Catalytic Converter System Using the Transmission Simulator Method

Matthew S. Allen and Daniel R. Roettgen

Abstract This paper contains an example of experimental substructuring using the transmission simulator method on an assembly of automotive catalytic converters. These structures could be challenging to model with finite elements because of uncertainties in the material properties of the catalytic converts and the joint between ceramic catalysts and metal housings. This system is of interest because it has a production joint that has been found to exhibit nonlinearity and linear modeling presented here will be a precursor to modeling the nonlinearity in the joint. The substructure being used is a single catalytic converter attached to a steel plate. A modal test was performed in order to obtain a model of the substructure. The substructure model was developed using elastic modes and rigid body modes that were analytically constructed from measured rigid body mass properties and extracted FRF test data. This substructure is replicated about the connection axis and coupled to itself to generate a model of the full system; this assumes that each catalytic converter is identical. The steel plate was attached to the substructure to serve as the transmission simulator, and thus was subtracted from the final assembly. The substructuring predictions from were then compared to a truth model which was derived from a modal test of a fully assembled system.

Keywords Experiment • MCFS • Dynamic substructuring • Transmission simulator • Exhaust system

8.1 Introduction

With the complexity of real world systems, it can be difficult to model the details of each part of the system and to properly account for connections between each part. Sometimes parts of the model are unknown, and sometimes they are too complicated the accurately model with reasonable effort. These situations lend themselves to dynamic substructuring. Dynamic substructuring allows for the pieces of a system to be analyzed, or measured, individually and then to be added together to determine the dynamic response of the full system. This paper contains a detailed example of dynamic substructuring on an assembly of off the shelf catalytic converters. The goal of this exercise is to provide an example of dynamic substructuring on a real world system using the transmission simulator method. This provides insight into the feasibility and limitations of this method in a real industrial setting, where finite element analysis models are not easily constructed. To complete this task multiple experiments were performed. The first is a modal test on a single catalytic converter attached to a steel plate which acts as a transmission simulator. The second is a pair of catalytic converters attached directly with use of a factory gasket seal.

The transmission simulator method was developed in the past decade to address issues when dealing with difficult to simulate the boundary conditions at the joint between subcomponents of a larger system. To simulate theses boundary conditions the transmission simulator acts to mass load and exercise these joint between subcomponents. This has been found to greatly increase the accuracy of dynamic substructuring over a more classical free-free modes approach. Additional details about the transmission simulator method including more examples can be found in [1–3].

M.S. Allen (✉)
Department of Engineering Physics, University of Wisconsin-Madison, 535 Engineering Research Building,
1500 Engineering Drive, Madison, WI 53706, USA
e-mail: msallen@engr.wisc.edu

D.R. Roettgen
Department of Engineering Physics, University of Wisconsin-Madison, 534 Engineering Research Building,
1500 Engineering Drive, Madison, WI 53706, USA
e-mail: droettgen@wisc.edu

M. Allen et al. (eds.), *Dynamics of Coupled Structures, Volume 4*, Conference Proceedings of the Society
for Experimental Mechanics Series, DOI 10.1007/978-3-319-15209-7_8

8.2 Test Objective and Methods

The objective of this exercise is to generate a full system model for a pair of catalytic converters, picture in Fig. 8.1, using the transmission simulator method. This mimics the problem of more practical interest, where substructuring would be used to develop a model for the upper part of the exhaust system including the engine and these two up-stream catalytic converters, including the compliance and nonlinear stiffness and damping of this full assembly. However, the engine was not available and so we simply seek to predict the response of the assembly shown below. These substructuring predictions will be compared to a "truth model" comprised of data from testing of the fully assembled system. The catalytic converters are connected by four bolts through the upper flanges of the system. From previous work [4], the frequency range of interest was defined as below 300 Hz and therefore frequencies up to 600 Hz were considered in the subcomponent models. After completing the modal testing the natural frequencies and damping ratios were extracted using the Algorithm of Mode Isolation (AMI) [5].

Tests were performed on two different structures: a subcomponent test was performed using just one catalytic converted attached to a transmission simulator, and a full assembly "truth" test was performed on the pair of converters shown in Fig. 8.1. A global coordinate scheme was used for both tests is also shown in Fig. 8.1 with the *z* direction pointing into the figure.

8.2.1 Subcomponent Test

The subcomponent consisted of the left hand catalytic converter from Fig. 8.1 and a steel plate used as the transmission simulator. The catalytic converter was instrumented with four pairs of uniaxial accelerometers. Each pair consisted of one accelerometer aligned with the global *x*-direction and one aligned with the global *z* direction. The transmission simulator was instrumented with two tri-axial accelerometers as well was two pairs of uniaxial accelerometers. Figure 8.2 shows the experimental set up for the substructure with the global *z* direction out of the page. Small metallic blocks were used to align the accelerometers into the global *xyz* coordinate system. A stick model showing the measured node locations is shown in Fig. 8.3.

The substructure was suspended using bungee cords to simulate free-free conditions as seen in Fig. 8.2. From [6] it is desired to have the largest rigid body mode to be at least ten times smaller than the first elastic mode in order to minimize error in the experiment. The lowest elastic mode occurred at 230 Hz and this system's rigid body modes were below 10 Hz so this condition was easily met.

The mass properties for the converter were obtained from the mass properties lab at Sandia National Labs and are presented in Table 8.1. These mass properties were determined assuming products of inertia were negligible and that the global coordinate system could be considered the principal coordinate system. Rigid body mode shapes were calculated

Fig. 8.1 Assembled catalytic converter system

Fig. 8.2 Subcomponent: single catalytic converter and transmission simulator

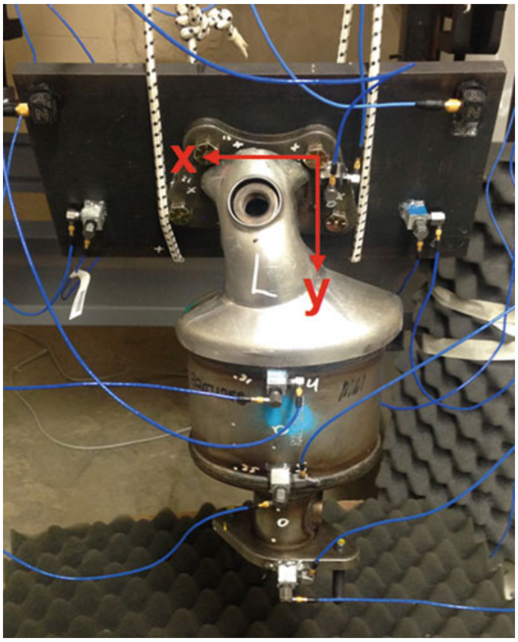

Fig. 8.3 Subcomponent stick model

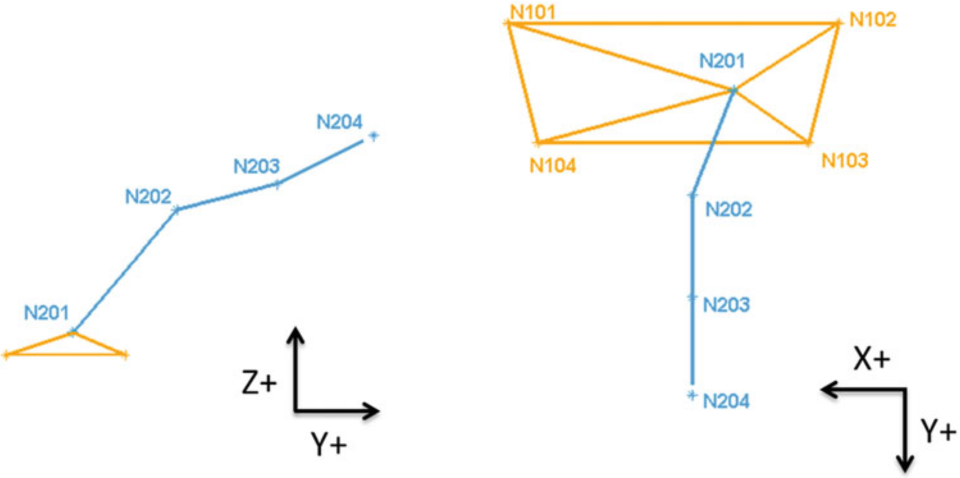

Table 8.1 Mass properties for subcomponent system

	Catalytic converter	Transmission simulator	Full subsystem
Mass [kg]	3.517	5.615	9.127
cg_x [m]	0.004	0.035	0.023
cg_y [m]	0.147	0.032	0.076
cg_z [m]	0.074	−0.011	0.013
I_{xx} [kg m^2]	0.03325	0.05525	0.12096
I_{yy} [kg m^2]	0.00036	0.00491	0.04058
I_{zz} [kg m^2]	0.01313	0.00453	0.11935

using the moments of inertia and center of gravity of the catalytic converter as well as the transmission simulator. The origin for these center of gravity measurements is the global coordinate system as labeled in for Fig. 8.2. The parallel axis theorem was used to combine these measured mass properties for the catalytic converter with the analytical mass properties for the transmission simulator. The transmission simulator mass properties were calculated using the mass of the part along with it's physical dimensions.

At low frequency the FRFs of a structure tend to a constant value caused by the sum of the rigid body modes, called mass lines. The mass lines generated from the mass properties in Table 8.1 can be compared to those extracted experimentally. When this was done, the mass lines constructed from the mass properties did not reproduce the mass lines of the experimental

Table 8.2 List of modes and descriptions for subcomponent test

Mode	Frequency [Hz]	Damping ratio ζ [%]	Description
1	0.00	1.00	*x* direction translation
2	0.00	1.00	*y* direction translation
3	0.00	1.00	*z* direction translation
4	0.00	1.00	rotation about *x*
5	0.00	1.00	rotation about *y*
6	0.00	1.00	rotation about *z*
7	230.49	0.519	1st bending
8	246.60	0.069	2nd bending
9	316.19	0.432	3rd bending
10	540.65	0.034	1st torsion
11	560.75	0.054	4th bending

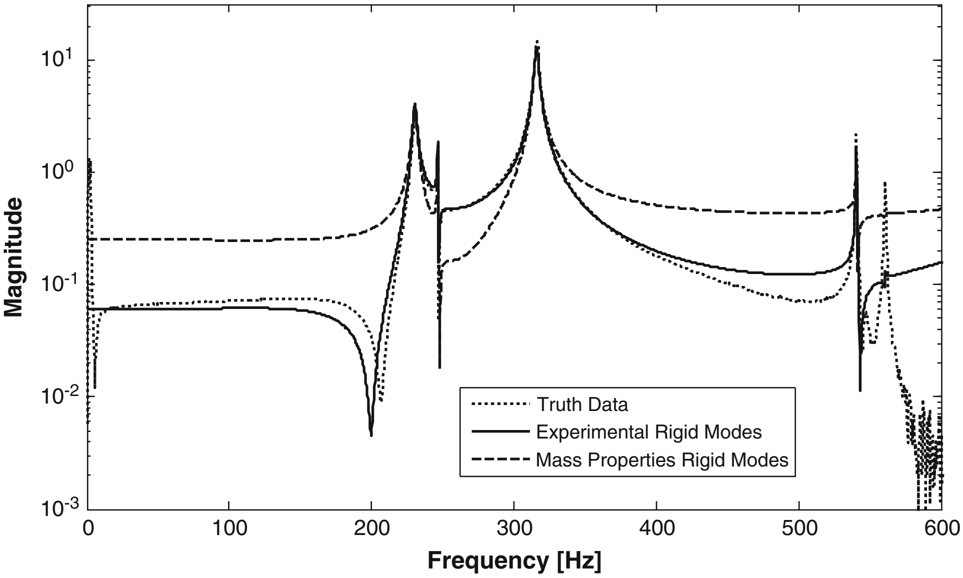

Fig. 8.4 Subcomponent FRF: [drive point 102-Z, response point 101-Z]

system and it was deduced this was due to missing product of inertia terms. In order to mitigate this error only the translational rigid body modes were used from the mass properties in Table 8.1. An alternative set of rotational rigid body modes were generated based on experimental data as detailed in Appendix 1.

The subsystem was excited with a modal impact hammer at several drive points in order to attempt to find the best location to excite each individual mode. Drive points were gathered both on the catalytic converter as well as the transmission simulator. Drive points on the catalytic converter were difficult to complete as it was difficult to hit in line with mounted accelerometers without risking the integrity of the measurement. Ultimately, the drive points on the transmission simulator yielded the best results, due to the difficulty of exciting at an appropriate location and in a precise direction on the catalytic converters.

The analytical rigid body modes were combined with five elastic modes extracted from this modal experiment. These modes are shown in Table 8.2. Drive points were taken at points 101, 102, 103, and 104 in the positive *z* direction as well as the *x* and *y* directions to generate the rotational rigid body modes. Figure 8.4 shows an FRF that provides a comparison of the truth data and the two ways of calculating the rigid body modes. From inspection it becomes obvious that the incomplete mass properties do no simulate the mass lines and rigid motion of the system very well.

8.2.2 Truth Test

With the subcomponent test complete a full system "truth" test was also conducted to be used as a baseline for the substructuring results. This truth test was completed using two catalytic converters pictured previously in Fig. 8.1. A stick model showing full system truth test node numbering is pictured in Fig. 8.5.

Fig. 8.5 Full system stick model

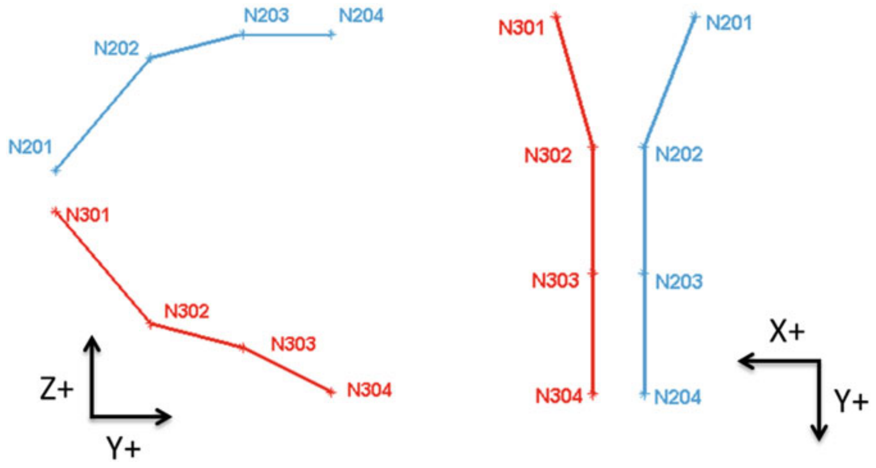

The full assembly system was excited at point 201 in the z direction, this allowed the structure to be hit in line with the accelerometer where this would have been more difficult at points on the catalytic converters bodies. Nine elastic modes were calculated to be compared with the substructuring predictions.

8.3 Substructuring Methodology

The transmission simulator method was utilized in order to assemble two copies of the experimentally derived model to estimate the modes of the full assembly as shown in Fig. 8.1. The second copy of this subsystem needs to be rotated 180° such that node 101 from the first copy will be constrained to node 102 of the second copy and vice versa. Table 8.3 contains the constrained degree of freedom pairs.

Note all of these points are located on the transmission simulator. With two copies of the subsystem included in the full assembly model two transmission simulators will need to be removed in order to complete the substructuring. The first elastic natural frequency of the transmission simulator was found to be 840 Hz. This frequency was beyond the bandwidth of interest so the transmission simulator was treated as rigid. A later exercise may be completed to add this mode into the system and see its impact on the substructuring results.

For the following calculations, the subscript A represents the first catalytic converter and transmission simulator pair with B representing the same system rotated 180°. The subscript C represents the fully assembled system and the subscript TS represents the transmission simulator. The modal parameters ω and ζ represent the natural frequencies and damping ratios of their respective subsystems and Φ represents the associated mode shapes. The physical degrees of freedom are represented by vectors denoted x and the modal degrees of freedom are denoted by vectors q. To begin, the system of equations is written in the standard mass-normalized modal representation of the equations of motion.

$$\begin{bmatrix} I_A & 0 & 0 \\ 0 & I_B & 0 \\ 0 & 0 & -2I_{TS} \end{bmatrix} \begin{Bmatrix} \ddot{q}_A \\ \ddot{q}_B \\ \ddot{q}_{TS} \end{Bmatrix} + \begin{bmatrix} {\omega_A}^2 & 0 & 0 \\ 0 & {\omega_B}^2 & 0 \\ 0 & 0 & -2{\omega_{TS}}^2 \end{bmatrix} \begin{Bmatrix} q_A \\ q_B \\ q_{TS} \end{Bmatrix} = \begin{Bmatrix} \Phi_A^T F_A \\ \Phi_B^T F_B \\ 2\Phi_{TS}^T F_{TS} \end{Bmatrix} \tag{8.1}$$

The following constraints between the physical displacements would enforce the connection between the two substructures. This equation only applies to the subset of degrees of freedom which act to connect the transmission simulator between substructures.

$$\begin{bmatrix} I & 0 & -I \\ 0 & I & -I \end{bmatrix} \begin{Bmatrix} x_A \\ x_B \\ x_{TS} \end{Bmatrix} = \begin{Bmatrix} 0 \\ 0 \\ 0 \end{Bmatrix} \tag{8.2}$$

Table 8.3 List of modes and descriptions for subsystem test

Subsystem 1 degree of freedom	Subsystem 2 degree of freedom
101 [*x*,*y*,*z*]	102 [*x*-,*y*,*z*-]
102 [*x*,*y*,*z*]	101 [*x*-,*y*,*z*-]
103 [*z*]	104 [*z*-]
104 [z]	103 [*z*-]

The constraint equation can then be rewritten in terms of modal coordinates as seen in Equation.

$$\begin{bmatrix} \Phi_A & 0 & -\Phi_{TS} \\ 0 & \Phi_B & -\Phi_{TS} \end{bmatrix} \begin{Bmatrix} q_A \\ q_B \\ q_{TS} \end{Bmatrix} = \begin{Bmatrix} 0 \\ 0 \\ 0 \end{Bmatrix} \tag{8.3}$$

In order to take advantage of the transmission simulator method, the constraints are now pre-multiplied by the pseudo-inverse of the transmission simulator mode shapes partitioned to the constraint degrees of freedom. This has the effect of constraining the estimated modal degrees of freedom of the TS to their projection on the A and B subcomponents.

$$\begin{bmatrix} \Phi_{TS}^{+} & 0 \\ 0 & \Phi_{TS}^{+} \end{bmatrix} \begin{bmatrix} \Phi_A & 0 & -\Phi_{TS} \\ 0 & \Phi_B & -\Phi_{TS} \end{bmatrix} \begin{Bmatrix} q_A \\ q_B \\ q_{TS} \end{Bmatrix} = \begin{Bmatrix} 0 \\ 0 \\ 0 \end{Bmatrix} \tag{8.4}$$

The rest of the steps are exactly as outlined in [1, 7]. The result is an estimate of modes of the assembly: ω_C, ζ_C and Φ_C.

8.4 Substructuring Results

The substructuring predictions will now be compared to the full assembly truth test briefly discussed previously in this paper. Comparisons of the frequencies, damping ratios are contained in Table 8.4. The Modal Assurance Criterion (MAC) between the “truth test' and the substructure predictions was also calculated and is contained in Table 8.4.

By inspection of Table 8.4 some trends can be identified. The first two elastic modes are more than 10 % off in frequency. Despite this the frequencies compare very well for some of the elastic modes (modes 9, 10 and 13). Damping proved harder to predict with errors as high as 95 %. The damping of the system was very light so small changes in damping ratio correspond to large changes in percent difference. The modal damping estimated in the truth or subcomponent tests varied up 15 % (e.g. a 10 % difference in ζ could correspond to damping ratios of 0.010 and 0.011) from one drive point to another. With such variation, larger errors in the damping predictions were expected. It was very difficult to get a good driving point on the subsystem which led to difficulty choosing one measurement over another.

Mode shapes were also correlated through MAC values and FRF reconstruction. A plot of the MAC values for the truth test shapes and substructured shapes is shown in Fig. 8.6. MAC values for the three rigid body translation modes correlated as expected. This verifies that the substructuring script is working since it is merely assembling the rigid body translation modes, and the rigid body modes that are predicted for the assembly are simply a sum of the mass properties of the two catalytic converters. The rotational modes did not correlate as well as the translational modes, but this was also expected as the mass properties used to generate full assembly rigid body modes were those mentioned earlier shown to have substantial error when comparing mass lines at the subcomponent level. Modes 7, 8, 10, and 12 also matched reasonably well but the MAC values for modes 9, 11, 13 and 14 were poor. The sensor set used was also limited so it proves difficult to distinguish all modes with such a small sensor set.

In addition to MAC correlation, mode shapes for the truth and substructured shapes were also visually compared. They are illustrated in the YZ and XZ planes in Fig. 8.7. In these modes shape plots the solid blue and red lines show the substructuring prediction representing the *A* and *B* catalytic converters respectively. The lines with markers are the truth test measurements and the dashed lines are the undeformed shapes of each converter.

In Fig. 8.7 the best match between the substructured and truth test modes appears in mode 7 which matches well with the calculated MAC values. For some of the more borderline MAC values, such as those in modes 8 and 10, visual comparison

Table 8.4 Substructuring results

	Truth test		Substructuring prediction					
Mode	Frequency [Hz]	Damping ratio [%]	Frequency [Hz]	Damping ratio [%]	Frequency % error	Damping ratio % error	MAC	Description
7	117.62	0.48	131.2	0.19	11.55	−59.45	.9850	Bending
8	235.05	0.43	203.34	0.44	−13.49	2.56	.6701	Torsion
9	245.18	0.12	246.84	0.08	0.68	−36.53	.4061	Torsion
10	251.78	0.24	250.37	0.11	−0.56	−52.90	.7930	Torsion
11	466.99	0.53	410.14	0.56	−12.17	6.13	.5811	Bending
12	510.56	0.85	542.34	0.04	6.22	−95.05	.7751	Bending
13	540.65	0.07	542.59	0.04	0.36	−44.79	.0089	Torsion
14	546.14	0.18	561.21	0.06	2.76	−66.19	.0014	Bending

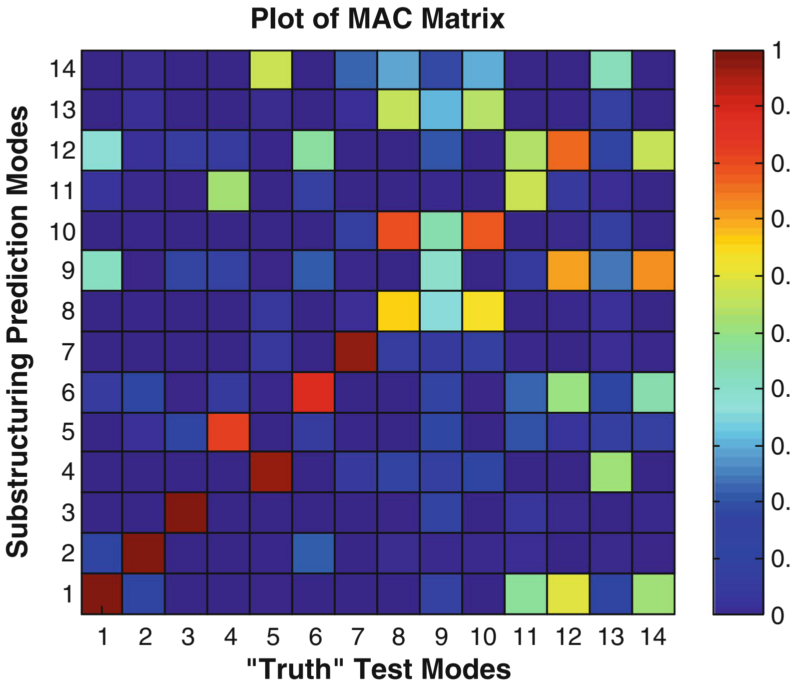

Fig. 8.6 Subsystem full system measurement degrees of freedom

of the mode shapes matched better than the MAC values would imply. For some the substructure seems to not have captured these mode shapes well (Modes 9, 13, and 14). These modes are predominantly torsional system modes and modes near the highest used sub-system frequency.

Often the purpose for performing substructuring is to estimate the response levels or strains at key points of interest. This was explored by reconstructing the FRFs at a few points and comparing them to the experimental test data. Three examples of reconstructed FRFs are shown in Figs. 8.8 and 8.9.

Figure 8.8 shows the drive point FRF for a strike and a measurement at location 201 in the *z* direction. Comparing this model to the measured truth data several more assessments can be made of the substructuring results. First, the mass lines match those of the experimental data fairly well. This indicates that the rigid body modes that were experimentally extracted from the single systems seem do predict those of the full assembly.

The prediction of the response for the elastic modes does not match the experimental data very well, but there is good qualitative agreement. The substructured mode shapes correctly assess the small response level for first elastic mode at the drive point as seen in Fig. 8.8. In contrast, a large response is correctly identified at point 203 as seen in Fig. 8.9. Both FRF plots show that the substructured model struggles to pick up the third elastic mode verifying the dissimilar mode shapes from Fig. 8.7 and the low MAC value for these modes. The predictions based on the substructuring results did not reconstruct the truth data perfectly, but one should bear in mind that on the first few iterations a finite element model would probably not provide a better prediction of the response, especially considering all of the uncertainties associated with the material

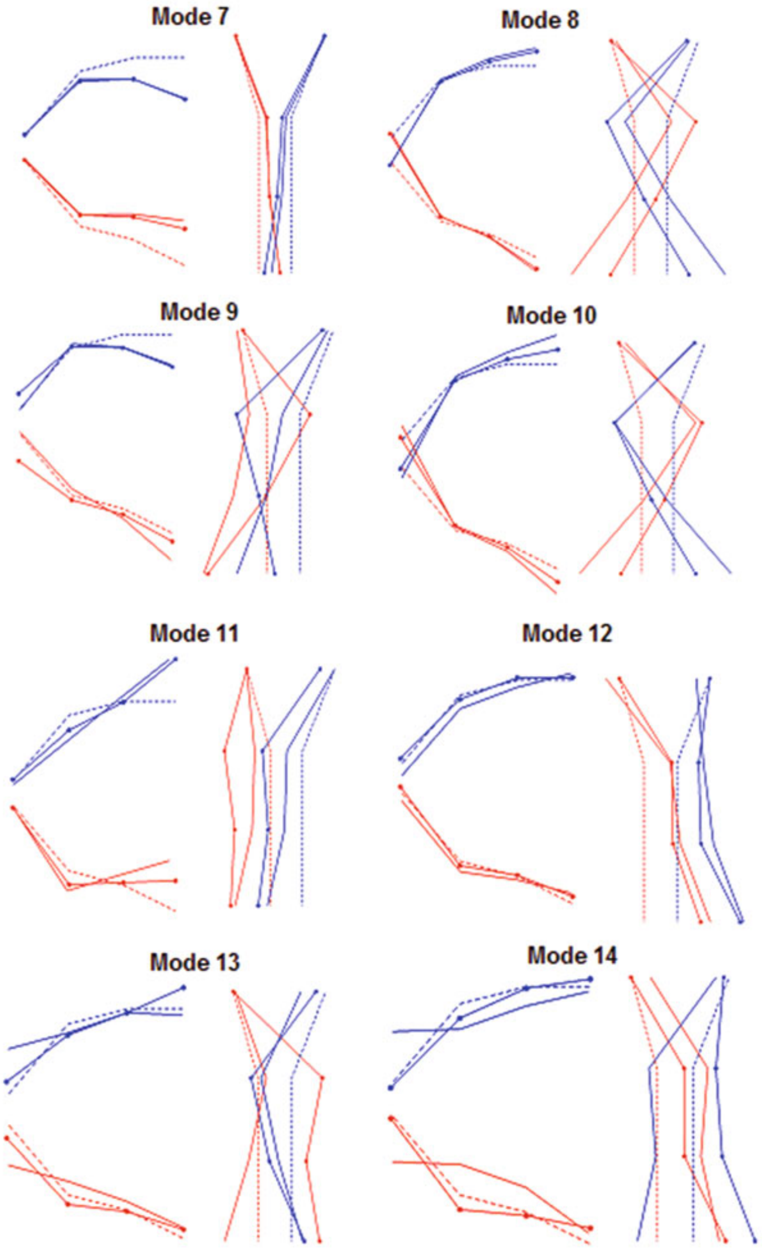

Fig. 8.7 Elastic mode shapes (*solid* – substructuring predictions, *solid with markers* – truth test, *dashed* – undeformed)

properties of the ceramic catalysts and the compliance of the joints in the system. Furthermore, the authors do not believe that these results represent the best that could be achieved with substructuring. The possible sources of error are discussed in the next section.

8.4.1 Possible Error Sources

Based on the errors seen in the substructuring predications some possible error sources were identified. Investigation and corrections of these sources may lead to an improved substructuring prediction for the fully assembled system. As mentioned previously, only one of the two catalytic converters was tested and it was assumed that the other was identical. In reality there are manufacturing tolerances that may cause differences. As a result, the substructuring results could give a better prediction of the response of an assembly of identical catalytic converters than the truth test did (although this is unlikely).

Fig. 8.8 FRF reconstruction: driving point 201Z, response point 201Z

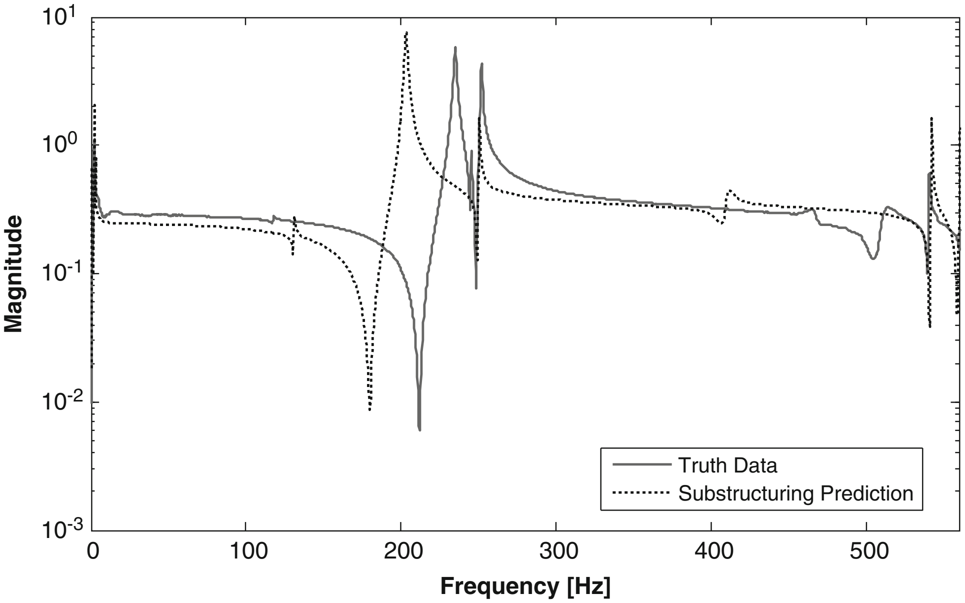

Fig. 8.9 FRF reconstruction: driving point 201Z, response point 203Z

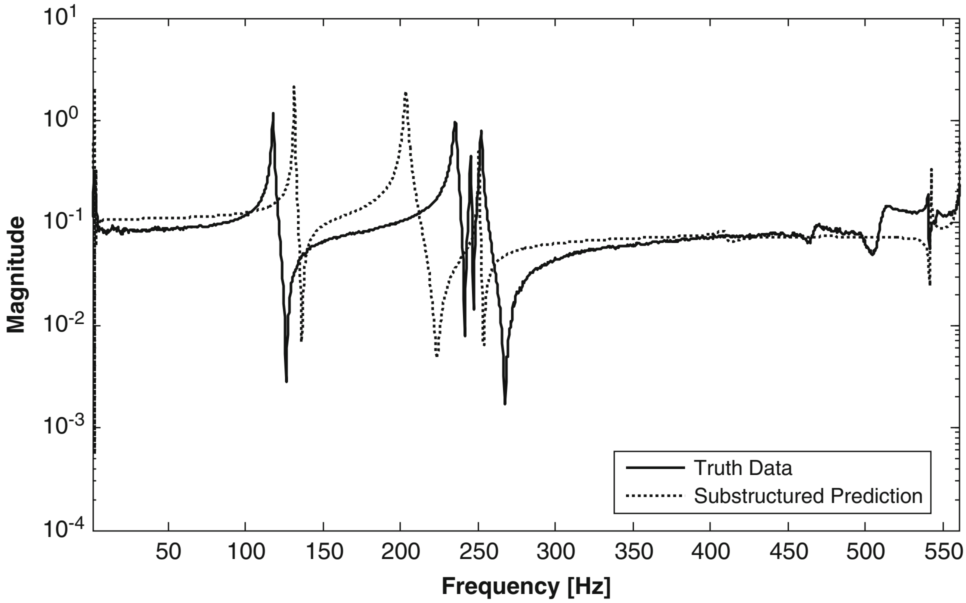

As mentioned above the mass properties originally used for the catalytic converter did not produce the correct mass lines of the subcomponent. Instead experimentally derived rigid body modes were used to simulate the system more accurately. The experiment was not set up to ideally capture these rigid body mode shapes. It was very difficult to get drive point excitations on the structure thus constructing these rigid body rotational modes from multiple drive points became difficult. The triangle method described in [8] could be used to create better drive point excitations. Furthermore, the accelerometers used were low sensitivity (to allow for high amplitude tests to evaluate nonlinearity) and were certainly not ideal for measuring rigid body motions. A more carefully designed experiment could be used to more accurately measure these rigid body modes and create a better subsystem model that may mitigate one potential error source. Appendix 2 explains the results of using the incorrect subsystem rigid body modes on our substructuring predictions.

Recall the largest MAC value deficiencies were observed in predominantly torsional modes. It is possible that the relatively poor results on the torsion modes arise because the subsystem measurements don't contain enough torsional motion. It may be useful to complete more subcomponent tests on the substructure to attempt to better excite the torsional modes and possibly include additional torsional modes in the subcomponent model. The bandwidth for the subcomponent experiment should probably be expanded to include additional modes and ensure all the data needed to predict these torsional modes is included.

Similarly, the transmission simulator was assumed to be rigid because the first elastic mode was outside the bandwidth of interest. Adding the first elastic mode of the transmission simulator to the substructure may provide additional information needed to bring down some of the errors seen in the substructuring predictions. This will require creating a finite element model for the transmission simulator and will be pursued in subsequent works.

8.5 Conclusions and Future Work

This effort created a substructuring prediction for an assembly of two catalytic converters by replicating and combing the results from a subcomponent modal test. The resulting substructuring prediction was then compared to an experiment conducted using two catalytic converters as a “truth test”.

After substructuring, the worst frequency error was observed to be 13.5 % although several of the modes were predicted quite accurately. The damping ratios were the more difficult to predict with error as high as 95 %. Mode shapes were compared using multiple methods. MAC values in the frequency bandwidth of interest ranged from as low as 0.4061 to as high as 0.985. For some of the questionable mode shapes visual matching show promising correlation between the substructured and truth mode shapes. With the largest MAC errors occurring predominantly in torsional modes it is possible that the frequency bandwidth was not adequate to describe the motions in the frequency range of interest. It was also observed that it was difficult to obtain good drive point measurements, so while the measurements were clean and could be curve fit easily, it was difficult to extract mode vectors that would correctly reconstruct the FRFs at all of the drive points. These substructuring predictions were not able to replicate the truth test perfectly but provided a qualitatively good estimate for the modes of interest and for the frequency response functions at several points, especially considering the time and effort that would be required to create and update a finite element model of comparable quality.

Acknowledgements This work was conducted/supported by Sandia National Laboratories. Sandia is a multi-program laboratory operated under Sandia Corporation, a Lockheed Martin Company, for the United States Department of Energy under Contract DE-AC04-94-AL85000.

Appendix 1: Alternate Rotational Rigid Body Mode Calculation

The large mismatch in mass lines when using the assumed mass properties, as seen in Fig. 8.4, led to the development of experimental rigid body rotational modes. This appendix details the calculation of these modes. The mass line for an FRF can be calculated as a sum of the six rigid body modes or residues for the FRF. This means the total mass line for an FRF can also be written as a sum of the translational mass lines and the rotational mass lines.

$$ML = \sum_{n=1}^{6} res_n \tag{8.5}$$

$$ML_{total} = ML_{translation} + ML_{rotation} \tag{8.6}$$

The translational mass lines can be calculated using the mass of the system leaving only three rotational mass lines to be solved for. These mass lines can be calculated as the translational mass lines (calculated analytically from a mass measurement) subtracted from the total mass lines (measured experimentally). This total set of mass lines can come from multiple drive point locations to ensure you excite all rotational rigid body modes and therefore account for all moments and products of inertia.

$$ML_{rotation} = ML_{total} - ML_{translation} \tag{8.7}$$

In order to calculate the rotational rigid body modes an eigen value problem for the rotational mass lines must be solved. The eigen values from this solution should be real and positive. Using the largest eigen values the approximate experimental rigid body modes are then calculated.

$$\phi_{rotation} = \frac{1}{\sqrt{\lambda}} ML_{rotation} \phi \tag{8.8}$$

These rigid body modes provided a much better match for the mass lines of the experimental subcomponent.

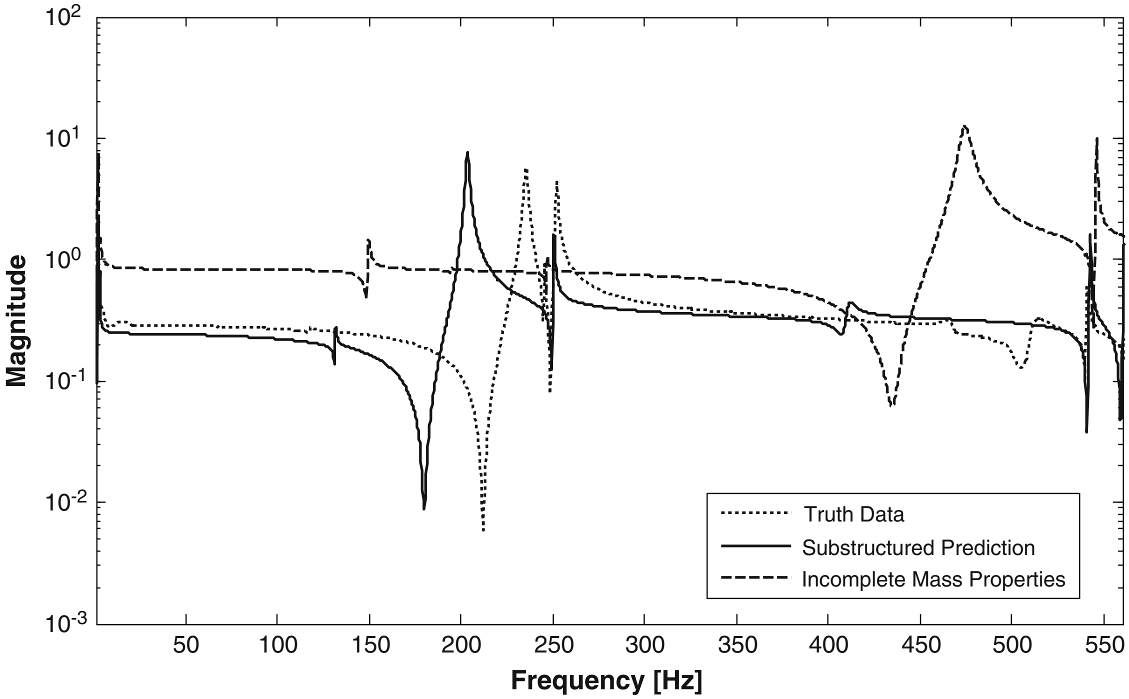

Fig. 8.10 Substructuring prediction FRF: driving point 201Z, response point 203Z

Appendix 2: Substructuring Prediction with Incomplete Mass Properties

As mentioned previously, incomplete mass properties led to errors in the subcomponent mass lines as displayed in Fig. 8.4. Matching these mass line is vital in order to obtain a quality substructuring prediction. Figure 8.10 shows an FRF reconstructed using both the incomplete mass properties and the experimentally derived rotational rigid body modes. Here the line in blue shows how the error effects not only the shapes but the frequencies that come out of in the substructuring prediction. In the displayed FRF the system's elastic modes are barley distinguishable above the rigid body mass line of the system which creates a poor prediction of mode shapes and frequencies. Checking the mass line of an experimental system with any rigid body modes created from mass properties is a good practice toavoid such errors.

References

1. Allen MS, Mayes RL, Bergman EJ (2010) Experimental modal substructuring to couple and uncouple substructures with flexible fixtures and multi-point connections. J Sound Vib 329:4891–4906. http://dx.doi.org/10.1016/j.jsv.2010.06.007
2. Mayes RL, Allen MS, Kammer DC (2013) Correcting indefinite mass matrices due to substructure uncoupling. J Sound Vib 332:5856–5866. http://dx.doi.org/10.1016/j.jsv.2013.05.025
3. Allen MS, Kammer DC, Mayes RL (2012) Metrics for diagnosing negative mass and stiffness when uncoupling experimental and analytical substructures. J Sound Vib 331:5435–5448. http://dx.doi.org/10.1016/j.jsv.2012.06.024
4. Roettgen DR, Allen MS, Osgood D, Gerger S (2014) Feasibility of describing joint nonlinearity in exhaust components with Modal Iwan models. In: Proceedings of the ASME 2014 international design engineering technical conference and computers and information in engineering conference. American Society of Mechanical Engineers
5. Allen MS, Ginsberg JH (2006) A global, Single-Input-Multi-Output (SIMO) implementation of the algorithm of mode isolation and applications to analytical and experimental data. Mech Syst Signal Process 20:1090–1111
6. Carne TG, Griffith DT, Casias ME (2007) Support conditions for experimental modal analysis. Sound Vib 41:10–16
7. Ginsberg JH (2001) Mechanical and structural vibrations: theory and applications. Wiley, New York
8. Schwarz B, Richardson M (2003) Scaling mode shapes obtained from operating data. In: International modal analysis conference XXI, Society for Experimental Mechanics (SEM), Curran Associates, Inc. (June 2007), Kissimmee, FL

Chapter 9
A Modal Craig-Bampton Substructure for Experiments, Analysis, Control and Specifications

Randall L. Mayes

Abstract This work was motivated by a desire to transform an experimental dynamic substructure derived using the transmission simulator method into the Craig-Bampton substructure form which could easily be coupled with a finite element code with the Craig-Bampton option. Near the middle of that derivation, a modal Craig-Bampton form emerges. The modal Craig-Bampton (MCB) form was found to have several useful properties. The MCB matrices separate the response into convenient partitions related to (1) the fixed boundary modes of the substructure (a diagonal partition), (2) the modes of the fixture it is mounted upon, (3) the coupling terms between the two sets of modes. Advantages of the MCB are addressed. (1) The impedance of the boundary condition for component testing, which is usually unknown, is quantified with simple terms. (2) The model is useful for shaker control in both single degree of freedom and multiple degree of freedom shaker control systems. (3) MCB provides an energy based framework for component specifications to reduce over-testing but still guarantee conservatism.

Keywords Experimental dynamic substructures • Substructuring • Craig Bampton • Shaker control • Six DOF shaker control • Environmental specifications • Energy methods

Nomenclature

CB	Craig-Bampton method of substructuring
CMIF	Complex mode indicator function
FE	Finite element model
MCB	Modal Craig-Bampton model form
TS	Transmission simulator – the fixture attached to the experimental substructure of interest
dof	Degree of freedom
sdof	Single degree of freedom
mdof	Multiple degree of freedom
p	Modal dof of the experimental substructure with fixed boundary
q	Modal dof of free modes extracted from experimental substructure with TS attached
s	Free modal dof of the transmission simulator
x	Physical displacement dof
ω	Frequency in radians per second
ζ	Modal damping ratio
K	Stiffness matrix
L_{fix}	Reduction matrix applying fixed boundary constraint to experimental equations of motion
M	Mass matrix
T	Transformation matrix to convert free modal model to modal CB model

---

Sandia National Laboratories is a multi-program laboratory managed and operated by Sandia Corporation a wholly owned subsidiary of Lockheed Martin Corporation, for the U.S. Department of Energy National Nuclear Security Administration under Contract DE-AC04-94AL85000.

R.L. Mayes (✉)
Experimental Mechanics, NDE and Model Validation Department, Sandia National Laboratories, P.O. Box 5800 – MS0557,
Albuquerque, NM 87185, USA
e-mail: rlmayes@sandia.gov

M. Allen et al. (eds.), *Dynamics of Coupled Structures, Volume 4*, Conference Proceedings of the Society
for Experimental Mechanics Series, DOI 10.1007/978-3-319-15209-7_9

Φ	Free mode shape matrix extracted for experimental substructure with TS attached
Ψ	Free mode shape matrix of the TS
Γ	Eigenvectors resulting from fixed boundary constraint of experimental equations of motion
b	Subscript for the fixture or boundary
fix	Subscript for the fixed boundary modes of the experimental substructure with TS as the boundary
$free$	Subscript for the free modes obtained in the modal test of the experimental substructure with TS
$+$	Superscript indicating the Moore-Penrose pseudo-inverse of a matrix

9.1 Introduction

The main value of this work comes as an accidental discovery in an investigation focused on experimental dynamic substructuring using the transmission simulator (TS) method [1]. The motivation of the work was to take the standard form of the TS method and convert it to a form that could be used as a standard Craig-Bampton substructure in FE codes. This is described more completely in another work [2]. After the associated theory was developed, the utility of the intermediate modal CB form was realized. In the modal CB form, the boundary degrees of freedom (dof) are characterized with generalized dof instead of the classic physical dof. In the method provided here, this can potentially provide a drastic reduction in the number of boundary dof with a mild cost in modal truncation error. The theory here utilizes a modal basis of free modes of the TS to quantify the boundary motion, but this is not a limitation, and it may be that other bases may be found that are more accurate.

For those who are not familiar with TS method, the TS is a fixture that is attached to the substructure of interest in exactly the same way as the complement of the real system will be attached, which might be modeled with FE or another experiment. The TS is instrumented with enough sensors to capture the motion adequately with a truncated set of modes to the desired frequency band. The TS instrumentation does not have to be located at every connection dof, and rotational dof are not required. However, the rotational and connection dof are inherently carried along in the modal dof of the TS. This method captures the stiffness and damping of the joint between the connected structures as well as the characteristics of the substructure of interest. All the measured dof on the TS are considered as part of the CB boundary dof, which leads to the utility to be discussed later.

In the following theory, it will be demonstrated that the experimental free modes model of the TS connected to the substructure of interest can be transformed to a matrix form called a modal CB. One partition of the stiffness, mass and damping matrices is diagonal. It is exactly the same as the standard CB form and accounts for the fixed boundary modes, where the TS fixture is considered the boundary. The other modal dof are associated with the motion of the TS. Coupling terms connect the two in some cases. The value here is that the motion of the substructure has been separated into the dof that strain the substructure, and the dof describing the motion of the base. This separation provides the capability to gain tremendous insight that is not possible when the motion of the boundary is described in standard physical coordinates. With this approach one acquires the following power directly from the analysis. (1) The effects of the impedance of the boundary are directly quantified, mode by mode. (2) The motion input to the boundary dof can be directly calculated to produce a desired substructure modal response (for example in sdof or mdof shaker control). (3) One can utilize the fixed base modal dof to specify energy based qualification testing for the substructure. This method drastically reduces the classic but unnecessary over-conservatism at many frequencies, but still theoretically guarantees conservatism at all frequencies of interest, which is not the case with current standard methodologies for dynamic testing.

Hereinafter is presented the theory of the transformation in Sect. 9.2, the value of the modal CB form for quantifying the uncertainty in the boundary condition (impedance) in Sect. 9.3, the value in sdof or mdof control in Sect. 9.4, and the value for superior qualification specifications in Sect. 9.5. Afterward are the conclusions in Sect. 9.6.

9.2 Theory

Consider an experimental substructure tested with the TS fixture attached. The test captures modal parameters for the free modes of the substructure and the attached TS fixture. It is desired to transform the experimental model to a modal CB form which contains fixed boundary modes for the substructure of interest, free modes of the fixture and coupling terms to connect the generalized dof. As an example, consider component A, the substructure of interest attached to a fixture, the TS, in Fig. 9.1. The test article would be instrumented according to the traditional TS method. The goal is to transform the

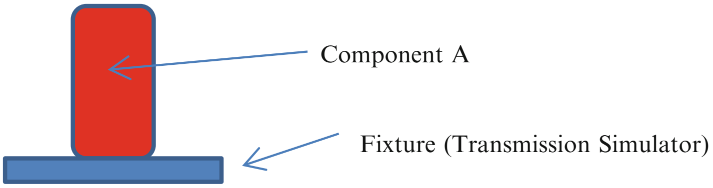

Fig. 9.1 Example component on test fixture

free mode test results to a modal CB form, which has useful properties that will then be examined. The free modal test will produce modal parameters associated with the q dof. After a transformation, the TS has free modal parameters associated with the s dof, and the motion of component A will be described with the fixed boundary modal dof p.

Generally, there is a FE model of the TS. The FE model is used in test planning to define measurement locations that will achieve independent mode shape measurements for all free modes of the TS slightly beyond the frequency band of interest. The TS fixture is thus instrumented. The transmission simulator hardware is attached to the experimental substructure and the free TS mode shapes are assumed to span the space of the fixture motion when connected to the experimental substructure. How well it spans the actual connection motion space affects the fidelity of the substructure model. The modal parameters from a free modal test of the experimental substructure with the TS attached can be used to produce the following equations of motion as

$$\left[\omega^2{}_{free} + j2\omega\omega_{free}\zeta_{free} - \omega^2 I\right]\overline{q} = 0 \tag{9.1}$$

where the subscript *free* represents the set of modes obtained from the experimental modal test. The subscript *free* is used because the structure is typically suspended by bungee cords or some very soft suspension whose mass, stiffness and damping are considered negligible. The mass-normalized mode shapes derived from the test will be contained in the measured mode shape matrix, Φ. For convenience, the rest of this derivation will drop the damping matrices, but they may easily be included. The goal is to derive a square matrix transformation, T, that will convert Eq. (9.1) to a modal CB form. Define the generalized coordinates, p, as the fixed-boundary modal coordinates and the generalized coordinates, s, as the coordinates that account for the motion of the TS, which is considered to be on the boundary of the experimental substructure as

$$\overline{q} = T\begin{Bmatrix} \overline{p} \\ \overline{s} \end{Bmatrix}. \tag{9.2}$$

First consider a constraint that ties the free TS to the tested structure. Use the modal approximations to set the motion of the experiment on the boundary (TS dof) to match the free modal motion of the TS as

$$\Phi_b\overline{q} \approx \Psi_b\overline{s} \tag{9.3}$$

where the subscript b dof will actually be a subset of the boundary dof where the measurements are made, Φ is the experimental mode shape and Ψ is the chosen truncated set of free modes of the TS. Ψ usually comes from a TS FE model, but could also be measured. Then the relation between q and s is

$$\overline{q} = \Phi_b^+\Psi_b\overline{s} \tag{9.4}$$

where the $+$ sign represents the Moore-Penrose pseudo inverse. This provides the right hand partition of the transformation, T, associated with the s dof.

To obtain the fixed boundary modal dof, p, describing the elastic motion of component A, fix the boundary dof with

$$\overline{x}_b = \Phi_b\overline{q} = 0. \tag{9.5}$$

Previous work [3] has shown that a practical way to accomplish Eq. (9.5) is to fix the TS dof with

$$\Psi_b^+\Phi_b\overline{q} = s = 0. \tag{9.6}$$

Using Rixen's primal assembly [4], the modal dof are replaced with

$$\overline{q} = L_{fix}\overline{\eta} \tag{9.7}$$

which is substituted back into Eq. (9.6) to obtain

$$\Psi_b^{+}\Phi_b L_{fix}\overline{\eta} = 0. \tag{9.8}$$

Since $\overline{\eta}$ can be many vectors, depending on the forcing motion, L_{fix} is chosen to guarantee satisfaction of the constraint as

$$L_{fix} = null\left(\Psi_b^{+}\Phi_b\right). \tag{9.9}$$

Pre and post-multiply Eq. (9.1) using the transformation L_{fix} appropriately to give

$$L_{fix}^{T}\left[\omega^{2}{}_{free} - \omega^{2}I\right]L_{fix}\overline{\eta} = 0. \tag{9.10}$$

Solve Eq. (9.10) to get the eigenvectors, Γ, and the eigenvalues to uncouple the dof, *p*. Then the relationship between *q* and the fixed boundary dof, *p*, is

$$\overline{q} = L_{fix}\Gamma\overline{p} \tag{9.11}$$

which provides the rest of the transformation. *T* is written from Eq. (9.4) and (9.11) as

$$T = \left[L_{fix}\Gamma \;\; \Phi_b^{+}\Psi_b\right]. \tag{9.12}$$

Pre multiplying Eq. (9.1) by the transpose of *T* and substituting Eq. (9.2) into Eq. (9.1) for *q* yields the following transformed equations of motion for free vibration

$$\left[\begin{bmatrix} {}^{\backprime}\omega^{2}_{fix\backslash} & K_{ps} \\ K_{ps}^{T} & K_{ss} \end{bmatrix} - \omega^{2}\begin{bmatrix} I & M_{ps} \\ M_{ps}^{T} & M_{ss} \end{bmatrix}\right]\begin{Bmatrix} \overline{p} \\ \overline{s} \end{Bmatrix} = 0 \tag{9.13}$$

for which the eigenvalue and eigenvector solution have not changed from Eq. (9.1). It has exactly as many dof as Eq. (9.1), but now they have been transformed to the fixed base modes associated with *p* and the free TS modes which were on the boundary as modal dof *s*. The upper left portion of the matrices is diagonal. Now there are coupling terms between the fixed base modes and the free TS motion. Considering the upper partition of Eq. (9.13) and moving the boundary TS dof, *s*, to the right hand side develops equations of motion from enforced boundary motion as

$$\left[\left[{}^{\backprime}\omega^{2}_{fix\backslash}\right] - \omega^{2}\left[I\right]\right]\{\overline{p}\} = \left[\left[0 \; -K_{ps_e}\right] + \omega^{2}\left[M_{ps_{rb}} \;\; M_{ps_e}\right]\right]\begin{Bmatrix} \overline{s}_{rb} \\ \overline{s}_{e} \end{Bmatrix} \tag{9.14}$$

where the *e* subscript is associated with the free elastic modes of the TS structure and the *rb* subscript is associated with the free rigid body modes of the TS structure. Notice that there is no coupling of the *p* dof with the s_{rb} dof through stiffness but there is coupling through mass terms. The *p* dof are coupled with the elastic s_e dof through both stiffness and mass terms. In general there are many *p*, six s_{rb}, and many s_e dof. For discussion purposes let us assume there is only one s_{rb} dof and one s_e dof. Since the left hand side is uncoupled, we can consider the scalar equation of motion for the very first *p* dof as

$$\left(\omega^{2}_{fixed\_1} - \omega^{2}\right)p_{1} = \omega^{2}m_{rb\_1}s_{rb\_1} + \left(-k_{e\_1} + \omega^{2}m_{e\_1}\right)s_{e\_1}. \tag{9.15}$$

Equation (9.15) determines how much elastic modal dof p_1 is excited by enforce rigid body motion and elastic motion of the TS.

9.3 Value of the Modal CB Form for Removing Uncertainty in the Boundary Condition

Suppose one performs a free modal test of the structure in Fig. 9.1, has a FE model of the fixture, and transforms the results of Eq. (9.1) into the modal CB form as in Eq. (9.14). One might also achieve the results of Eq. (9.14) with a modal model derived from a FE model of component A and the fixture. Such a model conveniently quantifies the effect of the boundary condition (the fixture) on the elastic motion of a substructure such as component A. Consider one mode of component A in Eq. (9.15). The elastic motion of component A characterized by generalized dof p_1 is influenced by each TS rigid body modal dof times its mass coupling term, which is classically called the modal participation factor [3]. In addition, mode p_1 is influenced by the elastic motion of each mode of the TS multiplied by both a stiffness and a mass coupling term. This immediately describes the impedance effects of the TS on component A on a mode by mode basis. All of these mass, stiffness and damping coupling terms come directly from the transformation that is applied to the free modal model of component A attached to the fixture (TS). This quantification removes the uncertainty associated with the boundary condition that has clouded virtually all component qualification testing.

It was observed by Savoie [4] that if a similar transformation were applied not only to component A with the TS as its vibration/shock testing fixture, but also to component A with the TS as the FIELD SYSTEM, the impedance effects could be directly compared between field environment and ground test to see how different they are. Many times there is a FE of the rest of the system that could be used as the TS. This difference between the field and test boundary conditions has always been a massive uncertainty using traditional methods of qualification specification and testing. In addition, environments engineers have related stories of overtesting of components at certain resonant frequencies associated with elastic modes of the fixture, s_{e_k}, which were not experienced in the actual field environment.

The reasoning in the paragraph above also suggests that we can quantify the quality of the test fixture in replicating the boundary conditions for the next higher level assembly. Future work could explore improving fixture design as well as test specification tailored to the different test fixtures used in qualification (e.g. different vibration fixtures for different axes, shock fixtures, etc.) [4].

9.4 Value of the Modal CB Form for Vibration Control in SDOF or MDOF Tests

Equation (9.14) could also be very useful from the standpoint of vibration control for testing of component A. The ideal fixture for shock or vibration control in qualification of a substructure like component A would be rigid, having only s_{rb} terms and no elastic s_e terms like the one shown in Eq. (9.15). Then one could excite the associated p_i terms exactly as desired by controlling the rigid body motion of the fixture and knowing the modal participation factors. This applies to the standard sdof (one translation direction) excitation as well as emerging mdof (e.g. 3 dof or 6 dof) shaker control. Unfortunately, there are usually elastic fixture modes in the bandwidth of interest. For sdof control, usually only one s_{rb} term (for one desired direction) is excited by the shaker, but there will also be elastic s_e terms excited. Using the modal CB model, one can see how much excitation of p_i comes from the desired rigid body fixture motion AND how much excitation comes from elastic motion of the fixture. Over-excitation of a particular p_i of component A due to elastic fixture modes can be remedied with this knowledge.

There is also the possibility of identifying uncontrollable input. For example, in a sdof shaker, the terms of the right hand side may add in such a way to produce a near zero value at some frequency. For a sdof shaker, all the s terms will be proportional to the input, i.e., the ratio of one s term to another is always the same. No matter what control algorithm is used, one will not have any control at this frequency. Nonlinearities in the system may produce undesired motion at this frequency. This formulation can warn the vibration engineer that there is danger of an uncontrollable frequency regime.

9.5 Value of the Modal CB Form as a New Paradigm for Qualification Specifications in the Energy Domain

At Sandia National Laboratories, energy methods are being used for quantification of environmental margin of components, such as component A. Edwards [5] has shown how such a method can predict the damaging energy absorbed by a test article subject to random vibration. Damage is generally induced in a component by elastic motion, not rigid body motion. Standard environmental specifications do not distinguish the rigid body motion from the elastic motion, i.e. these motions are confounded in the specification. A great advantage of the modal CB method is that it conveniently quantifies ONLY the damaging elastic motion with the generalized p dof, the motion of true interest for qualification. Based on Eqs. (9.14, 9.15) the amount of strain, dissipative or kinetic energy in the substructure may be determined for any specific mode as

$$SE = 1/2\omega_{fixed\_i}^2 p_i^2 \tag{9.16}$$

$$DE = \int 2\zeta_i \omega_{fixed\_i}\, \dot{p}_i\, p_i\, dp_i \tag{9.17}$$

$$KE = 1/2\dot{p}_i^2 \tag{9.18}$$

where *SE* is strain energy, *DE* is dissipative energy and *KE* is kinetic energy. To specify environments, one could quantify them in terms of these values. For example, if an environment causes a failure by strain, one could determine the maximum strain from an environment in each of the p modes. Uncertainty in the fixed base natural frequency could be included in Monte Carlo or other statistical analyses to determine the maximum SE that might be achieved in any subsystem for the environments being considered and a specification for the vibration or shock testing written based on each p. This would then be guaranteed to be conservative, unlike current acceleration frequency based specifications in a uniaxial direction. It has been shown for certain cases that the rate of fatigue damage is increased over uniaxial random input by a factor of two with more realistic three axis excitation [6]. However, the over-conservatism in many frequency lines of current acceleration frequency based specifications would be removed using energy methods with the fixed boundary modal dof. Equation (9.14) could then be used in the vibration test to perform the control for the qualification test.

Future work might also bring another enhancement to this model. Suppose there are some p_i dof that have no relevant contribution to the failure modes of component A. If even some of those can be identified, their effect could be minimized, or possibly even removed from the qualification specification [4].

9.6 Conclusions

The modal CB form conveniently separates the elastic response of the substructure of interest from the modal dof response of the structure that it is mounted upon, the TS. Simple coefficients relate the substructure response mode to the modal motion of the TS. The TS can be a test fixture, or it can be the entire system upon which the substructure is mounted. The differences in impedance between a test fixture and the field system can be quantified, which would introduce a new capability. The modal dof of the fixture can be used directly in establishing control parameters to excite the substructure in vibration or shock testing. This is of value for either traditional sdof input testing or emerging mdof testing capabilities. It is suggested that the energy methods, sometimes used in margin quantification, could be utilized with this modal CB form to specify environments in a way that guarantees conservatism, but reduces traditional over-conservatism in many frequency bands by a large margin.

Acknowledgments Notice: This manuscript has been authored by Sandia Corporation under Contract No. DE-AC04-94AL85000 with the U.S. Department of Energy. The United States Government retains and the publisher, by accepting the article for publication, acknowledges that the United States Government retains a non-exclusive, paid-up, irrevocable, world-wide license to publish or reproduce the published form of this manuscript, or allow others to do so, for United States Government purposes.

References

1. Allen MS, Mayes RL, Bergman EJ (2010) Experimental modal substructuring to couple and uncouple substructures with flexible fixtures and multi-point connections. J Sound Vib 329:4891–4906
2. Mayes RL (2015) A Craig-Bampton experimental dynamic substructure using the transmission simulator method. In: Proceedings of the 33rd international modal analysis conference, Orlando, February 2015, paper number 353
3. FEMA 451B Topic 4 notes. http://www.ce.memphis.edu/7119/fema_notes.htm
4. Technical discussion with Troy Savoie, SNLA, about the utility of the modal CB for environmental specifications, March–October 2014
5. Edwards TS (2009) Power delivered to mechanical systems by random vibrations. Shock Vib 16(3):261–271
6. Himelblau H, Hine MJ (1995) Effects of triaxial and uniaxial random excitation on the vibration response and fatigue damage of typical spacecraft hardware. In: Proceedings of the 66th shock and vibration symposium, Arlington

Chapter 10
A Comparison of the Dynamic Behavior of Three Sets of the Ampair 600 Wind Turbine

Andreas Linderholt, Thomas Abrahamsson, Anders Johansson, Daniel Steinepreis, and Pascal Reuss

Abstract The Ampair 600 wind turbine assembly has been modified to suit as a benchmark structure in the pursuit of finding best practices for experimental substructure coupling of structural dynamic systems. Seven such systems have been assembled in test laboratories in Europe and in the USA. We scrutinize the dynamic behavior of the total assembly of three of those by vibration testing and compare the test outcome from seemingly identical assemblies. The aim is to support future component synthesis activities with high fidelity data and support future model validation. Comparisons are made by evaluating deviations of measured frequency response functions, the differences of identified structural eigenfrequencies and the correlation between eigenvector estimates. The testing is made in two parts. First, a partly assembled system, not including the hub and blades, is tested. This constitutes one possible and logical subsystem splitting that is likely to appear in future substructure synthesis efforts. In the second part, the full system assembly is tested. The test procedure, the test setup, the obtained test data and test data statistics are presented.

Keywords Ampair 600 wind turbine • Substructuring • Model calibration • Manufacturing spread • Vibrational tests

10.1 Introduction

A production sequence will always contain uncertainties, causing a spread in dynamic properties between individuals in a produced population. This spread stems from a variety of sources, such as material spread, production process variability and finite precision in the assembly of components. In order to make qualified predictions on system modifications, quantification of such spread in seemingly equal systems is important [1]. Here, such variations are captured by vibrational data stemming from tests made on three individuals.

The SEM Substructuring Focus Group has chosen the Ampair 600 W (A600) wind turbine [2], shown in Fig. 10.1, as a benchmark test bed for studies of substructuring. Since its introduction at IMAC XXX [3], such studies have been carried out by several institutes in a number of countries, e.g. [4–6]. This study will focus on three A600 wind turbines. One is situated at Linnaeus University in Växjö and another at Chalmers University of Technology in Göteborg; both in Sweden. The third system is at the University of Stuttgart, Germany. The systems are tested in two configurations; the system without the hub and the blades as well as the complete wind turbine test bed. The reason for this is that the hub together with blades and the remaining system form two natural subsystems to be used in future substructuring exercises.

Previous measurements of the system have been made by Dan Rohe at the University of Wisconsin-Madison and at Sandia National Laboratories [7]. A lot of test data are shared on the SEM's focus group wiki page [8].

A. Linderholt (✉)
Department of Mechanical Engineering, Linnaeus University, Växjö, Sweden
e-mail: andreas.linderholt@lnu.se

T. Abrahamsson • A. Johansson
Department of Applied Mechanics, Chalmers University of Technology, Göteborg 41296, Sweden

D. Steinepreis • P. Reuss
Institute of Applied and Experimental Mechanics, University of Stuttgart, Pfaffenwaldring 9, Stuttgart 70550, Germany

M. Allen et al. (eds.), *Dynamics of Coupled Structures, Volume 4*, Conference Proceedings of the Society for Experimental Mechanics Series, DOI 10.1007/978-3-319-15209-7_10

Fig. 10.1 The Ampair 600 W turbine (Source: http://www.ampair.com/)

Table 10.1 The masses of the components building up the wind turbines tested

Component	LNU	Chalmers	Universität Stuttgart
Foot	110	N/A	N/A
Pole	3.20	N/A	3.19
Foot-pole connection	0.37	N/A	
Housing-pole-connection	2.90	N/A	
Housing without cover		7.55	2.75
Disk inside the housing	4.76		4.74
Housing cover with screws	0.88	0.89	0.87
Fin with screws	3.50	3.49	3.45
Hub	3.60	3.71	3.68
Blades	2.44	2.45	2.43

10.2 Tests on Three A600 Wind Turbines

Vibrational tests were made on one A600 system at each of Linnaeus University (LNU), Chalmers University of Technology, and University of Stuttgart. Several single input/multiple output (SIMO) stepped sine tests were made at LNU and Chalmers. The excitation frequencies span from 2.025 to 1,000 Hz and constant frequency steps of 0.025 Hz were used for all the tests. At Linnaeus University, an LMS measurement system together with a modal shaker, 2025E, was used for excitation. Furthermore, an impedance head, PCB 288D01, a triaxial accelerometer, PCB T356A16, and several single axial accelerometers, PCB 352A56, were used for sensing. Chalmers used a National Instruments PXIe rack mounted measurement system running in-house Matlab code, a Brüel and Kjær force transducer type 8203 and single axial PCB accelerometers of type 352C22 everywhere but at the baseplate, where type 333B32 was used instead. At Stuttgart, impact tests were made using an LMS measurement system, two triaxial accelerometers, PCB 356A24/NC and an impulse hammer, Kistler 9722 A500. Only the frequencies up to 400 Hz are reported in this paper. The masses of some components for the three systems are shown in Table 10.1.

10.2.1 *Partly Assembled Systems*

The first configuration that is tested is a partly assembled system consisting of the wind turbine structure without the hub and the blades. For this configuration, 24 degrees of freedom distributed at 18 points on the structure are measured. Four single axis sensors, measuring in the z-direction, are positioned at points 1–4 along the *x*- and *y*-axes (positive and negative directions) 25 mm from the edge. Four points (5–8) are defined on the pole at 100, 550, 1,000, 1,450 mm above the foot's surface and measurements are made in the *x*- and *y*-directions. On the A600 fin, five measurement points (9–13) are defined where lines drawn 15 mm from the edges cross each other; measurements in the *y*-direction are made here. Four points (14–17) are defined on the housing cover at all the combinations of ±60 mm in the *x*- and *y*-directions; here the accelerations in the *x*-direction are measured. In addition, measurements in the x-, y- and z-directions are made on the center of the housing cover (point 18). In practice, the measurements are made on a small aluminum cube attached to a pin bolt. As suspension, the rubber parts of four Cobra 6-in. dia. rubber plungers are used at LNU and Chalmers. At Stuttgart, the structure was supported on wheels, see Fig. 10.3c. Five of the defined dofs are also used, one at the time, for excitation. The measurement points together with the coordinate system and suspension used are shown in Fig. 10.2. Some pictures of a test made at LNU, where the excitation is on point 18 (the aluminum cube) in the negative Z-direction are shown in Fig. 10.3.

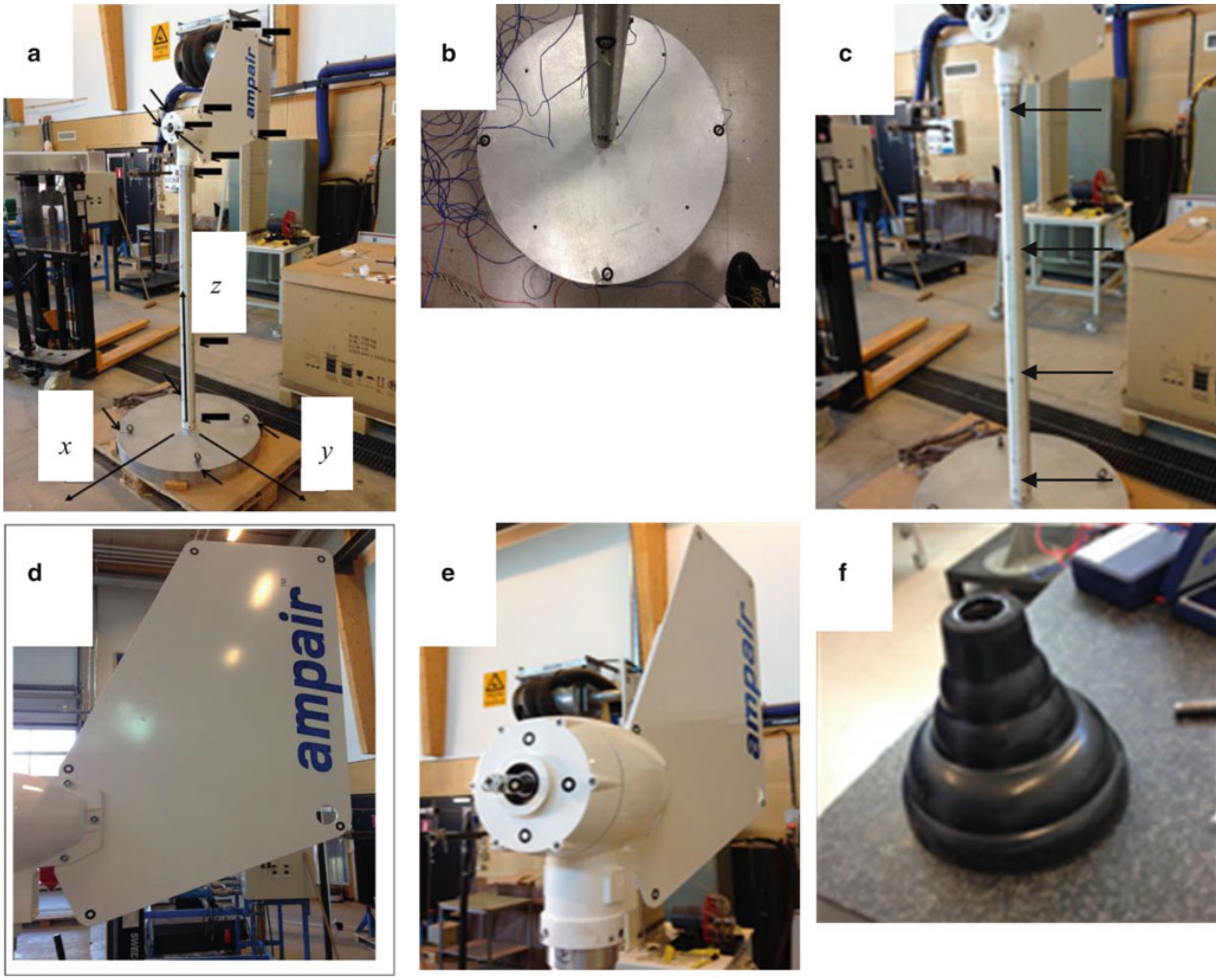

Fig. 10.2 (**a**) The coordinate system and the measurement points on the partly assembled system. (**b**) Four points on the foot; measurements in the z-direction. (**c**) Measurements in the x- and y-directions at four positions on the pole. (**d**) Measurements in the y-direction at five positions on the original (large) fin. (**e**) Measurements in the x-direction in four positions surrounding the center (at the shaft's hole) of the housing cover together with measurements in three directions on a cube mounted on the shaft positions. (**f**) One of four plungers used for suspension

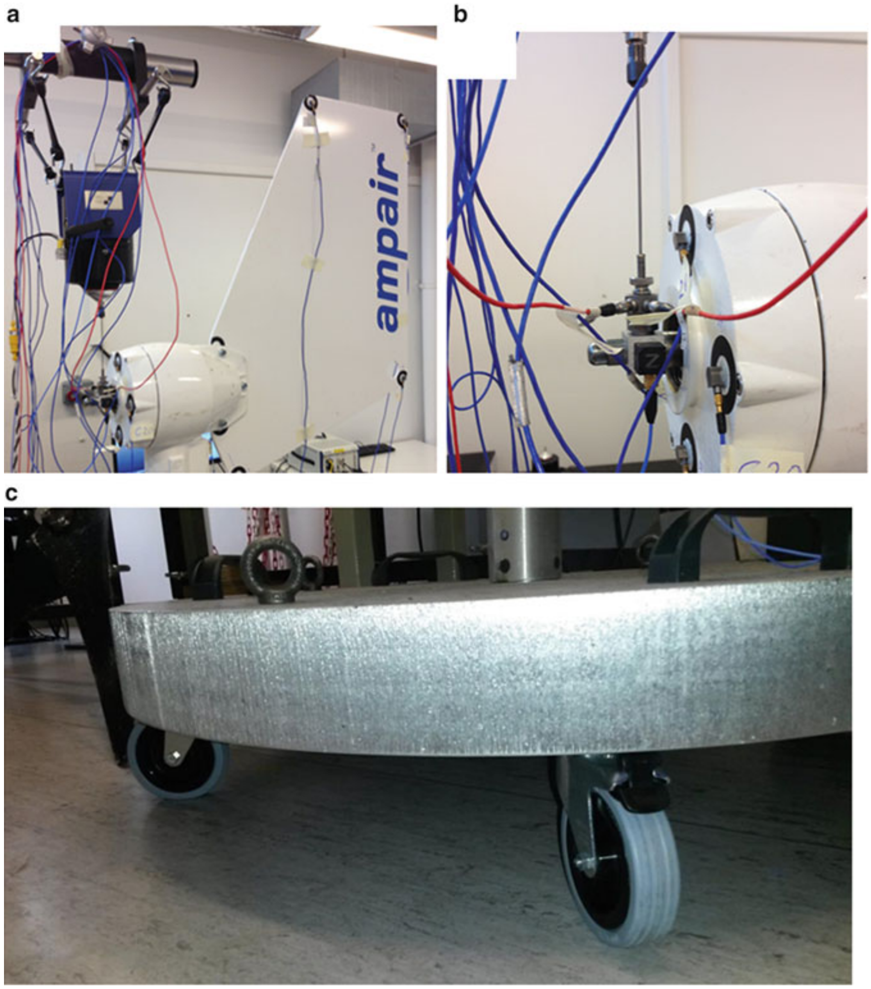

Fig. 10.3 (**a**) and (**b**) excitation on point 18, in the negative z-direction, on the partly assembled structure without hub and blades. The excitation is made on an aluminum cube added to the structure. The pictures are taken at LNU. (**c**) Support realization used in the test setup in Stuttgart

10.2.1.1 Frequency Response Functions for the Partly Assembled Systems

To illustrate the spread in dynamic characteristics between the three partly assembled systems, the direct point accelerances are shown in Fig. 10.4.

10.2.1.2 System Identification Results for the Partly Assembled Configuration

The real objective of the system identification procedure is to acquire frequency and shape information of the modes in the frequency range from 10 to 400 Hz. System identification for each of the data sets stemming from measurements made at the three universities were made using frequency data based state space subspace calibration by the n4sid algorithm in Matlab [9, 10]. The data sets were each split into a number of different frequency ranges, for which automated identification using a recently developed methodology to find the best model order was performed [11, 12]. However, where such an approach was deemed unsatisfying by the technician, manual interference was allowed. Examples of the quality of the system identification in terms of plots of FRFs stemming from test data overlaid by FRFs synthesized from system identification results are given in Fig. 10.5 in which the denotation #i,j refers to response in dof i due to excitation in dof j.

The mode shapes are compared using the modal assurance criterion (MAC); the plots of the MAC matrices are shown in Fig. 10.6. Overlaying illustrations of the extracted mode shapes for the three partly assembled systems are shown in Fig. 10.7. There are clear differences between the modes stemming from measurements made in Stuttgart and the ones stemming from Linnaeus and Chalmers. It is possible that mistakes were made during the collocation of test data. Differences in measurement techniques, for which nonlinearities may be more or less engaged, instrumentation and suspension are other possible causes. The explanation could also be differences in the physical properties of the seemingly identical components and assemblies. The causes have to be further investigated.

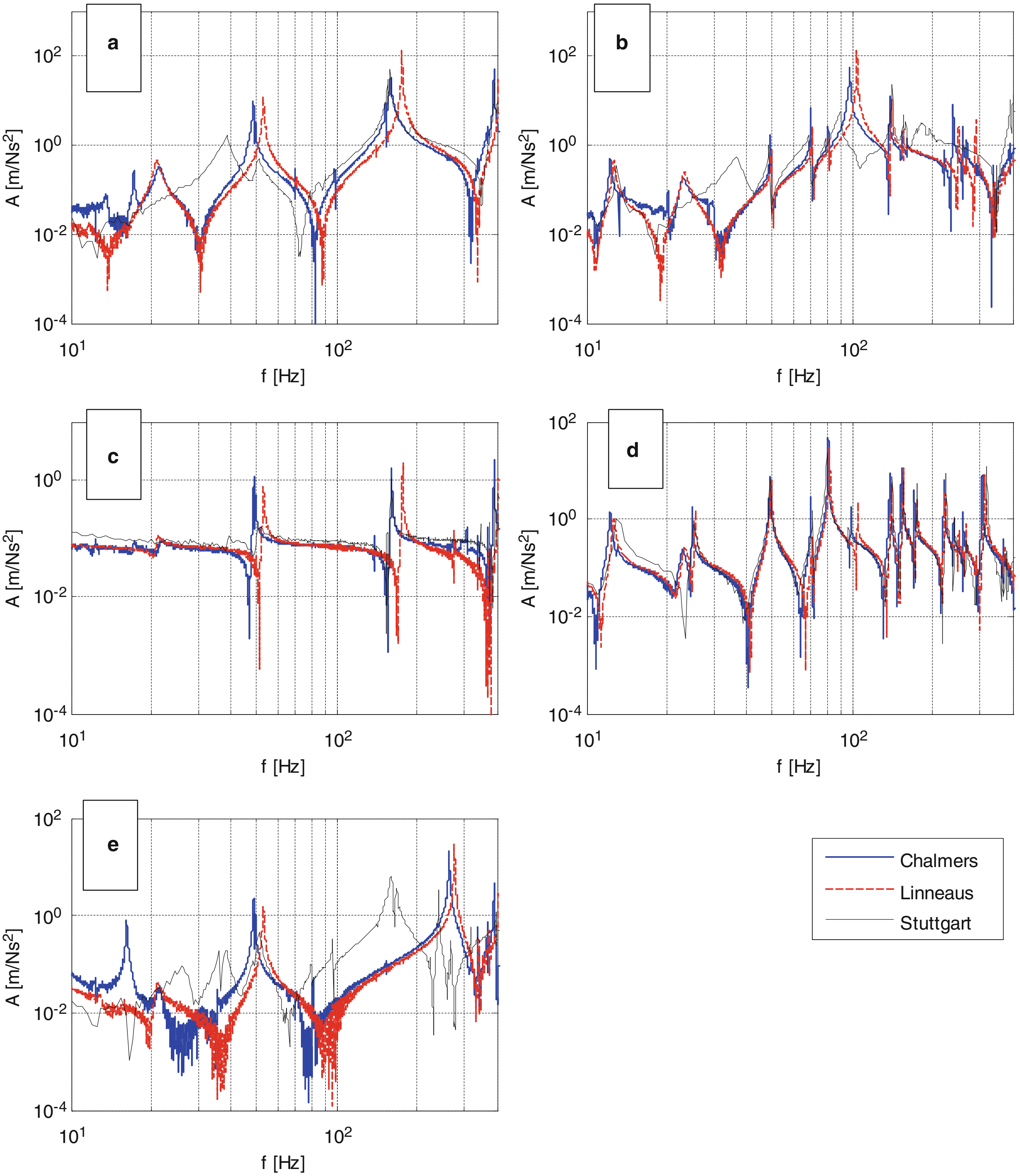

Fig. 10.4 Direct point accelerances for the systems without hub and blades. The *blue solid* FRFs stem from Chalmers, the *red dashed* FRFs stem from LNU and the black solid stem from Stuttgart. (**a**) Point 7, x-direction, (**b**) point 7, y-direction, (**c**) point 18, x-direction, (**d**) point 18, y-direction, (**e**) point 18, z-direction

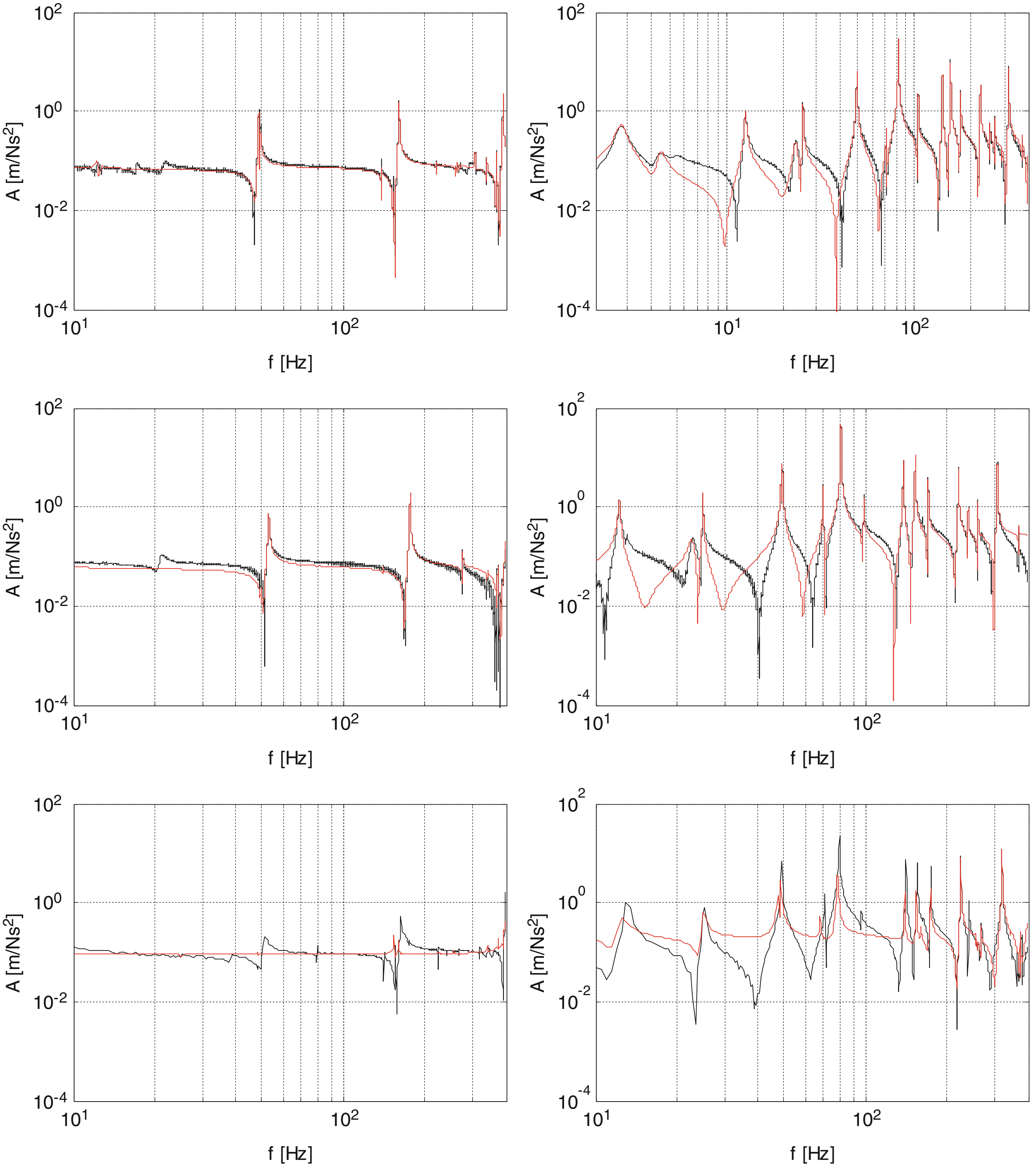

Fig. 10.5 (**c**) and (**d**) figures from Fig. 10.4 with identified models in *red*. Top to bottom: results for Chalmers, Lineaus and Stuttgart turbines

10.2.2 The Completely Assembled Systems

The second configuration to be tested is the complete benchmark structure selected by the SEM substructuring focus group. It differs from the previous setup in that the hub together with three blades is added to the structure. At the same time, the measurement point number 18 is moved to the tip of the hub. One single axis accelerometer is also added to each blade tip,

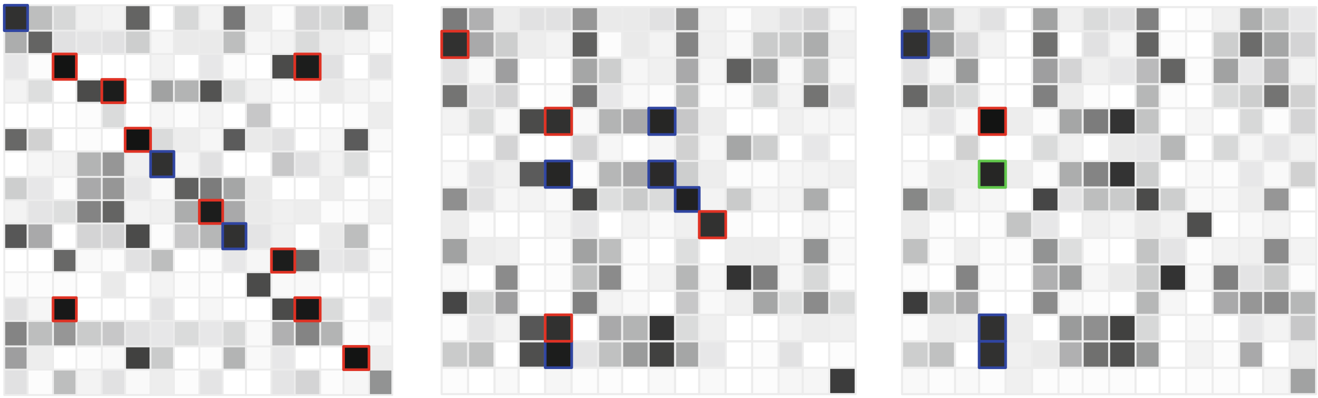

Fig. 10.6 MAC plots. Left to right: Chalmers-Linneaus, Chalmers-Stuttgart, Linneaus-Stuttgart

see Fig. 10.8. The exact blade tip positions are in accordance to the blade measurement points used by Harvie and Avitabile [13]. The blades used at LNU and Chalmers have previously been studied in detail [14] in which the mass and the center of gravity (CoG) were measured for each blade. Also the blade angles were measured; it was found that the tip angles had a spread of several degrees.

10.2.2.1 Frequency Response Functions of the Completely Assembled Systems

Comparisons between the three sets, of two direct point accelerances are shown in Fig. 10.9. Evidently, there is a resemblance between the FRFs stemming from Linnaeus and Chalmers whereas the FRFs stemming from Stuttgart deviates more. The reason may be mistakes made during the collocation of data, the differences in test setups or dynamic properties of the systems tested.

10.2.2.2 System Identification of the Completely Assembled Systems

The same basic approach to system identification was used for completely assembled systems as for the partly assembled, the only difference being that the frequency range was divided into a higher number of (that is, tighter) frequency intervals on account of the higher mode density. The results are shown in Figs. 10.10 and 10.11. The resemblance between the FRFs stemming from test data and their associated synthesized FRFs are in general good around the resonances. No residual terms were used. However, as seen, the degree of resemblance varies.

10.2.2.3 Results of Studies Made on the Completely Assembled Systems

The data indicate that the measured dynamics of the structures at Chalmers and Linnaeus are closely related although there are deviations. The data from Stuttgart differs more. The explanation can be that simple mistakes were made but differences in measurement techniques, for which nonlinearities may be more or less engaged, instrumentation and suspension are other possible causes. The explanation could also be differences in the physical properties of the seemingly identical components and assemblies. The causes have to be further investigated.

10.3 Conclusions

In this paper, three Ampair 600 W wind turbines, partly modified according to the SEM substructuring focus group's instructions for the benchmark structure, have been tested. One was tested at Linnaeus University in Växjö, one stryk at Chalmers University of Technology in Göteborg, and one stryk at the University of Stuttgart. Results from several

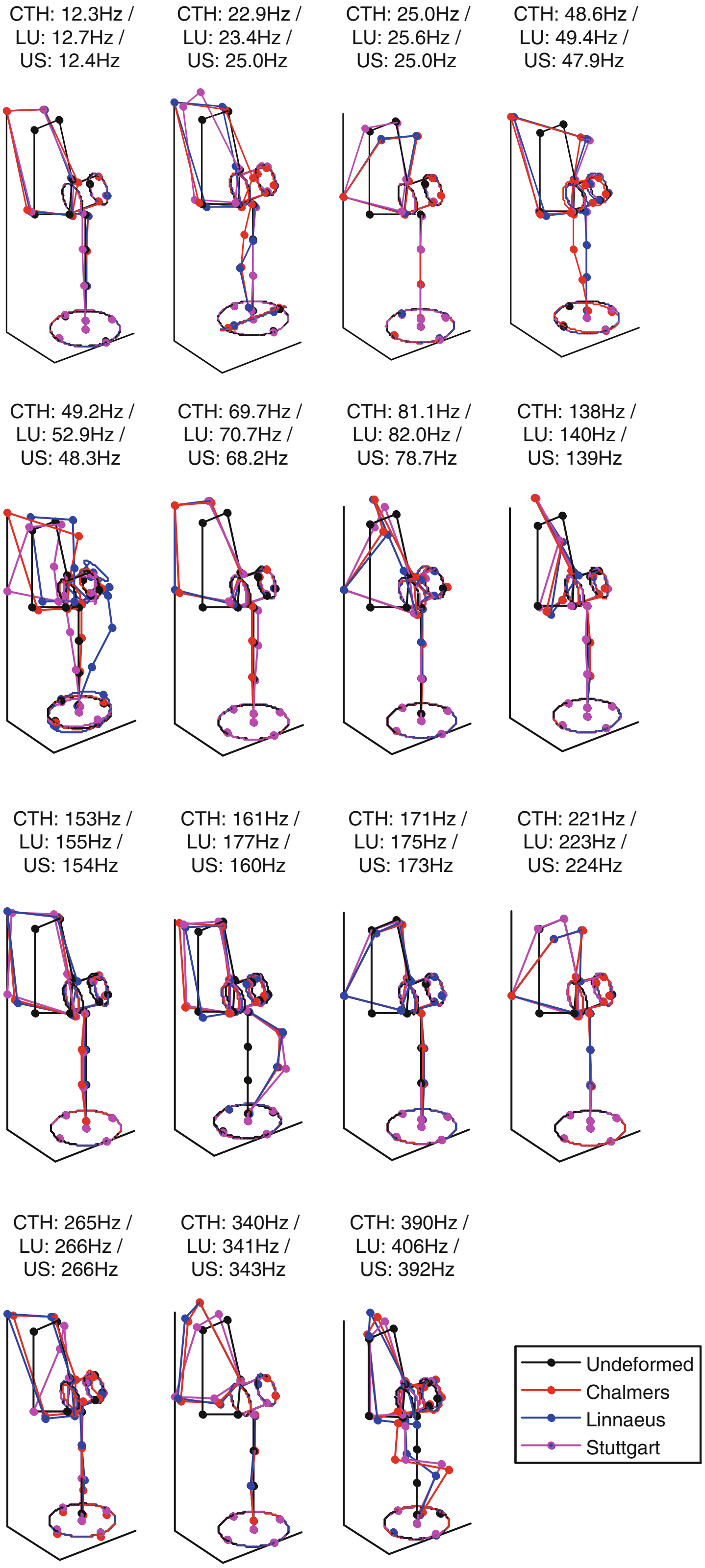

Fig. 10.7 Illustrations of mode shapes of the partly assembled systems at Chalmers, Linneaus and Stuttgart extracted by system identification

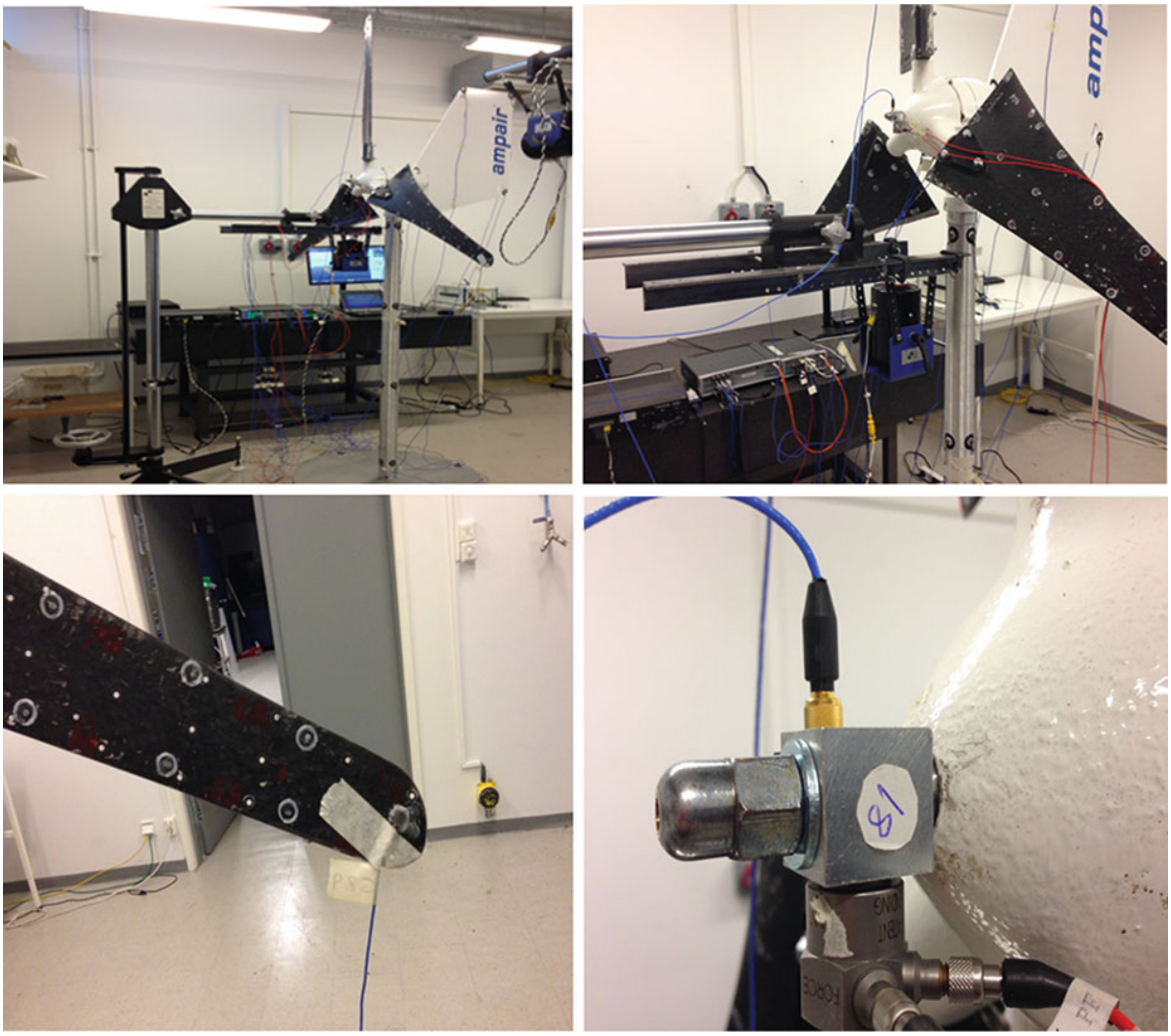

Fig. 10.8 Excitation on point 18, in the negative z-direction, on the completely assembled structure. The structure is located at Linnaeus University

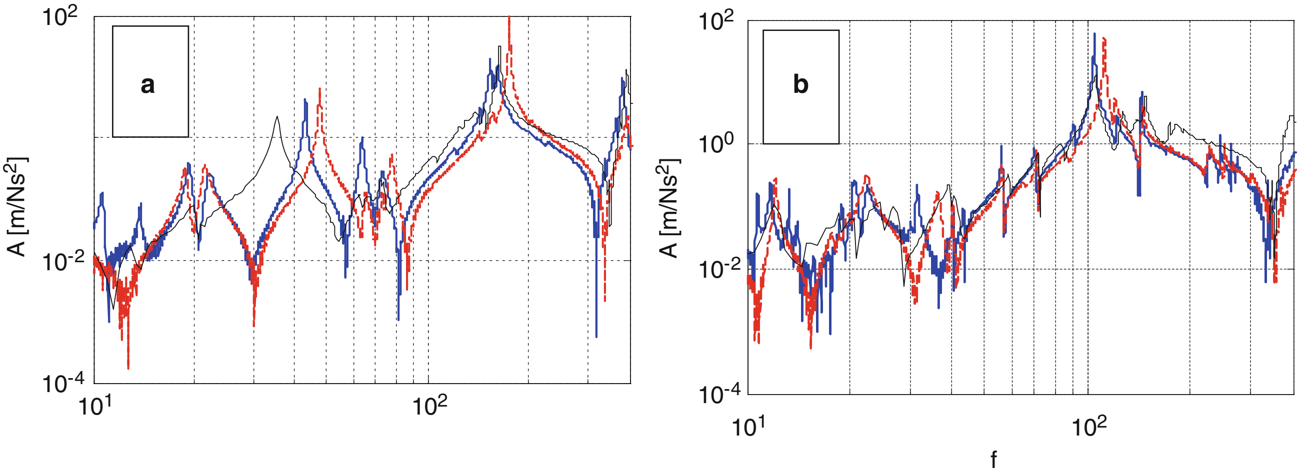

Fig. 10.9 Direct point accelerances for the completely assembled systems with hub and blades. The *blue solid* FRFs stem from Chalmers, the *red dashed* FRFs stem from LNU and the *black* FRFs stem from Stuttgart. (**a**) Point 7, x-direction, (**b**) point 7, y-direction, (**c**) point 18, x-direction, (**d**) point 18, y-direction, (**e**) point 18, z-direction

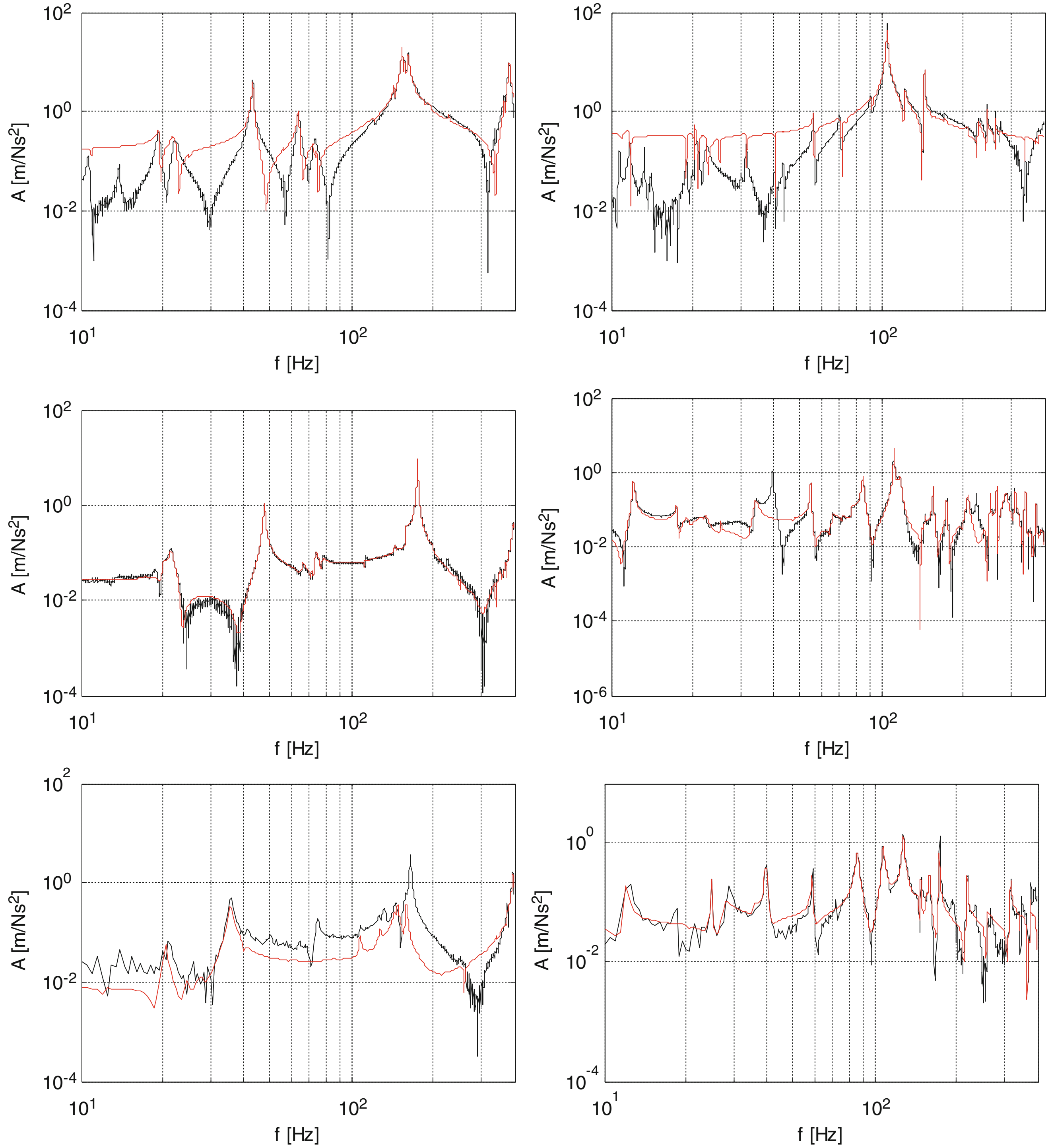

Fig. 10.10 (**c**) & (**d**) figures from previous figure with identified model in *red*. Top to bottom: results for Chalmers, Lineaus and Stuttgart turbines

single-input-multiple-output stepped sine as well as impact vibrational tests spanning from 2 to 400 Hz have been reported and compared.

The structures are seemingly identical. However, as shown in this paper, there is spread in the physical properties of components that should be identical. It is also believed that the assembling procedures used at the different universities introduced deviations. Furthermore, the excitation forces were not controlled to be identical but kept low. Some FRFs, here accelerances. stemming from different measurements show close resemblance whereas some show large deviations.

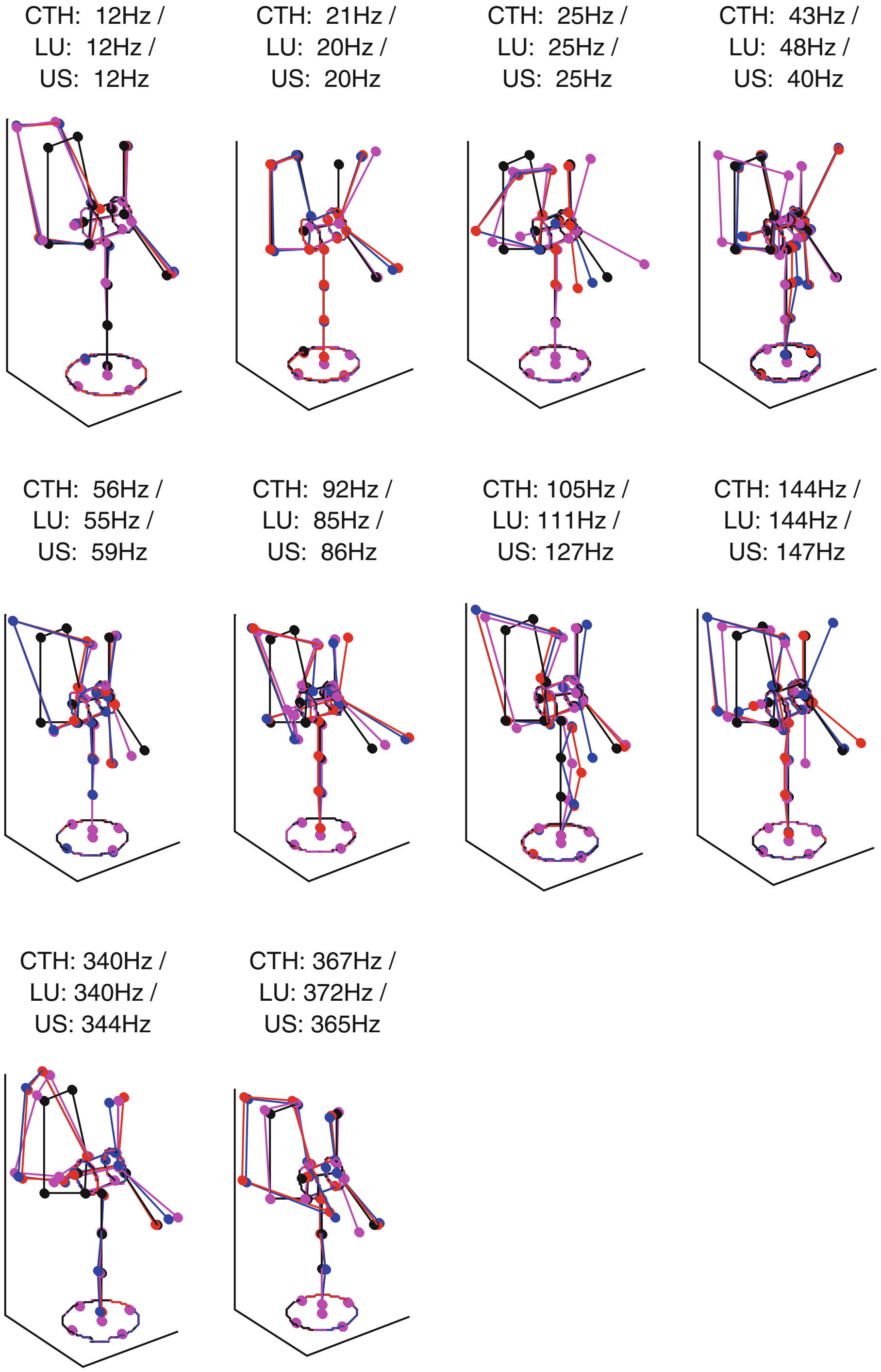

CTH: 12Hz /
LU: 12Hz /
US: 12Hz

CTH: 21Hz /
LU: 20Hz /
US: 20Hz

CTH: 25Hz /
LU: 25Hz /
US: 25Hz

CTH: 43Hz /
LU: 48Hz /
US: 40Hz

CTH: 56Hz /
LU: 55Hz /
US: 59Hz

CTH: 92Hz /
LU: 85Hz /
US: 86Hz

CTH: 105Hz /
LU: 111Hz /
US: 127Hz

CTH: 144Hz /
LU: 144Hz /
US: 147Hz

CTH: 340Hz /
LU: 340Hz /
US: 344Hz

CTH: 367Hz /
LU: 372Hz /
US: 365Hz

Fig. 10.11 Illustrations of mode shapes of the completely assembled systems at Chalmers, Linneaus, and Stuttgart extracted by system identification

Collocating and distributing test data, origin from different measurement systems and universities, close to the deadline for submission could be a source of error. However, the differences in methods and structures are other possible sources. The causes will be further investigated.

A certain amount of non-linearity is expected so the excitation forces may explain some differences. However, on a bigger scale, the direct point accelerances are qualitatively similar and the mode shapes, found by system identification, show good cross couplings. Some modes showing clear shapes and cross resemblances were further inspected. The deviation in eigenfrequencies between these paired modes were below 11 %; often much lower, for the configuration without hub and blades. The structures are found to be lightly damped which requires a good frequency resolution in measurement data.

In the same manner, an inspection of some selected, well paired, modes was made for the configuration with hub and blades. The deviations in frequencies are generally larger. One explanation is that the blades and the hubs have larger differences. The blades have different center of gravity as well as different blade twists. The hubs were severely modified, according to the SEM focus group's instructions, including filling them with plastics. It is believed that these processes were made quite differently.

Most likely, the hub together with the blades will form one natural substructure while the remaining parts form another, in future substructuring studies. Hence, measurement data, especially at the coupling point, will be most useful.

References

1. Hemez F, Doebling S (2001) Model validation and uncertainty quantification. In: Conference proceedings of the society for experimental mechanics, 19th IMAC
2. Ampair Energy Ltd (2012) Ampair wind, hydro and packaged power specialists.http://www.ampair.com/wind-turbines/ampair-600. Accessed 13 Mar 2013
3. Mayes RL (2012) An introduction to the sem substructures focus group test bed – the Ampair 600 wind turbine. In: Conference proceedings of the society for experimental mechanics series, 30th IMAC, a conference on structural dynamics
4. Rohe DP, Mayes RL (2013) Coupling of a bladed hub to the tower of the ampair 600 wind turbine using the transmission simulator method. In: Conference proceedings of the society for experimental mechanics series, 31th IMAC, a conference on structural dynamics
5. Rahimi S, de Klerk D, Rixen DJ (2013) The Ampair 600 wind turbine benchmark: results from the frequency based substructuring applied to the rotor assembly. In: Conference proceedings of the society for experimental mechanics series, 31th IMAC, a conference on structural dynamics
6. Macknelly D, Nurbhai M, Monk N (2013) Additional modal testing of turbine blades and the application of transmission simulator substructuring methodology for coupling. In: Conference proceedings of the society for experimental mechanics series, 31th IMAC, a conference on structural dynamics
7. Rohe DP (2012) Validation of experimental–analytical substructuring using the transmission simulator method. M.S. thesis, Engineering Physics, University of Wisconsin-Madison, Madison. Marquardt D, An algorithm for least-squares estimation of nonlinear parameters. J Soc Indust Appl Math 11, 1963
8. SEM substructure focus group wiki [online]. http://substructure.engr.wisc.edu
9. Ljung L (1999) System identification: theory for the user, 2nd edn. Prentice Hall, Englewood Cliffs
10. McKelvey T, Akcay H, Ljung L (1996) Subspace-based multivariable system identification from frequency response data. IEEE Trans Autom Control 41:960–979
11. Yaghoubi V, Abrahamsson T (2012) Automated modal analysis based on frequency response function estimates, vol 5, Topics in modal analysis I. Springer, New York, pp 9–18
12. Yaghoubi V, Abrahamsson T (2014) Automated modal analysis based on statistical evaluation of frequency responses, vol 7, Topics in modal analysis. Springer, New York, pp 479–486
13. Harvie J, Avitabile P (2012) Comparison of some wind turbine blade tests in various configurations. In: Conference proceedings of the Society for Experimental Mechanics series, 30th IMAC, a conference on structural dynamics, pp 73–79
14. Johansson A, Linderholt A, Abrahamsson T (2014) Model calibration and uncertainty of A600 wind turbine blades. In: Conference proceedings of the Society for Experimental Mechanics series, 32nd IMAC, a conference and exposition on structural dynamics

Chapter 11
Ampair 600 Wind Turbine Three-Bladed Assembly Substructuring Using the Transmission Simulator Method

Daniel R. Roettgen and Randall L. Mayes

Abstract This paper contains an example of the transmission simulator method for experimental dynamic substructuring using the Ampair 600 Wind Turbine. The structure of interest is the hub-and-three-bladed assembly. A single blade and hub is used as a substructure to develop a model for the hub-and-three-bladed assembly. The single-blade-and-hub substructure was developed from elastic modes of a free-free test and rigid body modes analytically derived from measured mass properties. This substructure can be rotated and replicated using the hub as a transmission simulator. Substructuring calculations were then performed using the transmission simulator method to derive a model of the hub-and-three-bladed assembly. This paper concludes with a comparison for this combined model to truth data derived from a free-free modal test of the entire rotor.

Keywords Experiment • MCFS • Dynamic substructuring • Transmission simulator • Wind turbine

11.1 Introduction

As manufactured systems become more complex a need for advanced analytical tools to analyze these systems becomes a necessity. Dynamic substructuring allows an analyst to predict the dynamic response of a complex system by analyzing or testing subcomponents. Thus, if subcomponents can be modeled or tested, the result for a full model can be predicted and these subcomponents can be modified to help mature the design. Experimental substructuring is particularly useful when a system is too large to test as an assembly, or when subcomponent hardware is available but the detailed design definition is not (for example, for a subcomponent produced by an outside company). This paper contains a detailed example of dynamic substructuring on the Ampair 600 Wind Turbine test bed. The goal of this exercise is to construct the dynamics of a three-bladed rotor experiment using the results from a single-blade-and-hub experiment. To complete this exercise, two experiments were performed. The first was a hub-and-three-bladed experiment that will be used as a truth model. The second was the testing of the subcomponent containing one blade and the rotor hub. In addition to the details of these experiments, this paper contains the substructuring methodology and some simple experimental checks used to help ensure the quality of the data that was taken experimentally. For this exercise the transmission simulator method was used.

Advantages of the transmission simulator method can be found in [1–3]. Here we focus on a few of the advantages for this application. The transmission simulator method is often used over more traditional substructuring methods when it is difficult to simulate the boundary conditions between individual pieces of a system. By using the hub as the transmission simulator two key advantages are gained. One is that the compliance and the damping of the joint connecting the blade and hub are captured. The second is that the hub mass loads the root of the blade so that blade stiffness at the root is appropriately exercised. Often a similar fixture is used as a transmission simulator, but for this exercise the actual part was used because it was readily available and was certain to simulate the interface conditions correctly. This provides the best possible simulation of the blade-to-hub joint as the actual joint dynamics are contained within the experiment.

Sandia National Laboratories is a multi-program laboratory managed and operated by Sandia Corporation, a wholly owned subsidiary of Lockheed Martin Corporation, for the U.S. Department of Energy's National Nuclear Security Administration under contract DE-AC04-94AL85000.

D.R. Roettgen (✉) • R.L. Mayes
Experimental Mechanics, NDE, and Model Validation Department, Sandia National Laboratories,
P.O. Box 5800 – MS 0557, Albuquerque, NM 87185, USA
e-mail: droettgen@wisc.edu; rlmayes@sandia.gov

M. Allen et al. (eds.), *Dynamics of Coupled Structures, Volume 4*, Conference Proceedings of the Society
for Experimental Mechanics Series, DOI 10.1007/978-3-319-15209-7_11

11.2 Test Objective and Methods

The objective for this exercise is to generate a dynamic model of the hub-and-three-bladed system, pictured in Fig. 11.1, from the Ampair 600 Wind Turbine using the transmission simulator method. This model will be compared to a "truth model" that was derived from a modal test of the pictured assembly. Previous tests containing these structures in similar configurations [4–6] show that the highest frequencies of interest would occur below 175 Hz, and thus the test range was set to 200 Hz for the truth model to allow the modes of interest (and a few higher) to be captured. For each test, a PCB 086C05 impact hammer was used to excite the structures' elastic modes. In an attempt to minimize non-linearities in the system, the output of the hammer was amplified allowing extremely soft taps to be used during testing. The auto spectrum of this input was monitored during testing to ensure quality data was gathered. After completing the modal testing, modes were extracted from the experimental data using the SMAC algorithm [7].

Tests were performed on two different structures in order to create both a full-assembly "truth" model and a sub-assembly "substructure" model that could be replicated and assembled into the complete hub-and-three-bladed assembly. The first structure was the hub connected to all three blades. Hardware assets were used from Sandia National Laboratories with the serial numbers for Blades A, B, and C being SNL009, SNL008, and SNL007, respectively. The second structure tested was the turbine hub assembly with just Blade A connected. The results from the substructure test will be replicated (and rotated) two times, so two additional hubs will need to be subtracted as they are the common piece being used as a transmission simulator.

Each third of the turbine was given its own Cartesian coordinate system with x along the blade, y perpendicular to x in the rotation plane, and z along the axis of rotation. The origin of these coordinates systems was defined at a common point on the center of the hub. Figure 11.2 shows these coordinate systems as they are aligned with each blade.

11.2.1 Hub-and-Three-Bladed Test (Truth Test)

11.2.1.1 Test Set-Up

The hub-and-three-bladed assembly was instrumented with 36 single axis accelerometers as well as three triaxial accelerometers. The primary blade (Blade A) was instrumented based on previous testing [4–6] such that all mode shapes up to the third out-of-plane bending mode would be independent. This primary blade was instrumented more heavily than the secondary blades as this instrumentation would remain in place to capture data during the subcomponent testing. Accelerometer locations and directions are depicted in Fig. 11.3.

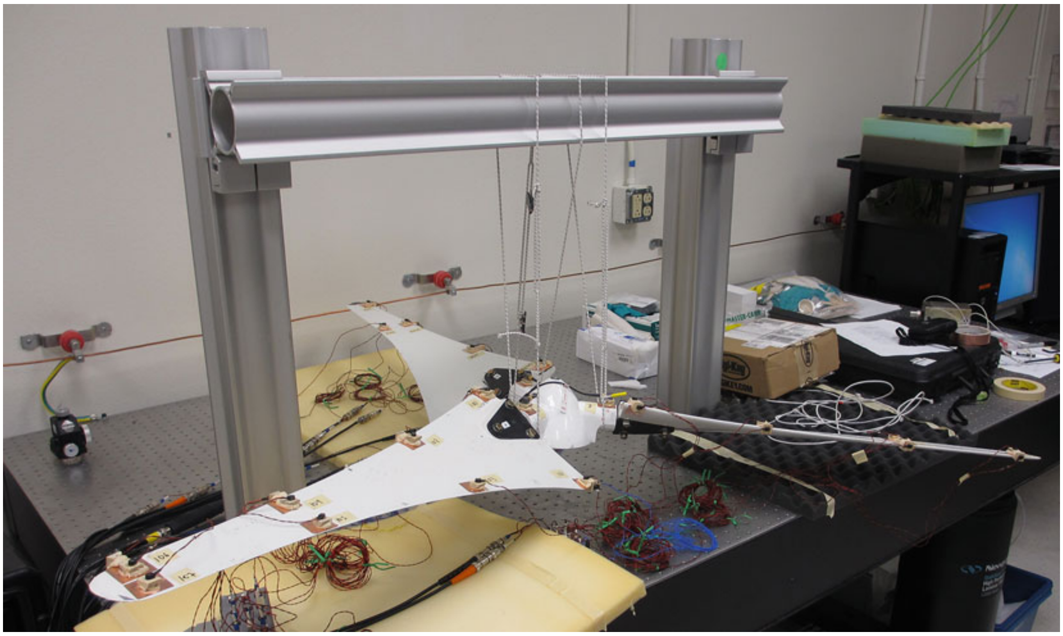

Fig. 11.1 Wind turbine truth assembly

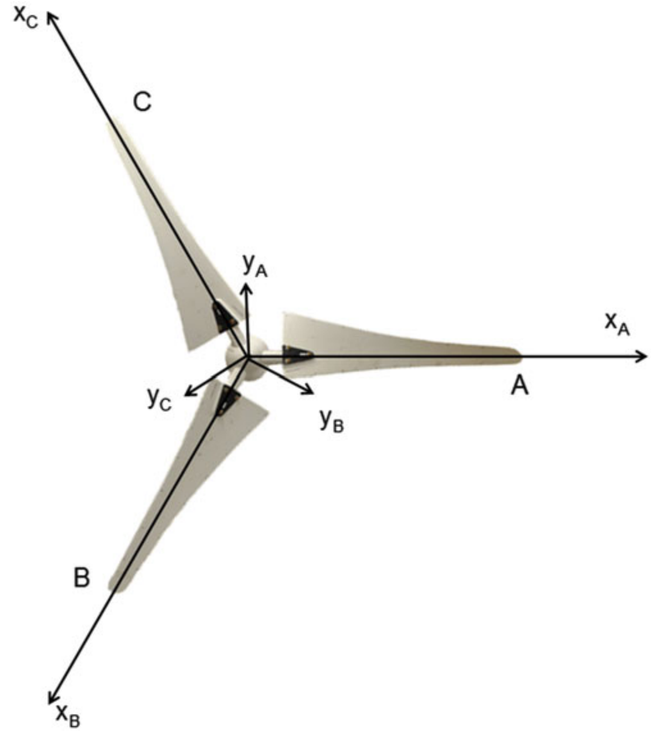

Fig. 11.2 Wind turbine coordinate system – truth test

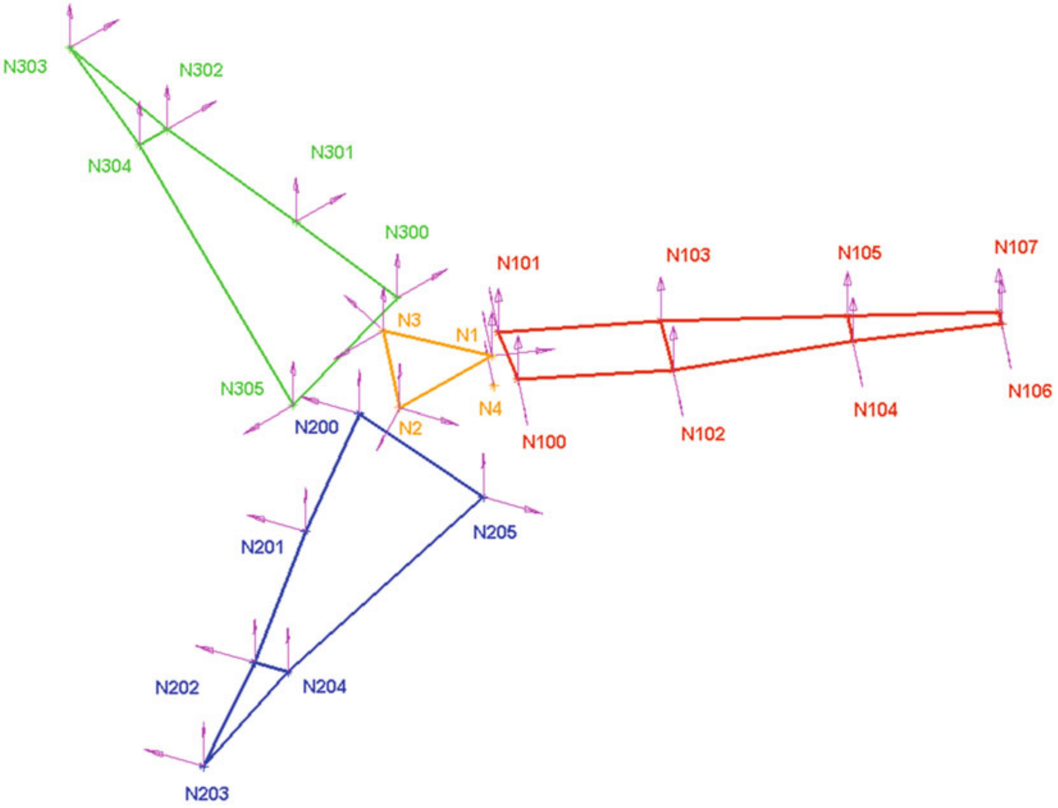

Fig. 11.3 Truth model assembly instrumentation Diagram

Two 2250 AM1-10 uniaxial accelerometers with a sensitivity of 10 mV/g were placed at four locations along the leading edge of each blade. These accelerometers were oriented with the *y* and *z* directions for each blade's local coordinate system. Accelerometers were also placed along the trailing edge of the blade but mainly oriented in the *z* direction with one accelerometer placed in the *y* direction at the trailing edge root of each blade.

The hub was instrumented with three tri-axial Endevco 65–100 accelerometers with a higher sensitivity of 100 mV/g. This higher sensitivity was required because hub motion tended to be very small compared to the light flexible blades. These tri-axial accelerometer was placed on the branch extending from the hub associated with each blade. Additionally, one 100 mV/g uniaxial PCB 352/A-24 accelerometer was placed on the Blade A third of the hub pointed in the *y* direction.

Blocks were used to align the accelerometers in the local blade displacement coordinate systems with accelerometers on the blade face pointing in the *z* direction and those on the trailing and leading edge in the *y* direction. These wood blocks were taken into account when analytically constructing rigid body modes for the different assemblies.

The hub-and-three-bladed assembly was suspended from a structure on an optical table using bungee cords to simulate a free-free condition as seen in Fig. 11.1. Previous work showed the lowest elastic mode to occur at about 20 Hz. In an effort to minimize error due to the boundary conditions, the bungee cords provided a rigid body bounce mode around 2 Hz. This achieved a desired ratio of 10 times in order to minimize frequency error due to boundary conditions as discussed in [8].

Analytical rigid body mode shapes were calculated using the moments of inertia and center of gravity detailed in [5]. With the larger number of accelerometers (and positioning blocks), it was decided that the mass of these items was not negligible in the calculation of the mass properties. These blocks were accounted for when calculating the mass properties used to determine rigid body modes. The mass properties are listed in Table 11.1.

The suspended structure was excited at several drive points in the usual attempt to find the best location to excite each individual mode. Drive points were gathered on the blades and on the rotor hub. The drive points on the rotor hub provided the best results, not because they excited the modes the most, but because they excited the modes well enough and produced FRFs with the most linear characteristics. To create a truth model for the hub-and-three-bladed assembly, the measured response from the best was used to calculate the modal parameters for each elastic mode. Modes 7, 8, 9, 12, and 15 were derived from excitations with a drive point at node 1 in the *z* direction; while modes 10 and 11 were derived from excitations at node 4 in the *y* direction, and modes 13 and 14 were derived from excitations at node 3 in the *z* direction.

11.2.1.2 Results

The analytically generated rigid body modes were combined with nine elastic modes extracted from the impact tests. These modes are detailed in Table 11.2. Light hammer excitations were used in an attempt to avoid non-linarites due to the jointed connection. Of particular note, modes 10 and 11 (elastic modes 4 and 5) exhibited a great deal of non-linearity and were particularity sensitive to the input force levels. Complex modal indicator functions (CMIFs) are shown for each of the drive points in Fig. 11.4. Note that no single reference excites all modes well. Circles in the figure show which modes were selected from each reference. We recognize that this truth test is only one realization of truth, since there is definitely variability in individual blades as well as the clearances in the hub brackets holding the blades.

Table 11.1 Mass properties for hub-and-three-bladed system

	Entire rotor
Mass	6.29 kg
cg_x	0.00 m
cg_y	0.00 m
cg_z	−0.0673 m
I_{xx}	0.221 kg-m^2
I_{yy}	0.224 kg-m^2
I_{zz}	0.441 kg-m^2

Table 11.2 List of extracted and analytically calculated modes from the hub-and-three-bladed test

Mode	Frequency (Hz)	Damping ratio ζ [%]	Description	Drive point
1	0.00	1.00	*x* direction translation	Analytical
2	0.00	1.00	*y* direction translation	Analytical
3	0.00	1.00	*z* direction translation	Analytical
4	0.00	1.00	Rotation about *x*	Analytical
5	0.00	1.00	Rotation about *y*	Analytical
6	0.00	1.00	Rotation about *z*	Analytical
7	20.56	1.00	First bending, three blades in phase	1Z
8	27.78	0.98	First bending, Blade C out of phase	1Z
9	29.03	0.87	First bending, Blade B out of phase	1Z
10	61.10	1.71	Edge-wise mode, Blade C out of phase	4Y
11	64.29	1.27	Edge-wise mode, Blade B out of phase	4Y
12	70.68	1.11	Second bending, three blades in phase	1Z
13	99.40	1.48	Second bending, Blade C out of phase	3Z
14	102.95	1.08	Second bending, Blade B out of phase	3Z
15	155.00	1.33	Third bending, three blades in phase	1Z

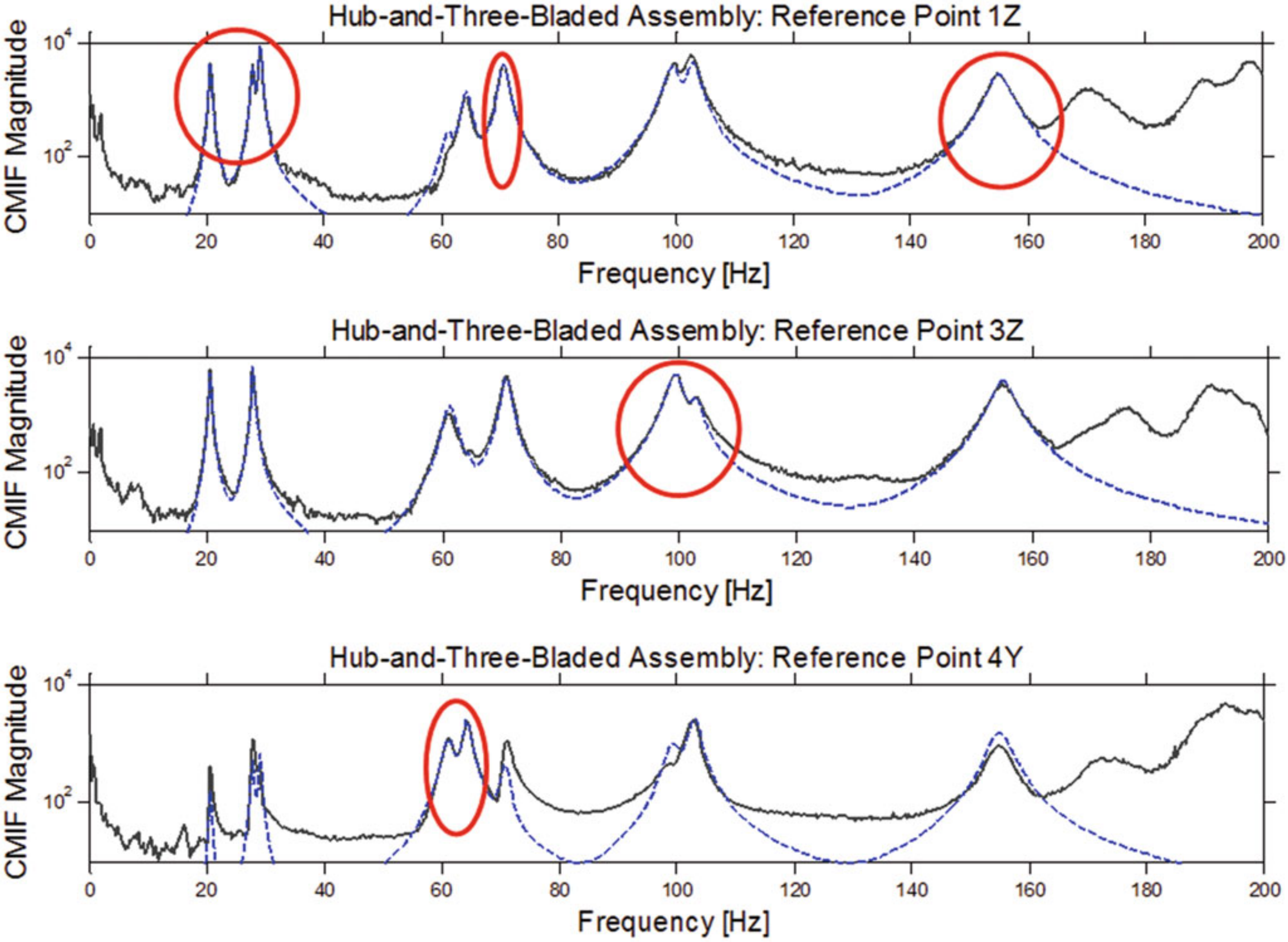

Fig. 11.4 CMIFs for truth model (*blue*) and drive point measurements (*black*). Drive points: 1Z (*top*), 3Z (*middle*), 4Y (*bottom*)

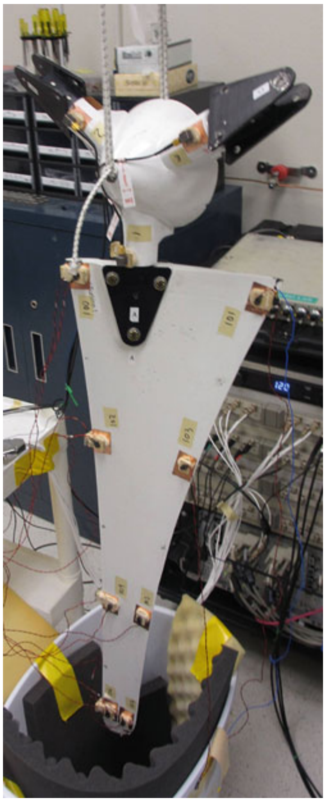

Fig. 11.5 Single-blade-and-rotor-hub experimental set-up

Table 11.3 Mass properties for single-blade-and-hub system

	Single-blade-and-hub assembly
Mass	4.52 kg
cg_x	0.0756 m
cg_y	0.000 m
cg_z	−0.0632 m
I_{xx}	0.0252 kg-m^2
I_{yy}	0.0972 kg-m^2
I_{zz}	0.1414 kg-m^2

11.2.2 Single-Blade-and-Hub Test (Substructure Test)

11.2.2.1 Test Set-Up

With one realization of a truth model established, the next test to be completed was the single-blade-and-hub test. Blades B and C were removed from the hub leaving Blade A. The accelerometers on Blade A were not removed to preserve their location relative to the hub-and-three-bladed testing. The same impact hammer and instrumentation set-up were used for Blade A and the hub. Measurements were taken up to 200 Hz in order to capture up to the first three out-of-plane bending modes. The test set-up for the single-blade-and-rotor-hub system can be seen in Fig. 11.5.

Mass properties of the substructure were calculated using geometry and assumed symmetry properties of the hub-and-three-bladed system. Analytical rigid body modes were again calculated using the mass properties of the system. Substructure moments of inertia were calculated based on geometry and symmetry conditions and are shown in Table 11.3. The instrumentation blocks located on the single-blade-and-hub assembly were accounted for in these calculations.

The subsystem was similarly tested at several drive points in order to determine the excitation locations that provided the best data for the subsystem's elastic modes. Modes 7, 8, 9, and 11 were derived from excitations at drive point location 3 in the z direction while mode 10 was derived from drive point location 4 in the y direction.

Table 11.4 List of extracted and analytically calculated modes from the single-blade-and-hub test

Mode	Frequency (Hz)	Damping ratio ζ [%]	Description	Drive point
1	0.00	1.00	*x* direction translation	Analytical
2	0.00	1.00	*y* direction translation	Analytical
3	0.00	1.00	*z* direction translation	Analytical
4	0.00	1.00	Rotation about *x*	Analytical
5	0.00	1.00	Rotation about *y*	Analytical
6	0.00	1.00	Rotation about *z*	Analytical
7	29.84	0.91	First bending	3Z
8	86.75	0.92	Second bending	3Z
9	149.82	1.51	Edgewise motion	3Z
10	178.25	2.62	First torsion	4Y
11	195.10	1.30	Third bending	3Z

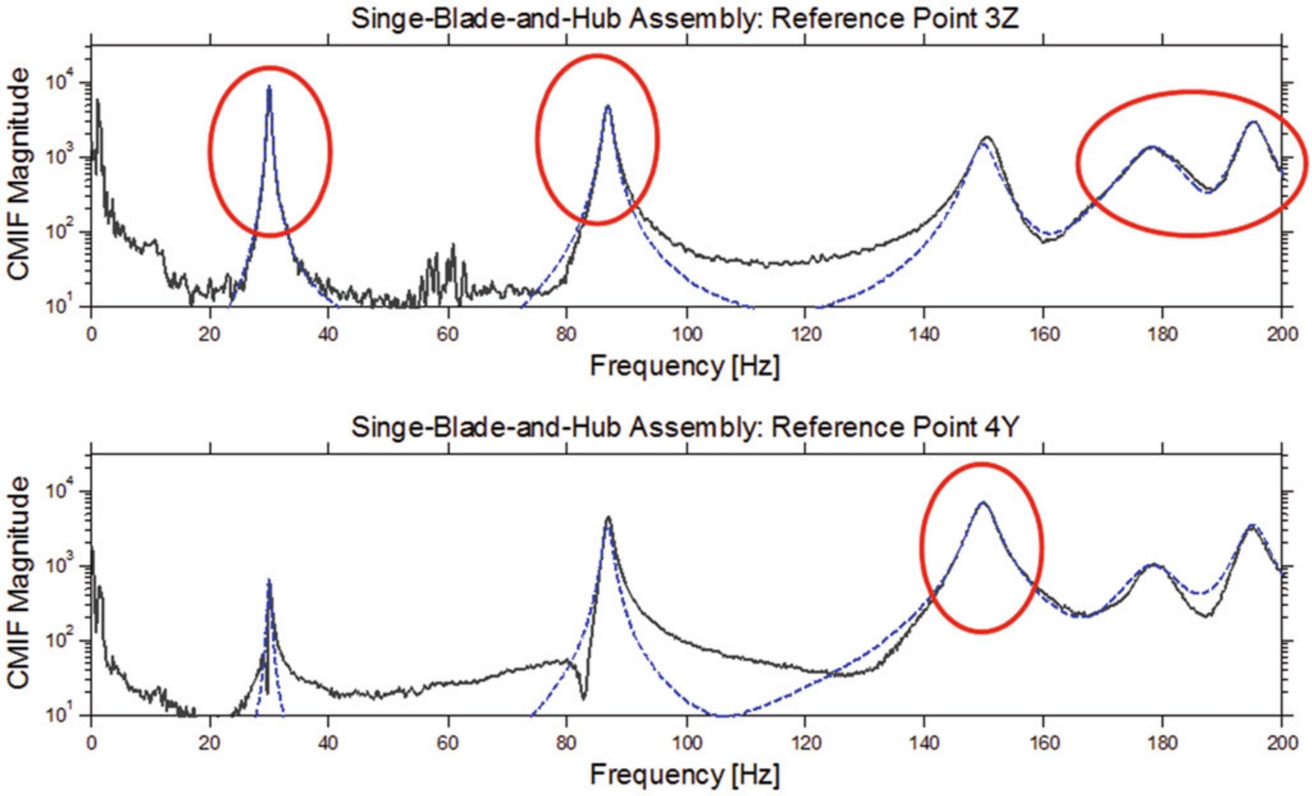

Fig. 11.6 CMIFs for substructure model (*blue*) and drive point measurements (*black*). Drive points: 3Z (*top*), 4Y (*bottom*)

11.2.2.2 Results

The six analytically generated rigid body modes were combined with five elastic modes extracted from the impact tests. These modes are detailed in Table 11.4. Again, each elastic mode was selected from the strongest responding drive point. CMIFs for those selected drive points can be seen in Fig. 11.6. Hammer strikes in the z-direction were found to easily excite bending and torsional modes while a *y* direction strike was again required to excite the blade in edgewise motion. The modes extracted from each reference are circled.

11.3 Substructuring Methodology

The transmission simulator method was utilized in order to assemble the single-blade-and-hub into the full system. The rotor hub was used as the transmission simulator fixture. Three copies of the subsystem were rotated and added together linking the rotated degrees of freedom associated with the tri-axial accelerometers located on the rotor hub (transmission simulator). With three copies of the substructure included, two analytical copies of the transmission simulator needed to be subtracted out of the combined system to achieve the proper results for the mass of the hub.

The same rotor hub was used as a transmission simulator in a past experiment and was found to have a first elastic natural frequency above 1,200 Hz [5]. This first elastic mode is far beyond the scope of the current test so only the rigid body modes of the transmission simulator will be used to couple the systems.

For the following calculations, the subscript *A* represents the first blade, Blade *A*, with *B*, and *C* representing the second and third blade respectively; the subscript *TS* represents the transmission simulator (rotor hub). The modal parameters ω and ζ represent the natural frequencies and damping ratios of their respective subsystems and Φ represents the associated mode shapes. The physical degrees of freedom are represented by vectors denoted x and the modal degrees of freedom are denoted by vectors q. To begin, the system of equations is written in the standard mass-normalized modal representation of the equations of motion.

$$\begin{bmatrix} I_A & 0 & 0 & 0 \\ 0 & I_B & 0 & 0 \\ 0 & 0 & I_C & 0 \\ 0 & 0 & 0 & -2I_{TS} \end{bmatrix} \begin{Bmatrix} \ddot{q}_A \\ \ddot{q}_B \\ \ddot{q}_C \\ \ddot{q}_{TS} \end{Bmatrix} + \begin{bmatrix} 2\zeta_A\omega_A & 0 & 0 & 0 \\ 0 & 2\zeta_B\omega_B & 0 & 0 \\ 0 & 0 & 2\zeta_C\omega_C & 0 \\ 0 & 0 & 0 & -4\zeta_{TS}\omega_{TS} \end{bmatrix} \begin{Bmatrix} \dot{q}_A \\ \dot{q}_B \\ \dot{q}_C \\ \dot{q}_{TS} \end{Bmatrix}$$

$$+ \begin{bmatrix} {\omega_A}^2 & 0 & 0 & 0 \\ 0 & {\omega_B}^2 & 0 & 0 \\ 0 & 0 & {\omega_C}^2 & 0 \\ 0 & 0 & 0 & -2{\omega_{TS}}^2 \end{bmatrix} \begin{Bmatrix} q_A \\ q_B \\ q_C \\ q_{TS} \end{Bmatrix} = \begin{Bmatrix} \Phi_A^T F_A \\ \Phi_B^T F_B \\ \Phi_C^T F_C \\ 2\Phi_{TS}^T F_{TS} \end{Bmatrix} \tag{11.1}$$

The physical constraints can be assembled equating the motion of each subsystem with that or the transmission simulator. This equation only applies to the subset of degrees of freedom which act to connect the transmission simulator between substructures.

$$\begin{bmatrix} I & 0 & 0 & -I \\ 0 & I & 0 & -I \\ 0 & 0 & I & -I \end{bmatrix} \begin{Bmatrix} x_A \\ x_B \\ x_C \\ x_{TS} \end{Bmatrix} = \begin{Bmatrix} 0 \\ 0 \\ 0 \\ 0 \end{Bmatrix} \tag{11.2}$$

The constraint equation can then be rewritten as modal coordinates as seen in Eq. 11.3.

$$\begin{bmatrix} \Phi_A & 0 & 0 & -\Phi_{TS} \\ 0 & \Phi_B & 0 & -\Phi_{TS} \\ 0 & 0 & \Phi_C & -\Phi_{TS} \end{bmatrix} \begin{Bmatrix} q_A \\ q_B \\ q_C \\ q_{TS} \end{Bmatrix} = \begin{Bmatrix} 0 \\ 0 \\ 0 \\ 0 \end{Bmatrix} \tag{11.3}$$

In order to take advantage of the transmission simulator method, the constraints are now pre-multiplied by the pseudo-inverse of the transmission simulator mode shapes partitioned to the constraint degrees of freedom.

$$\begin{bmatrix} \Phi_{TS}^+ & 0 & 0 \\ 0 & \Phi_{TS}^+ & 0 \\ 0 & 0 & \Phi_{TS}^+ \end{bmatrix} \begin{bmatrix} \Phi_A & 0 & 0 & -\Phi_{TS} \\ 0 & \Phi_B & 0 & -\Phi_{TS} \\ 0 & 0 & \Phi_C & -\Phi_{TS} \end{bmatrix} \begin{Bmatrix} q_A \\ q_{Bc} \\ q_C \\ q_{TS} \end{Bmatrix} = \begin{Bmatrix} 0 \\ 0 \\ 0 \\ 0 \end{Bmatrix} \tag{11.4}$$

The two leading matrices can now be collected to form a single matrix, A, that contains the constraints for the modal degrees of freedom.

$$A \begin{Bmatrix} q_A \\ q_B \\ q_C \\ q_{TS} \end{Bmatrix} = A\{q\} = 0 \tag{11.5}$$

These constrained modal degrees of freedom can be transformed by some matrix, L, into a set of unconstrained generalized coordinates, q_g.

$$\{q\} = L\{q_g\} \tag{11.6}$$

Using this substitution requires that L reside in the null space of A because $q_g = 0$ would be a trivial solution. This means that L must be orthogonal to A to fulfill Eq. 11.5.

$$AL\{q_g\} = 0 \tag{11.7}$$

This substitution is then used in Eq. 11.1 which is also pre-multiplied by AL^T resulting in the coupled equations of motion for the system. The modal properties for this system can then be found as the modal properties for the new analytically substructured system. A final transform is then used to bring the solution for the modal degrees of freedom back into the physical domain. Note the M, C and K are defined as shown in Eq. 11.1.

$$\overline{M}\ddot{q}_g + \overline{C}\dot{q}_g + \overline{K}q_g = 0$$

$$\overline{M} = L^T ML \; \overline{C} = L^T CL \; \overline{K} = L^T KL$$

$$x = \begin{bmatrix} \Phi_A & 0 & 0 & 0 \\ 0 & \Phi_B & 0 & 0 \\ 0 & 0 & \Phi_C & 0 \\ 0 & 0 & 0 & \Phi_{TS} \end{bmatrix} Lq_g \tag{11.8}$$

11.4 Substructuring Results

The experimental single-blade-and- hub system was used in the substructuring calculations detailed in the previous section to create a full hub-and-three-bladed turbine model. This substructured model will now be now compared to the results from the truth test described earlier in this paper. Because some modes of the system were found to be closely spaced these modes had to be correlated based on their Modal Assurance Criterion (MAC) values. This identification was important when looking at the 8th and 9th substructured modes as well as the 13th and 14th. These modes could be identified by MAC values as well as visual representation The MAC values and modal parameter comparisons can be seen in Table 11.5.

By inspection of Table 11.5, some trends can be identified. The first, second and third in-phase out-of-plane bending modes (Modes 7, 12 and 15) are too high in frequency. Three of the four anti-symmetric out of plane bending modes (9, 13 and 14) are low in frequency. The edgewise modes (10 and 11) are high in frequency.

The substructured damping ratios are a further off than the natural frequencies. Some modes (9 and 15) are quite close in damping while others are as high as 58 % off mark.

The correlation of modes between the substructured and truth models could be determined either by MAC as shown in Fig. 11.7 or visual comparison as shown in Figs. 11.8 and 11.9. Figure 11.8 contains the bending modes in an isometric view while Fig. 11.9 shows the edgewise modes in the xy plane.

Table 11.5 Substructuring results

Truth Mode	Frequency (Hz)	Damping ratio	Substr. mode	Substr. frequency (Hz)	Frequency error	Substr. damping	Damping error	MAC
7	20.56	1.00 %	7	23.49	14.26 %	0.73 %	–27.19 %	.9912
8	27.78	0.98 %	9	28.33	2.00 %	0.86 %	–12.07 %	.7655
9	29.03	0.87 %	8	28.03	–3.44 %	0.85 %	–1.88 %	.8808
10	61.10	1.71 %	10	66.53	8.91 %	0.71 %	–58.31 %	.9422
11	64.29	1.27 %	11	66.67	3.72 %	0.71 %	–44.03 %	.9787
12	70.68	1.11 %	12	77.33	9.41 %	0.84 %	–23.71 %	.9402
13	99.40	1.48 %	14	96.30	–1.75 %	1.00 %	–32.17 %	.8618
14	102.95	1.08 %	13	97.66	–6.45 %	0.99 %	–8.82 %	.8849
15	155.00	1.33 %	15	167.26	7.91 %	1.29 %	–3.05 %	.7850

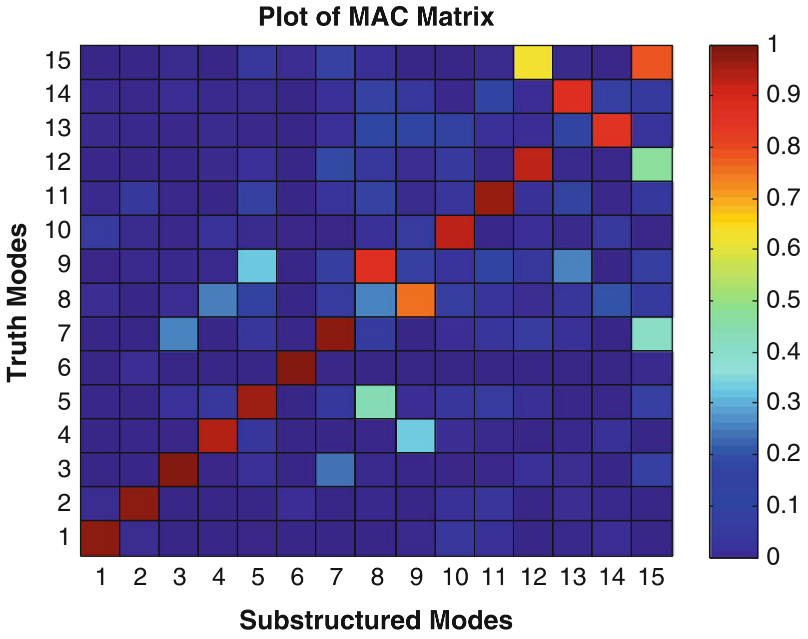

Fig. 11.7 MAC between truth and substructured modes

11.5 Possible Error Sources

There were errors of up to 15 % in natural frequency, 59 % in damping and MAC values as low as 0.7655. Several issues could lead to these errors that could be investigated further with additional study. Some important experimental check and possible error sources will be mentioned in this section. Modal truncation errors are known to exist but they are not addressed in this exercise.

11.5.1 Testing Checks and Validations

Previous work [9] has shown that the most important mode shapes to obtain accurately are the rigid body mode shapes. When analytically adding rigid body modes to the experimental data, a check can be performed to ensure the analytically derived rigid body modes are a good match of the system that was tested. In this case, we can take the derived rigid body mode FRF

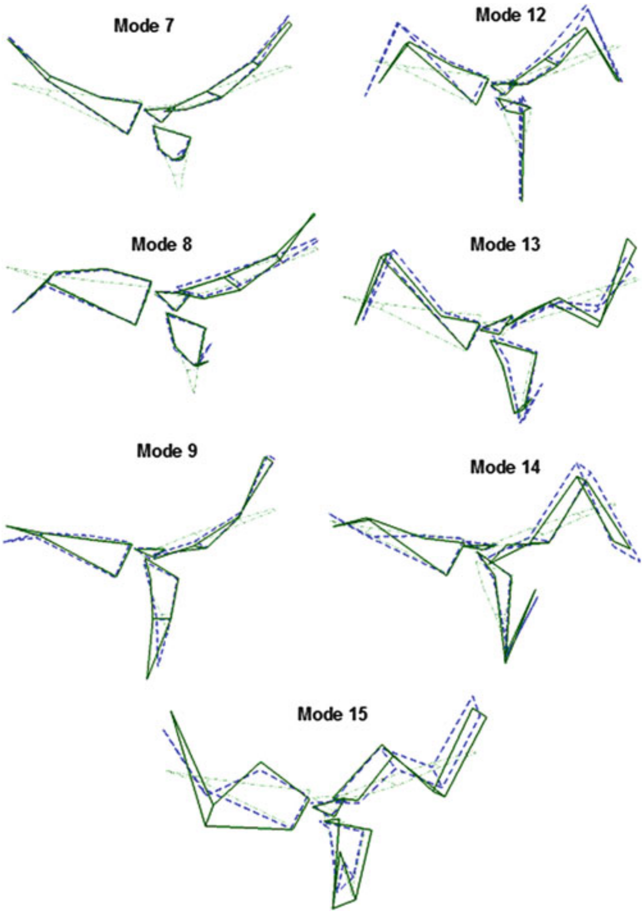

Fig. 11.8 Bending mode shape comparison (*blue* – substructured, *green* – truth test, *dashed* – undeformed)

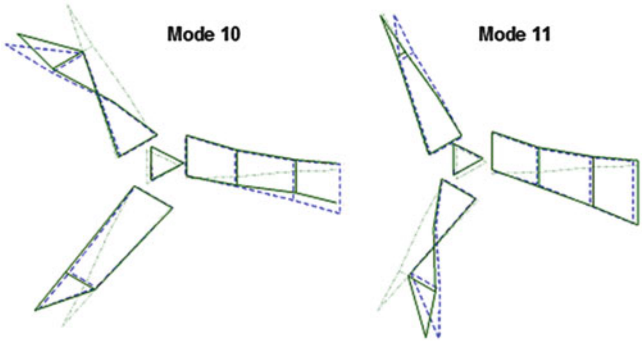

Fig. 11.9 Edgewise mode shape comparison (*blue* – substructured, *green* – truth test, *dashed* – undeformed)

and overlay the plot with the driving point FRF taken from experimental data. Rigid body modes are often hard to extract, but the masslines of these rigid body modes can be compared in such a plot. Figure 11.10 shows a massline comparison for our substructure. After the rigid body modes, around 1–2 Hz, the massline magnitude should be similar between the analytical and measured FRFs. If this is not true, the mass properties used to calculate the rigid body modes may be off and could be adjusted to get a better model of the system.

Additional best practices were followed when setting up and performing the experiments. Hammer calibration lab reports showed up to 15 % variation of hammer measurement sensitivity. To mitigate this large error source the hammer sensitivity was adjusted using a large block of known mass with a high sensitivity accelerometer attached. The hammer sensitivity was adjusted and checked to within accelerometer specified accuracy.

Also, as mentioned previously, multiple reference locations were used. In the final model the best fit for each elastic mode shape was utilized. The circles in Fig. 11.6 show which reference locations provided the best fit for each elastic mode.

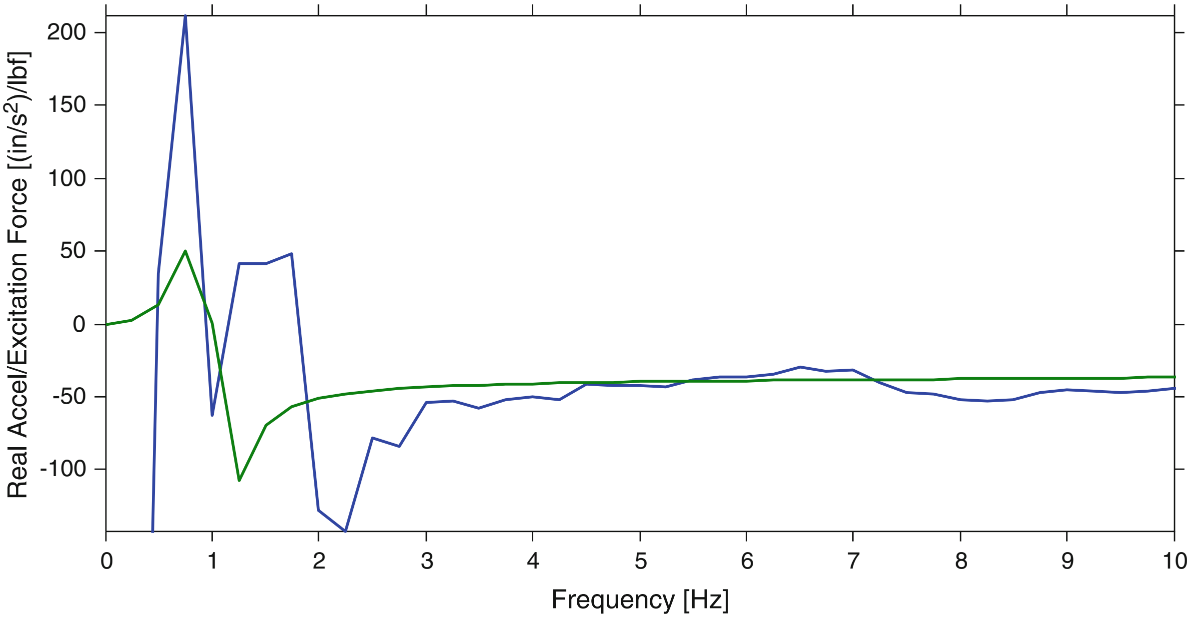

Fig. 11.10 Rigid body massline comparison: *blue* – measured data, *green* – analytical model

11.5.2 Transmission Simulator Stiffness

This exercise was completed assuming the transmission simulator was completely rigid and therefore only the rigid body modes of the transmission simulator were used. The flanges were mounted on a shaft that extends into a mechanism within the hub. This mechanism was potted, but it was observed that small amounts of flexibility may still be present. Ignoring this flexibility means the transmission simulator model was too stiff and may have led to the increased natural frequencies as seen in modes that strain this potting the most.

11.5.3 Accelerometer Mounting

The accelerometers used on the rotor hub and Blade A were not removed between the testing of the hub-and-three-bladed and single-blade-and-hub systems. Therefore, they are in the same position from test to test. Blades B and C were instrumented individually for the hub-and-three-bladed test. Small discrepancies were found in the placement of the accelerometers on Blades B and C when compared to those of Blade A. These deviations on the order of one-eighth of an inch could lead to errors when results from Blade A are rotated and assumed to be in the same locations but in the Blade B and C coordinate systems. An additional substructuring exercise was completed using the six degrees of freedom of the center of mass of the hub as the connection degrees of freedom to abate these measurement discrepancies. This method led to a small change in natural frequency (less than 2 %).

11.5.4 Damping Errors

Calculated damping ratios had the highest errors. When assembling the system the damping is all placed on the diagonal of the damping matrix when in reality there are coupled terms within the damping matrix. Neglecting these coupled terms makes the mathematics simpler but leads to less accurate results than desired. Further investigation would be warranted to attempt to include these coupled damping terms in the substructuring process.

11.6 Conclusions and Future Work

This exercise used results from a modal test of a single-blade-and-hub substructure to create a model of a full hub-and-three-bladed assembly. This substructure was rotated and linked together generating three blades and three hubs (transmission simulators), thus two of the hubs were analytically removed. The results of this substructuring exercise were then compared to an experiment conducted on the full hub-and-three-bladed assembly. The rigid body modes for these cases were constructed from mass properties.

After substructuring, all elastic modes could be correlated to the truth model either through MACs or using visual shapes. The worst frequency error was about 15 % in the first mode. The damping ratios were the most difficult to predict with error as high as 55 %. MAC values ranged from 0.77 to 0.99. Future work to improve these measurements could be completed by measuring the elastic modes of the transmission simulator by mass loading the flanges and completing another substructuring exercise. Further investigation of the system damping to include the coupling terms may also be of interest to look at improving substructure modal damping ratio predictions.

References

1. Allen M, Mayes R, Bergman E (2010) Experimental modal substructuring to couple and uncouple substructures with flexible fixtures and multi-point connections. J Sound Vib 329:4891–4906. doi:10.1016/j.jsv.2010.06.007
2. Mayes R, Allen M, Kammer D (2013) Correcting indefinite mass matrices due to substructure uncoupling. J Sound Vib 332:5856–5866. doi:10.1016/j.jsv.2013.05.025
3. Allen M, Kammer D, Mayes R (2012) Metrics for diagnosing negative mass and stiffness when uncoupling experimental and analytical substructures. J Sound Vib 331:5435–5448. doi:10.1016/j.jsv.2012.06.024
4. Mayes R (2012) An introduction to the SEM substructures focus group test bed – the Ampair 600 wind turbine. In: Proceedings of the 30th international modal analysis conference, Orlando, February 2012
5. Rohe D, Mayes R (2013) Coupling of a bladed hub to the tower of the Ampair 600 wind turbine using the transmission simulator method. In: Proceedings of the 31st international modal analysis conference, Garden Grove, February 2013
6. Gross J, Oberhardt T, Ruess P, Gaul L (2013) Model updating of the Ampair wind turbine substructures. In: Proceedings of the 32nd international modal analysis conference, Orlando, February 2013
7. Hensley D, Mayes R (2006) Extending SMAC to multiple references. In: Proceedings of the 24th international modal analysis conference, St. Louis, Missouri, pp 220–230, February 2006
8. Carne T, Griffith T, Casias M (2007) Support conditions for experimental modal analysis. Sound Vib 41:10–16
9. Rohe D, Allen M (2012) Investigation into the effect of mode shape errors on validation experiments for experimental-analytical substructuring. In: Proceedings of the ASME 2012 international design engineering technical conferences & computer and information in engineering conference, Chicago, August 2012

Chapter 12
Quantifying Epistemic and Aleatoric Uncertainty in the Ampair 600 Wind Turbine

Brett A. Robertson, Matthew S. Bonney, Chiara Gastaldi, and Matthew R.W. Brake

Abstract Determining the uncertainty in a mechanical joint is very important and very difficult. This paper presents two methods of determining the uncertainty in the joint: maximum entropy approach and sampling methods. Maximum entropy is an approach that can quantify the aleatoric and epistemic uncertainty independently. This approach is applied on a rigid connection of the Ampair 600 Wind Turbine and shows that the epistemic uncertainty of the system is very high. Sampling methods are used on an simplified representation of the wind turbine as a lumped mass approximation. The sampling methods are able to treat the joint in a nonlinear sense by using a discrete four-parameter Iwan model as the joint model. This is able to predict accurately the data within the uncertainty bounds when considering epistemic uncertainty. The Iwan joint model is then implemented on the high fidelity model and preliminary results are presented.

Keywords Uncertainty • Iwan models • Ampair wind turbine • Decoupling • Nonlinear • Joints

12.1 Introduction

Determining the uncertainty in a mechanical joint is vital to model correctly the global system. The dissipation of energy through a joint can lead to higher damped systems than what is designed. While characterizing the uncertainty, there are two main types of uncertainty that are important to consider: aleatoric (parameter-based) and epistemic (model-based) uncertainty. Aleatoric uncertainty accounts for part to part variability and epistemic uncertainty corresponds to the uncertainty due to the unknown physics in the system such as model form error. In order to characterize this uncertainty, two different methods are used in this research: maximum entropy and sampling methods.

Maximum entropy is an approach to quantify uncertainty that can determine the distribution of both the input and output variables [1]. This is combined with random matrix theory to create a set of model variables that maintain a positive definite matrix [2] and used for linear systems. Nonlinear systems can also use this method with some slight changes [3]. This approach is able to treat the aleatoric and epistemic uncertainty independently by determining the distribution of the parameters using experimental data to select an optimal dispersion parameter, which can be thought of similar to the coefficient of variation [4]. New advances in the maximum entropy approach are ongoing [5].

Sandia National Laboratories is a multi-program laboratory managed and operated by Sandia Corporation, a wholly owned subsidiary of Lockheed Martin Corporations, for the U.S. Department of Energy's National Nuclear Security Administration under Contract DE-AC04-94AL85000.

B.A. Robertson
Arizona State University, Phoenix, AZ, USA
e-mail: barober@sandia.gov

M.S. Bonney
University of Wisconsin-Madison, Madison, WI, USA
e-mail: msbonney@wisc.edu

C. Gastaldi
Politecnico di Torino, Torino, Italy
e-mail: chiara.gastaldi@polito.it

M.R.W. Brake (✉)
Sandia National Laboratories, Albuquerque, NM, USA
e-mail: mrbrake@sandia.gov

M. Allen et al. (eds.), *Dynamics of Coupled Structures, Volume 4*, Conference Proceedings of the Society for Experimental Mechanics Series, DOI 10.1007/978-3-319-15209-7_12

Sampling-based methods are the most robust uncertainty techniques available. They generate sets of samples according to the probability distributions of the uncertain variables and map them into corresponding sets of response functions. Advantages of sampling-based methods include their relatively simple implementation and their applicability to a various set of problems, including those with friction-induced nonlinearities. The importance of developing stochastic models of friction interfaces, such as bolted joints, is highlighted in [6]. The approach of [6] allows for parameter distributions to account for the joint-to-joint variability given by the extreme sensitivity to the exact conditions of the assembly.

The system chosen to test these methods is the Ampair 600 Wind Turbine [7, 8] because of the extensive data set for the experimental measurements from multiple labs available on-line [9]. Additional testing is needed for several types of data that are unavailable. There are three blades that connect to a hub that is significantly more massive. The bolted connections are of particular interest in describing the nonlinearities.

There are several ways to model a bolted joint. This research considers two methods: treating the joint as a rigid connection and treating the joint with a discrete four-parameter Iwan model [10]. This paper presents additional testing in Sect. 12.2 to compliment the available data that is online [9]. In Sect. 12.3, the maximum entropy approach is applied to the rigid connection. Section 12.4 develops a simplified model of the wind turbine in which the joint is modeled using the four-parameter Iwan model and the uncertainty is quantified with sampling methods. Preliminary results of the implementation of Iwan joints on the high fidelity finite element model of the wind turbine are also included. Lastly, conclusions are presented in Sect. 12.5.

12.2 Additional Testing

The system of investigation is the Ampair 600 Wind Turbine. The model for the Ampair 600 Wind Turbine is developed by [7]. The available test data does not contain all of the necessary measurements for model validation. Thus, in order to validate the model to a high accuracy level, additional testing is performed. Two sets of experiments are reported: a measurement of the hub by itself in order to calibrate the finite element (FE) model, and a measurement of the hub with a single blade attached in order to deduce the parameters for the Iwan model.

12.2.1 Hub Only Test

In order to build confidence in the models, it is important to have a sufficient set of experimental data to enable model validation. Experiments are conducted to ensure that the material properties of the components inside the hub are modeled correctly. In order to do this, an impact hammer test is performed to obtain the natural frequencies of the system and compare those to the results of an eigenvalue analysis using SIERRA [11], which is a FE code created by Sandia National Laboratories specializing in parallel solving of large FE problems. The impact hammer test consists of placing multiple single- and tri-axial accelerometers around the bungee-suspended hub and using a roving hammer technique to excite the system as seen in Fig. 12.1. The software used for these tests is NX-Ideas, and a Matlab program that uses the SMAC algorithm [12] is used to analyze the data received and create frequency response functions (FRFs).

The wind turbine hub is a system that exhibits a large number of nonlinear behaviors as there are many joints throughout it. Additionally, a resin fills all of the internal gaps in the hub in order to hold the components together. If the resin contains any holes or gaps that might allow sub-components to move, nonlinearities could be seen in the system's response.

The impact hammer test provide results for the first three natural frequencies at 800, 1,250, and 2,300 Hz. Due to similar test data and predicted values from the model [9], the natural frequencies at 1,250 and 2,300 Hz are used to further calibrate the model. The first natural frequency is neglected in the calibration as differences between the model and measurements persist that are most likely due to the degradation of the resin or possible damage that it could have experienced since assembly. The material properties of the hub and its components were obtained from [8].

12.2.2 Hub and One Blade: Testing for Nonlinearities

The second set of experiments is an impact hammer test on the hub with one blade attached. Accelerometers are placed on both the hub and blade. Different loading levels are used to see if there is an amplitude dependent nonlinearity in the system.

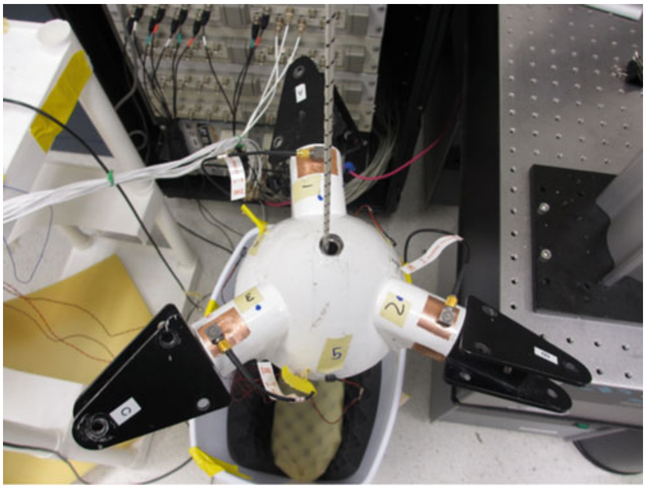

Fig. 12.1 Hub only impact hammer test

Fig. 12.2 Hub and one blade

The test apparatus includes two bungee cords, one around the hub and one around the blade, simulating a free-free system. Modes seen by resonance in the bungee cords (i.e. bungee modes) are significantly lower in frequency than the modes of this system. This apparatus and system can be seen in Fig. 12.2.

The impact hammer test included load levels of 4, 7, 10, and 45 pounds. Multiple hits are measured at multiple spots throughout the system and an averaging is used to calculate the FRF at each impact location. Figure 12.3 shows the differences in the FRFs for the different load levels.

For the first two natural frequencies, small changes are observed in the peak magnitudes and damping ratios, but not in the frequencies. For the third natural frequency, however, a nonlinear response is observed as the peak shifts 10 Hz in frequency between the 4 and 45 pound hammer impacts.

12.3 Maximum Entropy Approach

The goal of this research is to analyze the uncertainty quantification of the epistemic and aleatory uncertainty independently of each other. One way to achieve this is to performed a maximum entropy analysis. The approach used here is a combination of maximum entropy and random matrices as proposed by Soize [1]. This approach involves using independent domains for the parameter, or aleatoric, uncertainty and the model form, or epistemic, uncertainty.

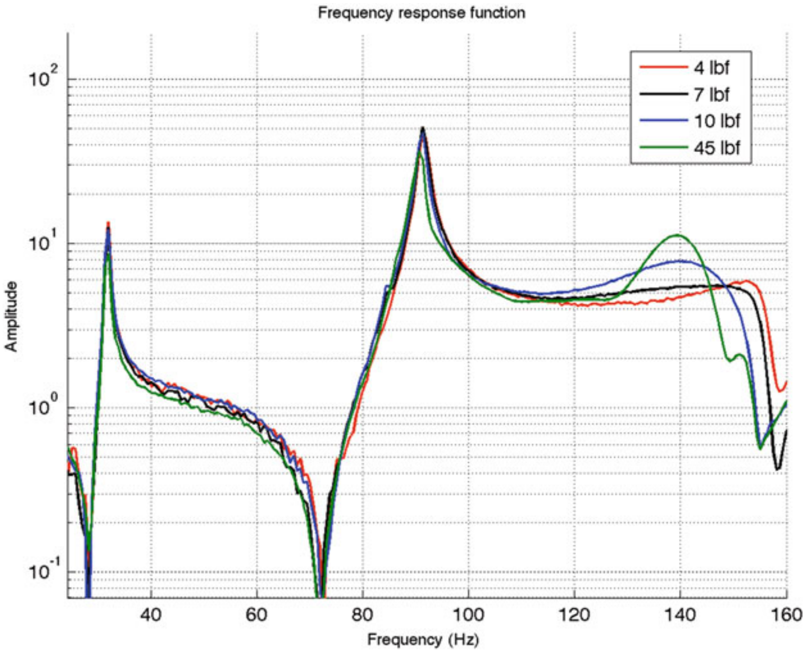

Fig. 12.3 Frequency response of hub and one blade system, different load levels performed

12.3.1 Background

Soize's method [3] is developed for two cases: (1) some experimental data is available, and (2) no experimental data is available. In the following research, some experimental data is available; thus, only the first case discussed in [3] is presented. In a typical model updating, there are many unknowns. This method, however, only uses select truth data in order to determine the unknowns [3]. For this analysis, two main pieces of data are used: the natural frequencies of the system along with the FRF at a specific point. The analysis allows for using the FRF at multiple points in order to get a more accurate system, but for the present research only one FRF is used. A more detailed explanation of how to implement this approach can be found in [4].

The first step to implement this approach is to develop a reduced order model (ROM) of the system that has been validated/calibrated to represent accurately the system. A ROM is important because of the computational burden of this approach, which involves several Monte-Carlo (MC) analyses. Along with the ROM, a set of truth or experimental data is required to use the format laid out in this section. The second step is to decide which variables would be considered parameter variables and which ones would be considered model variables. In [1], physical variables, such as Poisson's ratio and the elastic modulus, are considered parameter variables and model form variables, such as the mass matrix and the stiffness matrix, are classified as the model variables. Once the determination of which variables are parameter and which are model variables, each variables is treated stochastically.

For the next step, a sweep is done for the parameter variables. The sweep is to determine the uncertain dispersion variables for each parameter, which can be classified in several ways, for example: unbounded parameters, semi-positive parameters, and positive parameters. Each one of these cases have different distributions based on the maximum entropy of each probability density function (PDF). For the unbounded parameter (a range of $(-\infty, \infty)$), the distribution is that of a normal distribution and the uncertainty variable is considered the coefficient of variation. For a semi-bounded parameter of the range of $[0, \infty)$, a gamma distribution, which takes a special form as presented later in this section, is used with a scale parameter of one [2]. This distribution is implemented into random matrix theory in order to generate an ensemble of matrices that follow the characteristics of the mass and stiffness matrices. These characteristics are: positive definiteness and full rank. The random matrices used are forced to be positive definite, which prevents there from being any rigid body modes in the system. For more information about how to account for rigid bodies, refer to [4]. In order to generate this ensemble that meets all of the characteristics that are desired, a decomposition of the matrices is done. For this parameter sweep, each parameter is treated as a 1×1 matrix then randomized. The mass matrix, and any other matrix that is randomized, must still be positive definite, allowing for a Cholesky decomposition to be used to decompose the matrices. The Cholesky decomposition takes the form of Eq. (12.1), where [M] is the mass matrix in this example and $[L_M]$ is an upper-triangular matrix

$$[M] = [L_M]^T [L_M]. \tag{12.1}$$

Once the decomposition of the matrix is calculated, a random germ is added that generates a stochastic ensemble that meets the desired requirements. This addition can be seen in Eq. (12.2), where $[\boldsymbol{G}]$ is the random germ

$$[\boldsymbol{M}] = [L_M]^T [\boldsymbol{G}][L_M]. \tag{12.2}$$

The random germ is a nearly diagonal matrix where the expected value of the matrix is an identity matrix. The random germ is created by using a gamma distribution on the diagonal terms and zero mean normal variables on the off-diagonal terms. All of the terms in the random germ depend on the dispersion variable, which is the value that is swept. The dispersion variable is not dependent on the size of the system but is bounded by it. The range on the variable is $[0, \sqrt{\frac{n+1}{n+5}})$, where n is the size of the matrix or the number of degrees of freedom. This random germ is also positive definite so it can be decomposed by using a Cholesky decomposition. The off-diagonal terms in the Cholesky decomposition are determined by using Eq. (12.3), and the diagonal terms are determined via Eq. (12.4)

$$\sigma_n = \frac{\delta}{\sqrt{n+1}} \ [\boldsymbol{L}_{\boldsymbol{g}}]_{ij|j>i} = \sigma_n \boldsymbol{Z_{ij}} \ \boldsymbol{Z_{ij}} \sim N(0,1) \tag{12.3}$$

$$[\boldsymbol{L}_{\boldsymbol{g}}]_{jj} = \sigma_n \sqrt{2\boldsymbol{V_{jj}}} \ \boldsymbol{V_{jj}} \sim \Gamma(\tfrac{n+1}{2\delta^2} + \tfrac{1-j}{2}) \tag{12.4}$$

where $\boldsymbol{Z_{ij}}$ is a standard normal distribution, σ_n is a scaling factor, and $[\boldsymbol{L}_{\boldsymbol{g}}]$ is an upper triangular matrix used in the Cholesky decomposition of the random germ. For the parameter sweep $n = 1$, which results in the dispersion variable ranging from [0,1/3). A MC analysis is conducted for each combination of values for the dispersion variables, and the number of MC samples is determined based on the number of parameters in the analysis. For each MC analysis, the probability that the experimental data lies within the calculated PDF is needed. This probability is calculated via the maximum likelihood criterion [3], which uses the measured natural frequencies and is given in Eq. (12.5). In order to reduce the complexity of this problem, it is assumed that each natural frequency is independent. Taking the natural log of this function allows the product of probabilities to become a summation. The natural log is also a monotonic function so the maximum of the natural log of a function occurs at the same location as the maximum of the original function. The final form of the likelihood function is shown in Eq. (12.5), where δ_k is the dispersion variable, $P_i(X_{truth}|\delta_k)$ is the probability that the truth value lies within the distribution with the given dispersion variable, which is calculated with a histogram within a tolerance of the true value, δ^{opt} is the dispersion variable that provides the optimal distribution to match the experimental data, and i is the index on the truth data such as each natural frequency

$$\delta^{opt} = \text{argmax} \sum_i \ln[P_i(X_{truth,i}|\delta_k)]. \tag{12.5}$$

The likelihood function is compared for each combination k of dispersion variables. The combination of dispersion variables that creates the maximum value is then selected as the dispersion variables for each parameter and these dispersion variables are then fixed for the rest of the analysis.

The next step is to analyze the model form error. This step involves performing a sweep of the dispersion variables for the matrices being used. This analysis uses a linear system in order to solve for the natural frequencies and FRFs. The matrices that are used are the mass and stiffness matrices. Each of these matrices follow the positive definite stochastic matrices as previously discussed. The main difference between the two sweeps is that for the model variable sweep, the FRF is used to calculate the likelihood function while the parameter variable sweep uses the natural frequencies to calculate the likelihood function. The frequency response function is not directly used to compute the likelihood function, instead a Z variable is used to consider the FRF in terms of a decomposition that is a statistical reduced representation, similar to a Karhunen-Loeve expansion [3].

In order to use this reduced representations, several new variables are defined. The first vector that is defined is the random observed vector $\mathbb{Y}$ which is a $n_{obs} \times n_{freq}$ vector where n_{obs} is the number of MC samples used and n_{freq} is the number of frequency points that is done experimentally. This vector is defined for each combination of values of the dispersion variable for the model variables. The mean and covariance of each of these vectors are defined according to Eq. (12.6) where $\mathbb{M}_{\mathbb{Y}}(\delta_G)$ is the mean vector, $[C_{\mathbb{Y}}(\delta_G)]$ is the covariance matrix, and $E[]$ is the expected value function

$$\mathbb{M}_{\mathbb{Y}}(\delta_G) = E[\mathbb{Y}]\ [C_{\mathbb{Y}}(\delta_G)] = E[(\mathbb{Y} - \mathbb{M}_{\mathbb{Y}}(\delta_G))(\mathbb{Y} - \mathbb{M}_{\mathbb{Y}}(\delta_G))^T]. \tag{12.6}$$

Once these variables are calculated, the covariance matrix is then decomposed by performing an eigenvalue decomposition, with the jth eigenvalue $\lambda_j(\delta_G)$ and the jth eigenvector $\mathbb{H}^j(\delta_G)$ both sorted in descending order. After these variables are calculated, the Z variable is defined. The jth value of Z is calculated via to Eq. (12.7), with the inner product denoted by $<, >$

$$Z_j = \frac{1}{\sqrt{\lambda_j(\delta_G)}} < \mathbb{Y} - \mathbb{M}_{\mathbb{Y}}(\delta_G), \mathbb{H}^j(\delta_G) > . \tag{12.7}$$

Not every value of Z needs to be computed. A subset of Z can be used to decrease computation time since these vectors can be very large. The same transformation as in Eq. (12.7) can be done for the experimental FRF. Once the Z parameters are compared by using the likelihood function, the maximum of the likelihood function is used to determine the dispersion variables for each of the matrices as seen in Eq. (12.5), where i is the number of Z parameters that are used in the comparison. Since the dispersion variable is then known for each the parameters and for the model form, a large MC analysis is done in order to get final distributions of the desired quantities.

12.3.2 Results

Maximum entropy [1] is applied to the Ampair 600 wind turbine [8] in order to calculate the distribution of the natural frequencies for two cases: when only aleatoric uncertainty is considered, and when both aleatoric and epistemic uncertainty are considered. The first five natural frequencies predicted by the analysis are compared to those of the measurements of the single bladed assembly (Sect. 12.2.2). Known epistemic uncertainty is introduced through modeling the bolted connection between the blade and the hub as a rigid attachment. Results from this over-simplifying assumption are able to serve as a baseline for comparison with other methods in order to determine an accuracy verses time investment for different methods of modeling the bolted connection in this system.

A high fidelity model developed using SIERRA [11] is reduced by considering the model in the modal domain. This allows for quicker computations and for a more in depth investigation to be performed. For this investigation, the first five natural frequencies are of interest, which spanned up to 200 Hz. The reduced model consists of the first nine modes, which spanned up to 400 Hz. The number of MC samples is picked to be 500 for the determination of the likelihood function and 100,000 to calculate the final PDFs with only aleatoric uncertainty and with both aleatoric and epistemic uncertainty. In this analysis, six parameter variables (the elastic moduli of five different materials and the shear modulus of blade's orthotropic shell) and two model form variables (the mass and stiffness matrices) are used, and damping is added to the model form as 1.0 % modal damping in order to prevent computational instabilities at the natural frequencies.

The results show that the dispersion variable for each of the parameter variables to be less than 0.5 %. The model variables had considerable large dispersion variables of 55 % and 75 % for the stiffness and mass matrices respectively. Due to the size of the system the upper range for the dispersion variable is 85 %. The largest effect of this can be seen in the first natural frequency. The PDF of the first natural frequency can be seen in Fig. 12.4, which shows the histogram while only considering aleatoric uncertainty (Fig. 12.4a), and the histogram when both aleatoric and epistemic uncertainty is considered (Fig. 12.4b). The vertical line represents the measured natural frequency.

The main result from Fig. 12.4 is that the mean of the natural frequency closer approximated the natural frequency that is obtained experimentally when epistemic uncertainty is accounted for. The results from the MC analysis are presented in Table 12.1. For the first two modes, accounting for both aleatoric and epistemic uncertainty made the mean of the PDF closer to the experimental data. For the higher modes, it is less clear if the consideration of epistemic uncertainty improved the results. It is expected that expanding the ROM to include more modes will yield better accuracy of the higher frequency modes because this mitigates the error due to modal truncation.

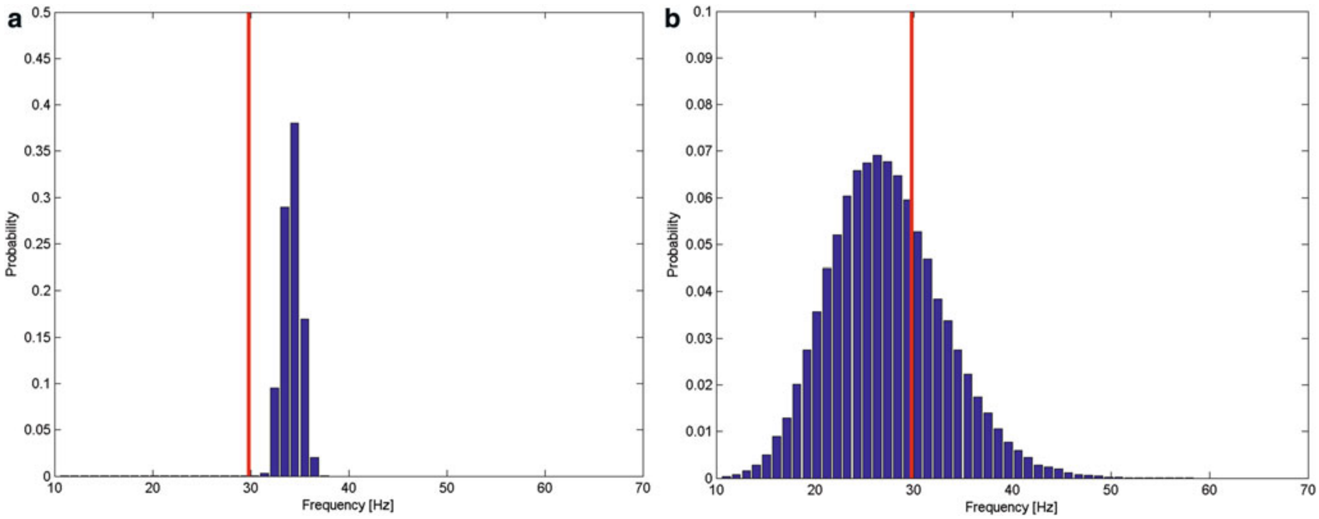

Fig. 12.4 Histograms of first natural frequency where the *red line* is the experimental data and the *blue curve* is the histogram for (**a**) with only aleatoric uncertainty and (**b**) with both aleatoric and epistemic uncertainty (Color figure online)

Table 12.1 Mean natural frequencies from different uncertainty models (Hz)

Mode	Experimental	Nominal model	Aleatoric only	Aleatoric and epistemic
1	29.839	34.667	33.717	29.824
2	86.75	95.877	92.93	79.638
3	150.65	160.82	154.54	123.19
4	178.25	177.38	171.45	164.64
5	195.1	191.36	186.38	216.17

12.4 Iwan Joint

Following the application of Soize's method [1] to a linearized system, a more realistic system that models the bolted connections with Iwan models is considered. The four-parameter Iwan model [10] is used to characterize the nonlinear and dissipative behavior observed at the bolted joint interface between hub and blade. The sensitivity to the exact conditions of the assembly and the difficulty in determining exact values of contact parameters calls for an uncertain formulation of such a model.

In what follows, a parametrically defined probability density function (due to the limited availability of data) is used in the analysis with assumptions stated in Sect. 12.4.1 and the framework for a nondeterministic sampling method presented in Sect. 12.4.2. The model is based on a lumped mass system that represents the mass-hub portion of the Ampair 600 Wind Turbine. The analysis focuses on both uncertainty quantification and parameter sensitivity: exploring the input domain to obtain a better understanding of the variability of the outputs provides an added value to any design tool, especially in cases (such as contact models) where it is difficult to estimate the input parameters. Section 12.4.3 describes the implementation of an Iwan joint into the high fidelity model within Sierra.

12.4.1 Assumptions for the Parameter Distributions

Useful strategies to calculate appropriate distributions include expansion-type representations (e.g. polynomial chaos) and maximum entropy concepts. In this paper the maximum entropy concept is selected by choosing distributions which maximize the spread of each variable. The assumptions made to perform the parametrization are stated beforehand.

- Due to the lack of data coming from the direct experimental observation of the Ampair 600 Wind Turbine the parameters χ, β and K_{Tbolt} are deduced from the available database constructed from other single-bolt jointed interfaces available at Sandia National Laboratories. These parameters are considered independent from each other.

Table 12.2 Iwan model parameters distributions

Parameters	Method	α	λ
$\chi + 1$	Moments	90.025	0.0029218
	Max. likelihood	87.642	0.0030012
β	Moments	0.83801	0.088759
	Max. likelihood	1.6684	0.044584
K_{Tbolt}	Moments	77.986	1.25e+005
	Max. likelihood	67.211	1.458e+005

- The stiffness of a single bolt can be deduced from the available data on similar joints, as described above. However since the goal is to characterize an interface jointed by three bolts an additional assumption has been made. Using the available experimental data as a comparison the stiffness of the interface $K_{Tinterface} = 2 \cdot K_{Tbolt}$.
- The mean value of the slip force F_S is deduced from the following empirical calculation and assumptions. Each bolted interface is composed by three 5/16″–18 bolts, each of which, when tightened to the prescribed torque value of 157 $in \cdot lbf$, exerts an axial clamping force of 3,072 lbf. Assuming a friction coefficient that can vary between 0.2 and 0.8 the limiting friction force is assumed to have a uniform distribution [614–2,457] lbf. These values are consistent with the ones coming from the database (min $=$ 100 max $=$ 5,000 lbf). Considering three bolts are clamping together the interface the final distribution will be [1,842–7,371] lbf = [$8183 - 32.7 \cdot 10^3$] N.
- Apart from the parameter F_S, which has already been assigned a uniform distribution, the other three parameters still need to be assigned a proper distribution shape. Referring to [6], since the parameter χ must be larger than -1, it is proposed that $\chi + 1$ be represented in terms of a Gamma random variable. A similar modeling of the stiffness K_{Tbolt} and the coefficient β is also proposed.

The parameters for each of the gamma distributions are derived using both the moments and the maximum likelihood method on the available database. The two approaches yield comparable results (as shown in Table 12.2), but the maximum likelihood approach is preferred since the method of moments yields for the case of β a distribution that is almost exponential. Due to the fact that it is not feasible to have a null β (it would mean no stiffness discontinuity at macroslip, therefore an infinite number of elements) the exponential approximation is not the correct fit.

12.4.2 Uncertainty Propagation on a Lumped Mass Model

Once the Iwan-model parameters are made uncertain, their effect is evaluated on the output quantities of interest. Sampling-based methods are the most robust uncertainty techniques available, are applicable to almost all simulations, and possess rigorous error bounds; consequently, they can be used whenever the function is relatively inexpensive to compute and adequate sampling can be performed. The main drawback of these techniques is the large number of function evaluations needed to generate converged statistics. Latin HyperCube Sampling (LHS) techniques, in general, require fewer samples than traditional Monte Carlo for the same accuracy in statistics. The LHS package is offered by Dakota, which is used to perform this analysis [13].

12.4.2.1 Tuning Protocol

The lumped mass model is composed of a set of masses and a set of springs plus an Iwan element chosen to simulate the hub + blade system (see Fig. 12.5). The mass and springs values are tuned, in both cases, to match the first three measured frequencies in the macroslip stage (see Fig. 12.3). This corresponds to exciting the actual hub with a 45 lbf hammer hit. This assumption is justified by the significant frequency shift of the third mode and by the nonlinearity shown by the Zeroed Early FFT method [14] (see Fig. 12.6). An impulse forcing function representing a hammer hit is used, with the magnitude varied across multiple simulations to excite the system in both microslip (with increasing percentage of contact elements slipping) and macroslip. To find the right force levels to excite the system in the macroslip and microslip states, a parameter sweep is been performed with Dakota, using the mean values of the Iwan parameters.

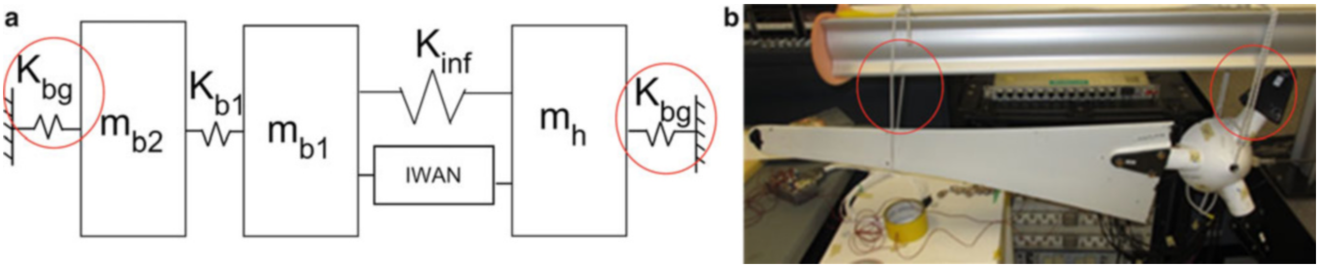

Fig. 12.5 (**a**) Lumped mass model of hub-blade system. (**b**) Hub-blade system experimental set-up

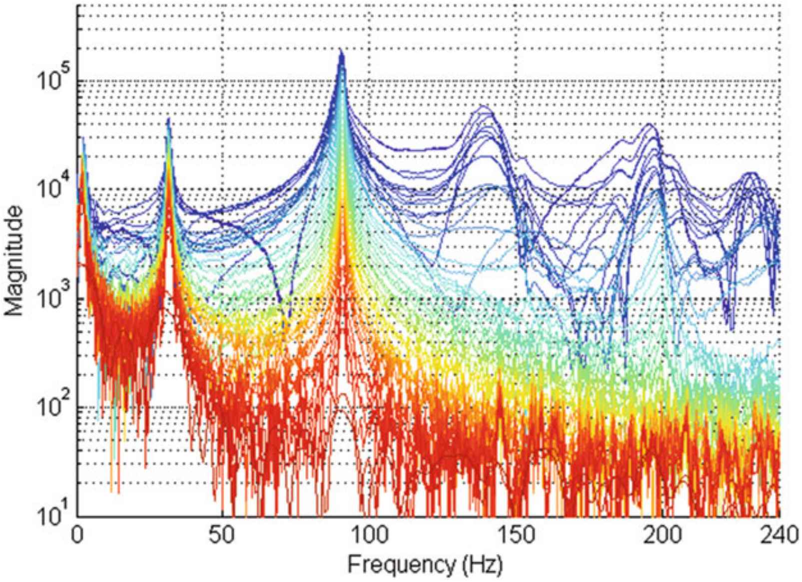

Fig. 12.6 Zeroed early fast Fourier transform of 45 lbf hammer hit showing strong nonlinearities. The *color of the lines* indicates the different ZEFFTs for an increasing zero time t_z: from 0 s (*dark blue*) to 248.4 ms (*cyan*) to 1,494 ms (*dark red*) (Color figure online)

Given the discrete nature of the model, the simulated hammer hit that causes macroslip is one order of magnitude higher than the experimental counterpart. Since this is a simple heuristic model, this is considered acceptable; the comparison with true force magnitude excitations is performed on the high fidelity model. In order to compare the results of the heuristic model with the experimental data, the forces are normalized by the values (numerical and experimental respectively) needed to obtain macroslip.

12.4.2.2 Influence of Parameters on Modes' Frequencies

The performance of the model is been verified against a broad range of forcing function levels, and compared with the experimental data available. The first mode, does not exhibit any frequency shift. This behavior is consistent with the available experimental data, despite the predicted value shifting from the experimental data (by 1 Hz). The Iwan model has no qualitatively observable effect over the frequency of this mode; in fact, no uncertainty band is obtained, which is due to the first two masses m_h and m_{b1} moving in phase. In the physical system, the first mode is a bending mode of the blade, which does not excite the bolted interface.

The second mode exhibits a slight dependence on the force level. Once again, despite a small shift (2 Hz) between the experimental and the predicted values, the behavior of the frequencies is the same: a decrease of 0.5 Hz during the transition from microslip to macroslip regime. In this case the uncertainty band is present, but its width is not sufficient to cover the gap between the experimental and the predicted values. This is due to the fact that two masses linked by the Iwan element do show a small relative motion in this mode. In the physical system the second mode is also a bending mode.

The third mode is quite sensitive to the excitation force level. In this case, the two masses connected by the Iwan element vibrate 180° out of phase. The predicted response matches the experimental data (except for one force level: 7 lbf), as shown in Fig. 12.7. In the physical system at the third mode, the blade shows an in-plane rotation against the hub.

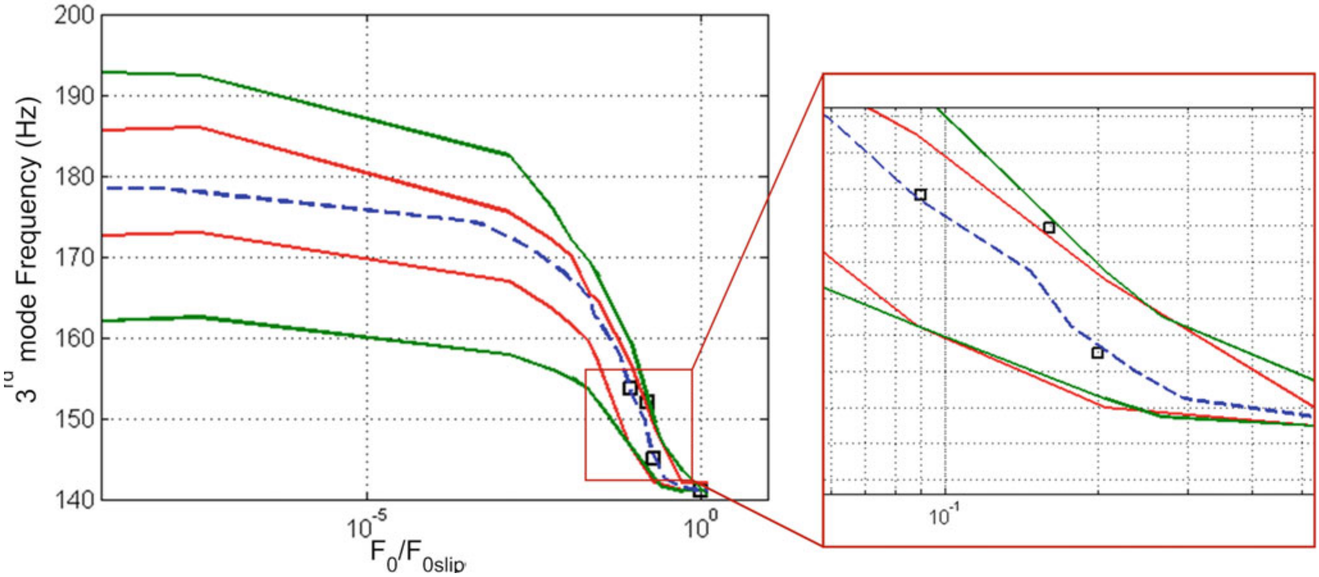

Fig. 12.7 Uncertain third mode frequency as a function of input force level. *Blue dashed line*: nominal parameter curve. *Red lines*: 5–95 % parameter uncertainty bands. *Green lines*: 5–95 % epistemic and parameter uncertainty bands. The *black squares* represent the experimental data points (Color figure online)

12.4.2.3 Accounting for Epistemic Uncertainty

Up to now the stiffness of the jointed interface is accounted for as twice that of a single bolt. However the true stiffness may be different: a reasonable assumption is a range varying from one to three times (three parallel bolts) the stiffness of a single bolt. The epistemic uncertainty regarding the joints' stiffness is turned into parametric uncertainty $K_{Tint} = s \cdot K_{Tbolt}$ where the PDF of s has a uniform distribution with bounds $[1, 3]$. The resulting uncertainty bands regarding the position of the third mode's frequency are reported in Fig. 12.7. The experimental values (represented by the black squares) now all fall within the uncertainty bands.

12.4.2.4 Sensitivity Analysis

In addition to confidence intervals, LHS accounts for correlation among variables, a useful indicator of the sensitivity of each output with respect to the input contact parameters. The nonlinearity of the model manifests itself in the behavior of the parameters, and their influence of the relevant output quantities (dependent on the excitation force). Therefore different correlation matrices are obtained depending on the excitation force level.

If the exciting force is not enough to cause slip of any of the contact elements of the Iwan model, the Iwan model itself behaves like a linear spring (see Fig. 12.8a); consequently, the parameters that most influence the position of the modes' frequencies are those connected to the stiffness of the joint (s and K_{Tbolt}). The higher the stiffness, the higher the third natural frequency. If the forcing function increases (see Fig. 12.8b), F_s (limiting friction force) gains a stronger influence (it influences the number of slipping elements) and therefore a loss of stiffness results. Parameters s and K_{Tbolt} now show a negative correlation since, the higher they are, the larger the loss of stiffness due to slipping. This happens because the distribution of the parameter β covers values close to 0, therefore the majority of the stiffness is lost during the early stages of microslip, as in Fig. 12.8b. The second mode is now affected by the parameters' variations since, given the moderate relative motion, with the right combination of parameters some slipping can be produced even at that frequency. Excitation force levels well above the macroslip limit served as a control case: the variation of parameters has no relevance since macroslip is being forced on the system.

Sensitivity analysis is performed on another quantity of interest: the dissipation per cycle. In this case the system was excited by a sinusoidal forcing function at different amplitudes and frequencies in the range (135–170 Hz). A LHS procedure with 1,000 samples is used to investigate the influence of the input contact parameters on the dissipation per cycle.

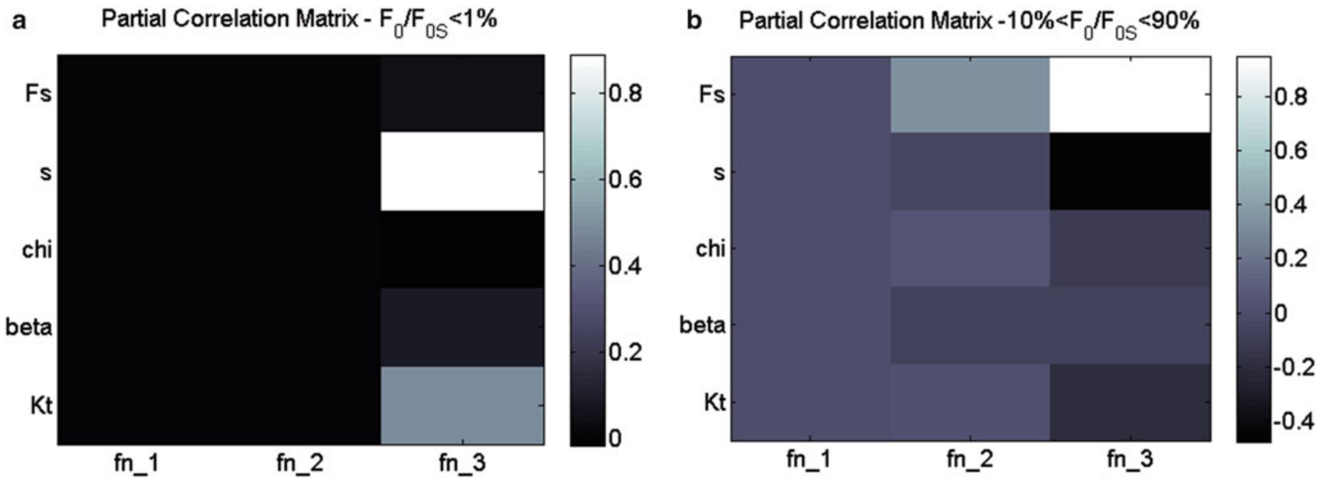

Fig. 12.8 Partial correlation matrix between inputs (Iwan model parameters) and outputs (modes' frequency). (**a**) Stick regime. (**b**) Microslip regime

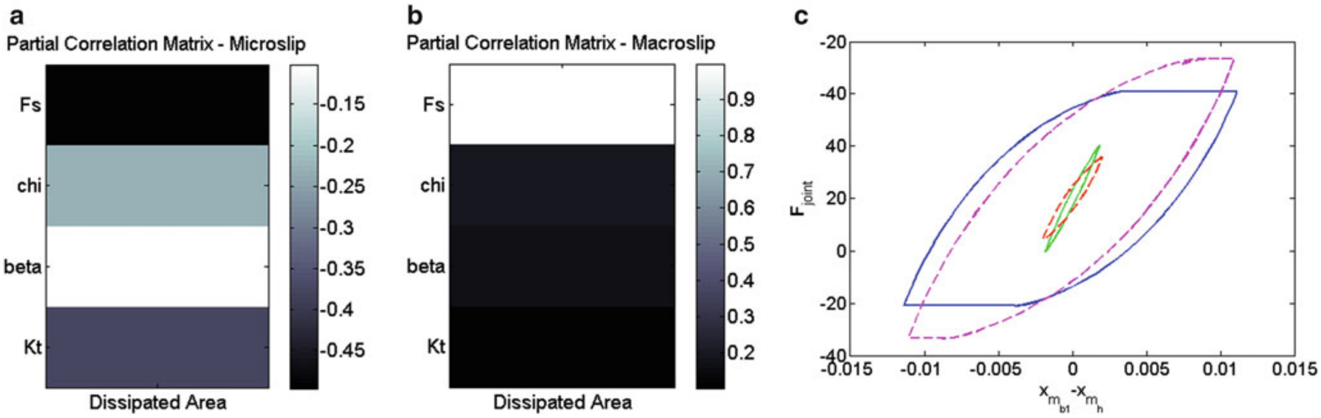

Fig. 12.9 (**a**) Partial correlation matrix between inputs (Iwan model parameters) and outputs (dissipated area per cycle) in microslip regime—small F_0 amplitude. (**b**) Partial correlation matrix in macroslip regime—large F_0 amplitude. (**c**) Hysteresis cycles for different values of parameter F_S. *Green cycle*: nominal microslip case. *Red dashed cycle*: microslip case with $F_s = 1.5 \cdot F_{snom}$. *Blue cycle*: nominal macroslip case. *Magenta dashed cycle*: macroslip case with $F_s = 1.5 \cdot F_{snom}$ (Color figure online)

As expected, the changing frequency influences the amplitude of the forcing function for which the system enters macroslip. The correlation between input parameters and dissipation is different depending on the amplitude of the forcing function and on the regime (macro or microslip). An example is given in Fig. 12.9, the two matrices have been obtained for the same frequency and different amplitude of forcing function.

It is worth noting how, when the combination of frequency and amplitude of excitation force is large enough to guarantee macroslip for any choice of the contact parameters, the limiting friction force F_S and the tangential contact stiffness $K_{Tinterface}$ are positively correlated to the output: the higher they are, the larger the area within the curve is (see Fig. 12.9c). Conversely, when the regime is microslip, F_S and $K_{Tinterface}$ are negatively correlated to the output, since the higher their value, the lower the number of contact elements inside the Iwan model to reach the slip condition.

The behavior of χ is dependent on the amplitude of the exciting force: as described by Segalman [10], the dissipation per cycle given by a harmonic input force F_0 is $D(F_0) = \nu \cdot F_0^{\chi+3}$. By computing $\frac{\partial D(F_0)}{\partial \chi}$ it is possible to find the value of $F_0 = F_0^*$ above which χ will start influencing $D(F_0)$ in a positive way. This distinction can correspond, as in Fig. 12.9, to different contact states; however, there may be cases for which an input force $F_0 < F^*(0)$, applied to a frequency close to resonance, could produce a negative correlation between $D(F_0)$ and χ even if during macroslip. Vice-versa, there could be cases where, even though $F_0 > F_0^*$, the combination of contact parameters and frequency is not enough to cause macroslip, which would result in a case of microslip with a positive correlation between χ and $D(F_0)$.

Fig. 12.10 Spider connecting interface nodes on blade

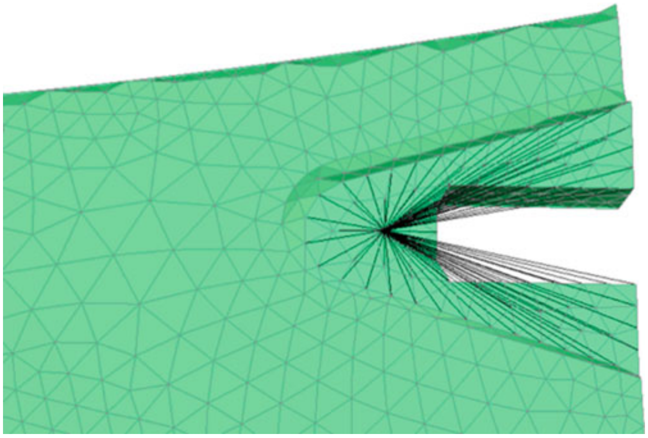

Fig. 12.11 Spider connecting interface nodes on hub flange

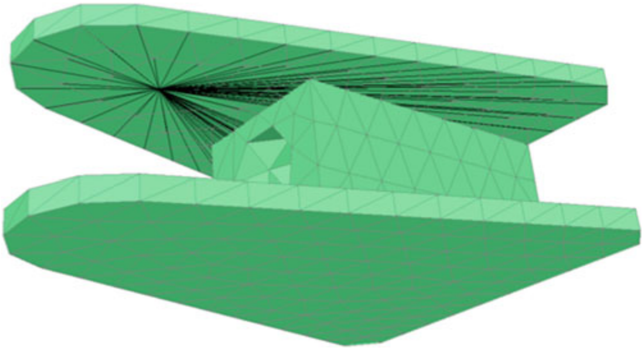

12.4.3 *Implementing Iwan Elements in High Fidelity Models*

The simplified model gives a good approximation of the system in lower order, in order to get a higher order representation, the Iwan model is implemented in the high fidelity model in order to reveal the nonlinearities in the system using SIERRA. The current process for adding an Iwan element to a model includes making a “spider-web” of rigid bars centered at a single node and extending to all of the interface nodes. An example of this “spider-web” is shown in Fig. 12.10 for the blade and in Fig. 12.11 for the hub connecting flange. Each block being connected has a center node and “spider-web” and to tie them together. The two center nodes are connected using a Joint2G with four Iwan parameters, χ, β, K_t, F_s. The Joint2G element is a spring element defined in SIERRA, which connects two nodes that can be adjusted to act as an Iwan joint for nonlinear analysis or a linear spring.

Sierra is used to replicate an impact hammer test: a haversine pulse is applied at a single node on the hub, and the response at a node on the blade is observed. Different load levels are used to see if nonlinearities exist in the system. Load levels of 5 and 5,000 N are tested in order to magnify the nonlinearities in the system. To make sure the model is correct and the Joint2G is connected correctly, the first test is run using a linear spring. The FRF for the linear transient test shows natural frequencies matching those of a test run using a model where the hub and blade are merged together.

Now that the model is verified for a linear system, the Iwan model is implemented. The Joint2G contains six degrees of freedom, each can be specified as linear or nonlinear. For the model, since the load is in the Z-axis and the first modes are rotational about the X-axis, the K_z and K_{rx} terms (i.e. stiffness in these respective dimensions) are specified as nonlinear Iwan elements and the remaining four degrees of freedom are still considered linear springs with high spring coefficients to simulate a bolted joint. A nonlinear transient test is set up with a load of a haversine pulse with amplitude and period very close to that of the impact hammer pulse from the experiment. Results from this transient test are shown in Fig. 12.12. Slight differences in the frequency response can be seen between the different load levels. The differences become more apparent as the frequency increases. Current efforts to improve these results include using a reduced model in SIERRA containing super-elements. This will allow the time step of the transient test to be reduced significantly and will possibly help solver convergence.

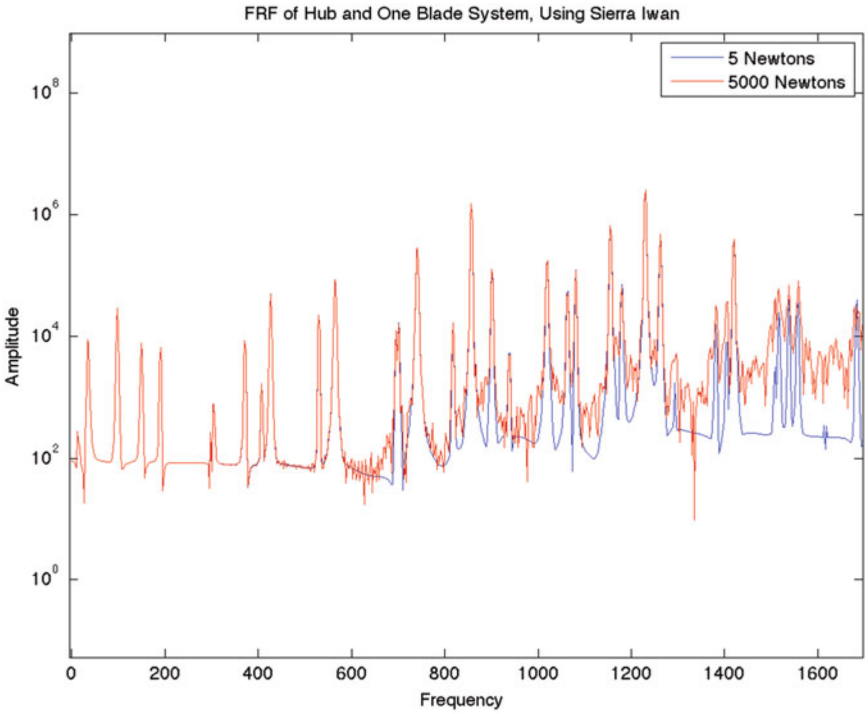

Fig. 12.12 FRF of Sierra nonlinear transient test

12.5 Conclusions and Future Work

This paper uses several methods to account for the various sources of uncertainty affecting the Ampair 600 Wind Turbine and its model. The maximum entropy method is able to describe the model form and parameter uncertainty independently. This is, however, only done for a linear system and rigid connections due to the computational requirements. The Latin hypercube sampling method is a robust and useful tool to gain an insight on the relevance of Iwan parameters (and their uncertainty) on the output quantities of interest. Investigations on simplified systems can give a valuable insight into the inner mechanism of contact models, highlighting relations between variables (see Sect. 12.4.2.4) useful for any subsequent application of the Iwan contact model. Moreover the methodology here developed is fit to be applied to more complex FE models.

Both the maximum entropy approach and the Latin hypercube sampling method show that accounting for epistemic uncertainty yields good agreement with the experimental results but, at the same time, broadens the uncertainty bands. Recognizing and accounting for the presence of epistemic uncertainty can be useful to highlight the critical areas affecting the model, but it is only the first step towards the real goal, which should be the minimization of epistemic uncertainty.

Expected future work in this field include the following: implementing the uncertain Iwan model in the high fidelity finite element model, implementing maximum entropy to decouple uncertainty in an Iwan joint connection, investigating the influence of Iwan parameters over other quantities such as damping, and investigating the accuracy of different Iwan models, such as modal Iwan, in the turbine system.

References

1. Soize C (2001) Maximum entropy approach for modeling random uncertainties in transient elastodynamics. J Acoust Soc Am 5:1979–1994
2. Soize C (2004) Random matrix theory for modeling uncertainties in computational mechanics. Comput Methods Appl Mech Eng 194: 1333–1366
3. Soize C (2010) Generalized probabilistic approach of uncertainties in computational dynamics using random matrices and polynomial chaos decompositions. Int J Numer Methods Eng 81:939–970
4. Bonney MS, Brake MRW (2014) Utilizing Soize's approach to identify parameter and model uncertainties, SAND2014-19209. Sandia National Laboratories, Albuquerque
5. Batou A, Soize C, Audebert S (2014) Model identification in computational stochastic dynamics using experimental modal data. Mech Syst Signal Process 50–51: 307–322. https://www.hal-upec-upem.archives-ouvertes.fr/hal-00989208

6. Wang XQ, Mignolet MP (2014) Stochastic Iwan-type model of a bolted joint: formulation and identification. In: Proceedings of the 24th international modal analysis conference, 2014, pp 752–760
7. Gross J, Oberhardt T, Reuss P, Gaul L (2014) Model updating of the Ampair wind turbine substructures. In: Proceedings of the 32th international modal analysis conference
8. Mayes RL (2012) An introduction to the SEM substructures focus group test bed - the Ampair 600 wind turbine. In: Proceedings of the 30th international modal analysis conference
9. Allen MS, Blecke J, Roettgen D (2014) A wiki for sharing substructuring methods measurements and information. In: Proceedings of the 32th international modal analysis conference
10. Segalman DJ (2010) A four-parameter Iwan model for lap-type joints. ASME J Appl Mech 72:752–760
11. Edwards HC (2002) Sierra framework version 3: core services theory and design, SAND2002-3616. Sandia National Laboratories, Albuquerque
12. Hensley D, Mayes RL (2006) Extending SMAC to multiple references. In: Proceedings of the 24th international modal analysis conference, 2006, pp 220–230
13. Adams BB, Bohnhoff WJ, Dalbey KR, Eddy JP, Eldred MS, Gay DM, Haskell K, Hough PD, Swiler LP (2015) A multilevel parallel object-oriented framework for design optimizations, parameter estimation, uncertainty quantifications, and sensitivity analysis. Technical report SAND2010-2183
14. Allen MS, Mayes RL (2010) Estimating degree of nonlinearity in transient responses with zeroed early-time fast fourier transforms. Mech Syst Signal Process 24:2049–2064

Chapter 13
A Craig-Bampton Experimental Dynamic Substructure Using the Transmission Simulator Method

Randall L. Mayes

Abstract Experimental dynamic substructures in both modal and frequency response domains using the transmission simulator method have been developed for several systems since 2007. The standard methodology couples the stiffness, mass and damping matrices of the experimental substructure to a finite element (FE) model of the remainder of the system through multi-point constraints. This can be somewhat awkward in the FE code. It is desirable to have an experimental substructure in the Craig-Bampton (CB) form to ease the implementation process, since many codes such as Nastran, ABAQUS, ANSYS and Sierra Structural Dynamics have CB as a substructure option. Many analysts are familiar with the CB form. A square transformation matrix is derived that produces a modified CB form that still requires multi-point constraints to couple to the rest of the FE model. Finally the multi-point constraints are imported to the modified CB matrices to produce substructure matrices that fit in the standard CB form. The physical boundary degrees-of-freedom (dof) of the experimental substructure matrices can be directly attached to physical dof in the remainder of the FE model. This paper derives the new experimental substructure that fits in the CB form, and presents results from an analytical and an industrial example utilizing the new CB form.

Keywords Experimental dynamic substructures • Substructuring • Craig Bampton

Nomenclature

CB	Craig-Bampton method of substructuring
CMIF	Complex mode indicator function
FE	Finite element model
FRF	Frequency response function
MCFS	Method of constraint for fixture and subsystem
MPC	Multi-point constraint
TS	Transmission simulator – the fixture attached to the experimental substructure of interest
dof	Degree of freedom
sdof	Single degree of freedom
p	Modal dof of the experimental substructure with fixed boundary
q	Modal dof of free modes extracted from experimental substructure with TS attached
s	Free modal dof of the transmission simulator
x	Physical displacement dof
ω	Frequency in radians per second
ζ	Modal damping ratio
K	Stiffness matrix
L_{fix}	Reduction matrix applying fixed boundary constraint to experimental equations of motion

---

Sandia National Laboratories is a multi-program laboratory managed and operated by Sandia Corporation, a wholly owned subsidiary of Lockheed Martin Corporation, for the U.S. Department of Energy National Nuclear Security Administration under Contract DE-AC04-94AL85000.

R.L. Mayes (✉)
Experimental Mechanics, NDE and Model Validation Department, Sandia National Laboratories,
P.O. Box 5800 – MS0557, Albuquerque, NM 87185, USA
e-mail: rlmayes@sandia.gov

M. Allen et al. (eds.), *Dynamics of Coupled Structures, Volume 4*, Conference Proceedings of the Society for Experimental Mechanics Series, DOI 10.1007/978-3-319-15209-7_13

M	Mass matrix
T	Transformation matrix to convert free modal model to modified CB model
Φ	Mode shape matrix extracted for experimental substructure with TS attached
Ψ	Free mode shape matrix of the TS
Γ	Eigenvectors resulting from fixed boundary constraint of experimental equations of motion
b	Subscript for the fixture or boundary
fix	Subscript for the fixed boundary modes of the experimental substructure with TS as the boundary
$free$	Subscript for the free modes obtained in the modal test of the experimental substructure with TS
$+$	Superscript indicating the Moore-Penrose pseudo-inverse of a matrix

13.1 Introduction and Motivation

Experimental dynamic substructuring has experienced a resurgence in the last 10 years. Multiple groups have been motivated to couple experimental substructures with FE substructures to obtain full system response. In general, one cannot couple the physical connection dof of the experimental substructure to the physical dof of the FE model because small errors in the experimental model will cause the coupling to be so ill conditioned that the effort will fail. There are additional challenges including:

1. Rotational connection dof are difficult to measure but can be important;
2. Translation connection dof may not be measurable either (often the connection dof are in a joint interface where transducers cannot be installed);
3. The connection dof may not actually be discrete, i.e. the connection may be a large surface contact;
4. The basis vectors from a standard free modal test may not span the space of the true connected motion well;
5. The joint stiffness and damping are often uncharacterized and usually ignored.

A method using an instrumented fixture known as a transmission simulator (TS), originally dubbed the method of constraint for fixture and subsystem (MCFS) [1], mitigates these problems. By attaching the fixture to the desired substructure in the same way it will be attached to the rest of the system, which will be modeled as a FE substructure, the joint stiffness and damping are captured. The TS can be instrumented at only translational dof that capture the motion of the connected TS in a truncated set of the free modes of the TS. Generally, the TS is a relatively simple structure that can be modeled with FE to help plan where to mount the instrumentation. The fixture is designed so that accelerometers may be mounted in convenient locations and directions. Ultimately the generalized dof of the TS are used to couple the experimental substructure to the FE model of the rest of the system. Because the generalized dof inherently contain the rotational dof, these are no longer being neglected. As long as the retained modes of the TS capture the connected motion, the method can even capture continuous, not just discrete, connections. For this reason, the method becomes a tremendous tool for providing a reduced order model. Originally, the TS method utilized multi-point constraints (MPC's) to couple the experimental substructure generalized coordinates to the FE model of the rest of the system, which removed most of the ill conditioning that is seen when one attempts to couple the measured physical dof directly. This improvement is due to a least squares fitting of the physical motion to the generalized dof that does not require that the errors in the experimental measurements have perfect continuity with the physical FE dof to which they will ultimately be attached.

However, this approach has been utilized mostly in third party codes such as MATLAB for the coupling, since FE codes often do not allow MPC's to couple generalized to generalized or generalized to physical dof. This makes it awkward to implement the experimental model directly in the FE code, which would be the ideal approach for the FE analyst. However, the Craig Bampton substructure is already implemented into several FE codes such as NASTRAN, ABAQUS, ANSYS and the Sierra Structural Dynamics code at Sandia National Laboratories. Researchers have developed a couple of methods to utilize the CB form of the TS method in FE codes [2]. Here, another transformation is developed, dubbed the Craig-Mayes method, which transforms the free modes from the experimental model with the TS mode shapes into a modified CB form. This method preserves the experimentally extracted modal parameters exactly.

This paper will present the theory first, an analytical problem applying the method next, and finally an industrial problem applying the method. Some discussions on maintaining good conditioning for the matrices follows, and then conclusions are presented.

13.2 Theory

Consider an experimental substructure tested with the TS fixture attached. An experimental substructure that can be implemented in the Craig-Bampton form is desired. An example, which will be developed fully hereinafter, is the beam pictured in Fig. 13.1. The red beam is the experimental structure for which a substructure in the CB form is desired. It is tested in a free-free modal test with the TS fixture, the magenta beam, attached. The goal is to transform the test results so that there is a substructure of the red beam that fits in the CB form. To achieve this, the magenta TS must be subtracted. The modal test will produce modal parameters associated with the q dof. The TS has free modal parameters associated with the s dof, and the final desired substructure in the CB form will have stiffness, mass and damping matrices associated with the physical boundary dof, x_b, and the fixed boundary modal dof p.

Generally, there is a FE model of the TS. The FE model is used in test planning to define measurement locations that will achieve independent mode shape measurements for all free modes of the TS slightly beyond the frequency band of interest. The TS fixture is thus instrumented. The transmission simulator hardware is attached to the experimental substructure and the free TS mode shapes are assumed to span the space of the motion when connected to the experimental substructure. How well it spans the actual connection motion space affects the fidelity of the substructure model. Ultimately, the TS stiffness, mass and damping will be subtracted from the experimental substructure, so that the experimental substructure may then be coupled with the FE model of the rest of the system. The modal parameters from a free modal test of the experimental substructure with the TS attached can be used to produce the following equations of motion as

$$\left[\omega^2{}_{free} + j2\omega\omega_{free}\zeta_{free} - \omega^2 I\right]\bar{q} = 0 \tag{13.1}$$

where the subscript *free* represents the set of modes obtained from the experimental modal test of the experimental substructure attached to the TS in which there are generally no additional constraints added to the structure (The structure is typically suspended by bungee cords or some very soft suspension whose mass, stiffness and damping are considered negligible). The mass-normalized mode shapes derived from the test will be contained in the measured mode shape matrix, Φ. For convenience, the rest of this derivation will drop the damping matrices, but they may easily be included. Now we wish to derive a square matrix transformation, T, that will convert Eq. (13.1) to a modified CB form. Here we consider the generalized coordinates, p as the fixed-boundary modal coordinates and the generalized coordinates, s as the coordinates that account for the motion of the TS, which is considered the boundary of the experimental substructure as

$$\bar{q} = T\begin{Bmatrix} \bar{p} \\ \bar{s} \end{Bmatrix}. \tag{13.2}$$

The first constraint ties the TS to the tested structure. Use the modal approximations to set the motion of the experiment on the boundary (TS dof) to match the free modal motion of the TS as

$$\Phi_b\bar{q} \approx \Psi_b\bar{s} \tag{13.3}$$

where the subscript b dof will actually be a subset of the boundary dof where the measurements are made, Φ is the experimental mode shape and Ψ is the chosen truncated set of free modes of the TS. Ψ usually comes from a TS FE model, but could also be measured. Then the relation between q and s is

$$\bar{q} = \Phi_b^{+}\Psi_b\bar{s} \tag{13.4}$$

where the $+$ sign represents the Moore-Penrose pseudo inverse. This provides the s portion of the transformation, T.

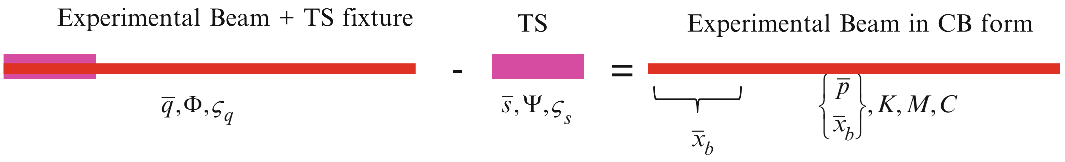

Fig. 13.1 Example experimental substructure – tested structure – TS = experimental substructure

To obtain the fixed boundary modal dof, p, fix the boundary dof with

$$\bar{x}_b = \Phi_b \bar{q} = 0. \tag{13.5}$$

Previous work [3] has shown that a practical way to accomplish Eq. (13.5) is to fix the TS dof with

$$\Psi_b^+ \Phi_b \bar{q} = s = 0. \tag{13.6}$$

With Rixen's primal assembly [4], the modal dof are replaced with

$$\bar{q} = L_{fix} \bar{\eta} \tag{13.7}$$

which is substituted back into Eq. (13.6) to obtain

$$\Psi_b^+ \Phi_b L_{fix} \bar{\eta} = 0. \tag{13.8}$$

Since $\bar{\eta}$ can be anything, depending on the forcing motion, L_{fix} is chosen to guarantee satisfaction of the constraint as

$$L_{fix} = null\left(\Psi_b^+ \Phi_b\right). \tag{13.9}$$

Pre and post-multiply Eq. (13.1) using the transformation L_{fix} appropriately to give

$$L_{fix}^T \left[\omega^2{}_{free} - \omega^2 I\right] L_{fix} \bar{\eta} = 0. \tag{13.10}$$

Solve Eq. (13.10) to get the eigenvectors, Γ, and the eigenvalues to uncouple the dof, p. Then the relationship between q and the fixed boundary dof, p, is

$$\bar{q} = L_{fix} \Gamma \bar{p} \tag{13.11}$$

which provides the rest of the transformation written from Eqs. (13.4) and (13.11) as

$$T = \left[L_{fix}\Gamma \;\; \Phi_b^+ \Psi_b\right]. \tag{13.12}$$

Pre multiplying Eq. (13.1) by the transpose of T and substituting Eq. (13.2) into Eq. (13.1) for q yields the following transformed equations of motion for free vibration

$$\left[\begin{bmatrix} \lceil \omega^2_{fix} \rfloor & K_{ps} \\ K_{ps}^T & K_{ss} \end{bmatrix} - \omega^2 \begin{bmatrix} I & M_{ps} \\ M_{ps}^T & M_{ss} \end{bmatrix}\right] \begin{Bmatrix} \bar{p} \\ \bar{s} \end{Bmatrix} = 0 \tag{13.13}$$

for which the eigenvalue and eigenvector solution have not changed from Eq. (13.1). It has exactly as many dof as Eq. (13.1), but now they have been transformed to the fixed base modes associated with p and the TS modes which were on the boundary as modal dof s. The upper left portion of the matrices is diagonal. Now there are coupling terms between the fixed base modes and the TS motion. The shapes associated with p are $\Phi L_{fix} \Gamma$ which one can see by pre-multiplying Eq. (13.11) by Φ. To obtain the experimental substructure without the TS attached, simply subtract the TS stiffness and mass from the lower right partition which corresponds to the boundary motion, as

$$\left[\begin{bmatrix} \lceil \omega^2_{fix} \rfloor & K_{ps} \\ K_{ps}^T & K_{ss} - \lceil \omega^2_{TS} \rfloor \end{bmatrix} - \omega^2 \begin{bmatrix} I & M_{ps} \\ M_{ps}^T & M_{ss} - I \end{bmatrix}\right] \begin{Bmatrix} \bar{p} \\ \bar{s} \end{Bmatrix} = 0. \tag{13.14}$$

This is almost in the form of CB matrices, but the generalized dof, s, must be converted to physical dof, x_b, to couple it with the FE model of the rest of the system in codes with CB substructure capability.

Since

$$\bar{x}_b = \Psi_b \bar{s} \tag{13.15}$$

write a transformation

$$\begin{Bmatrix} \overline{p} \\ \overline{s} \end{Bmatrix} = \begin{bmatrix} I & 0 \\ 0 & \Psi_b^+ \end{bmatrix} \begin{Bmatrix} \overline{p} \\ \overline{x}_b \end{Bmatrix} \tag{13.16}$$

and, similar to Eq. (13.10), pre and post-multiply Eq. (13.14) appropriately by this transformation to produce the modified CB form as

$$\left[\begin{bmatrix} {}^{\backprime}\omega^2_{fix\backslash} & K_{ps} \\ K_{ps}^T & \Psi_b^{+^T} \left[K_{ss} - {}^{\backprime}\omega^2_{TS\backslash} \right] \Psi_b^+ \end{bmatrix} - \omega^2 \begin{bmatrix} I & M_{ps} \\ M_{ps}^T & \Psi_b^{+^T} \left[M_{ss} - I \right] \Psi_b^+ \end{bmatrix} \right] \begin{Bmatrix} \overline{p} \\ \overline{x}_b \end{Bmatrix} = 0. \tag{13.17}$$

This form is slightly modified from the normal CB in that there are non-zero stiffness coupling terms, K_{ps}, which are zero in the normal CB form. However, this can now be implemented directly in the FE model as a CB type substructure. The author calls this form Craig-Mayes. Note the damping can be carried along in an analogous way. One disturbing issue about the Craig-Mayes form is that Eq. (13.17) has become rank deficient, unlike Eq. (13.14), so it is not useful to solve Eq. (13.17) by itself. This is because the length of vector $\overline{x}_b$ is greater than the length of vector $\overline{s}$. However, as pointed out by Simmermacher [5], when coupled with another FE substructure, the entire system will not be rank deficient because of the stiffness and mass added by the FE substructure to the $\overline{x}_b$ dof. As a final note, the basis shapes chosen in Eq. (13.3) need not necessarily be the free shapes of the TS. Other basis shapes may prove to give more accurate or robust solutions. If one uses the free shapes, the result in coupling the Craig-Mayes substructure of Eq. (13.17) with the FE model is exactly what is obtained with the standard TS method when Eq. (13.1) is coupled to a FE substructure through MPC's.

13.3 Beam Example

In this analytical example, a beam is the experimental structure. A short beam is attached at one end which is the TS. This system is converted to the Craig-Mayes substructure and coupled to a FE model of a second beam to produce the response of two beams attached to one another. The results are compared to the FE model of the entire system which acts as the truth model. Figure 13.2 shows the beam substructures. In this problem the right beam is 15 units long and the TS simulator is a short beam 4 units long that overlaps the left most 4 units of the right beam. The experimental structure is the right beam with TS beam attached. The FE substructure is the left beam that is 20 units long and is ultimately to be coupled with the right beam in the substructuring process. The FE substructure overlaps the right beam by four units. Figure 13.3 shows the first four elastic bending modes of the "truth" assembly. The circle/asterisk dof in the middle are where the two beam overlap and are connected.

The FE model of seven modes (up 5,876 Hz) of the right beam with the short TS attached was used to create the virtual test and the resulting experimental structure. The TS had six measured dof, three vertical translations and three horizontal translations at the three nodes located at the TS beam left end, center, and right end. Four modes of the TS were retained (three rigid body modes and one elastic bending mode). The Craig-Mayes substructure was created using the TS shapes and the seven virtual test shapes. It had three fixed base modes and six connection dof. This was coupled to the FE model of the 20 unit long left beam at the six "measured" connection dof. The frequency comparisons of the truth beam and the substructured beam are given in Table 13.1.

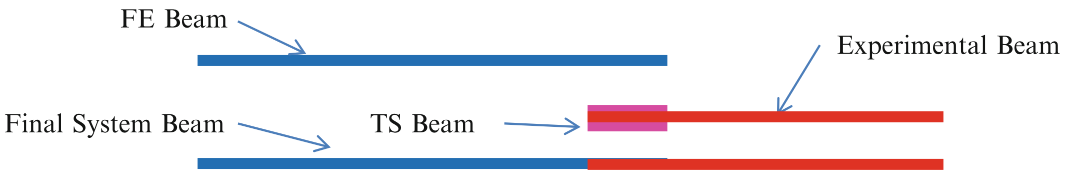

Fig. 13.2 Beam substructures and final assembled beam

Fig. 13.3 Bending mode shapes of truth beam

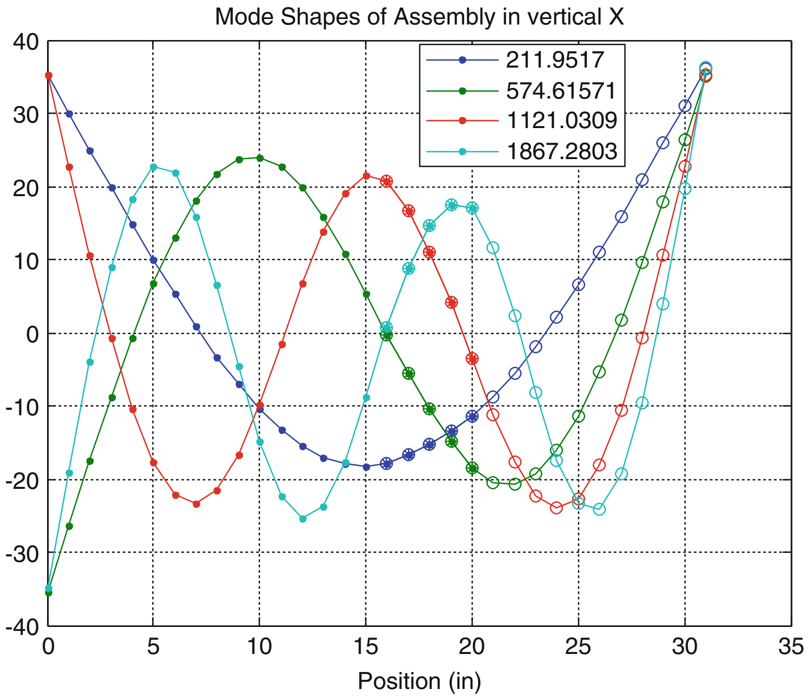

Table 13.1 Comparison of beam truth frequency and Craig-Mayes substructure frequency (elastic modes only)

Truth frequency (Hz)	Substructured frequency (Hz)	Error in frequency (%)
212.0	209.7	−1.1
574.6	571.5	−0.5
1,121.0	1,131.4	0.9
1,867.3	1,877.4	0.5
2,750.2	2,782.4	1.2
3,341.7	3,398.4	1.7
3,949.6	4,034.7	2.2
5,115.9	5,167.6	1.0
*5,965.5	5,946.9	−0.3

*Highest frequency experimental substructure mode retained was 5,876 Hz

13.4 Industrial Example

The industrial hardware consisted of a shell with dozens of internal components. The shell is chosen as the TS, and a FE model of the shell exists. The shell is relatively easy to model, but the internal parts are not easily modeled with FE. Dozens of internal accelerometers measured response of internal components of interest. Figure 13.4 shows a schematic representation of the test setup.

13.4.1 Description of Transmission Simulator Model

A FE eigenvalue analysis of a large number of the external translation dof of the empty shell for the first 200 free modes was performed. From this analysis, 38 modes of the TS were chosen to attempt to obtain response out to 2,000 Hz. Analysis to select measurement dof on the outside of the shell was performed. The algorithm selected measurement dof by attempting to keep the condition number of the mode shape matrix to a minimum. The condition number for the selected 84 measured dof and 38 modes was 3.54. When one more mode was added the condition number jumped to 7.2. The frequency of the 38th mode was 2,285 Hz. Seven modes had frequencies above the desired 2,000 Hz. After the dof selection was performed, the external shell was instrumented per the dof selection analysis. Optimal driving points based on the mode shapes of the free TS were also chosen.

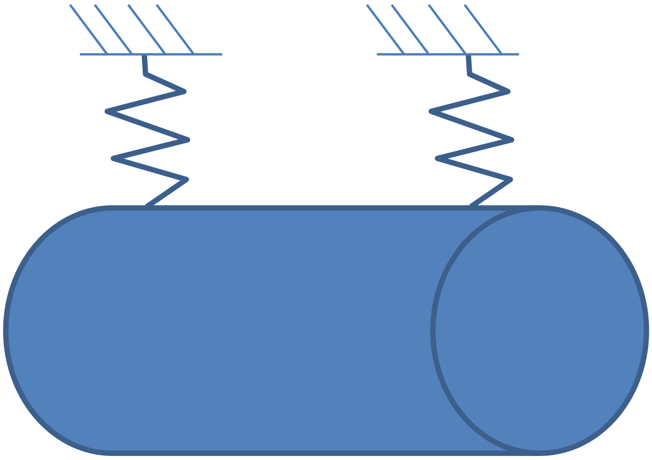

Fig. 13.4 Schematic of free modal test of shell with internal components

13.4.2 *Modal Test of Industrial Structure with Transmission Simulator*

The structure was supported by bungee cords, and a modal test was performed with an impact hammer. Twelve reference input locations were used in the analysis. Each reference was analyzed separately because the structure was slightly nonlinear, so multi-reference algorithms could not handle the frequency shifts of like modes extracted from one reference to another. The SMAC algorithm [6] in automated mode was utilized to extract the modes. The option to extract real modes was utilized. Almost 500 modes were extracted in the 12 data sets. Many of these were redundant extractions of the same mode already in another data set, and some modes were poorly excited. The modal parameters were culled to 110 elastic modes with the six rigid body modes (calculated analytically from mass properties) for the experimental model with the TS associated with Eq. (13.1).

13.4.3 *Craig-Mayes Experimental Substructure Coupled to FE Model: Comparison with Free Modal Model*

The TS fixture is the actual part that the internal components are mounted within. This allows us to have a convenient “truth” comparison. A Craig-Mayes substructure was developed by taking the experimental model and subtracting the 38 mode FE TS. The Craig-Mayes substructure was then added to a 200 mode modal substructure of the shell derived from the FE model of the shell. This was coupled together in MATLAB. This result is utilized to attempt to reproduce the original modal test FRF data. In Fig. 13.5 the top level complex mode indicator function (CMIF) is plotted for the experimental data (blue), the extracted modal model (green), and the Craig-Mayes substructure coupled with the 200 mode FE model of the shell (magenta). The CMIF plots incorporate all the FRF data together in one plot. Differences between the experimental and modal model CMIFs show errors in the modal fitting. Differences between the modal model and the substructured CMIF show errors due to the truncated modal model used for the TS and errors due to the FE model. To the extent the TS mode shapes do not span the space of the true experimental motion, constraining errors are introduced which can move the resonant frequencies and change the amplitudes of certain mode shapes. If one compares the modal model (green) and substructured CMIFs (magenta), one can see that the results below 1,000 Hz are nearly identical, but the substructured CMIF results above 1,000 Hz are not quite as good as the original modal extraction for the experiment. The constraining process pollutes the higher frequency modes either because the 38 TS mode shapes did not perfectly reproduce the motion that was actually experienced in the modal test on the shell, and the FE model of the shell is not perfect.

Figure 13.6 shows sample experimental FRFs (blue), FRFs synthesized from extracted modal parameters (green), and FRFs synthesized from the Craig-Mayes substructure coupled to the 200 mode FE model of the shell (magenta). The pattern is similar to the CMIFs in that the accuracy of the substructured FRFs deteriorates some with higher frequency. However, if one considers only the amplitude for defining specification envelopes, and one is willing to accept a factor of two in the uncertainty of the amplitude at certain frequencies, even the high frequency results in the magenta curves of the substructured model might be considered “useful”. The responses are all from different forcing input locations. The first row shows two responses on the outside shell. The second row shows two responses on substantial internal components. The third row shows two responses from small internal components.

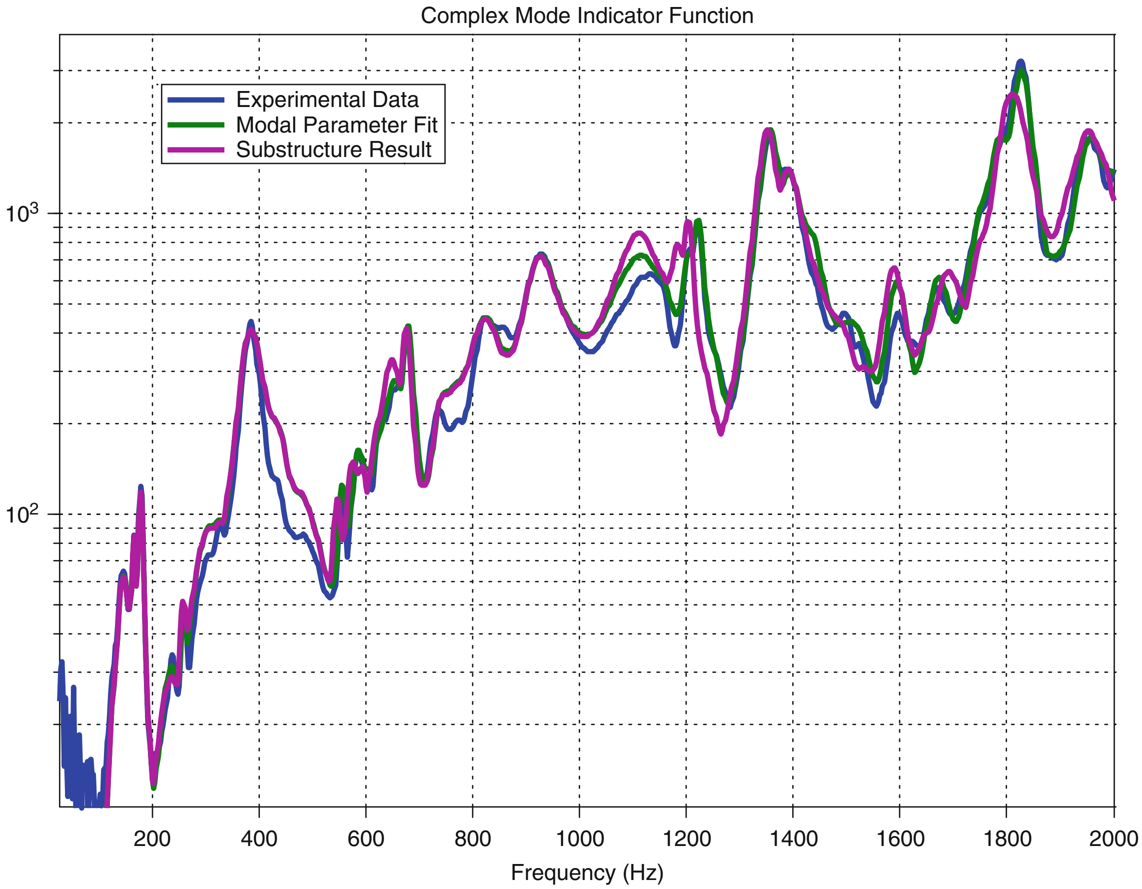

Fig. 13.5 CMIF experiment (*blue*) vs modal model (*green*) vs Craig-Mayes substructure added to 200 modes of FE shell (*magenta*)

13.5 Discussion on Conditioning of the Matrices

As mentioned in Sect. 13.4.1, the condition of the TS mode shape matrix, Ψ, is kept low by using as few modes as possible to span the desired bandwidth and placing accelerometers at appropriate dof to keep the mode shapes independent. The number of measured dof is large enough so the least squares estimate of s is accurate (typically 1.5–2 times the number of TS modes retained). The author has not studied the effect of increasing the condition number significantly above four.

It was discovered that the condition number of a matrix from Eq. (13.4), $\Phi_b^+\Psi_b$, was found to be important in maintaining the conditioning of the entire substructuring problem. In the beam problem, when Ψ_b had four shapes, a condition number of 10.5 was calculated for $\Phi_b^+\Psi_b$. However, when Ψ_b was increased to five shapes, the condition of $\Phi_b^+\Psi_b$ was 1.02×10^{14}, even though the condition of Ψ_b was 2.3. With the large condition number of $\Phi_b^+\Psi_b$, the coupling in the physical dof gave negative eigenvalues for the stiffness matrix, and the coupling with the FE beam failed. In the industrial problem, the condition number of $\Phi_b^+\Psi_b$ was 130, which may be near the limit of allowing a successful substructuring problem even with condition number of Ψ_b at 3.5 as it was here. Adding one more mode to Ψ_b caused the condition number of Ψ_b to double to 7.2 and the condition number of $\Phi_b^+\Psi_b$ to go up to 134, but then the coupling with the FE model of the shell produced a negative eigenvalue when the eigen analysis of the full system was performed in MATLAB. A negative eigenvalue is not desirable in a FE code, and can cause a fatal error. Negative eigenvalues can be removed from either a substructure's mass or stiffness matrix using methods described in previous work [7]. If the negative eigenvalues are not too large, they can be removed with only minor degradation of the resulting solution.

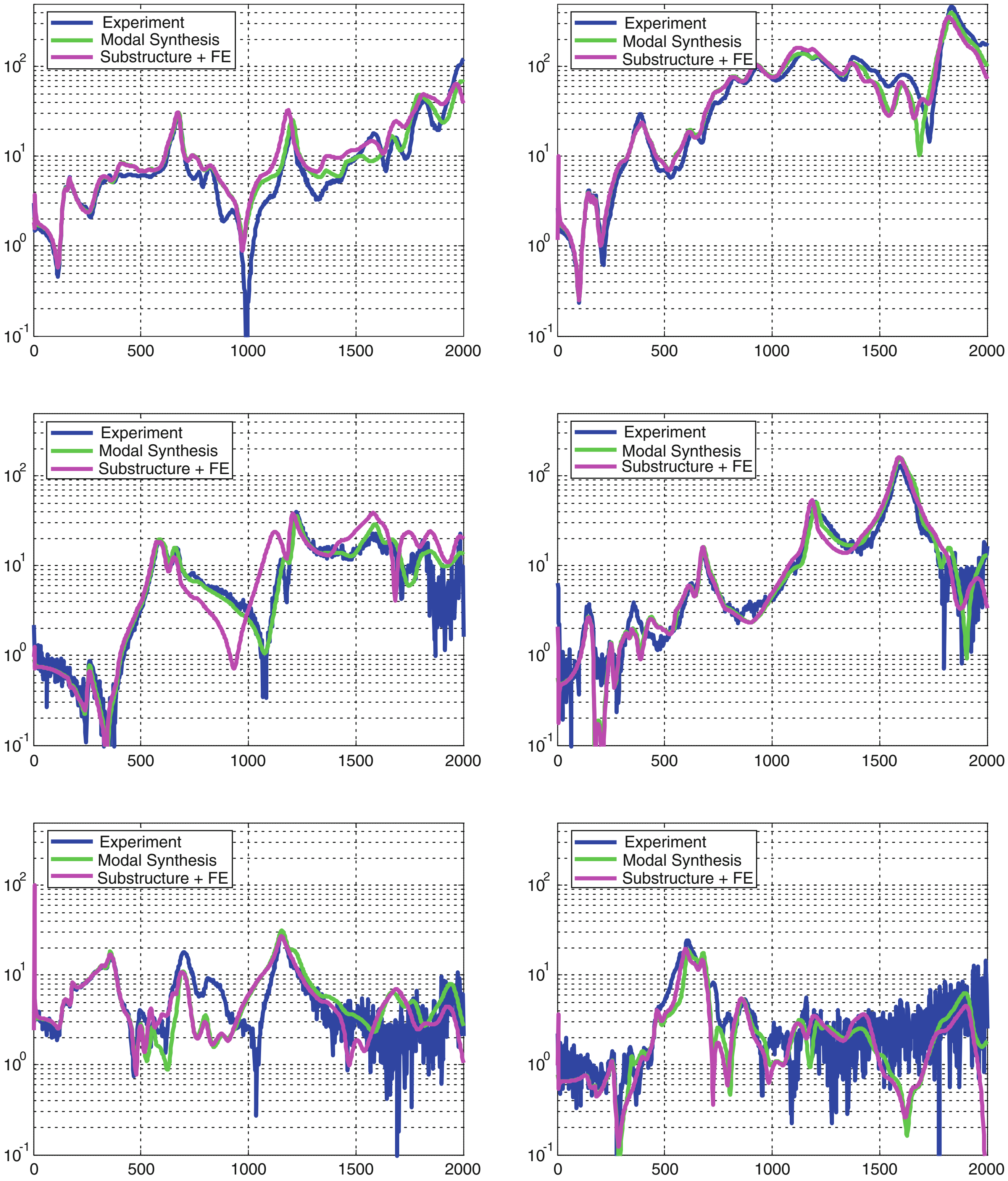

Fig. 13.6 Sample FRFs from experiment (*blue*), synthesized modal parameters (*green*), and from the Craig-Mayes substructure Plus 200 mode FE model of shell (*magenta*) – *Row 1* external responses on shell, *Row 2* substantial internal responses, *Rows 3* small internal component responses

13.6 Conclusions

The standard free modes transmission simulator (TS) substructuring capability has been augmented by providing a transformation to convert the free modes substructure to a modified Craig-Bampton form called the Craig-Mayes substructure. This form can fit directly into a FE code with the Craig-Bampton substructure capability to couple the Craig-Mayes substructure directly with an FE model of the complement of the full system to provide full system response calculations. The experimental substructure includes the damping that occurred in the experimental substructure as well as its connection to the next substructure. The theory was presented along with results from an analytical example and an actual industrial substructure with 116 experimental modes. The effects of the constraining process were noted. New insight for the conditioning of certain important matrices was presented.

Acknowledgments Notice: This manuscript has been authored by Sandia Corporation under Contract No. DE-AC04-94AL85000 with the U.S. Department of Energy. The United States Government retains and the publisher, by accepting the article for publication, acknowledges that the United States Government retains a non-exclusive, paid-up, irrevocable, world-wide license to publish or reproduce the published form of this manuscript, or allow others to do so, for United States Government purposes.

References

1. Allen MS, Mayes RL, Bergman EJ (2010) Experimental modal substructuring to couple and uncouple substructures with flexible fixtures and multi-point connections. J Sound Vib 329:4891–4906
2. Allen MS, Kammer DC, Mayes RL (2014) Experimental based substructuring using a Craig-Bampton transmission simulator model. In: Proceedings of the 32nd international modal analysis conference, Orlando, February 2014, paper number 171
3. Mayes RL (2012) Refinements on estimating fixed base modes on a slip table. In: Proceedings of the 30th international modal analysis conference, Jacksonville, February 2012, paper number 162
4. De Klerk D, Rixen DJ, Voormeeren SN (2008) General framework for dynamic substructuring: history, review, and classification of techniques. AIAA J 46(5):1169–1181
5. Technical conversation with Todd Simmermacher, Sandia National Laboratories Albuquerque, Simmermacher suggested moving the multi-point constraint inside the experimental substructure, so that it could connect directly to physical dof as the normal Craig-Bampton substructure does. I pointed out that this would introduce more singularities in the CB stiffness matrix since there were more physical connection dof than generalized connection dof. Simmermacher reminded me that the FE substructure should provide adequate stiffness and mass for the physical dof so that the full system matrices would not be unduly singular. March 2014
6. Hensley DP, Mayes RL (2006) Extending SMAC to multiple references. In: Proceedings of the 24th international modal analysis conference, pp 220–230, St. Louis, MO, February 2006
7. Mayes RL, Allen MS, Kammer DC (2013) Correcting indefinite mass matrices due to substructure uncoupling. J Sound Vib 332:5856–5866. doi:10.1016/j.jsv.2013.05.025

Chapter 14
A Parallel Solution Method for Structural Dynamic Response Analysis

Vahid Yaghoubi, Majid Khorsand Vakilzadeh, and Thomas Abrahamsson

Abstract With the continuous improvements of technology in and around multi-core CPU:s and GPU:s there is a strong desire to exploit this technology in its full potential. For structural dynamics problems, the domain decomposition is a very mature technique that is well adapted to parallel computations in multi-core machines as it is almost trivially parallelizable. However, competing alternatives with model reduction without parallel computation has also reached an extremely high level of maturity and are thus highly competitive. In this paper, a domain decomposition method, in a procedure named the split-stitch-spread (S3) procedure, is proposed to do transient analysis of large finite element models in parallel. In the method, the structure splits into model substructures with elastic interfacial substructures coupling them together. Each of them can be sent to different computer cores to do time discretization. The model substructures stitch to each other by using interfacial forces and as a result, the systems' state sequence will be obtained. The solution can then be spread into the substructures and response quantities can be evaluated in parallel processing. The method is applied to a multi-story building subjected to earthquake loading and the results are compared with mode displacement method as a model reduction method with focus on computational efficiency.

Keywords Domain decomposition • Parallel substructure • Transient analysis • Interfacial coupling • Elastic interface

14.1 Introduction

Dynamic analysis of large-scale structures usually requires considerable execution time and large memory usage due to the large amount of matrix operations. These obstacles prevent researchers from getting more accurate results by using higher resolution meshes and smaller time increments. Two approaches can be used to solve larger and more complex structures numerically. One approach is to develop more efficient solution schemes in the sense of the time and memory storage. Fast integration methods and model order reduction algorithms are examples of this approach which in the context of structural dynamics are well developed for both second-order systems [1] and first-order systems [2]. The alternative approach is in accordance with continuous improvements of technology in multi-core CPU:s and GPU:s, to better exploit advanced computer hardware and software technology. This utilizes the more powerful computer systems to analyze larger engineering problems. Parallel equation solver methods and parallel domain decomposition methods are two most well-known strategies of this approach. Obviously, these two approaches can be applied simultaneously to solve larger engineering problems in more efficient ways.

As mentioned, structures can be simulated efficiently in both first-order and second-order form. Parallel equation solver methods which focus on solving the linear equations in parallel either direct [3] or iteratively, can be considered as extension of integration methods in parallel computing. A family of the integration methods that stems from exact solution of first-order differential equation is exponential integrators [4]. In a recent paper, a very efficient and accurate exponential predictor-corrector integrator is used to simulate structures with local nonlinearity [5]. It was also shown that simulating a first-order system imposes two time-consuming steps when working with large structures. The first step consists of transferring the second-order to first-order differential equation form and the next step is the time-discretization of the model. The latter of these two steps often takes more time than the simulation time. If discretization in time is done in parallel, it means a big improvement in the overall simulation time. It is worth to mention that even in model reduction methods often the most time-consuming part is solving the eigenvalue problem in order to reduce the model order and not solving the resulting system equation. Therefore using parallel computers to find eigenvalues of the systems is also of great interest.

V. Yaghoubi • M.K. Vakilzadeh (✉) • T. Abrahamsson
Department of Applied Mechanics, Chalmers University of Technology, Gothenburg, Sweden
e-mail: khorsand@chalmers.se

M. Allen et al. (eds.), *Dynamics of Coupled Structures, Volume 4*, Conference Proceedings of the Society
for Experimental Mechanics Series, DOI 10.1007/978-3-319-15209-7_14

Domain decomposition methods utilize a partitioning scheme such that the structure is decomposed into several substructures. For each substructure, which is spatially discretized using finite element methods before or after partitioning, the equation system is formed and interface equation system is generated. Then each substructure is assigned to different cores and computational operations can be done in parallel with no between-cores communication. Solving the interface equation usually needs communication between the cores. After solving the interface equations, the back-substitution of results to each substructure can be made in parallel. Parallel substructuring methods [6] and finite element tearing and interconnecting (FETI) [7, 8] are some of the most well-known domain decomposition methods in structural analysis.

In the FETI-1 method, the continuity of the structure is established only at convergence by introducing Lagrange multipliers technique. In FETI-DP the continuity of the solution is held throughout the iteration in the primal variables while at dual variables continuity imposed only at convergence using Lagrange multipliers. Gonzales and Park [9] presented an explicit-implicit FETI method that separate rigid-body modes from flexible modes in each substructures and use an explicit integration method to solve the rigid-body (d'Lamaber Lagrange principal) equations and an implicit integration method to solve for the flexible modes. Tak and Park[10] presented a method that prescribed Dirichle boundary condition to all subdomains to remove rigid body modes.

In this paper a method is proposed to decompose the model into several subdomains in which each subdomain can be reduced, transferred to first-order systems, discretized in time and block-diagonalized in their own CPU core without any communication between the cores. Then, the condensed sparse time-discretized and real block-diagonal state-space matrices are assembled in the main core and simulation of the interface is done sequentially in one core or in GPUs. In the method, rigid body modes in floating substructures are constrained using interfacial force and interface compatibility is achieved by elastic interfacial substructure and fixed-point iteration coupling. In the following chapters, the theory behind the method is presented and the method is applied to a large-scale 3D building in an earthquake response analysis.

14.2 Theory

A finite element model of a structure is presented in the form of

$$\boldsymbol{M}\ddot{\boldsymbol{q}} + \boldsymbol{V}\dot{\boldsymbol{q}} + \boldsymbol{K}\boldsymbol{q} = \boldsymbol{R}^{u}\boldsymbol{u}\left(\boldsymbol{t}\right) \tag{14.1}$$

in which $\boldsymbol{M}\ddot{\boldsymbol{q}}$, $\boldsymbol{V}\dot{\boldsymbol{q}}$ and $\boldsymbol{Kq}$ are the inertial, dissipative and elastic forces, $\boldsymbol{q} \in \mathscr{R}^{n}$ is the displacement vector and $\boldsymbol{u} \in \mathscr{R}^{n}$ is the external stimuli vector consisting of non-zero localized forces and couples. $\boldsymbol{R}^{\boldsymbol{u}}$ is a boolean matrix that distribute the external forces on the system's degrees-of-freedom (DOF).

There are several method in the literature to solve the second-order differential equation numerically [11, 12] but transferring that to first order differential equation form and then solve is an alternative that can utilize efficient and accurate solvers [5, 13] in order to make that adaptable for control purposes.

we recast to state-space form, Eq. (14.1) into

$$\begin{aligned} \dot{\boldsymbol{x}} &= \boldsymbol{A}\boldsymbol{x}\left(\boldsymbol{t}\right) + \boldsymbol{B}\boldsymbol{u}\left(\boldsymbol{t}\right) \\ \boldsymbol{y} &= \boldsymbol{C}\boldsymbol{x}\left(\boldsymbol{t}\right) + \boldsymbol{D}\boldsymbol{u}\left(\boldsymbol{t}\right) \end{aligned} \tag{14.2a,b}$$

Where (14.2a) is obtained using the following matrices

$$\boldsymbol{A} = \begin{bmatrix} 0 & \boldsymbol{I} \\ -\boldsymbol{M}^{-1}\boldsymbol{K} & -\boldsymbol{M}^{-1}\boldsymbol{V} \end{bmatrix}, \ \boldsymbol{B} = \begin{bmatrix} 0 \\ \boldsymbol{M}^{-1}\boldsymbol{R}^{u} \end{bmatrix}. \tag{14.3a,b}$$

For an n-DOF structure with m inputs and p outputs, $\boldsymbol{A} \in \mathscr{R}^{2n\mathrm{x}2n}$, $\boldsymbol{B} \in \mathscr{R}^{2n\mathrm{x}m}$, $\boldsymbol{C} \in \mathscr{R}^{p\mathrm{x}2n}$ and $\boldsymbol{D} \in \mathscr{R}^{p\mathrm{xm}}$. Here $\boldsymbol{x} \in \mathscr{R}^{2n}$ being the state vector and $\boldsymbol{y} \in \mathscr{R}^{p}$ is the system output. $\boldsymbol{C}$ is used for linear mapping of the states to the output $\boldsymbol{y}$ with entities selected with the application in mind. $\boldsymbol{D}$ is the associated direct throughput matrix. Accelerations, velocities, relative and absolute displacements, stresses and strains are normal ingredients of $\boldsymbol{y}$ for mechanical system analysis.

The state variables in $\boldsymbol{x}$ can be linearly transformed according to $\overline{\boldsymbol{x}} = \boldsymbol{T}\boldsymbol{x}$, which state-space matrices pertinent to the transformed coordinate presented in the following

$$\overline{\boldsymbol{A}} = \boldsymbol{T}^{-1}\boldsymbol{A}\boldsymbol{T},\ \overline{\boldsymbol{B}} = \boldsymbol{T}^{-1}\boldsymbol{B},\ \overline{\boldsymbol{C}} = \boldsymbol{C}\boldsymbol{T},\ \overline{\boldsymbol{D}} = \boldsymbol{D} \tag{14.4}$$

Diagonalizing any state-space representation is accomplished by means of a particular similarity transformation specified by the eigenvectors of the state transition matrix **A**. An eigenvector of the square matrix **A** is any vector ψ_i for which

$$\boldsymbol{A}\psi_i = \lambda_i\ \psi_i \tag{14.5}$$

where the eigenvalue λ_i may be complex valued. In other words, when the matrix $\boldsymbol{T}$ of the similarity transformation is composed of the eigenvectors of **A**,

$$\boldsymbol{T} = [\ \psi_1 \ldots \psi_n],\tag{14.6}$$

so,

$$\boldsymbol{A}\boldsymbol{T} = \boldsymbol{T}\boldsymbol{\Lambda},\tag{14.7}$$

where

$$\boldsymbol{\Lambda} = diag\ (\lambda_1,\ \lambda_2, \ldots, \lambda_n).\tag{14.8}$$

the transformed system will be diagonalized into

$$\overline{\boldsymbol{A}} = \boldsymbol{T}^{-1}\boldsymbol{A}\boldsymbol{T} = \boldsymbol{T}^{-1}\boldsymbol{T}\boldsymbol{\Lambda} = \boldsymbol{\Lambda}\tag{14.9}$$

Here the diagonal matrix $\bar{\boldsymbol{A}}$ having the (complex) eigenvalues of $\boldsymbol{A}$ along the diagonal. With the notation of Eq. (14.4), $\overline{\boldsymbol{B}}$, $\overline{\boldsymbol{C}}$ and $\overline{\boldsymbol{D}}$ can be easily found. The complex-valued quadruple $\left\{\overline{\boldsymbol{A}}, \overline{\boldsymbol{B}}, \overline{\boldsymbol{C}}, \overline{\boldsymbol{D}}\right\}$, is a diagonal state-space representation. For simulation this requires complex arithmetic. An alternate block-diagonal real form, that does not need complex arithmetic exist and maybe an alternative.

To obtain a numerical solution, the continuous-time ordinary differential equation (ODE) of Eq. (14.6), needs to be discretized in a time-marching algorithm with time step T. This can be made through the recursive formula

$$\boldsymbol{x}_{k+1} = \boldsymbol{A}_{\mathrm{d}}\boldsymbol{x}_k + \boldsymbol{B}_{\mathrm{d}}\boldsymbol{u}_k, \qquad \boldsymbol{y}_k = \boldsymbol{C}_{\mathrm{d}}\boldsymbol{x}_k + \boldsymbol{D}_{\mathrm{d}}\boldsymbol{u}_k \tag{14.10a,b}$$

in which subscript $(.)_k$ stands for time $t = kT$. The state simulation result at $t = (k+1)T$ is obtained from data given by the previous step at $t = kT$. The exact coefficient matrices of the discretized form can be shown to be

$$\boldsymbol{A}_{\mathrm{d}} = \mathrm{e}^{\boldsymbol{A}T}$$

$$\boldsymbol{B}_{\mathrm{d}}\boldsymbol{u} = \boldsymbol{B}\int_{kT}^{kT+T} \mathrm{e}^{\boldsymbol{A}(kT+T-\tau)}\boldsymbol{u}(\tau)\,d\tau \tag{14.11}$$

The integral expression for the source term $\boldsymbol{B}_{\mathrm{d}}\boldsymbol{u}$ can be established only approximately for a general loading $\boldsymbol{u}(t)$. this elaborate more on the following.

Based on superposition principle, for a linear system with m inputs Eq. (14.10) can be rewritten as

$$\boldsymbol{x}_{k+1}^{(\xi)} = \boldsymbol{A}_{\mathrm{d}}\boldsymbol{x}_k^{(\xi)} + \boldsymbol{B}_{\mathrm{d}}^{(\xi)}u_k^{(\xi)}, \qquad \boldsymbol{y}_k^{(\xi)} = \boldsymbol{C}_{\mathrm{d}}\boldsymbol{x}_k^{(\xi)} + \boldsymbol{D}_{\mathrm{d}}^{(\xi)}u_k^{(\xi)} \tag{14.12a,b}$$

in which $\boldsymbol{x}_{k+1}^{(\xi)}$ and $\boldsymbol{y}_k^{(\xi)}$ $\xi = 1, 2, \ldots, m$ are state responses and system responses of the ξ^{th} input and the total responses are

$$\boldsymbol{x}_k = \sum\nolimits_{\xi=1}^{m} \boldsymbol{x}_k^{(\xi)}, \qquad \boldsymbol{y}_k = \sum\nolimits_{\xi=1}^{m} \boldsymbol{y}_k^{(\xi)}. \tag{14.13a,b}$$

14.3 Split-Stitch-Spread (S3) Algorithm

In this chapter the Split-Stitch-Spread algorithm for parallel finite element analysis is presented. In this method, the domain Ω is decomposed to create model substructures Ω_i $i = 1,2,\ldots,l$ and elastic, massless interfacial substructures Γ_{jk} $j = 1,2,\ldots,r$ and $k = 1,2,\ldots,s$ placed between Ω_j and Ω_k . Here we note that $\Omega = \bigcup \Omega_i$ and we let $\Gamma = \bigcup \Gamma_{jk}$. For an illustration see the L-shape domain Ω shown in plot (a) of Fig. 14.1 that is decomposed into three model substructures and two interfacial substructures. The massless coordinates in the interfacial substructures are called interfacial coordinates and the elements that coupled theses coordinates to each other are called interfacial elements. The coordinates in the subdomain Ω_i which are close to interfacial substructure Γ_{jk} are called adjacent coordinates, ω_i^{jk} and let $\omega = \bigcup \omega_i^{jk}$. Because of continuity, the interfacial coordinates have the same displacement and velocity with their corresponding adjacent coordinates. The interior coordinates of i^{th} substructure is denoted by q_o^i and the adjacent coordinates coordinate in the i^{th} subdomain is denoted by q_a^i, (see Fig. 14.1) and therefore $q = \{q_o^1; q_a^1; q_o^2; q_a^2; \ldots; q_o^p; q_a^p\}$.

Let the global assembled stiffness matrix of the interfacial substructure be $\boldsymbol{K}^{\text{a}}$ and the assembled stiffness matrix of the model substructures be $\boldsymbol{K}^{\text{o}}$. Then Eq. (14.1) can be rewritten in closed matrix form as

$$\boldsymbol{M}\ddot{\boldsymbol{q}} + \boldsymbol{V}\dot{\boldsymbol{q}} + (\boldsymbol{K}^{\text{o}} + \boldsymbol{K}^{\text{a}})\,\boldsymbol{q} = \boldsymbol{R}^{\boldsymbol{u}}\boldsymbol{u}\,(\boldsymbol{t}) \tag{14.14}$$

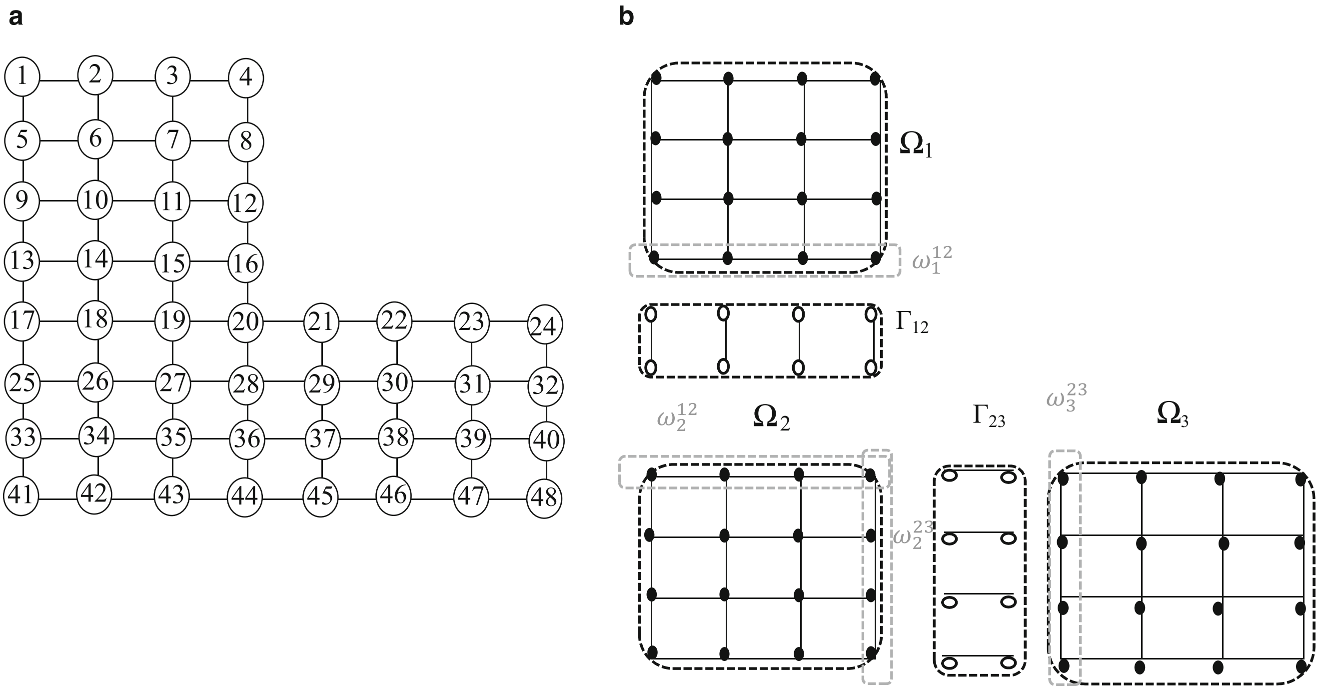

Fig. 14.1 (**a**) main domain Ω, (**b**) decomposed domain, *black bullet* are coordinates with mass, and circles are massless coordinates

or in open matrix form as

$$
\begin{aligned}
&\begin{bmatrix}
\begin{bmatrix} M_{oo}^{\Omega_1} & M_{oa}^{\Omega_1} \\ M_{ao}^{\Omega_1} & M_{aa}^{\Omega_1} \end{bmatrix} & 0 & 0 \\
0 & \ddots & 0 \\
0 & 0 & \begin{bmatrix} M_{oo}^{\Omega_l} & M_{oa}^{\Omega_l} \\ M_{ao}^{\Omega_l} & M_{aa}^{\Omega_l} \end{bmatrix}
\end{bmatrix}
\begin{Bmatrix} \ddot{q}_o^1 \\ \ddot{q}_a^1 \\ \vdots \\ \ddot{q}_o^l \\ \ddot{q}_a^l \end{Bmatrix}
+
\begin{bmatrix}
\begin{bmatrix} V_{oo}^{\Omega_1} & V_{oa}^{\Omega_1} \\ V_{ao}^{\Omega_1} & V_{aa}^{\Omega_1} \end{bmatrix} & 0 & 0 \\
0 & \ddots & 0 \\
0 & 0 & \begin{bmatrix} V_{oo}^{\Omega_l} & V_{oa}^{\Omega_l} \\ V_{ao}^{\Omega_l} & V_{aa}^{\Omega_l} \end{bmatrix}
\end{bmatrix}
\begin{Bmatrix} \dot{q}_o^1 \\ \dot{q}_a^1 \\ \vdots \\ \dot{q}_o^l \\ \dot{q}_a^l \end{Bmatrix} \\
&+
\begin{bmatrix}
\begin{bmatrix} K_{oo}^{\Omega_1} & K_{oa}^{\Omega_1} \\ K_{ao}^{\Omega_1} & K_{aa}^{\Omega_1} \end{bmatrix} & 0 & 0 \\
0 & \ddots & 0 \\
0 & 0 & \begin{bmatrix} K_{oo}^{\Omega_l} & K_{oa}^{\Omega_l} \\ K_{ao}^{\Omega_l} & K_{aa}^{\Omega_l} \end{bmatrix}
\end{bmatrix}
\begin{Bmatrix} q_o^1 \\ q_a^1 \\ \vdots \\ q_o^l \\ q_a^l \end{Bmatrix} \\
&+
\begin{bmatrix}
\begin{bmatrix} 0 & 0 \\ 0 & \sum\limits_{k=1}^{l} K_{aa}^{\Gamma_{1k}} \end{bmatrix} & \begin{bmatrix} 0 & 0 \\ 0 & K_{aa}^{\Gamma_{12}} \end{bmatrix} & \cdots & \begin{bmatrix} 0 & 0 \\ 0 & K_{aa}^{\Gamma_{1l}} \end{bmatrix} \\
\begin{bmatrix} 0 & 0 \\ 0 & K_{aa}^{\Gamma_{21}} \end{bmatrix} & \begin{bmatrix} 0 & 0 \\ 0 & \sum\limits_{k=1}^{l} K_{aa}^{\Gamma_{22}} \end{bmatrix} & \cdots & \begin{bmatrix} 0 & 0 \\ 0 & K_{aa}^{\Gamma_{2l}} \end{bmatrix} \\
\vdots & \ddots & \ddots & \\
\begin{bmatrix} 0 & 0 \\ 0 & K_{aa}^{\Gamma_{l1}} \end{bmatrix} & \begin{bmatrix} 0 & 0 \\ 0 & K_{aa}^{\Gamma_{l2}} \end{bmatrix} & \cdots & \begin{bmatrix} 0 & 0 \\ 0 & \sum\limits_{k=1}^{l} K_{aa}^{\Gamma_{ll}} \end{bmatrix}
\end{bmatrix}
\begin{Bmatrix} q_o^1 \\ q_a^1 \\ \vdots \\ q_o^l \\ q_a^l \end{Bmatrix}
= \boldsymbol{R}^{u}\boldsymbol{u}\left(\boldsymbol{t}\right)
\end{aligned}
\tag{14.15}
$$

in which the first stiffness matrix is K^{o} and the second one is K^{a}. The structures of the stiffness matrices for the L-shape structure are illustrated in Fig. 14.2. $K^{\mathrm{a}}q^{\mathrm{a}}$ can be transferred to the right hand side of equation and consider as a pseudo force applied to the system as,

$$
\boldsymbol{M}\ddot{\boldsymbol{q}} + \boldsymbol{V}\dot{\boldsymbol{q}} + \boldsymbol{K}^{\mathrm{o}}\boldsymbol{q} = \boldsymbol{R}^{u}\boldsymbol{u}\left(\boldsymbol{t}\right) - \boldsymbol{K}^{\mathrm{a}}\boldsymbol{q}^{\mathrm{a}} \tag{14.16}
$$

In which, ***M*, *V*** and $\boldsymbol{K}^{\mathrm{o}}$ are block diagonal and $\boldsymbol{K}^{\mathrm{a}}$ is normally a very sparse matrix.

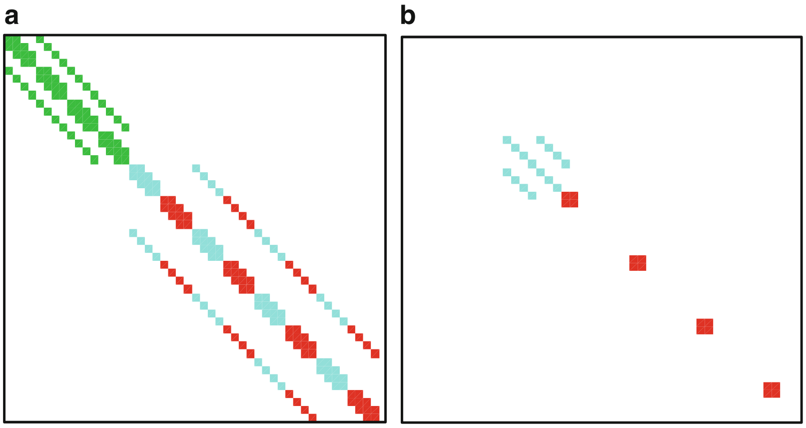

Fig. 14.2 (**a**) K^{o}, different colors for stiffness matrix of different model substructures. (**b**) K^{a}, different colors for stiffness matrix of different interfacial substructures

14.3.1 Splitting

In the splitting procedure, each block of matrices that are associated to the subdomain's interior coordinates can be sent to one CPU for processing. There they are transferred to the first-order model using Eq. (14.2). No interprocess communication with other CPUs is required in this process. To make the matrices sparser, by using Eqs. (14.4, 14.5, 14.6, 14.7, 14.8, 14.9) the state-space matrices may be transformed to real block-diagonal form. The systems are discretized temporally using Eq. (14.11) and simulated at their internal coordinate using their individual external forces i.e. $\boldsymbol{y}_{\mathrm{k}}^{\Omega,\boldsymbol{u}}$ by using Eq. (14.10a, b).

14.3.2 Stitch

At this step model substructures stitch to each other by using interfacial forces. All sparse, real block-diagonal (tridiagonal) and time-discretized matrices collect at a main core to be solved numerically at the adjacent coordinates. This equates to the motion at corresponding interfacial coordinates, $\boldsymbol{y}_k^{\omega} = \boldsymbol{q}_k^{\mathrm{a}}$ because of continuity of the structure at the interfaces. By use of the interfacial stiffness $\boldsymbol{K}^{\mathrm{a}}$ and the motion at the interfacial coordinates, interfacial forces can be calculated using Eq. (14.17b). In order to have the full system response at the interface, interfacial forces use as pseudo-forces in the assembled system using the following,

$$\boldsymbol{y}_k^{\omega} = \boldsymbol{y}_{\mathrm{k}}^{\omega,\boldsymbol{u}} + \boldsymbol{C}_{\mathrm{d}}^{\omega}\boldsymbol{x}_k^{\boldsymbol{f}} + \boldsymbol{D}_{\mathrm{d}}^{\omega}\,\boldsymbol{f}_k,\ \ \boldsymbol{f}_{\mathrm{k}} = -\boldsymbol{K}^{\mathrm{a}}\boldsymbol{y}_k^{\omega} \tag{14.17a,b}$$

in which $\boldsymbol{x}_k^{\boldsymbol{f}}$ is the state-response of the systems due to interfacial force. It can be rewritten as

$$\boldsymbol{y}_k^{\omega} = \left[\boldsymbol{I} + \boldsymbol{D}_{\mathrm{d}}^{\omega}\boldsymbol{K}^{\omega}\right]^{-1}\left(\boldsymbol{y}_k^{\omega,\boldsymbol{u}} + \boldsymbol{C}_{\mathrm{d}}^{\omega}\boldsymbol{x}_k^{\boldsymbol{f}}\right) \tag{14.18}$$

With the displacement solution $\boldsymbol{y}_k^{\omega}$ at the adjacent coordinate, the full state response of the structure can be obtained using

$$\boldsymbol{x}_{k+1}^{\boldsymbol{f}} = \boldsymbol{A}_{\mathrm{d}}\boldsymbol{x}_k^{\boldsymbol{f}} + \boldsymbol{B}_{\mathrm{d}}^{\omega}\boldsymbol{f}_k = \boldsymbol{A}_{\mathrm{d}}\boldsymbol{x}_k^{\boldsymbol{f}} - \boldsymbol{B}_{\mathrm{d}}^{\omega}\boldsymbol{K}^{\mathrm{a}}\boldsymbol{y}_k^{\omega} \tag{14.19}$$

with $\boldsymbol{B}_{\mathrm{d}}^{\omega}$ is time-discretized form of $\boldsymbol{B}^{\omega}$ and

$$\boldsymbol{B}^{\omega} = \begin{bmatrix} 0 \\ \boldsymbol{M}^{-1}\boldsymbol{R}^{\boldsymbol{a}} \end{bmatrix} \tag{14.20}$$

with $\boldsymbol{R}^{\boldsymbol{a}}$ being a boolean matrix that distribute the pseudo-forces on the system's degrees-of-freedom(DOF). Therefore, at the end of this step, the system response at the interface is calculated along with state-response of interfacial force at all DOFs.

14.3.3 Spread

In a spreading step, the interfacial forces are spread into the substructures and system response at all DOFs will be obtained. At the preceding *split*ting step, the system response due to external force $\boldsymbol{y}_k^{\Omega,\boldsymbol{u}}$ was obtained and proceeded with a *stitch*ing step in which the final system response at in the interfacial coordinates, $\boldsymbol{y}_k^{\omega}$, along with state-response of the structure due to interfacial force, $\boldsymbol{x}_k^{\boldsymbol{f}}$,were obtained. At *spread*ing step, by using the superposition principle, the full system response will be found using

$$\boldsymbol{y}_k^{\Omega} = \boldsymbol{y}_k^{\Omega,\boldsymbol{u}} + \boldsymbol{y}_k^{\Omega,\boldsymbol{f}} \tag{14.21}$$

or,

$$\boldsymbol{y}_k^{\Omega} = \boldsymbol{y}_k^{\Omega,\boldsymbol{u}} + \boldsymbol{C}_{\mathrm{d}}^{\Omega}\boldsymbol{x}_k^{\boldsymbol{f}} + \boldsymbol{D}_{\mathrm{d}}^{\Omega}\,\boldsymbol{f}_k \tag{14.22}$$

A flowchart of the presented algorithm is shown in Fig. 14.3.

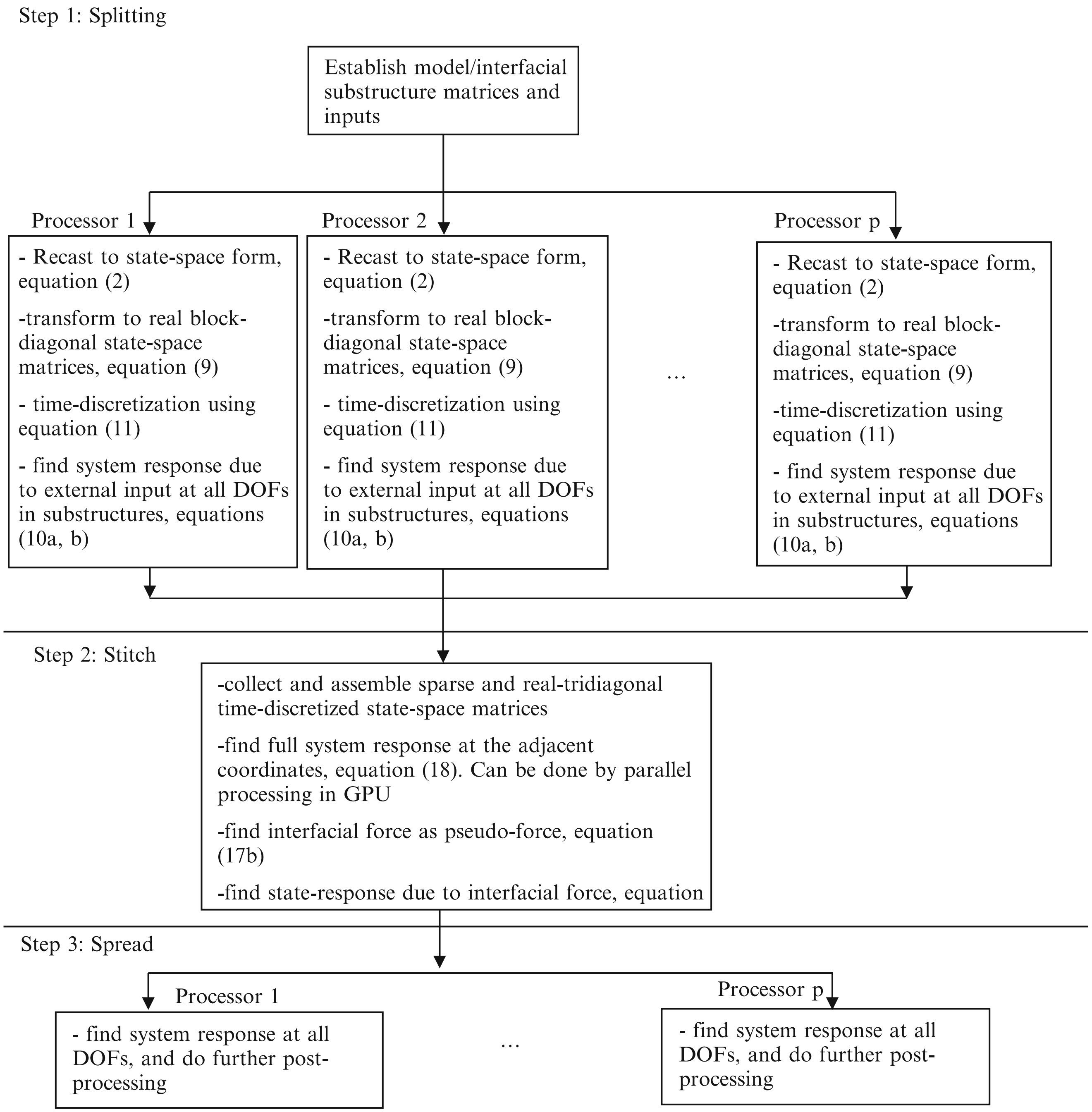

Fig. 14.3 Flowchart of the presented algorithm for parallel substructure method

14.4 Stability Consideration and Discretization

By substituting Eq. (14.20b) into Eq. (14.19) we have,

$$\boldsymbol{x}_{k+1} = \boldsymbol{A}_{\mathrm{d}}\boldsymbol{x}_k - \boldsymbol{B}_{\mathrm{d}}^{\omega}\boldsymbol{K}^{\mathrm{a}}\boldsymbol{y}_k^{\omega} \tag{14.23}$$

using $\boldsymbol{y}_k^{\omega}$ from Eq. (14.18) results in

$$\boldsymbol{x}_{k+1} = \boldsymbol{\Xi}\boldsymbol{x}_k + \boldsymbol{\Pi}\boldsymbol{y}_k^{\omega,\boldsymbol{u}} \tag{14.24}$$

in which

$$\Xi = \left(\boldsymbol{A}_{\mathrm{d}} - \boldsymbol{B}_{\mathrm{d}}^{\omega}\boldsymbol{K}^{\omega}\left[\boldsymbol{I} + \boldsymbol{D}_{\mathrm{d}}^{\omega}\boldsymbol{K}^{\omega}\right]^{-1}\boldsymbol{C}_{\mathrm{d}}\right),\ \Pi = -\boldsymbol{B}_{\mathrm{d}}^{\omega}\boldsymbol{K}^{\omega}\left[\boldsymbol{I} + \boldsymbol{D}_{\mathrm{d}}^{\omega}\boldsymbol{K}^{\omega}\right]^{-1} \tag{14.25a,b}$$

The system is stable when all the eigenvalues of $\boldsymbol{\Xi}$ are located inside of the unit disc i.e. $|\mathrm{eig}(\boldsymbol{\Xi})| < 1$. The method of discretization has effect on the stability and accuracy of the results. it has been found that if triangular-hold interpolation is used to approximate the loading, the result is very accurate but the integration scheme gives only small time-stepping range of stability while bilinear or Tustin discretization result in less accurate results but with wider time-stepping stability range. On the other hand, when a triangular-order hold scheme is used for discretization, the stability of the method can be enforced by small time step for simulation while for the Tustin method, it is the required accuracy that set the limit for time step increments.

14.5 Application

In this section the S3 method has been applied to a large scale structural problem to illustrate its efficiency. The building structure's response to an earthquake loading has been simulated in a Dell Optiplex 980, with a processor of 3.33 GHz and 8 GB of RAM. Matlab R2013a was used get the results.

The 20-story frame building, see Fig. 14.4, has a height of 8 m in first story and 4 m in the next 19 stories, leading to 84 m total height. It has a 40 m × 30 m rectangular 5 × 3-bay plane in the first five stories, then set back to 3 × 2-bay in 5 stories and 2 × 2-bays in the top half of the building. Cross braces on all external faces provide additional lateral and torsional stiffness. The columns and floor beams are modeled with Euler-Bernoulli beam elements; the beam-column connections are rigid. The cross braces carry only axial loads; their connections are hinges. Cross elements in the plane of the floors provide additional in-plane stiffness of the floors.

The building consists of a 1620-DOF finite element model that connects to a very massive body resembling the ground, about 300 times heavier than the whole building. The body moves in 3D and the input in the form of forces that provide the specified earthquake motion. The ground acceleration, recorded with a sample rate of 50 Hz is taken to be the N-S El Centro record of the 18 May 1940 Imperial Valley earthquake (Fig. 14.4). To make the data smoother, they are upsampled 10 times faster, i.e. at 500 Hz.

The equation of motion of the structure is

$$\boldsymbol{M}\ddot{\boldsymbol{q}} + \boldsymbol{V}\dot{\boldsymbol{q}} + \boldsymbol{K}\boldsymbol{q} = \boldsymbol{R}^{u}\boldsymbol{u}(t) \tag{14.26}$$

where $\boldsymbol{M}, \boldsymbol{V}$ and $\boldsymbol{K}$ are mass, damping and stiffness matrices of the superstructure, $\boldsymbol{q}$ is the displacement vector of the structural joints and $\boldsymbol{R}^{u}$ indicates location of the input force. The model decomposed into several parts and 25 s loading is simulated based on the S3 algorithm. Figure 14.5 illustrates the building decomposed to three model substructures and 2 interfacial substructures in front view (left plot) and left view (right plot).

Figure 14.6 shows results for 25-s simulation of the top floor of the structure. It is simulated sequentially using the full model, reduced model and the parallel method. The simulation results are in good agreement with each other. The required time for transferring to first order differential equation and its time-discretization using triangular-hold interpolation and also required time for solving the equation numerically are tabulated in Table 14.1. To reduce the model order, the mode displacement method has been applied to the structure equation and it took about 100 sec to solve full eigenvalue problem but in order to reduce the model order sparse eigenvalue calculation is used to find first 100 modes and it took about and it imposed 0.15 % error to the simulation results, see Table 14.1. Error defined by the relative Frobenious norm of difference between the simulated and reference responses at the time samples, as

$$e = \frac{||\boldsymbol{X} - \boldsymbol{X}_{\mathrm{ref}}||_{\mathrm{F}}}{||\boldsymbol{X}_{\mathrm{ref}}||_{\mathrm{F}}} \times 100 \tag{14.27}$$

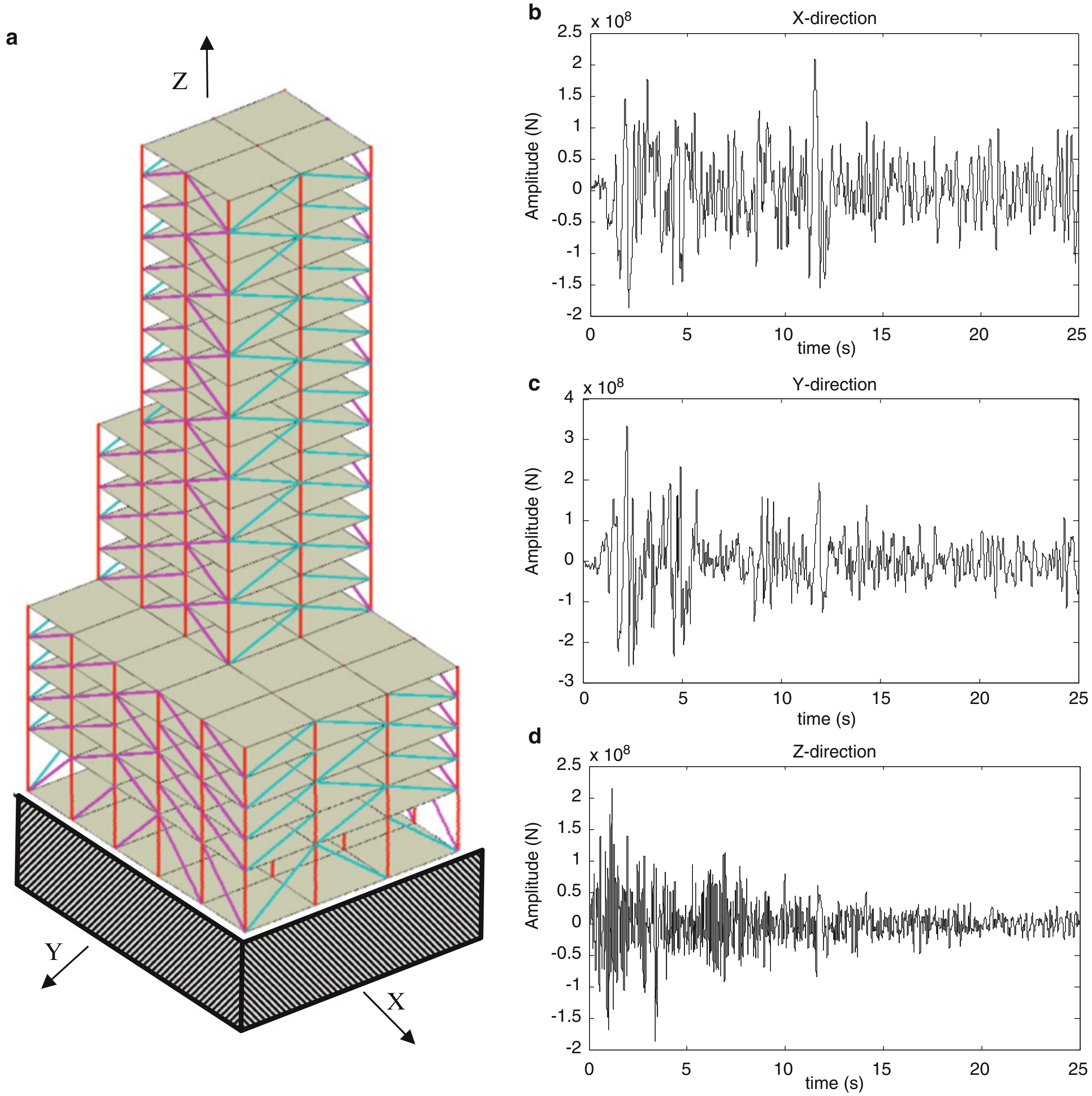

Fig. 14.4 (**a**) the three dimensional 20-story building connected to a massive body. (**b-d**) time history of the applied force at ground mass in X, Y and Z-directions

where $\boldsymbol{X}$ and $\boldsymbol{X}_{\mathrm{ref}}$ are the $n \times n_t$ response matrices in which n is the number of DOFs and n_t is the number of time steps used for simulation. $\boldsymbol{X}$ is given either by the reducing the model and solving sequentially or simulating using proposed parallel algorithm. $\boldsymbol{X}_{\mathrm{ref}}$ is the reference response matrix given by full model simulation that is discretized temporally by the triangular hold interpolation method.

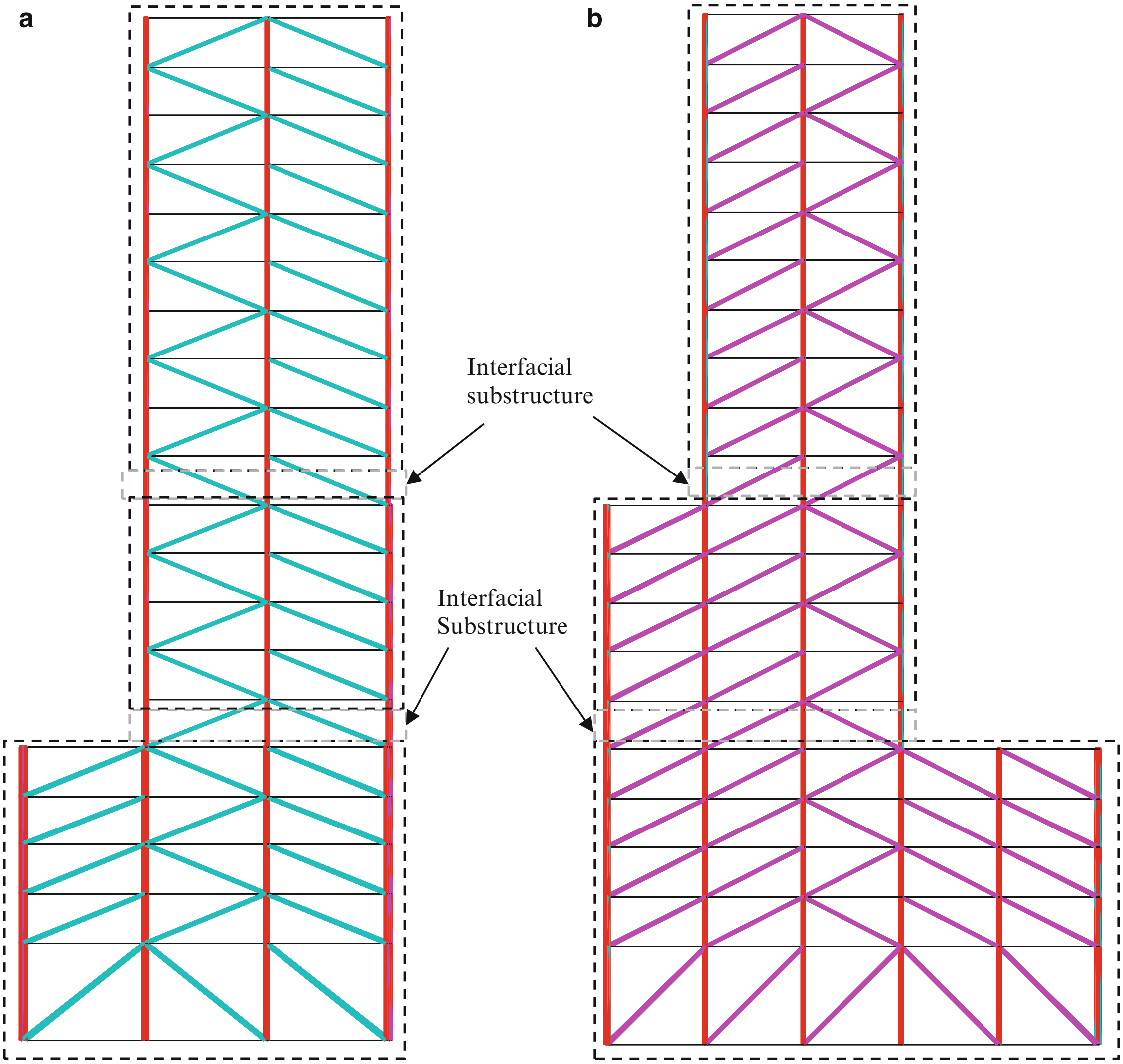

Fig. 14.5 View of structure splitted into three substructures and two interfacial substructures. (**a**) front view, (**b**) left view

Table 14.2 shows the effect of decomposing the structure into several parts in both simulation time and error analysis. The number of DOFs at each substructure is also shown in Table 14.2. The simulation time at each step of the S3 algorithm is shown in. It indicates that decomposing the model into more parts can speed up the simulation in the splitting step but it reduces the efficiency in the stitching step. There is not much time variation in the spreading step, therefore when it comes to the number

of decompositions, there is tradeoff between decreasing the simulation time by splitting into more parts and increasing that by stitching more parts to each other. The effect of decomposition on accuracy of the results is presented in Table 14.2 and indicates that by increasing the decomposed parts the error will increase (Fig. 14.7).

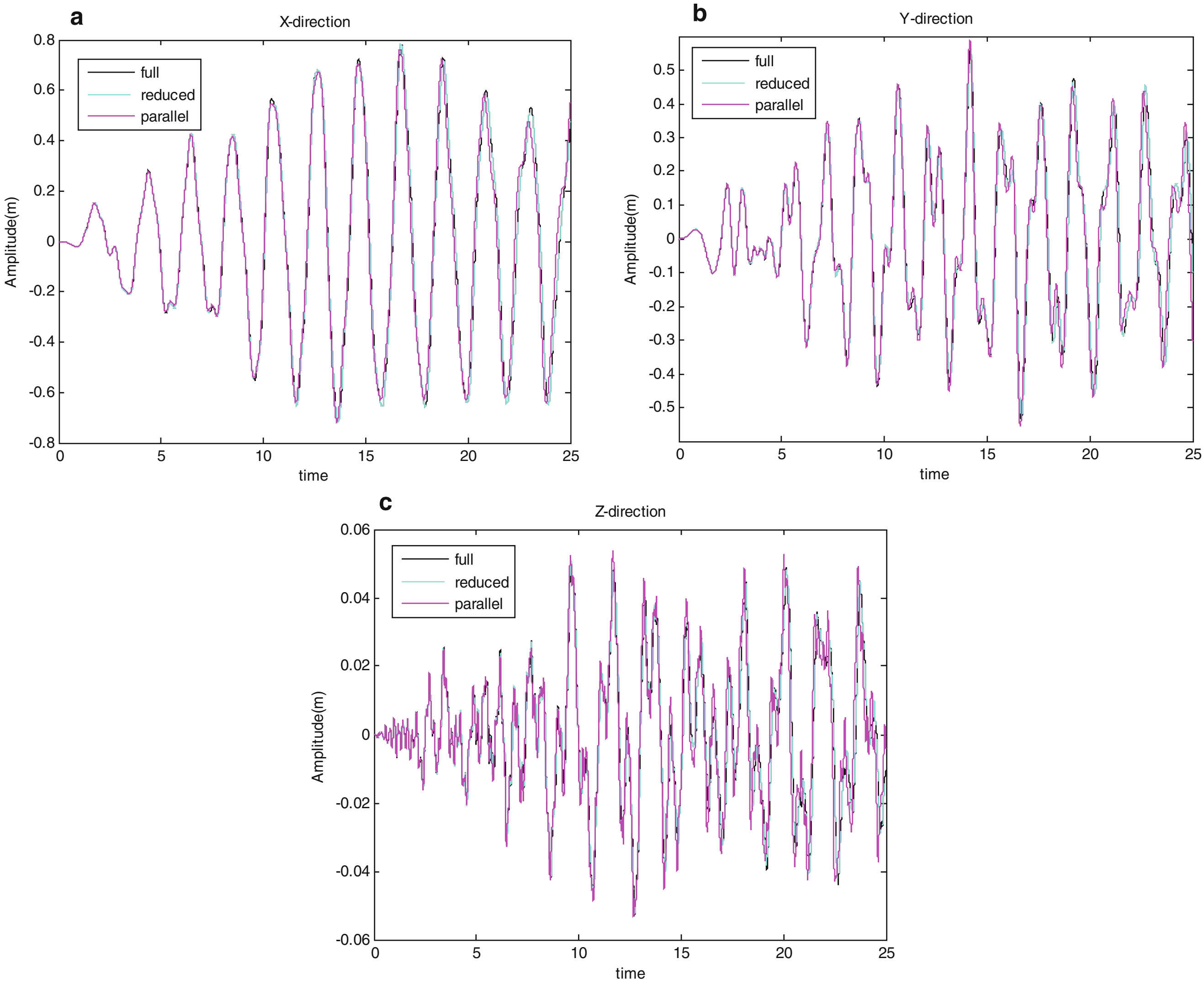

Fig. 14.6 Simulation result at top floor of the building with time-step increments 2 ms and 3 substructures for parallel simulation. (**a**) in X-direction, (**b**) in Y-direction and (**c**) in Z-direction

Table 14.1 Required time to do reduction, discretization and simulation for 25 s with time step increments of 2 ms

	Reduction	To first order DE	Discretization	Simulation time	Overall	Error (%)
Full model	–	3.22	37.46	109.11	149.79	–
Mode displacement	15.11	0.014	0.077	0.6	15.70	0.15

Table 14.2 Effect of decomposition, the number of DOFs at each substructure. Overall simulation time including all S3 steps and accuracy for simulating the substructures for 25 s with time step increment of 2 ms

No. substructures	1	2		3			4			
No. DOFs	1,623	867	756	723	360	540	723	360	270	270
Overall simulation time (s)	149.79	56.79		43.54			42.53			
Error (%)	–	3.37		4.24			6.77			

Fig. 14.7 Required time at each step of the method

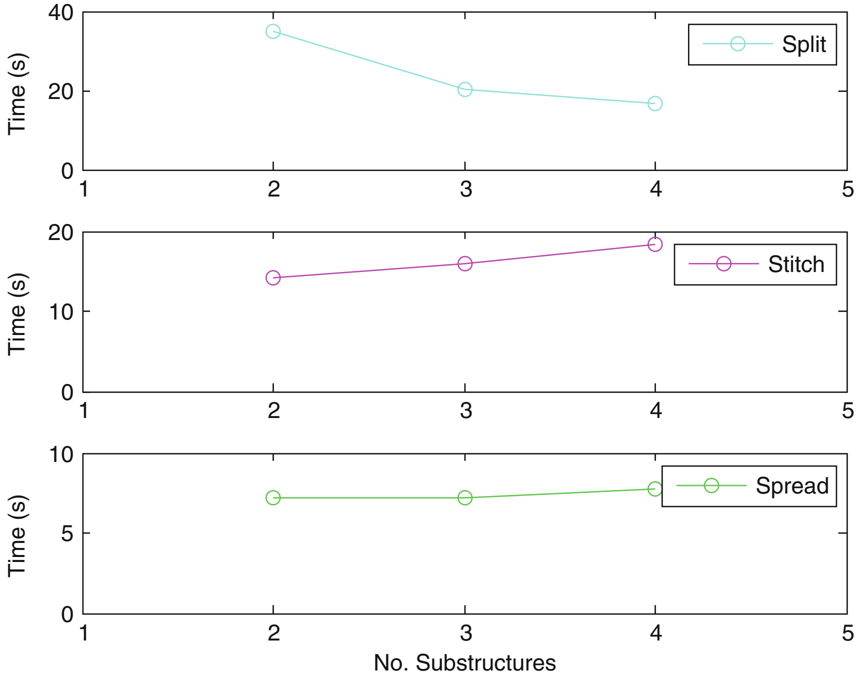

14.6 Conclusion and Future Work

In this paper the Split-Stitch-Spread (S3) algorithm for parallel finite element analysis has been presented. The method consists of three steps, in the first step, the structure is splitted into several parts and each part send to a CPU core to do reduction, discretization and simulation due to external force. At the next step, the substructures stitch to each other through elastic and massless interfacial substructures using interfacial forces. At the end, the motion of the interfacial substructures is spread into all DOFs of the structure. The method is applied to earthquake response of a 3D building. Results show that parallelization speed up the split step but slow down the stitch step with small effect on spread step. Since the assembled matrices in the stitching step are very sparse and matrix-vector multiplication is quit fast in GPUs, as the future work, implementation of the stitching part in a GPU will be investigating to see the potential speeds up. The results have been compared with a reduction method, the mode displacement, with focus on time efficiency. Results indicate that in the reduction method the most time consuming part is calculating the eigenvalues of the matrix and not in the simulation based on large sparse matrices. It was found that the presented parallel algorithm can compete favorably with reduction methods.

References

1. Dickens JM, Nakagawa JM, Wittbrodt MJ (1997) A critique of mode acceleration and modal truncation augmentation methods for modal response analysis. Comput Struct 62(6):985–998
2. Rahrovani S, Khorsand Vakilzadeh M, Abrahamsson T (2014) Modal dominancy analysis based on modal contribution to frequency response function -norm. Mech Syst and Signal Processing 48(1–2): 218–231
3. Davis TA (2004) Algorithm 832: UMFPACK V4.3 – an unsymmetric-pattern multifrontal method. ACM Trans Math Softw 30(2):96–199
4. Hochbruck M, Ostermann A (2010) Exponential integrators. Acta Numer 19:209–286
5. Yaghoubi V, Abrahamsson T (2014) An efficient simulation method for structures with local nonlinearity. In: Kerschen G (ed) Nonlinear dynamics. Conference proceedings of the society for experimental mechanics series. vol 2. Springer International Publishing, pp 141–149. doi:10.1007/978-3-319-04522-1_13
6. Yang Y-S, Hsieh S-K, Hsieh T-J (2012) Improving parallel substructuring efficiency by using a multilevel approach. J Comput Civ Eng 26(4):457–464
7. Farhat C, Crivelli L, Roux F-X (1994) A transient FETI methodology for large-scale parallel implicit computations in structural mechanics. Int J Numer Methods Eng 37(11):1945–1975
8. Farhat C, Roux F-X (1991) A method of finite element tearing and interconnecting and its parallel solution algorithm. Int J Numer Methods Eng 32(6):1205–1227

9. Gonzales J, Park KC (2012) A simple explicit–implicit finite element tearing and interconnecting transient analysis algorithm. Int J Numer Methods Eng 89(10): 1203–1226
10. Tak M, Park T (2013) High scalable non-overlapping domain decomposition method using a direct method for finite element analysis. Comput Methods Appl Mech Eng 264:108–128
11. Tianyun L, Chongbin Z, Qingbin L, Lihong Z (2012) An efficient backward Euler time-integration method for nonlinear dynamic analysis of structures. Comput Struct 1 volumes 06–107: 20–28
12. Felippa CA, Park KC (1979) Direct time integration methods in nonlinear structural dynamics. Comput Methods Appl Mech Eng 17(18): 277–313
13. Gaurav, Wojtkiewicz SF, Johnson EA (2011) Efficient uncertainty quantification of dynamical systems with local nonlinearities and uncertainties. Probab Eng Mech 26:561–569

Chapter 15
Structural Coupling of Two-Nonlinear Structures

Cagri Tepe and Ender Cigeroglu

Abstract In mechanical design, modeling and analysis of a complex structure can be simplified with dividing the structure into substructures; therefore, any change in the structure can be addressed easily which is referred as "structural coupling". Utilization of proper coupling techniques, it is possible to understand the behavior of the whole structure by considering the behavior of its substructures. For linear structures, coupling is a common technique; however, in most of the engineering structures, nonlinearities are also encountered; therefore, it is required to extend linear coupling methods to nonlinear systems. Although, there exists studies on nonlinear coupling, existing methods are limited to coupling of structures where one substructure is linear and the other is nonlinear or two linear substructures coupled with a nonlinear element. In this paper, a structural coupling method is proposed to couple two-nonlinear substructures. Similar to linear coupling methods, the proposed method considers the compatibility of internal forces at the connection degrees of freedom in addition to displacements. Since, the substructures are nonlinear, the resulting system of nonlinear differential equations are converted into a set of nonlinear algebraic equations by using Describing Function Method, which are solved by using Newton's method with arc-length continuation.

Keywords Structural coupling • Nonlinear structural coupling • Vibration of nonlinear structures

15.1 Introduction

In the design of mechanical systems, engineers should test and analyze each prototype created in order to provide a qualified and optimized design which has a wide range of requirements. Over the last 40 years, engineering structures are analyzed by the finite element method which is proven to be a reliable tool. However, in order finalize the design, whole structure has to be analyzed several times; therefore, an alternative approach is required in order to decrease the number of analyses and tests. Utilizing structural coupling, modeling and analysis of a complex structure can be simplified by dividing the structure into substructures and applying the required changes only on one or some of the substructures, where each substructure can be analyzed individually.

Substructure analysis of linear systems is a well-known subject dated back to 1960s by the works of Bishop and Johnson [1] on Receptance method and Hurty [2] on Component Mode Synthesis which was a simplified version of the method developed by Craig and Bampton [3]. Many different substructure and coupling methods for linear structures are developed by Rubin [4], Przemieniecki [5], Urgueira [6], Ewins [7], Klosterman and Lemon [8] and Ren and Beards [9]. All of these methods are developed for linear systems and the methodology is based on the compatibility of internal forces at the connection degrees of freedom in addition to the compatibility of the displacements. However, there is a need to extend linear coupling methods to non-linear systems; since many structures, which are considered as linear, are nonlinear in reality.

Analysis of nonlinear systems is much more complicated compared to linear systems [10] due to their response dependent behavior. In this paper, Describing Function Method (DFM) is used for the solution of nonlinear systems which was introduced by Krylov and Bogolyubov [11] in order to analyze nonlinear control problems based on an earlier work of Van der Pol [12]. Later, Taylor [13] replaced each nonlinear element with a quasilinear descriptor to define this approach.

C. Tepe
Middle East Technical University, Ankara 06800, Turkey

Microelectronics, Guidance and Electro-Optics Division, ASELSAN Inc., Ankara 06750, Turkey

E. Cigeroglu (✉)
Middle East Technical University, Ankara 06800, Turkey
e-mail: ender@metu.edu.tr

M. Allen et al. (eds.), *Dynamics of Coupled Structures, Volume 4*, Conference Proceedings of the Society
for Experimental Mechanics Series, DOI 10.1007/978-3-319-15209-7_15

Solution of multi degree of freedom nonlinear system with symmetrical nonlinearities is introduced by Budak and Özgüven [14, 15], which utilizes a special algebra. Later, Tanrıkulu [16] and Tanrıkulu et al. [17] extended this formulation for any type of nonlinearity by replacing this special algebra with describing functions.

Although, several studies on structural coupling of linear systems and modelling systems with nonlinearities are available in literature, the numbers of studies that consider nonlinear structural coupling are limited. Existing studies on nonlinear structural coupling are focused on coupling of structures where one substructure is linear and the other one is nonlinear or coupling of two linear substructures with a nonlinear coupling element. Watanabe and Sato [10] suggested “Nonlinear Building Block” approach, for coupling of linear substructures with nonlinear coupling elements. Cömert and Özgüven [18] developed a method for coupling of linear substructures with nonlinear connecting elements by using DFM, in which FRFs of the linear substructures are used. Ferreira and Ewins [19] proposed a new Nonlinear Receptance Coupling Approach and Ferraira [20] extended the approach with Multi-Harmonic Nonlinear Receptance Coupling Approach. Both approaches are capable of coupling a linear structure with a nonlinear structure with different types of joints. Chong and Imregün [21] suggested an iterative algorithm for the coupling of nonlinear structures with linear ones.

In this paper, an approach is developed to dynamic reanalysis of nonlinear substructures. Different from the existing methods in literature, proposed method is capable of coupling of two nonlinear substructures. Moreover, with the proposed coupling method, in addition to linear coupling elements, nonlinear coupling elements can as well be used. The proposed method considers the compatibility of internal forces at the connection degrees of freedom in addition to the displacements, and uses both of these equations to couple nonlinear substructures. Since, the substructures are nonlinear, the resulting system of nonlinear differential equations are converted into a set of nonlinear algebraic equations by using Describing Function Method, which are solved by using Newton’s method with arc-length continuation.

15.2 Theory

15.2.1 Structural Coupling of Linear Substructures

Consider two substructures A and B, shown in Fig. 15.1, where internal DOFs are represented by subscripts, i_A and i_B respectively and the connection DOFs are represented by subscripts c_A and c_B, respectively.

The corresponding equilibrium of each substructure can be written as

$$\begin{Bmatrix} \{f_{i_A}\} \\ \{f_{c_A}\} \end{Bmatrix} = \begin{bmatrix} [Z_{i_A i_A}] & [Z_{i_A c_A}] \\ [Z_{c_A i_A}] & [Z_{c_A c_A}] \end{bmatrix} \begin{Bmatrix} \{x_{i_A}\} \\ \{x_{c_A}\} \end{Bmatrix}, \tag{15.1}$$

$$\begin{Bmatrix} \{f_{i_B}\} \\ \{f_{c_B}\} \end{Bmatrix} = \begin{bmatrix} [Z_{i_B i_B}] & [Z_{i_B c_B}] \\ [Z_{c_B i_B}] & [Z_{c_B c_B}] \end{bmatrix} \begin{Bmatrix} \{x_{i_B}\} \\ \{x_{c_B}\} \end{Bmatrix}, \tag{15.2}$$

where $\{x_{i_A}\}$ and $\{x_{i_B}\}$ are generalized displacement vectors for internal DOFs, $\{x_{c_A}\}$ and $\{x_{c_B}\}$ are generalized displacement vectors for coupled DOFs of substructures A and B, respectively. $\{f_{i_A}\}$ and $\{f_{i_B}\}$ are internal forcing vectors for internal DOFs, $\{f_{c_A}\}$ and $\{f_{c_B}\}$ are coupled forcing vectors for internal DOFs of substructures A and B, respectively. Lastly, $[Z_A]$ and $[Z_B]$ are the impedance matrices of substructures A and B. Equilibrium of the forces between the connection DOFs can be written as

$$\{f_c\} = \{f_{c_A}\} + \{f_{c_B}\}, \tag{15.3}$$

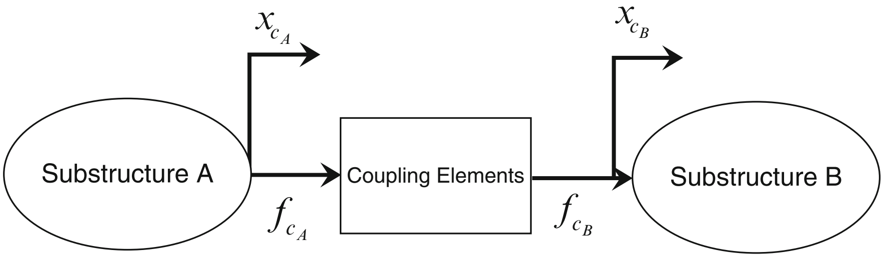

Fig. 15.1 Schematic view of structural coupling

where $\{f_c\}$ is the external force acting on the connection DOFs. Considering the compatibility of displacements of the substructures the following relation can be written

$$\left[D_{coupling}\right]\left(\{x_{c_A}\}-\{x_{c_B}\}\right)=\{f_{c_A}\}, \tag{15.4}$$

where $[D_{coupling}]$ is dynamic stiffness matrix of coupling elements. Substituting compatibility and equilibrium equations, i.e. Eqs. (15.3) and (15.4), into Eqs. (15.1) and (15.2), the overall impedance of the assembled system can be written as

$$[Z]=\begin{bmatrix} [Z_{i_Ai_A}] & [0] & [Z_{i_Ac_A}] \\ [0] & [Z_{i_Bi_B}] & [Z_{i_Bc_B}] \\ [Z_{c_Ai_A}] & [Z_{c_Bi_B}] & [Z_{c_Ac_A}]+[Z_{c_Bc_B}] \end{bmatrix}. \tag{15.5}$$

15.2.2 Structural Coupling of Two Nonlinear Substructures

The equation of motion of the nonlinear substructures A and B excited with a harmonic external forcing $\{f(t)\}$, can be written as

$$\begin{aligned} &[M_A]\{\ddot{x}_A(t)\}+[C_A]\{\dot{x}_A(t)\}+i\,[H_A]\{x_A(t)\}+[K_A]\{x_A(t)\}+\{f_{N_A}(t)\}=\{f_A(t)\}, \\ &[M_B]\{\ddot{x}_B(t)\}+[C_B]\{\dot{x}_B(t)\}+i\,[H_B]\{x_B(t)\}+[K_B]\{x_A(t)\}+\{f_{N_B}(t)\}=\{f_B(t)\} \end{aligned} \tag{15.6}$$

where $[M]$, $[C]$, $[H]$ and $[K]$ are the mass, viscous damping, structural damping and stiffness matrices of the linear system and $\{f_N(t)\}$ is the nonlinear forcing vector. Generalized displacement vectors $\{x_A(t)\}$ and $\{x_B(t)\}$ can be written as

$$\{x_A(t)\}=\left\{\begin{matrix}\{X_{i_A}\}\\ \{X_{c_A}\}\end{matrix}\right\},\ \{x_B(t)\}=\left\{\begin{matrix}\{X_{i_B}\}\\ \{X_{c_B}\}\end{matrix}\right\}, \tag{15.7}$$

and external forcing vectors $\{f_A(t)\}$ and $\{f_B(t)\}$ can be written as

$$\{f_A(t)\}=\left\{\begin{matrix}\{F_{i_A}\}\\ \{F_{c_A}\}+\{f_{c_A}\}\end{matrix}\right\},\ \{f_B(t)\}=\left\{\begin{matrix}\{F_{i_B}\}\\ \{F_{c_B}\}+\{f_{c_B}\}\end{matrix}\right\}, \tag{15.8}$$

where $\{F_{i_A}\}$ and $\{F_{i_B}\}$ are external forcing vectors acting on internal DOFs and $\{F_{c_A}\}$ and $\{F_{c_B}\}$ are external force vectors acting on the coupled DOFs. If the external forcing, $\{F(t)\}$ is periodic, response of the system, $\{x(t)\}$, can as well be assumed periodic, which can be expressed as follows

$$\{f(t)\}=\{F\}_0+\operatorname{Im}\left[\sum_{m=1}^{\infty}\{F\}_m\cdot e^{im\psi}\right], \tag{15.9}$$

$$\{x(t)\}=\{X\}_0+\operatorname{Im}\left[\sum_{m=1}^{\infty}\{X\}_m\cdot e^{im\psi}\right]. \tag{15.10}$$

Utilizing Describing Function Method (DFM) [14, 22] and substituting Eqs. (15.7) and (15.8) into Eq. (15.6) as the following result is obtained

$$\begin{aligned} &\left(-\omega^2[M]+i\cdot\omega[C]+i\,[H]+[K]+[\Delta]\right)\left\{\begin{matrix}\{X_{i_A}\}\\ \{X_{c_A}\}\end{matrix}\right\}=\left\{\begin{matrix}\{F_{i_A}\}\\ \{F_{c_A}\}+\{f_{c_A}\}\end{matrix}\right\}, \\ &\left(-\omega^2[M]+i\cdot\omega[C]+i\,[H]+[K]+[\Delta]\right)\left\{\begin{matrix}\{X_{i_B}\}\\ \{X_{c_B}\}\end{matrix}\right\}=\left\{\begin{matrix}\{F_{i_B}\}\\ \{F_{c_B}\}+\{f_{c_B}\}\end{matrix}\right\} \end{aligned} \tag{15.11}$$

where, [Δ] is the "nonlinearity matrix", which is function of the displacement vector. The elements of nonlinearity matrix are defined as

$$\begin{aligned} [\Delta]_{kj} &= \sum_{j=1}^{n} \nu_{kj} \qquad k = j, \\ [\Delta]_{kj} &= -\nu_{kj} \qquad k \neq j \end{aligned} \tag{15.12}$$

where ν_{kj} is describing function of the nonlinearity between the kth and the jth degrees of freedom, which is a quantity complex in general. For $k = j$ nonlinearity is between the kth degrees of freedom and the ground. Details of DFM can be found in [14, 22].

Internal forcing vector $\{f_{c_A}\}$ can be written as

$$\{f_{c_A}\} = \left[D^{NL}_{\text{coupling}}\right]\left(\{X_{c_A}\} - \{X_{c_B}\}\right) = \left(-\omega^2\,[M] + i\cdot\omega\,[C] + i\,[H] + [K] + [\Delta]\right)\left(\{X_{c_A}\} - \{X_{c_B}\}\right), \tag{15.13}$$

where, $[D^{NL}_{\text{coupling}}]$ is the nonlinear dynamic stiffness matrix of the connection elements. Substituting Eqs. (15.3) and (15.13), into Eq. (15.11), equation of motion can be obtained as

$$\begin{aligned} \left(-\omega^2\,[M] + i\cdot\omega\,[C] + i\,[H] + [K] + [\Delta]\right)\begin{Bmatrix}\{X_{i_A}\}\\ \{X_{c_A}\}\end{Bmatrix} &= \begin{Bmatrix}\{F_{i_A}\}\\ \{F_{c_A}\} + \left[D^{NL}_{\text{coupling}}\right]\left(\{X_{c_A}\} - \{X_{c_B}\}\right)\end{Bmatrix}. \\ \left(-\omega^2\,[M] + i\cdot\omega\,[C] + i\,[H] + [K] + [\Delta]\right)\begin{Bmatrix}\{X_{i_B}\}\\ \{X_{c_B}\}\end{Bmatrix} &= \begin{Bmatrix}\{F_{i_B}\}\\ \{F_{c_B}\} + \{f_c\} - \left[D^{NL}_{\text{coupling}}\right]\left(\{X_{c_A}\} - \{X_{c_B}\}\right)\end{Bmatrix} \end{aligned} \tag{15.14}$$

Equation (15.14) can be solved by a nonlinear equation solver and in this paper; Newton's method with arc-length continuation [23] is used. Algorithm of the proposed nonlinear coupling method is given in Fig. 15.2.

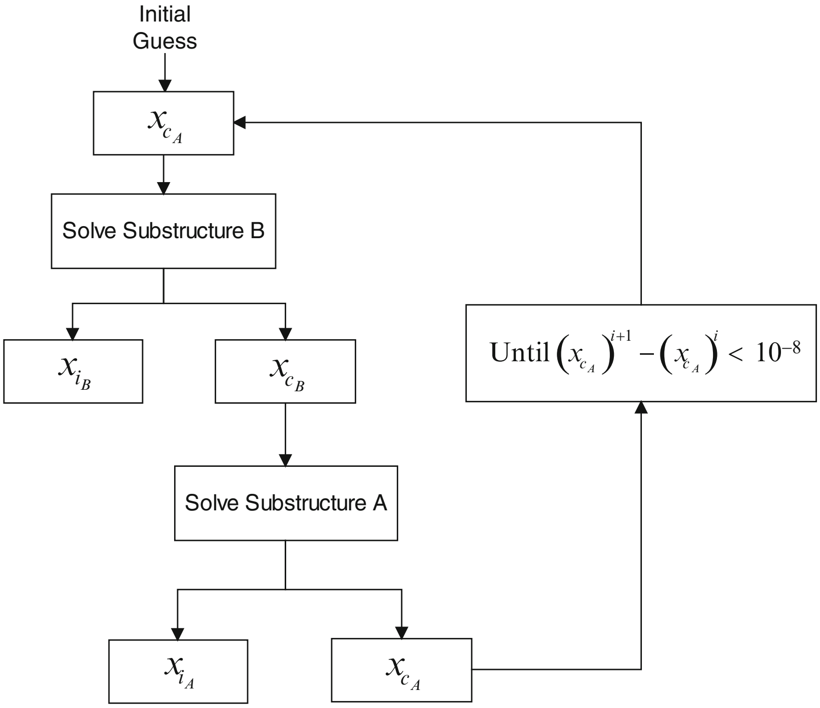

Fig. 15.2 Algorithm of the proposed method

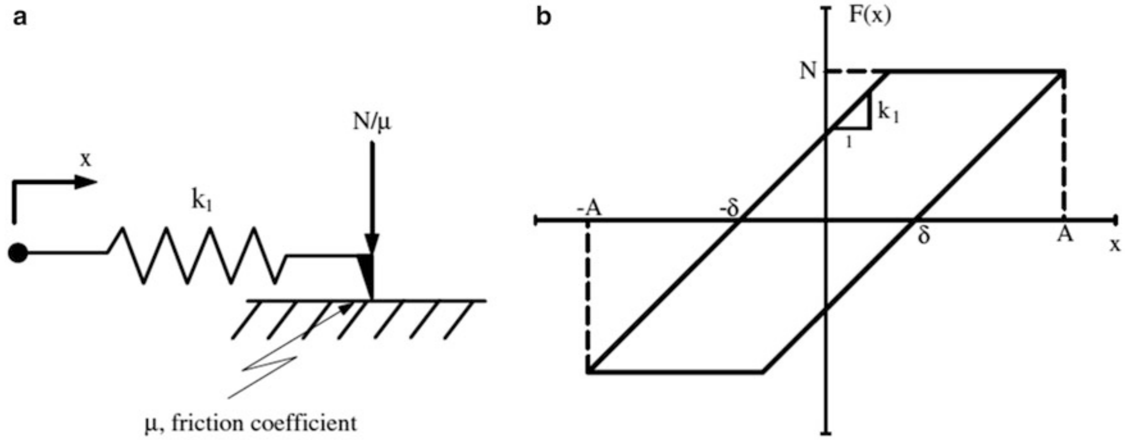

Fig. 15.3 (**a**) Schematic drawing, (**b**) corresponding hysteresis curve for dry friction nonlinearity [22]

15.2.3 Describing Functions of the Nonlinear Elements Used

In this paper, cubic stiffness and hysteretic dry friction are used as nonlinear elements in the substructures. The nonlinear forcing in a cubic stiffness element can be given as

$$F_N = k_c \cdot x^3, \tag{15.15}$$

where k_c is the coefficient of the cubic stiffness nonlinearity. Describing function of the cubic stiffness nonlinearity is given as

$$\nu = \frac{3}{4} \cdot k_c \cdot X^2, \tag{15.16}$$

where X is the amplitude of the relative displacement between the two ends of the cubic stiffness element.

There exists several friction models in the literature and in this paper, a one-dimensional Coulomb friction model with constant normal load is used. One-dimensional dry friction element and the corresponding hysteresis curve for a single harmonic input are given in Fig. 15.3.

Describing function of the hysteresis curve given in Fig. 15.3a can be written as [22, 24]

$$\nu = \begin{cases} \left[\frac{1}{\pi} \left(k - \frac{2\cdot\mu\cdot N}{X} \right) \sqrt{1 - \left(\frac{k\cdot X - 2\cdot\mu\cdot N}{k\cdot X} \right)^2} + \frac{k\cdot\psi_1}{\pi} - \frac{k}{2} \right] - i \left[\frac{4\cdot\mu\cdot N(\mu\cdot N - k\cdot X)}{\pi\cdot k\cdot X^2} \right] & \text{for } |k\cdot X| > \mu N \\ k & \text{for } |k\cdot X| \le \mu N \end{cases}, \tag{15.17}$$

where, k is the contact stiffness between rubbing surfaces, N is the constant normal force, μ is the dry friction coefficient and ψ_1

$$\psi_1 = \pi - a\sin\left(\frac{k \cdot X - 2 \cdot \mu \cdot N}{k \cdot X} \right). \tag{15.18}$$

15.3 Case Studies

In this section, the proposed coupling method is demonstrated on different model. In the first one, substructures are coupled from a single DOF whereas in the second one, they are coupled from two DOFs.

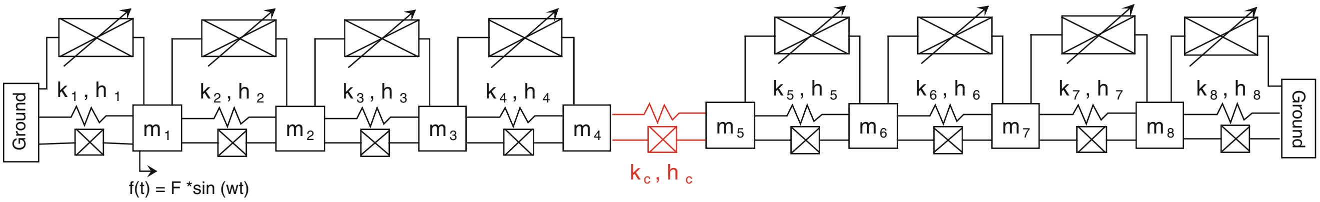

Fig. 15.4 Schematic view of 8-DOF coupled system

Table 15.1 Parameters of substructures *A* and *B*

Substructure *A*				Substructure *B*			
m_1 [kg]	m_2 [kg]	m_3 [kg]	m_4 [kg]	m_5 [kg]	m_6 [kg]	m_7 [kg]	m_8 [kg]
1	0.75	2	1	0.75	1	1	2
k_1 [N/m]	k_2 [N/m]	k_3 [N/m]	k_4 [N/m]	k_5 [N/m]	k_6 [N/m]	k_7 [N/m]	k_8 [N/m]
5,000	2,000	4,000	6,000	3,000	2,000	5,000	3,000
h_1 [N/m]	h_2 [N/m]	h_3 [N/m]	h_4 [N/m]	h_5 [N/m]	h_6 [N/m]	h_7 [N/m]	h_8 [N/m]
50	20	40	60	30	20	50	30

Table 15.2 Parameters of coupling elements

k_c [N/m]	h_c [N/m]
4,000	40

Table 15.3 Nonlinear elements of substructures *A* and *B* in case study 1

Nonlinear connection DOFs	Nonlinearity type [N/m^3]	Nonlinearity coefficients
1-Ground	Cubic stiffness	-1×10^5
1-2	Cubic stiffness	-2×10^5
2-3	Cubic stiffness	-10×10^5
3-4	Cubic stiffness	-1×10^5
5-6	Cubic stiffness	-1×10^5
6-7	Cubic stiffness	-3×10^5
7-8	Cubic stiffness	-1×10^5
8-Ground	Cubic stiffness	-5×10^5

15.3.1 Example 1: Coupling from a Single DOF

In the first example, application of the proposed approach is presented on a simple 8-DOF system shown in Fig. 15.4. Parameters of substructures *A* and *B* are given Table 15.1 and coupling elements at Table 15.2. The nonlinear elements used in the first case study, case study 1, are defined in Table 15.3.

Normalized response of the 1st and the 8th DOFs obtained from the proposed nonlinear coupling method and by solving the entire system directly are given in Figs. 15.5 and 15.6. The response of the system is obtained for three different excitation amplitudes, 8 N, 12 N and 16 N in order to observe the effect of cubic stiffness nonlinearity.

It can be seen from the Figs. 15.5 and 15.6 that, natural frequency is shifted due to cubic stiffness nonlinearity. Furthermore, more importantly the proposed method is in exact agreement with the ones obtained from entire system solution, even in unstable regions where the path turns back or intersects itself.

In the second case study, case study 2. 8-DOF system is obtained from the coupling of a 6-DOF, 2-DOF systems as shown in Fig. 15.7. Parameters of substructures *A* and *B*, and coupling elements are given in Tables 15.4 and 15.5, respectively. The nonlinear elements present in the system are defined in Table 15.6.

Corresponding response plots are plotted in Figs. 15.8 and 15.9 for the 1st DOF. Normalized responses of the coupled structure obtained from the proposed nonlinear coupling method and by solving the entire system directly are compared in Figs. 15.8 and 15.9. In Fig. 15.8, the response of the coupled system is obtained for 12 N, 24 N and 36 N excitation force amplitudes, while the slip load of dry friction nonlinearities are kept constant as $\mu N = 100$N. In Fig. 15.9, responses of the coupled structure are given for an external forcing of $F = 12$N and for different slip loads. Perfect agreement between the results obtained from the proposed nonlinear coupling method and the entire system solution is observed which verifies the developed coupling method.

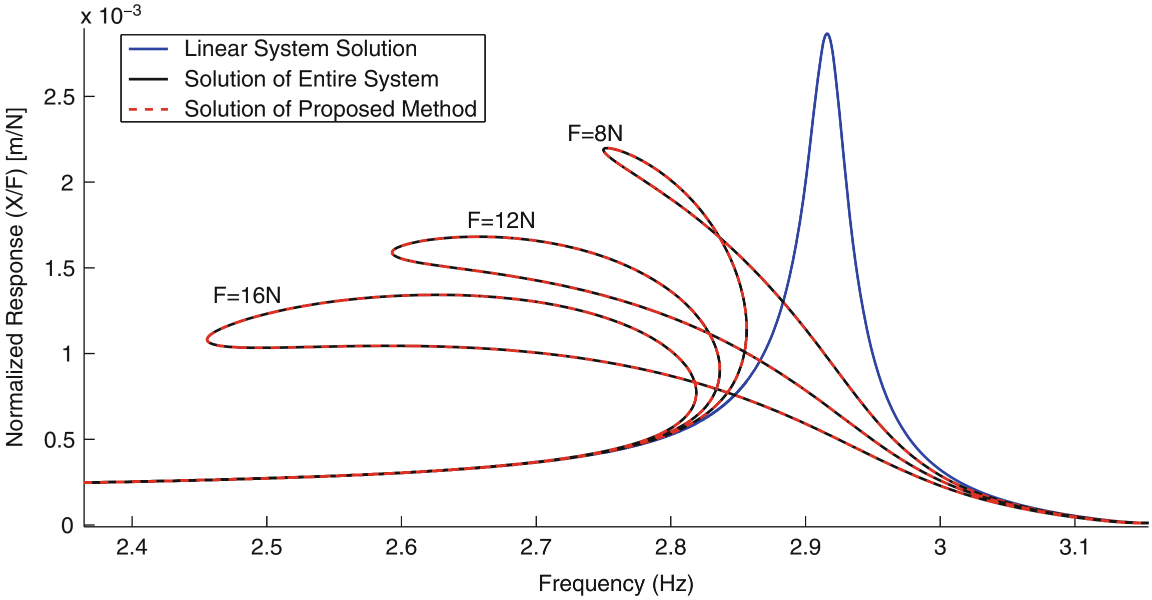

Fig. 15.5 Normalized response of the 1st DOF in case study 1

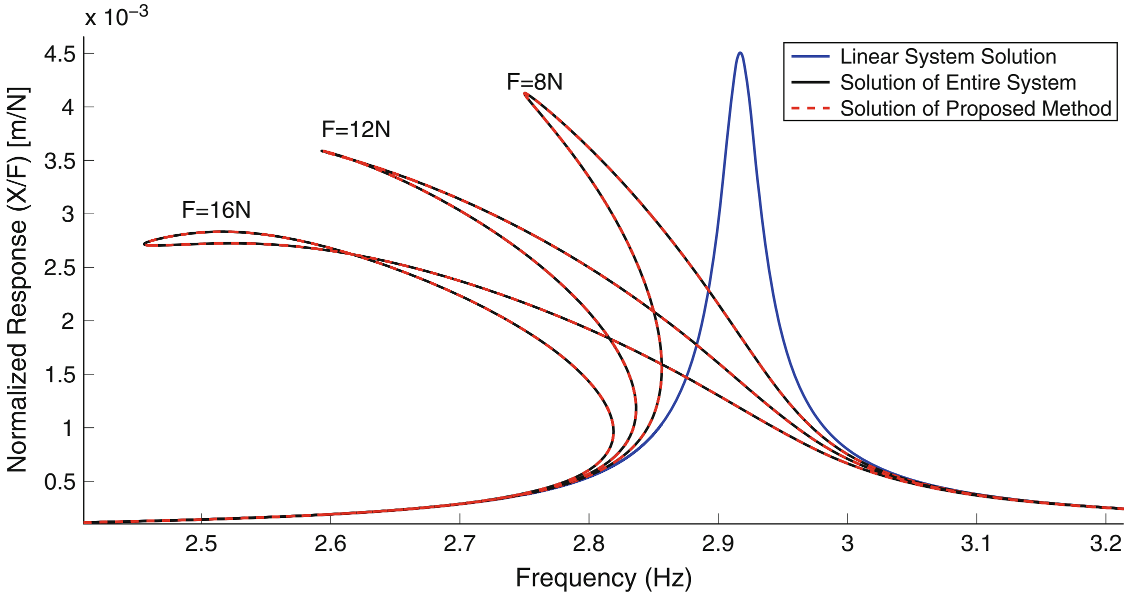

Fig. 15.6 Normalized response of the 8th DOF in case study 1

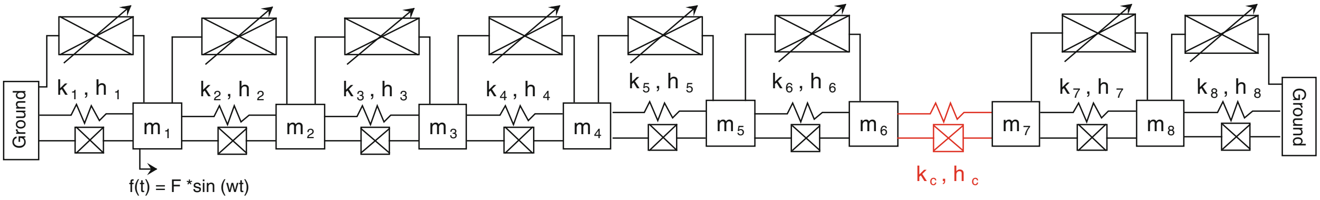

Fig. 15.7 Schematic view of 8-DOF coupled system

Table 15.4 Parameters of substructures *A* and *B*

Substructure *A*						Substructure *B*	
m_1 [kg]	m_2 [kg]	m_3 [kg]	m_4 [kg]	m_5 [kg]	m_6 [kg]	m_7 [kg]	m_8 [kg]
0.75	2	1	1	2	0.75	2	2
k_1 [N/m]	k_2 [N/m]	k_3 [N/m]	k_4 [N/m]	k_5 [N/m]	k_6 [N/m]	k_7 [N/m]	k_8 [N/m]
3,000	5,000	4,000	6,000	6,000	5,000	3,000	5,000
h_1 [N/m]	h_2 [N/m]	h_3 [N/m]	h_4 [N/m]	h_5 [N/m]	h_6 [N/m]	h_7 [N/m]	h_8 [N/m]
60	100	80	120	120	100	60	100

Table 15.5 Parameters of coupling elements

k_c [N/m]	h_c [N/m]
2,000	40

Table 15.6 Nonlinear elements of substructures *A* and *B* in case study 2

Nonlinear connection coordinates	Nonlinearity type	Nonlinearity coefficients
1-Ground	Cubic stiffness [N/m^3]	1×10^5
1-2	Cubic stiffness [N/m^3]	2×10^5
2-3	Cubic stiffness [N/m^3]	1×10^5
3-4	Dry friction [N]	μN
4-5	Cubic stiffness [N/m^3]	1×10^5
5-6	Cubic stiffness [N/m^3]	3×10^5
7-8	Cubic stiffness [N/m^3]	1×10^5
8-Ground	Dry friction [N]	μN

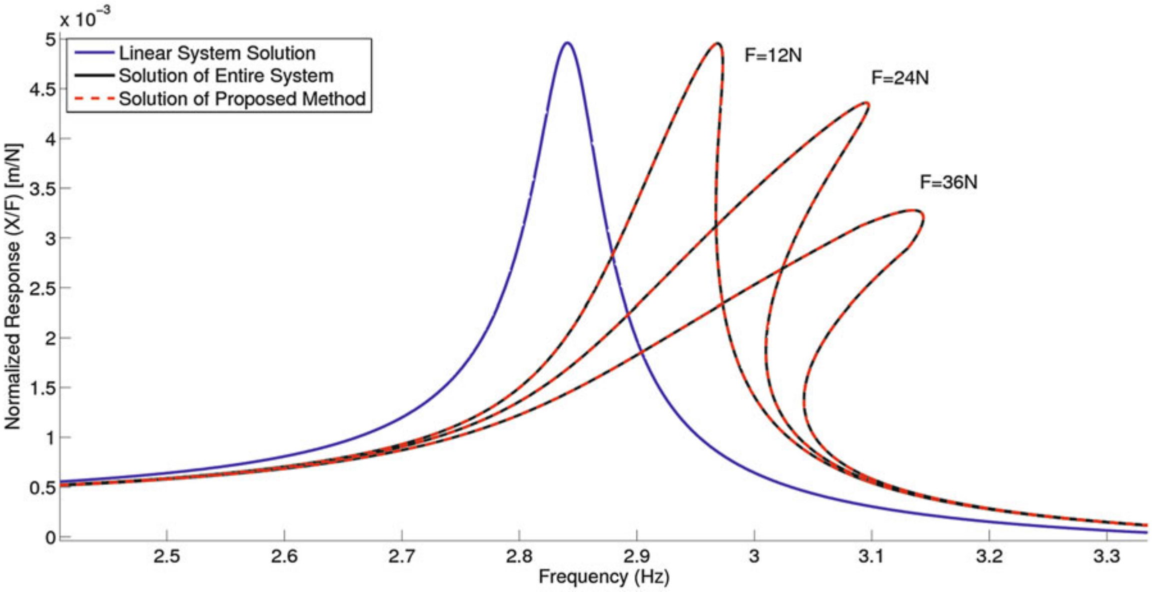

Fig. 15.8 Normalized response of the 1th DOF in case study 2

15.3.2 *Example 2: Coupling from Multiple DOFs*

In this section, a 6-DOF system is used as a case study as shown in Fig. 15.10. Parameters of substructures *A* and *B*, and coupling elements are given in Tables 15.7 and 15.8. The nonlinear elements used in the third case study, case study 3, are defined in Table 15.9.

Normalized response of the 1st DOF obtained from the proposed nonlinear coupling method and by solving the entire system directly is given in Fig. 15.11. The response of the system is obtained for three different excitation amplitudes, 6 N, 9 N and 12 N. It is observed that the results obtained from the proposed nonlinear coupling method and the entire system solution are in perfect agreement, for this case as well.

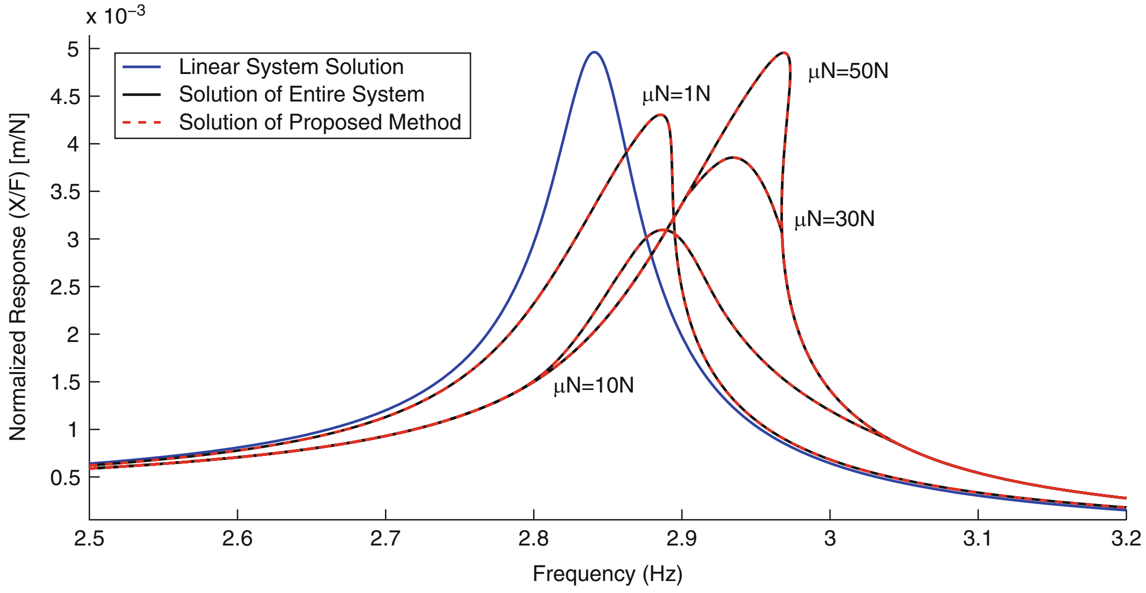

Fig. 15.9 Normalized response of the 1th DOF in case study 2

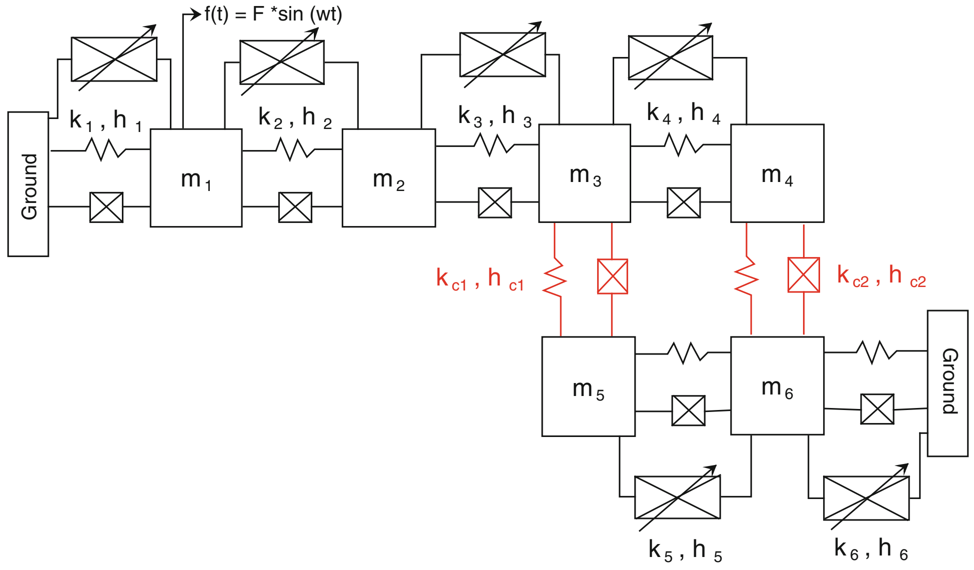

Fig. 15.10 Schematic view of 6-DOF coupled system

Table 15.7 Parameters of substructures *A* and *B*

Substructure *A*				Substructure *B*	
m_1 [kg]	m_2 [kg]	m_3 [kg]	m_4 [kg]	m_5 [kg]	m_6 [kg]
1	0,75	2	1	0,75	1
k_1 [N/m]	k_2 [N/m]	k_3 [N/m]	k_4 [N/m]	k_5 [N/m]	k_6 [N/m]
5,000	4,000	3,000	4,000	3,000	5,000
h_1 [N/m]	h_2 [N/m]	h_3 [N/m]	h_4 [N/m]	h_5 [N/m]	h_6 [N/m]
25	20	15	20	15	25

Table 15.8 Parameters of coupling elements

k_{c_1} [N/m]	h_{c_1} [N/m]	k_{c_2} [N/m]	h_{c_2} [N/m]
5,000	25	3,000	15

Table 15.9 Nonlinear elements of substructures *A* and *B* in case study 3

Nonlinear connection coordinates	Nonlinearity type [N/m^3]	Nonlinearity coefficients
1-Ground	Cubic stiffness	1×10^5
1-2	Cubic stiffness	2×10^5
2-3	Cubic stiffness	1×10^5
3-4	Cubic stiffness	2×10^5
5-6	Cubic stiffness	1×10^5
6-Ground	Cubic stiffness	2×10^5

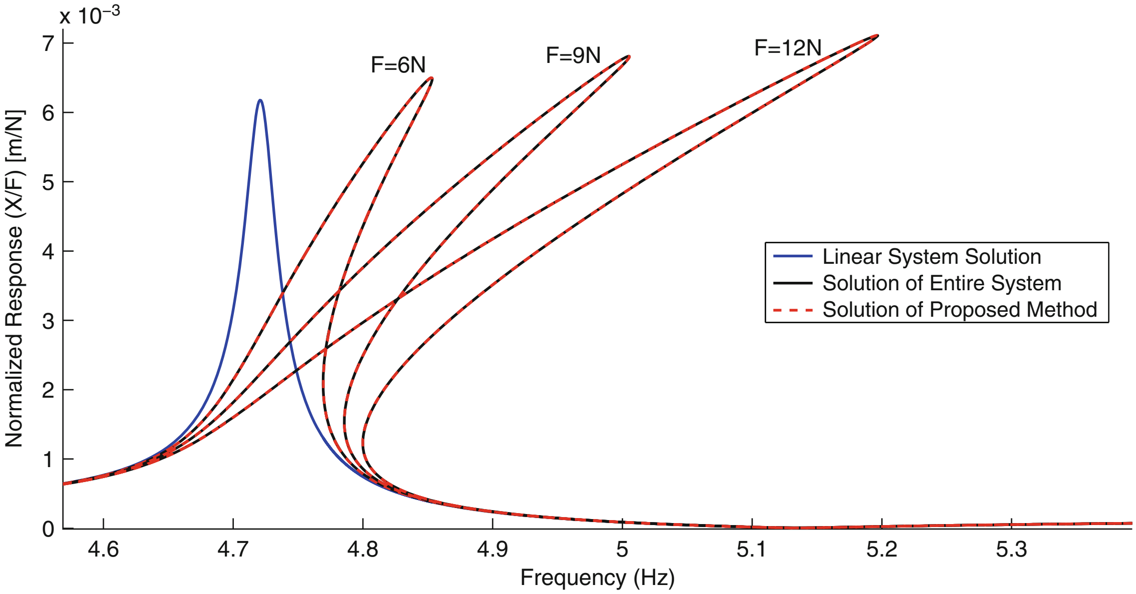

Fig. 15.11 Normalized response of the 1th DOF in case study 3

15.4 Discussion and Conclusion

In this paper, a new structural coupling method is introduced which is capable of coupling of two nonlinear substructures, where the connection elements can be nonlinear as well. Compatibility and equilibrium equations, which are derived from existing linear coupling methodology, are added to nonlinear equations of motions in order to model coupled system. The resulting nonlinear equations of motion of the coupled system are solved by using Newton's method with arc-length continuation. Cubic stiffness and hysteretic dry friction are used as nonlinear elements in the substructures. Applications of the proposed nonlinear coupling approach are demonstrated by numerical case studies. Two examples are considered in the case studies. In the first one two substructures are coupled from a single DOF; whereas, in the second example, two substructures are coupled from two DOFs. Normalized responses of the selected DOFs obtained from the proposed nonlinear coupling method and by solving the entire system directly are compared in order to verify the proposed method for different nonlinear systems. The results obtained from the proposed method and the ones obtained by directly solving the entire system agree perfectly with each other, which verifies the developed nonlinear coupling method.

References

1. Bishop RED, Johnson DC (1960) The mechanics of vibration. Cambridge University Press, New York
2. Hurty WC (1965) Dynamic analysis of structural systems using component modes. Am Inst Aeronaut Astronaut J 3:678–685
3. Craig RR, Bampton MCC (1968) Coupling of substructures for dynamic analysis. Am Inst Aeronaut Astronaut J 6:1313–1319
4. Rubin S (1975) Improved component mode representation for structural dynamic analysis. Am Inst Aeronaut Astronaut J 13:995–1006
5. Przemieniecki JS (1963) Dynamic analysis of structural systems using component modes. Am Inst Aeronaut Astronaut J 1:129–141
6. Urgueira APV (1989) Dynamic analysis of coupled structures using experimental data. Imperial College of Science, Technology and Medicine University of London, London

7. Ewins DJ (1986) Analysis of modified or coupled structures using frf properties. Internal report, Department of Mechanical Engineering, Imperial College of London, London
8. Klosterman AL, Lemon JR (1969) Building block approach to structural dynamic. America Society of Mechanical Engineering Annual Vibrations Conference 30, New York, 1969
9. Ren Y, Beards CF (1993) A generalized receptance coupling technique. 11th IMAC conference, Orlando, pp 868–871
10. Watanabe K, Sato H (1988) Development of nonlinear building block approach. J Vib Stress Reliab Des 110:36–41
11. Krylov N, Bogolyubov N (1947) Introduction to nonlinear mechanics. Princeton University Press, Princeton
12. van der Pol B (1927) Forced oscillations in a circuit with non-linear resistance. Lond Edinb Dublin Philos Mag J Sci 3:65–80
13. Taylor JH (1999) Describing functions, in electrical engineering encyclopedia. Wiley, New York
14. Budak E, Özgüven HN (1990) A method for harmonic responses of structures with symmetrical nonlinearities. In: Proceedings of the 15th international seminar on modal analysis and structural Dynamics, Leuven, vol 2, pp 901–915
15. Budak E, Özgüven HN (1993) Iterative receptance method for determining harmonic response of structures with symmetrical non-linearities. Mech Syst Signal Process 7(1):75–87
16. Tanrikulu Ö (1991) Forced periodic response analysis of non-linear structures for harmonic excitation. Master's thesis, Department of Mechanical Engineering, Imperial College, London
17. Tanrikulu Ö, Kuran B, Özgüven HN, Imregün M (1993) Forced harmonic response analysis of non-linear structures using describing functions. AIAA J 31(7):1313–1320
18. Cömert MD, Özgüven HN (1995) A method for forced harmonic response of substructures coupled by nonlinear elements. In: Proceedings of the 13th international modal analysis conference, Nashville, pp 139–145
19. Ferreira JV, Ewins DJ (1996) Nonlinear receptance coupling approach based on describing functions. In: Proceedings of 14th international modal analysis conference, Dearborn, pp 1034–1040
20. Ferreira JV (1998) Dynamic response analysis of structures with nonlinear components. Imperial College of Science, Technology and Medicine University of London, London, p 21, 1998
21. Chong YH, Imregun M (2000) Coupling of non-linear substructures using variable modal parameters. Mech Syst Signal Process 14(5): 731–746
22. Cigeroglu E, Özgüven HN (2006) Nonlinear vibration analysis of bladed disks with dry friction dampers. J Sound Vib 295:1028–1043
23. Cigeroglu E, Samandari H (2012) Nonlinear free vibration of double walled carbon nanotubes by using describing function method with multiple trial functions. Physica E 46:160–173
24. Boral C, Cigeroglu E, Korkmaz I (2010) Effect of intentional dry friction damping on the performance of an elastomeric engine mount. In: Proceedings of the ASME 2010 10th biennial conference on engineering systems design and analysis, Istanbul, pp 59–66